

An Assessment of the Sensitivity of a Low Pressure
Time Projection Chamber to the Direction of
WIMP-Induced Nuclear Recoils

by

Shawn Wesley Henderson

B.S. in Physics, University of Kansas (2006)

B.S. in Mathematics, University of Kansas (2006)

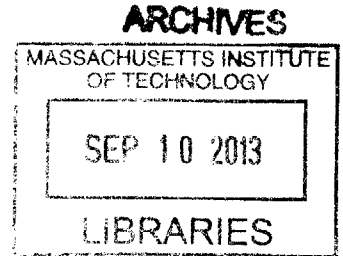
Submitted to the Department of Physics
in partial fulfillment of the requirements for the degree of
Doctor of Philosophy

at the

MASSACHUSETTS INSTITUTE OF TECHNOLOGY

September 2013

© Massachusetts Institute of Technology 2013. All rights reserved.



Author
Department of Physics
July 27, 2013

Certified by
Peter Fisher
Professor of Physics
Thesis Supervisor

Certified by
Jocelyn Monroe
Assistant Professor of Physics
Thesis Supervisor

Accepted by
John Belcher
Professor of Physics
Associate Department Head for Education

An Assessment of the Sensitivity of a Low Pressure Time Projection Chamber to the Direction of WIMP-Induced Nuclear Recoils

by

Shawn Wesley Henderson

Submitted to the Department of Physics
on August 34, 2013, in partial fulfillment of the
requirements for the degree of
Doctor of Philosophy

Abstract

Direct directional detection of dark matter could provide an unambiguous observation of dark matter due to the predicted directional anisotropy of dark matter particles in the galactic reference frame. The Dark Matter Time Projection Chamber (DMTPC) collaboration develops TPCs with optical readout whose goal is the detection of the sense and direction of nuclear recoils generated by dark matter interactions with carbon and fluorine atoms in low pressure CF_4 gas, from which the direction of the incident dark matter particle can be inferred. The TPC contains a mesh based amplification stage that facilitates the two-dimensional imaging of nuclear recoil tracks using CCD cameras. Reconstructing the direction of recoils has been a subject of intensive R&D over the past several years, culminating in the design and construction of a current generation detector, the “4-shooter.” The 4-shooter is prototyping several new detector techniques for a larger (1 m^3) detector. The third dimension of recoils will be reconstructed in this detector using PMTs and the timing of induced charge signals in the detector amplification region. The 4-shooter’s performance has been studied extensively on the surface of the Earth at MIT using alpha particles, low energy neutrons, and X-rays. This thesis reports on surface commissioning data taken with the 4-shooter.

Thesis Supervisor: Peter Fisher
Title: Professor of Physics

Thesis Supervisor: Jocelyn Monroe
Title: Assistant Professor of Physics

Acknowledgments

Foremost I would like to thank my family whose unfailing love and support made this work possible. My mother Marilyn, my father Wes, my sister Katie, my mother's parents Jimmy and Geneva, and my father's parents, Betty and Dex.

Warmest thanks to Dave Besson, my undergraduate advisor at the University of Kansas, whose mentorship continues to exert a profoundly positive influence on my life.

I am very thankful to my advisors, Peter Fisher and Jocelyn Monroe, for their support and guidance. I'd also like to thank my thesis committee, Joseph Formaggio and Jesse Thaler.

I am thankful to have had the opportunity to work closely with Jeremy Lopez and Cosmin Deaconu, the two other graduate students in my group, and under James Battat when he was a postdoc at MIT. I am grateful that Jeremy, Cosmin, and James have allowed me to include some of their work in this thesis, where it helped to enhance my work. I am very grateful to James whose mentorship and support has far exceeded what was required of him.

None of this work would have been possible without the excellent support and staff of the Laboratory for Nuclear Science at MIT. I'd like to thank former administrative assistant Sheela Marston for her kindness to me. I would also like to thank Mark Belanger, the manager of the Edgerton Center Shop, for his guidance and incredible patience.

A big thanks to my friends at MIT for their support over the last 7 years. I'd particularly like to thank Parthi Santhanam, Rachel VanCott, Donny Winston, Beth Quill, Steve Jaditz, Jim Hays-Wehle, and Steven Kleiner for their support.

Last but not least, I am grateful to Caterina Schweidenback for her continual love and support.

Contents

List of Figures	11
List of Tables	33
1 Introduction	37
1.1 Direct detection	39
1.2 Directional direct detection	43
2 High Energy Neutron Backgrounds : The Neutron Veto	49
2.1 The Neutron Veto Detector	50
2.1.1 Liquid scintillator	50
2.1.2 Optics	52
2.1.3 Electronics and readout	54
2.2 LANSCE Weapons Neutron Research Facility	54
2.2.1 Purpose	55
2.2.2 Experimental configuration	56
2.2.3 Data sets	57
2.2.4 Event selection	59
2.2.5 Results	67
2.3 Waste Isolation Pilot Plant	73
2.3.1 Purpose	73
2.3.2 Experimental configuration	74
2.3.3 Data sets	76

2.3.4	Analysis and event selection	76
2.3.5	The flux at WIPP not due to muons	83
2.4	Conclusions	84
3	The 4-shooter detector	89
3.1	Detector internals	89
3.2	Vacuum and gas	99
3.3	The proto-typical event	100
3.3.1	Trigger	102
3.3.2	Optical sensors	102
3.3.3	Charge sensors	108
3.4	Software	114
3.4.1	Data acquisition and slow control	114
3.4.2	Off-line analysis	116
3.4.3	Monte Carlo	120
4	Detector calibration	123
4.1	Charge coupled devices	124
4.1.1	Total CCD Noise Per-Pixel	125
4.1.2	Gain spatial dependence	126
4.1.3	Energy scale	130
4.1.4	Length Calibration	141
4.2	Central anode electrode charge readout	143
5	²⁴¹Am-Be(α,n) directionality study	147
5.1	Detector operation and configuration	147
5.2	Data sets	153
5.3	Event selection	155
5.4	Data-Monte Carlo comparisons	166
5.4.1	Monte Carlo bias and resolution	168
5.4.2	Data-Monte Carlo comparisons	174

6	Conclusions and outlook	191
6.1	Nuclear recoil detection efficiency	191
6.2	Sensitivity to the WIMP-induced nuclear recoil direction	195
6.3	Sensitivity to the WIMP-matter interaction cross-section	197
6.4	Sensitivity to the WIMP-wind direction	201
6.5	Conclusions	203
7	Bibliography	207

List of Figures

1-1	A composite optical, X-ray (in red), and weak lensing (in blue) image of the Bullet cluster (1E 0657-558), two galaxy clusters that collided approximately 100 million years ago [1]. The red X-ray intensity traces the baryon density in the two clusters, while the blue traces the majority of the mass in the two clusters as inferred from weak lensing observations, indicating that the majority of the matter in the two clusters was undisturbed by their collision.	37
1-2	The predicted differential rate of WIMP- ¹⁹ F recoils per kg per day in the energy of the fluorine recoils, assuming a total spin-dependent WIMP- ¹⁹ F interaction cross-section of 1 picobarn. The differential rate is shown for three hypothetical WIMP masses, 10 GeV/c ² , 100 GeV/c ² , and 1000 GeV/c ² . The details of how these curves are computed are given at the beginning of Chapter 6.	42
1-3	The predicted differential rate of WIMP- ¹⁹ F recoils per kg per day in the angle γ of fluorine recoil directions from the mean WIMP-wind direction. The differential rate is shown for a 100 GeV/c ² hypothetical WIMP mass, for fluorine recoil energy detection thresholds of 25 keV, 50 keV, and 100 keV. The differential rates for each threshold have been scaled to have unit normalization. The method used to compute these curves is given at the beginning of Chapter 6. A strong preference for the fluorine recoils to scatter along the WIMP-wind direction is evident, particularly for recoils with large energies.	44

1-4	All known limits set on the spin-dependent WIMP-proton interaction cross-section σ_{xp}^{SD} by dark matter direct detection experiments with some sensitivity to the direction of nuclear recoils. Limits set on the Earth's surface include those by NEWAGE (2007) [64] and DMTPC (2011) [65]. Limits have been set underground by DRIFT-IIId (2012) [46] and NEWAGE (2010) [48]. Unpublished underground limits presented at CYGNUS2013 [66] are shown from DRIFT-IIId (2013) [67, 68] and NEWAGE (2013) [66]. Also shown are the best limits on σ_{xp}^{SD} obtained to date by direct detection experiments without directional sensitivity [69], including results from the PICASSO (2012) [24], SIMPLE (2012) [23], and COUPP (2012) [17] experiments.	47
2-1	A CAD drawing of the neutron detector. Given dimensions are in inches.	51
2-2	A close-up of one of the two neutron detector photo-multiplier tubes (PMTs) showing how it is coupled to the active liquid scintillator volume.	51
2-3	The neutron interaction cross-section as a function of neutron kinetic energy for elemental hydrogen and carbon, taken from the ENDF/B-VII.1 database [83], both elastic and total. Also shown are the elemental hydrogen, carbon and BC-517L liquid scintillator neutron interaction cross-sections in the GEANT4 LHEP_BERT_HP physics list. On the right, the neutron on BC-517L interaction cross-section has been converted into the corresponding neutron interaction length. The blue axis only applies to the blue curve.	53
2-4	An overlay of the XP4500B PMT quantum efficiency [85] and the emission spectrum of BC-517L liquid scintillator [80] versus photon wavelength. Also shown is a reference curve for the optical transmission versus photon wavelength of 7740 Pyrex [84], although the curve shown is for 3.2 mm thick glass.	55

2-5	The neutron flux at the Los Alamos National Lab (LANL) Weapons Neutron Research Facility (WNR) [91] versus neutron kinetic energy with the neutron transmission probability through 4" of polyethylene versus neutron kinetic energy overlaid in red. 4" of polyethylene was placed in the beam between the neutron source and the detector to absorb low energy neutrons. The left, black axis corresponds to the black curve while the right, red axis corresponds to the red curve. . .	58
2-6	Left, a photograph of the configuration of the neutron detector for the calibration at LANL. The detector is on the left, a LANL fission ionization chamber is shown in the center of the image, and the stainless-steel beam collimator is shown in the upper right. Right, a schematic of the configuration of the neutron detector at LANL, as viewed from above.	59
2-7	A block diagram of the triggering logic at LANL for neutron data-taking. N1 and N2 correspond to the two PMTs coupled to the detector. V1 and V2 correspond to the two plastic scintillator veto paddles. The T0 logic signal derived from the proton beam is used to trigger readout of the detector.	60
2-8	A typical LANL neutron event on the four neutron detector channels. Channels 1 and 2 are the detector PMTs. Channels 3 and 4 are the plastic scintillator veto paddles. Channels 2, 3 and 4 have been offset from 0V by -0.8V, -1.6V and -2.0V, respectively, so that all channels are simultaneously visible.	62
2-9	Fission ionization chamber raw ADC spectrum showing the neutron selection cut and the fits used to estimate alpha contamination. Events above 198 ADC units are selected as good neutron candidates. The majority of events below 198 ADC units are due to the spontaneous α decay of ^{238}U . The red and blue curves are gaussian fits to the α and neutron distributions used to estimate the number of α particles which leak into the signal region (the red hatched region) and the number of neutrons which leak out of the signal region (the blue hatched region).	63

2-10	The time-of-flight (TOF) spectra in the fission ionization chamber and the neutron detector, after all selection cuts have been applied. Two datasets for the fission ionization chamber are shown. The high statistics (blue) fission ionization chamber run was taken with less restrictive collimation of the neutron beam in order to precisely determine the position of the γ -flash in the fission ionization chamber Time of flight (TOF) spectrum.	65
2-11	Counts versus kinetic energy for the neutron detector and fission ionization chamber datasets, after all selections. The fission ionization chamber spectrum has been scaled by a factor of 257, roughly the difference in neutron interaction cross-section between the two detectors, so that their features may be more easily compared.	67
2-12	The neutron interaction cross-section as a function of neutron kinetic energy for neutron-induced fission on ^{238}U in the fission ionization chamber. Data taken from ENDF [83] and unpublished LANL measurements [92].	69
2-13	The denominator in red (the neutron interaction cross-section-corrected fission ionization chamber neutron energy spectrum) and numerator in black (the dead-time-corrected neutron detector neutron energy spectrum) of the detector neutron efficiency measurement (see Figure 2-14).	70
2-14	The neutron detection efficiency measured at LANL as a function of neutron kinetic energy with statistical and systematic errors. The gray bars indicate the statistical errors in each bin alone.	71
2-15	Left, a photograph of the configuration of the neutron detector at WIPP. The detector is at the bottom of the image, about a foot above the floor of the Dark Matter Time Projection Chamber (DMTPC) underground laboratory. Right, a schematic of the configuration of the neutron detector at WIPP, as viewed from above.	75

2-16	A block diagram of the triggering scheme at WIPP. V1 and V2 are the two detector PMTs. The trigger at WIPP was formed from the coincidence of the two detector PMT outputs using Nuclear Instrument Module (NIM) logic units.	75
2-17	The number of events recorded by the detector at WIPP versus time and the trigger rate per each 100 events versus time, with and without the selection cuts described in Section 2.3.4.	76
2-18	A typical WIPP coincidence event which passes the analysis cuts of Section 2.3.4. Channels 1 and 2 are the two detector PMTs. Channel 2 has been offset from 0V by -1.5V so that both channels are simultaneously visible	77
2-19	Single-photo-electron (PE) spectra from both PMTs measured <i>in situ</i> at WIPP in the exact same detector configuration as normal data-taking. Also shown are gaussian fits to these spectra used to extract the mean charge corresponding to 1 PE in each PMT. The upper edge of the noise pedestal is simultaneously fit by an exponential.	78
2-20	A schematic illustrating the setup for the single-PE characterization measurements at WIPP. A Light-Emitting Diode (LED) was driven with the same square voltage pulse used to trigger readout of the two detector PMTs. The amplitude of the voltage pulse was adjusted until many fewer than one photon arrived at each PMT per pulse, allowing a measurement of each PMT's <i>in situ</i> single photo-electron response.	79
2-21	Right, the PE-asymmetry A_{PE} for data taken at WIPP. Events in the red hatched regions are cut by selection WIPP-V. The PE-asymmetry is plotted only for events with fewer than 50,000 PE on both PMTs. Left, the PMT PE spectra in both detector PMTs, after all selection cuts, including $ A_{PE} < 0.5$	81

2-22	Left, the total detector PE spectrum with a Landau and exponential background fit to extract the energy scale. The energy calibration is obtained by comparing the most probable value of the fitted data Landau distribution to the expected most probable energy loss of muons in the detector from a GEANT4 Monte Carlo model. Right, the energy spectrum obtained after applying this calibration.	81
2-23	Left, the difference in reconstructed start time for the pulses on the two detector PMTs, $\Delta T_{\text{start}} = T_1^{\text{start}} - T_2^{\text{start}}$, for events that pass all selection cuts. Shown in blue, red and green are gaussian fits to ΔT_{start} for narrow slices of PE-asymmetry, $ A_{PE} $. Right, the fitted mean gaussian ΔT_{start} for narrow slices of $ A_{PE} $. For $ A_{PE} < 0.5$ the relationship is linear and given by Equation 2.7.	82
3-1	An image of the 4-shooter detector in Building 24, Room 036 at MIT. The vacuum vessel is open, showing the Time Projection Chamber (TPC). The four blue charged-coupled device (CCD) cameras are visible at the top of the image.	90
3-2	a close-up image of the field cage with the vacuum bell-jar removed. The resistor chain which distributes voltage over the TPC field cage rings is visible on the left and the right, running along the white delrin field cage support posts.	92
3-3	A CAD drawing of the field cage as seen from the side.	93
3-4	A CAD drawing of the anode plate with dimensions and electrodes labeled. All given dimensions are in inches.	94
3-5	A close-up image of the fully assembled amplification stage showing the amplification stage mesh and spacers (the vertical lines) epoxied to the anode plate. Unlike the 4-shooter's anode, this anode has been polished to enhance light collection.	95

3-6	Left, the high-voltage feedthrough used to power the 4-shooter's cathode, inside of its custom light-tight cover, on the underside of the baseplate of the 4-shooter vacuum vessel. The red cable delivers voltage to the feedthrough. Right, the same feedthrough but with its custom light-tight cover removed. The inside of the cover and its Buna-N o-ring are shown in the lower left.	96
3-7	Left, the vacuum-side electrical connection to the two central anode electrodes. The vacuum-side of the feedthrough is visible on the lower right of the image. The insulated high-voltage wires connect to the vacuum-side of the feedthrough with beryllium copper set-screw connectors, and to the anode through eyelet connectors held in place with #0-80 nylon screws. The nylon screws are secured on the underside of the anode by a shared rectangular G-10 washer and stainless-steel nuts. Right, the vacuum-side electrical connection to the amplification mesh. The connection scheme is identical to the other two anode connections excepting a rectangular copper washer on the top of the anode which holds a small patch of mesh captive against the outer annular electrode of the anode, ensuring electrical contact with the mesh. . .	97
3-8	A schematic of the 4-shooter gas and vacuum system.	99
3-9	A typical curve showing the pressure in the 4-shooter over the course of an evacuation and CF ₄ refill. The capacitance diaphragm gauge bottoms out at approximately 0.3 Torr, and the Bayard-Alpert Pirani (BAP) combination gauge is used to measure very low pressures in the detector. Note the discrepancy between the two gauges above 1 Torr due to the gas dependence of the BAP gauge.	101
3-10	Data from Run 07723, event 953, scope trigger #7. Zooms of the charge waveforms are given in Figures 3-14, 3-17, and 3-19. A nuclear recoil is present in CCD 100534 at $(X, Y) \approx (300 \text{ px}, 700 \text{ px})$. A close-up of this recoil is shown in Figure 3-20.	103

3-11	Schematic of the top flange of the 4-shooter showing the layout of the four 6" CF ports for the CCDs and the center 2 ³ / ₄ " CF port for the PMTs. Dimensions are in inches.	104
3-12	Cut-away of the assembled 6" CF optical feedthrough and mount for the 4-shooter CCDs.	106
3-13	Exploded view of PMT coupling parts with labels. At the lower right is the 2 ³ / ₄ " CF optical feedthrough that couples the PMT assembly to the 4-shooter. Electrical connections to the PMTs (not shown) are made through the holes in the circular plate in the upper left.	107
3-14	The three PMT signals from the nuclear recoil event in Figure 3-10 overlaid in black, red and blue. A bandwidth mismatch between the PMTs and the digitizer generates considerable parasitic after-pulsing.	108
3-15	Overlay of the Hamamatsu R7400U-20 PMT's quantum efficiency, the Apogee U6 CCD's quantum efficiency, the CF ₄ transmission spectrum, [113] and the PMT and CCD window light transmission versus wavelength.	109
3-16	Simplified equivalent circuit of the 4-shooter detector including the TPC electrodes and charge readout channels. In the bottom right, from left to right, are the amplifiers connected to the grounded amplification stage mesh, the outer veto ring electrode on the anode of the amplification stage, and the central electrode on the anode of the amplification stage. Also shown, in the bottom left, are the high voltage supplies used to bias the TPC electrodes. Solid black lines denote electrical connections.	110
3-17	The fast amplifier mesh signal from the nuclear recoil event in Figure 3-10. The two-peaked shape of this pulse is characteristic of nuclear recoils, and is exploited to discriminate between nuclear recoils and energy depositions due to other particles interacting in the detector like electrons or γ -rays [71, 114].	111

3-18	Filter used for the $\pm 12V$ power inputs of the mesh HS-AMP-CF amplifier. The filter is designed to eliminate high frequency noise from low frequency signal lines.	111
3-19	The anode and veto signals from the nuclear recoil event in Figure 3-10. Even though the nuclear recoil did not occur over the veto electrode, a small signal is present on the veto channel due to cross-talk between the two electrodes.	112
3-20	A close-up of the nuclear recoil event in Figure 3-10 in CCD 100534. The yellow halo shows the boundaries of the track as determined by the seed cluster track finding algorithm in <code>cleanSkim</code> . The white arrow shows the two-dimensional vector direction reconstructed for this track based on its principle axes and ionization profile. The subset of the CCD image shown is $14.436 \text{ mm} \times 14.436 \text{ mm}$, the track has a projected range of 8.36 mm, and the track has a total energy of 417 keV_{ee}	119
4-1	For each 4-shooter sensor, a list of the characteristics of tracks in the detector to which that sensor is known to have sensitivity. Only the calibration of the bold entries under each sensor heading will be discussed in this chapter.	123
4-2	The total noise in ADU per pixel in each CCD, as a function of exposure time, as determined from differencing dark frames as described in Section 4.1.1. The fit error on the total noise is less than 0.3% and is smaller than the data points. For exposures of length 10 sec or less with the Alta U6 CCD, the total noise is dominated by the CCD read-noise. Each plot is labeled by its corresponding CCD in the upper left. . .	126

- 4-3 A map of the relative pixel-to-pixel gain variations in the 4-shooter CCDs, obtained with a radioactive ^{57}Co source as described in Section 4.1.2. The spacers are clearly visible as locations of reduced gain. The exposures have been stitched together to form a composite mosaic image, based on the known relative positioning of the four 4-shooter cameras. The intensity scale is arbitrary, although red areas correspond to high gain zones, and blue to low gain zones. 129
- 4-4 A comparison for each of the four 4-shooter CCDs, of direct measurements of the decrease in relative light intensity with increasing radius from the center of each CCD's image due to total optical vignetting in red [130] and the observed radial decrease in the relative gain with a ^{57}Co source in black. Each plot is labeled by its corresponding CCD in the upper left. 130
- 4-5 Four ^{241}Am α tracks emitted by sources in each of the four cameras during a typical α energy calibration described in Section 4.1.3. The exposures have been stitched together to form a composite image, based on the known relative positioning of the four 4-shooter cameras. The images are actually from different events, but the same run. The dashed white circle shows the circular boundary of the central anode electrode of the amplification stage. 132
- 4-6 Typical spectra from a ^{241}Am α calibration dataset in one CCD with the cuts in Section 4.1.3 shown as dashed red lines. Upper left, the energy spectrum and cut $^{241}\text{Am-V}$. The second peak just above 60,000 ADU corresponds to pile-up events where two α tracks are emitted on top of one another in the same exposure and are reconstructed as one track. Upper right, the projected range distribution and cut $^{241}\text{Am-IV}$. Lower left, the two-dimensional angle ϕ distribution and cut $^{241}\text{Am-VII}$. Lower right, the α energy versus projected range with a box overlaid corresponding to cuts $^{241}\text{Am-IV}$ and $^{241}\text{Am-V}$ 133

4-7	The average longitudinal projection of α tracks in a typical calibration dataset (black) compared with the tuned Monte Carlo prediction (red), for data taken in 60 Torr CF ₄ . The normalization of the Monte Carlo curve has been fit to the data to extract the total CCD gain in ADU/keV _{ee} . Each plot is labeled by its corresponding CCD in the upper left.	135
4-8	The lateral electron diffusion coefficient as a function of drift distance determined from the transverse width of α tracks in calibration datasets taken with ²⁴¹ Am α sources at varying heights z above the amplification stage in the 4-shooter. The diffusion coefficient is determined by tuning its value in the Monte Carlo until agreement is obtained with the average transverse width of α tracks in the data. Determined in this way at a variety of heights, the z -dependence of the coefficient is extracted with the line fit shown. Each plot is labeled by its corresponding CCD in its legend.	137
4-9	The measured CF ₄ transverse electron diffusion coefficient $\sigma_{T,z}$ in mm (see Equation 3.2) for -5000 kV cathode bias with the four 4-shooter CCDs. Overlaid is the recommended transverse diffusion coefficient as a function of cathode bias from Christophorou <i>et al.</i> [115].	138
4-10	The CCD gain in ADU/keV _{ee} for the four 4-shooter cameras as a function of source height z above the amplification stage measured with ²⁴¹ Am α tracks in 60 Torr CF ₄ . No systematic variation is observed with source height. Each plot is labeled by its corresponding CCD in its legend.	140
4-11	The amplification stage discharge rate versus amplification stage bias voltage with ²⁴¹ Am α sources at different heights z above the amplification stage in 60 Torr CF ₄ . As the sources are moved closer to the amplification stage, the discharge rate in the amplification stage is observed to systematically increase for a fixed bias voltage.	142

- 4-12 Images taken while the 4-shooter anode was under LED illumination. The exposures have been stitched together to form a composite image, based on the known relative positioning of the four 4-shooter cameras. Features with well known physical dimensions are clearly visible like the veto and anode electrode boundaries, the spacers, and the inner edges of the TPC field cage rings. The bright red spot in the lower right is a reflection of the LED used to illuminate the chamber. . . . 143
- 4-13 Left, a typical ^{55}Fe event in 60 Torr CF_4 corresponding to a $5.9 \text{ keV}_{\text{ee}}$ X-ray. Right, the spectrum of many ^{55}Fe events in 60 Torr CF_4 with 600 V bias on the amplification stage and -5 kV on the drift stage clearly showing a $5.9 \text{ keV}_{\text{ee}}$ X-ray line. The red curve shows a Crystal Ball function fit to the spectrum used to extract the energy scale. A Crystal Ball function is a gaussian with a low energy power law tail. . 144
- 4-14 Left, from left to right in the figure, the ^{55}Fe -derived gas gain versus anode bias voltage for 45 Torr, 60 Torr, and 75 Torr. Right, the ^{55}Fe -derived gas gain as a function of time over a 24 hour period. This dataset was taken in 75 Torr CF_4 with 720 V bias on the amplification stage and -5 kV on the drift stage. The data on the right was taken without attenuating the ^{55}Fe source, resulting in a systematically lower measured gain than in the left figure, as discussed in the text. 145
- 5-1 Schematic of the Am-Be source and 4-shooter setup as described in Section 5.1. These drawings are to scale. Top, a view of the setup from the side. Bottom, a view from above, with the source pointing to the left. The four 4-shooter cameras and their relative orientation to the source direction is illustrated by blue and magenta arrows. For each CCD, the blue arrow points in the $\phi = 0$ direction and the magenta arrow points in the $\phi = +\pi/2$ direction. 148

5-2	A photograph of the Am-Be setup sketched in Figure 5-1. The Am-Be source is in the center of the image, underneath a sheet of RICORAD, and behind a single lead brick, on the cart with wheels. The 4-shooter is on the right in the image, and the edge of the 4-shooter electronics rack is just visible on the far right.	149
5-3	The red curve shows the neutron energy spectrum from a typical $^{241}\text{Am-Be}(\alpha, n)$ source [146]. Overlaid on the Am-Be spectrum are the neutron-carbon and neutron-fluorine total (solid curves) and elastic (dashed curves) interaction cross-sections spanning the Am-Be neutron energies. The cross-sections have been taken from ENDF [83] . .	150
5-4	Spark rate contours in CF_4 pressure and gas gain, sampled at 15 Torr, 30 Torr, 45 Torr, 60 Torr and 75 Torr CF_4 pressure. The gas gain for the 15 Torr and 30 Torr pressure points are estimated based on linear fits to the pressure dependence of the parameters in Equation 4.3. . .	151
5-5	The amplification stage discharge rate versus amplification stage bias without the Am-Be source present, with the Am-Be source present and no shielding between the source and the 4-shooter, and with 2" of lead between the Am-Be source and the 4-shooter. Measurements in 60 Torr CF_4 . The spark rate is noticeably higher in the presence of the Am-Be source, even after the detector has been shielded from the Am-Be source's γ and X-rays with 2" of lead.	152
5-6	Am-Be nuclear recoil candidates, 60 Torr CF_4 , 670V bias on the amplification stage, and -5 kV on the drift stage. From left to right moving down the rows, a 105 keV _{ee} recoil in CCD 110121, a 148 keV _{ee} recoil in CCD 110121, a 171 keV _{ee} recoil in CCD A80333, a 116 keV _{ee} recoil in CCD A80334, a 243 keV _{ee} recoil in CCD 100534, a 168 keV _{ee} recoil in CCD A80333, a 65 keV _{ee} recoil in CCD A80333, a 303 keV _{ee} recoil in CCD A80333, and a 132 keV _{ee} recoil in CCD 100534. Each image is 14.44 mm on a side.	154

5-7	Nuclear recoil candidate locations (mean positions) in each camera for the Am-Be run. Scatter plot, for each 4-shooter CCD of the centroids of nuclear recoil candidates without fiducialization cuts AMBE-III, AMBE-IV and AMBE-V in black, and after these cuts in red. Each plot is labeled by its corresponding CCD in the upper left.	158
5-8	Left, a discharge in the amplification stage. The exposures have been stitched together to form a composite image, based on the known relative positioning of the four 4-shooter cameras. The discharge occurred in the bottom right CCD, near $(X, Y) = (400 \text{ px}, -200 \text{ px})$. The scale is in CCD ADU counts, and the log of the intensity is plotted in each pixel. Right, the upper left panel is a closeup of the spark on the left. From left to right moving down the rows, the 1-second exposures immediately following the anode discharge are shown, exhibiting a residual image in the CCD at the discharge position that fades gradually with time.	159
5-9	The black line shows the mean ^{55}Fe peak-height as a function of time on the central anode preamplifier, measured as described in Section 4.2. During the time period shown, the 4-shooter amplification stage discharged twice, leading to a loss of gain. Overlaid in blue is the current drawn by the anode bias high voltage supply, in which the discharges are detected as spikes in the current drawn by the supply. Nuclear recoil candidates occurring in the red hatched time intervals are cut by AMBE-VIII due to their proximity in time to the discharges sensed on the supply current monitor.	160
5-10	Am-Be nuclear recoil candidates, 60 Torr CF_4 , 670V bias on the amplification stage, and -5 kV on the drift stage. The difference between the energy of the recoils determined with the CCDs, E_{CCD} , and the energy determined with the charge integrating preamplifier, E_{anode} . The red dashed lines illustrate events cut by AMBE-XII. Each plot is labeled by its corresponding CCD in the upper left.	163

- 5-11 The fisher discriminant of cut AMBE-XIII applied to its training datasets, data taken with the TPC voltages off consisting entirely of CCD artifacts (red) and Monte Carlo nuclear recoils (black). Each plot is labeled by its corresponding CCD in the upper left. In the Am-Be analysis, events with Fisher discriminant less than 0 are discarded as likely CCD artifacts. 164
- 5-12 The fisher discriminant of cut AMBE-XIII applied to the Am-Be dataset, with the charge cuts AMBE-IX through AMBE-XII (in black and gray) and without them (in blue). Each plot is labeled by its corresponding CCD in the upper left. The charge cuts are observed to eliminate the majority of events independently determined to be CCD artifacts by the Fisher discriminant analysis. 166
- 5-13 The neutron energy spectrum from a typical $^{241}\text{Am-Be}(\alpha,n)$ source [146] (black) and the energy spectrum predicted with GEANT4 for neutrons which make it into the TPC through the lead, air, stainless-steel, inactive CF_4 and copper in between the Am-Be source and the sensitive volume of the 4-shooter (blue) if the black curve is the Am-Be neutron energy spectrum at the source. Both histograms have been normalized such that the sum over all bins is equal to one. 167
- 5-14 Am-Be nuclear recoil Monte Carlo. The black points are the reconstructed CCD energy in ADU divided by the true recoil energy in keV_{ee} , versus the reconstructed energy. The dashed red line shows the $\text{ADU}/\text{keV}_{ee}$ gain specified in the Monte Carlo. The solid red line shows the rational polynomial fits used to estimate the energy reconstruction bias as a function of reconstructed energy as described in Section 5.4. The results of these fits are given in Equation 5.1. Each plot is labeled by its corresponding CCD in the upper left. 169

5-15	Am-Be nuclear recoil Monte Carlo. The residuals between the true energy of Monte Carlo nuclear recoils and the reconstructed CCD energy. The gray bars indicate the standard deviation of the residuals in each energy bin. Each plot is labeled by its corresponding CCD in the upper left.	171
5-16	Am-Be nuclear recoil candidates, 60 Torr CF ₄ , 670V bias on the amplification stage, and -5 kV on the drift stage. The recoil energy in keV _{ee} determined from the CCDs versus the recoil energy determined from the preamplifier on the amplification stage central electrode. The solid blue lines show the rational polynomial fits used to estimate the relationship between the two energy determinations. Only the magenta points are included in the fits. The black outlier points are not included in the fits because they fall 3 RMS deviations away from the mean value of the ratio of the CCD-derived energy to the charge-derived energy. Each plot is labeled by its corresponding CCD in the upper left. . . .	172
5-17	Am-Be nuclear recoil Monte Carlo. The black points are the reconstructed CCD projected range in mm versus the true recoil projected range in mm. The solid red lines show the line fits used to estimate the projected range reconstruction bias as a function of reconstructed projected range as described in Section 5.4. The dashed part of each red line is not included in the fits but is used to estimate the true projected range of recoils from the reconstructed projected range. The results of these fits are given in Equation 5.2. Each plot is labeled by its corresponding CCD in the upper left.	173
5-18	Am-Be nuclear recoil Monte Carlo. The residuals between the true projected range of Monte Carlo nuclear recoils and the reconstructed CCD projected range. The gray bars indicate the standard deviation of the residuals in each projected range bin. Each plot is labeled by its corresponding CCD in the upper left.	175

5-19	Am-Be nuclear recoil candidates, 60 Torr CF ₄ , 670V bias on the amplification stage, and -5 kV on the drift stage. Data energy distribution (black and gray) versus Monte Carlo energy distribution (red). The normalization of the Monte Carlo has been adjusted so that the data and Monte Carlo have the same number of events between 0 keV _{ee} and 200 keV _{ee} . Each plot is labeled by its corresponding CCD in the upper left.	176
5-20	Am-Be nuclear recoil candidates, 60 Torr CF ₄ , 670V bias on the amplification stage, and -5 kV on the drift stage. Data energy distribution (black and gray) versus Monte Carlo energy distribution (red) for energies less than 150 keV _{ee} . The normalization of the Monte Carlo has been adjusted so that the data and Monte Carlo have the same number of events between 0 keV _{ee} and 200 keV _{ee} . Each plot is labeled by its corresponding CCD in the upper left.	177
5-21	Am-Be nuclear recoil candidates, 60 Torr CF ₄ , 670V bias on the amplification stage, and -5 kV on the drift stage. Data projected range distribution (black and gray) versus Monte Carlo projected range distribution (red). The normalization of the Monte Carlo has been adjusted so that the data and Monte Carlo have the same number of events between 0 keV _{ee} and 200 keV _{ee} . Each plot is labeled by its corresponding CCD in the upper left.	178
5-22	Am-Be nuclear recoil candidates, 60 Torr CF ₄ , 670V bias on the amplification stage, and -5 kV on the drift stage. Data transverse width distribution (black and gray) versus Monte Carlo transverse width distribution (red). The normalization of the Monte Carlo has been adjusted so that the data and Monte Carlo have the same number of events between 0 keV _{ee} and 200 keV _{ee} . Each plot is labeled by its corresponding CCD in the upper left.	179

5-23	Am-Be nuclear recoil candidates, 60 Torr CF ₄ , 670V bias on the amplification stage, and -5 kV on the drift stage. Recoil energy versus projected range. Overlaid are SRIM-2006 predictions for the mean full recoil range versus energy for carbon (blue) and fluorine (red) recoils. Each plot is labeled by its corresponding CCD in the upper left. . . .	180
5-24	Am-Be nuclear recoil candidates, 60 Torr CF ₄ , 670V bias on the amplification stage, and -5 kV on the drift stage. The reconstructed ϕ in the readout plane in data versus Monte Carlo, for recoils with energies greater than 250 keV _{ee} and projected ranges greater than 4 mm. Each plot is labeled by its corresponding CCD in the upper left.	181
5-25	Am-Be nuclear recoil candidates, data versus Monte Carlo. 60 Torr CF ₄ , 670V bias on the amplification stage, and -5 kV on the drift stage. The fraction of recoil candidates whose reconstructed angle ϕ in the 4-shooter readout plane is within 90° of the mean Am-Be neutron direction in the readout plane as a function of energy. Each plot is labeled by its corresponding CCD in the upper left.	182
5-26	Am-Be nuclear recoil candidates, data versus Monte Carlo. 60 Torr CF ₄ , 670V bias on the amplification stage, and -5 kV on the drift stage. The fraction of recoil candidates whose reconstructed angle ϕ in the 4-shooter readout plane is within 45° of the mean Am-Be neutron axis in the readout plane. Each plot is labeled by its corresponding CCD in the upper left.	183
5-27	Am-Be nuclear recoil candidates, the reconstructed ϕ in the readout plane in data versus Monte Carlo, for recoils with energies between 0 keV _{ee} and 50 keV _{ee} (0 keV _r to 84 keV _r). 60 Torr CF ₄ , 670V bias on the amplification stage, and -5 kV on the drift stage. The solid blue line shows the expected mean ϕ of the Am-Be neutrons. Each plot is labeled by its corresponding CCD in the upper left.	185

- 5-28 Am-Be nuclear recoil candidates, the reconstructed ϕ in the readout plane in data versus Monte Carlo, for recoils with energies between 50 keV_{ee} and 100 keV_{ee} (84 keV_r to 148 keV_r). 60 Torr CF₄, 670V bias on the amplification stage, and -5 kV on the drift stage. The solid blue line shows the expected mean ϕ of the Am-Be neutrons. Each plot is labeled by its corresponding CCD in the upper left. 186
- 5-29 Am-Be nuclear recoil candidates, the reconstructed ϕ in the readout plane in data versus Monte Carlo, for recoils with energies between 100 keV_{ee} and 200 keV_{ee} (148 keV_r to 263 keV_r). 60 Torr CF₄, 670V bias on the amplification stage, and -5 kV on the drift stage. The solid blue line shows the expected mean ϕ of the Am-Be neutrons. Each plot is labeled by its corresponding CCD in the upper left. 187
- 5-30 Am-Be nuclear recoil candidates, the reconstructed ϕ in the readout plane in data versus Monte Carlo, for recoils with energies between 200 keV_{ee} and 300 keV_{ee} (263 keV_r to 367 keV_r). 60 Torr CF₄, 670V bias on the amplification stage, and -5 kV on the drift stage. The solid blue line shows the expected mean ϕ of the Am-Be neutrons. Each plot is labeled by its corresponding CCD in the upper left. 188
- 5-31 Am-Be nuclear recoil candidates, the reconstructed ϕ in the readout plane in data versus Monte Carlo, for recoils with energies between 300 keV_{ee} and 400 keV_{ee} (367 keV_r to 465 keV_r). 60 Torr CF₄, 670V bias on the amplification stage, and -5 kV on the drift stage. The solid blue line shows the expected mean ϕ of the Am-Be neutrons. Each plot is labeled by its corresponding CCD in the upper left. 189

6-1	Isotropic Monte Carlo ^{19}F recoils, assuming 60 Torr CF_4 , 670V bias on the amplification stage, and -5 kV on the drift stage. The nuclear recoil detection efficiency for CCD cuts only versus keV_T expected for isotropic fluorine recoils. The solid red line shows the error function fits used to estimate the nuclear recoil detection efficiency as a function of recoil energy as described in Section 6.1. The results of these fits are given in Equation 6.1. Each plot is labeled by its corresponding CCD in the upper left.	193
6-2	Am-Be nuclear recoil candidates, 60 Torr CF_4 , 670V bias on the amplification stage, and -5 kV on the drift stage. The ratio of the energy spectra with and without charge cuts AMBE-VIII through AMBE-XII, and with a very restrictive cut on the Fisher discriminant. Each plot is labeled by its corresponding CCD in the upper left.	194
6-3	For a sample of fixed recoil energies, the probability that the WIMP recoil is reconstructed within 45° of the WIMP wind axis, for each 4-shooter CCD, as a function of recoil energy for a $100 \text{ GeV}/c^2$, $1,000 \text{ GeV}/c^2$, and $10,000 \text{ GeV}/c^2$ mass WIMP. The dashed lines show the error function fits used to estimate the reconstructed nuclear recoil axial asymmetry as a function of recoil energy. Each plot is labeled by its corresponding CCD in the upper left.	197
6-4	For a sample of fixed recoil energies, the probability that the WIMP recoil is reconstructed pointing in the same hemisphere as the WIMP wind direction, for each 4-shooter CCD, as a function of recoil energy for a $100 \text{ GeV}/c^2$, $1,000 \text{ GeV}/c^2$, and $10,000 \text{ GeV}/c^2$ mass WIMP. The dashed lines show the error function fits used to estimate the reconstructed nuclear recoil forward/backward asymmetry as a function of recoil energy. Each plot is labeled by its corresponding CCD in the upper left.	198

- 6-5 The predicted detected WIMP- ^{19}F recoil rate per kilogram per day in the 4-shooter assuming a 1 picobarn WIMP- ^{19}F spin-dependent interaction cross-section $\sigma_{\chi F}^{SD}$ as a function of hypothetical WIMP mass. These curves are generated by integrating the predicted dark matter recoil rate from the MICROMEGAS [154] code against the 4-shooter nuclear recoil detection efficiencies for each CCD given in Equation 6.1. 199
- 6-6 The projected background-free sensitivity of the 4-shooter to the WIMP-proton spin-dependent interaction cross-section as a function of WIMP mass assuming a year of continuous operation (solid black line). The dashed black line shows the sensitivity achievable assuming zero backgrounds for a larger m^3 -sized detector if it had the same response to nuclear recoils as the 4-shooter. Also shown are the best limits on $\sigma_{\chi p}^{SD}$ obtained to date by direct detection experiments without directional sensitivity [69], including results from the PICASSO (2012) [24], SIMPLE (2012) [23], and COUPP (2012) [17] experiments. 200
- 6-7 Each curve represents the number of detected WIMP-induced nuclear recoils that would be required to observe a statistically significant asymmetry in the two-dimensional recoil direction, at a level of significance ξ where ξ is the ratio of the statistical error on the measured asymmetry to the measured asymmetry value. The cases $\xi = 1, 0.5,$ and 0.1 are considered for both a vector total recoil asymmetry ($\langle A_{\text{vector}}^{2D} \rangle$ in the text) and an axial total recoil asymmetry ($\langle A_{\text{axial}}^{2D} \rangle$ in the text). The energy dependence of the axial and vector recoil asymmetry given by Equation 6.3 was assumed to be the same as that for a $100 \text{ GeV}/c^2$ WIMP for WIMP masses less than $100 \text{ GeV}/c^2$ in making this plot. 203

List of Tables

1.1	Standard assumed astrophysical parameters associated with a smooth spherical isothermal dark matter halo used to compute the expected rate of WIMP-induced nuclear recoils in Earth-based dark matter direct detection experiments, from Behnke <i>et al.</i> [17]. v_0 is the Maxwellian dispersion velocity of the dark matter in the halo of the Milky Way, v_{\odot} is the Sun's velocity relative to the rest frame of the Milky Way, v_{esc} is the maximum speed a dark matter particle may have and still be bound in the Milky Way's halo, and ρ_{DM} is dark matter halo mass density at Earth.	40
2.1	The physical properties of BC-517L liquid scintillator most relevant to this detector's design and performance. The light yield of anthracene is 1 blue photon per 65 eV of deposited energy [81].	51
2.2	A list of all datasets taken at LANL. The datasets taken with the neutron detector are labeled by the date on which a run was started, while the fission ionization chamber datasets are labeled by a unique run number. N_{T0} is the number of micro-pulses delivered to the detectors during each run and $N_{\text{triggers}}^{\text{NV}}$ ($N_{\text{triggers}}^{\text{FC}}$) is the number of triggers the detector (fission ionization chamber) recorded during each run. D^{NV} (D^{FM}) is the average detector (fission ionization chamber) dead-time over the course of the run.	61

2.3	LANL neutron detector data selection cuts, with the number events that passes each cut, as the cuts are sequentially applied. Each cut is described in Section 2.2.4.	85
2.4	Systematic and statistical errors assessed on the LANL neutron detection efficiency measurement. Each contribution to the total systematic error is described in detail in Section 2.2.5. The total error is assessed by combining each of the individual sources in quadrature. The efficiency averaged error is given by $\sum_i \sigma(\text{KE}_i)\epsilon(\text{KE}_i) / \sum_j \epsilon(\text{KE}_j)$, where the sums are over bins of neutron kinetic energy KE, and is provided to give a sense of the average error.	86
2.5	A list of all datasets taken at WIPP. Datasets are labeled by the date on which a run was started. $N_{\text{triggers}}^{\text{NV}}$ is the number of triggers recorded by the detector during the course of each run.	87
2.6	WIPP neutron detector data selection cuts, with the number events that pass each cut, as the cuts are sequentially applied. Each cut is described in Section 2.3.4.	88
4.1	The CCD gain in ADU/keV _{ee} for the four 4-shooter cameras measured with ²⁴¹ Am α tracks in 60 Torr CF ₄ and averaged over the different heights in Figure 4-10. The first error is the fit error on the CCD gain from a degree-0 polynomial fit to the gain versus height in Figure 4-10, while the second error is the Root Mean Square (RMS) deviation of the gain measurements at different heights. Data at lower heights was taken with lower bias on the amplification stage (635V instead of 670V) to counteract the higher spark rate due to the sources' proximity to the amplification stage.	141
5.1	The digitizer settings for the Am-Be runs listed in Table 5.2.	155

5.2	<p>Statistics relating to the Am-Be dataset. Each line represents approximately one day's worth of back-to-back 1000 event runs, where each run is designated by a unique 5-digit number. N_{images} is the total number of images taken across all four cameras in each range of runs (so the number of exposures per CCD was $N_{\text{images}}/4$). The 4-shooter was evacuated and refilled with 60 Torr CF_4 between each series of runs, or lines in this table. The six 4-shooter digitizer channels were triggered on the central anode electrode preamplifier at the voltage thresholds listed. All data was taken in 2013.</p>	156
5.3	<p>Cuts applied to the track candidates in the Am-Be dataset to select nuclear recoils, as described in Section 5.3. Line one in this table corresponds to AMBE-I in the text, line two to AMBE-II, etc.. For each camera, the number of track candidates surviving each cut is given. A total of 4,337 nuclear recoil candidates survive all selections across the four 4-shooter cameras.</p>	165

Chapter 1

Introduction

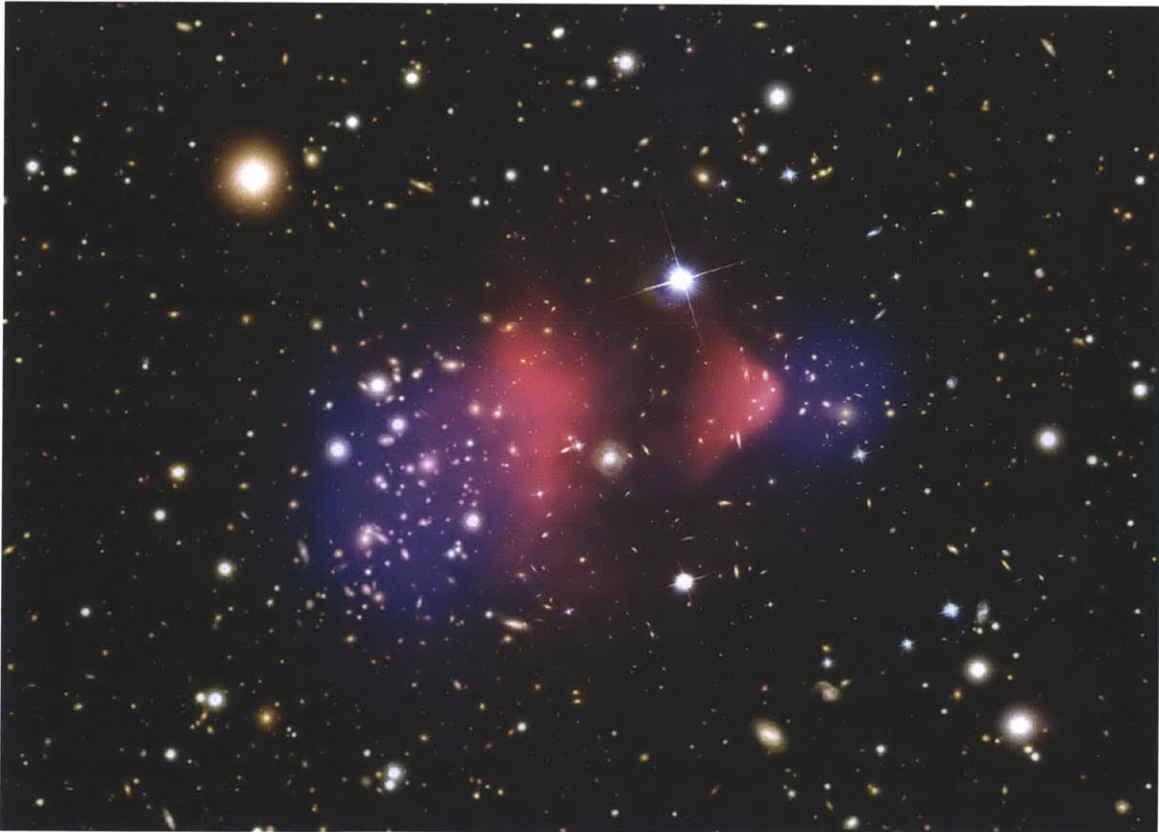


Figure 1-1: A composite optical, X-ray (in red), and weak lensing (in blue) image of the Bullet cluster (1E 0657-558), two galaxy clusters that collided approximately 100 million years ago [1]. The red X-ray intensity traces the baryon density in the two clusters, while the blue traces the majority of the mass in the two clusters as inferred from weak lensing observations, indicating that the majority of the matter in the two clusters was undisturbed by their collision.

Figure 1-1 is a now-famous composite image of the Bullet Cluster (1E 0657-558),

two enormous galaxy clusters that collided violently with one another approximately 100 million years ago [2]. Overlaid on the optical image of stars and galaxies are X-ray measurements from the Chandra satellite in red and the mass density of the cluster as inferred from weak gravitational lensing in blue [1]. The hot, X-ray emitting baryonic matter in the two colliding clusters has been severely deformed by the cluster collision, but most of the mass continues to travel along the original trajectories of the two clusters, as if unaffected by the collision. The spatial decoupling of the baryonic matter in the Bullet Cluster from the majority of its two colliding clusters' masses (in blue) implies that the bulk of the matter in the two clusters interacts extremely weakly with itself and the normal matter in the clusters' component galaxies, stars, and X-ray emitting gas (in red). The bulk of the matter in the two clusters interacts with the known constituents of the universe much more weakly than even the weak nuclear force, including with photons, rendering it non-luminous. The elucidation of the nature of this “dark matter” is presently the focus of a world-wide, multi-front scientific endeavor (see, for instance, [3]).

Recent Planck collaboration analyses of the Cosmic Microwave Background (CMB) temperature power spectrum find that the observed power spectrum is consistent with the six-parameter Λ CDM cosmology if matter composes $31.5_{-1.8}^{+1.6}\%$ of the energy density of the universe, but only if $(84.5 \pm 2.4)\%$ of that matter is pressureless and non-interacting [4]. If this matter is stable on cosmological time-scales, it is an excellent candidate for the non-interacting matter observed in the Bullet cluster and an enormous host of other astrophysical systems [5]. A large body of scientific evidence has been accrued to the effect that no known Standard Model particle can fully comprise the dark matter, and that the dark matter composes the vast majority of the matter in the universe [5, 6, 7].

At present it is unknown what specific particles compose the dark matter, although many theoretical candidates have been proposed. If the recently discovered 125 GeV/ c^2 boson at the Large Hadron Collider [8, 9] is the one elementary Higgs boson of the Standard Model [10], then the Standard Model is complete, and incapable of providing a candidate for the dark matter. Presently, the most popular

class of theoretical candidates is Weakly Interacting Massive Particles, or WIMPs. WIMPs are primarily motivated by the theoretical observation that a cosmologically stable, 10 GeV–1 TeV particle with weak-strength interactions, if produced in thermal equilibrium in the early universe, would evolve to the present day with roughly the same density as the observed dark matter [11]. Supersymmetric (SUSY) theories of physics beyond the Standard Model provide the most popular WIMP candidates [12]. In particular, the lightest neutralino χ , a linear combination of the superpartners of the photon, Z^0 , and Higgs [11], and the lightest superparticle (LSP) in many SUSY theories, is the most widely studied SUSY candidate [5]. Other perfectly viable theoretical dark matter candidates include primordial black holes, axions, and sterile neutrinos [6].

1.1 Direct detection

Theoretically, WIMPs may scatter off of atomic nuclei with weak scale cross-sections [13]. The standard WIMP scatters with nuclei elastically in the extreme non-relativistic limit, in which only the axial vector current coupling the WIMP to the spin of the nucleus (known as the spin-dependent interaction) and the scalar current coupling the WIMP to the mass of the nucleus (known as the spin-independent interaction) [11, 13] contribute to the scattering amplitude. Once an experiment has chosen a specific target nucleus (or nuclei) to instrument, the rate of WIMP scatters on that nucleus is calculable given the nuclear form factor of the target and an assumption on the flux profile of the WIMPs at the Earth’s surface [14].

An assumption made to simplify the problem is that the dark matter forms a smooth, non-rotating spherical halo centered on the spiral arms of the galaxy with an isotropic Maxwellian velocity distribution. This assumption, although simplistic and incomplete [15], allows for the calculation of the rate of WIMP-induced nuclear recoils per unit mass per day in a block of matter, given the Sun’s velocity relative to the galaxy rest frame, v_{\odot} , the maximum velocity a dark matter particle can have and still be gravitationally bound to the galaxy, v_{esc} , an assumption of dark matter’s Maxwellian dispersion velocity, v_0 , and the dark matter density at the Earth, ρ_{DM} .

For the sake of standardizing the interpretation of experimental results, it has become customary to use the values in Table 1.1 for the computation of expected rates and experimental sensitivities [14], even though more realistic estimates of these parameters and their uncertainties exist in the literature [16].

WIMP Parameter	Standard Assumed Value
v_0	230 km/s
v_{\odot}	244 km/s
v_{esc}	544 km/s
ρ_{DM}	0.3 GeV/c ² /cm ³

Table 1.1: Standard assumed astrophysical parameters associated with a smooth spherical isothermal dark matter halo used to compute the expected rate of WIMP-induced nuclear recoils in Earth-based dark matter direct detection experiments, from Behnke *et al.* [17]. v_0 is the Maxwellian dispersion velocity of the dark matter in the halo of the Milky Way, v_{\odot} is the Sun’s velocity relative to the rest frame of the Milky Way, v_{esc} is the maximum speed a dark matter particle may have and still be bound in the Milky Way’s halo, and ρ_{DM} is dark matter halo mass density at Earth.

Surveys of SUSY parameter space have found that the spin-independent WIMP-nucleus interaction dominates the scattering amplitude for nuclei with atomic masses $A \gtrsim 30$ [11], while only isotopes with spin undergo spin-dependent interactions. A natural division may therefore be made between experiments possessing large expected spin-independent scattering amplitude sensitivity (typically utilizing high A nuclei like Xe, I and Ge) and those with large expected spin-dependent scattering amplitude sensitivity such as ^{19}F , ^{73}Ge , ^{129}Xe , and ^{131}Xe .

In the absence of the observation of WIMPs scattering with nuclei in their detectors, direct detection experiments report their results as upper limits on the WIMP-nucleus spin-dependent or spin-independent interaction cross-section, as a function of the mass assumed for the WIMP. The quantity typically reported by experiments is the implied upper limit on the WIMP-proton or WIMP-neutron interaction cross-section [14], which facilitates the comparison of these upper limits between groups

utilizing different target nuclei. For the vanilla Majorana WIMP, the scalar WIMP-neutron coupling and scalar WIMP-proton coupling are essentially the same [18, 11], allowing experiments to simply report upper limits on the WIMP-*nucleon* interaction cross-section. Spin-dependent experiments do not enjoy this luxury, and therefore report upper limits on either the spin-dependent WIMP-proton scattering cross-section, $\sigma_{\chi p}^{\text{SD}}$ or the spin-dependent WIMP-neutron scattering cross-section, $\sigma_{\chi n}^{\text{SD}}$. Each experiment's sensitivity to $\sigma_{\chi p}^{\text{SD}}$ and $\sigma_{\chi n}^{\text{SD}}$ varies widely with the chosen target, with some targets preferentially sensitive to $\sigma_{\chi p}^{\text{SD}}$ (like ^{23}Na , ^{127}I and ^{19}F) and others to $\sigma_{\chi n}^{\text{SD}}$ (like ^{73}Ge , $^{129}\text{Xe}/^{131}\text{Xe}$ and ^{43}Ca) [14].

The best current limit on the spin-independent WIMP-nucleon cross-section is that of the XENON collaboration [19], obtained with the 1.2 kg XENON10 [20] detector for WIMP masses below $8 \text{ GeV}/c^2$ and with the 34 kg XENON100 detector for WIMP masses above $8 \text{ GeV}/c^2$ [21]. The XENON10 and XENON100 detectors are both two-phase (gas-liquid) Xenon time projection chambers. XENON100's data has also been used to set the leading limit on the spin-dependent WIMP-neutron interaction cross-section [22].

The best upper limit on the spin-dependent WIMP-proton cross-section has been set by the COUPP collaboration with a 4 kg CF_3I bubble chamber for WIMP masses $M_\chi > 60 \text{ GeV}/c^2$ [17], by the SIMPLE collaboration using superheated C_2ClF_5 droplets suspended in gel matrices for WIMP masses between $8 \text{ GeV}/c^2 < M_\chi < 60 \text{ GeV}/c^2$ [23] and by the PICASSO collaboration using emulsions loaded with superheated C_4F_{10} droplets for WIMPs with masses $5 \text{ GeV}/c^2 < M_\chi < 8 \text{ GeV}/c^2$ [24]. All three experiments exploit the theoretical prediction that ^{19}F is the most favorable target for probing $\sigma_{\chi p}^{\text{SD}}$ [25]. Figure 1-4 displays these limits on $\sigma_{\chi p}^{\text{SD}}$ as a function of WIMP mass.

Statistically significant recoil rate excesses over those expected from background have been reported by the CoGeNT collaboration using p-type point contact germanium detectors [26] and by the CRESST-II collaboration using CaWO_4 crystals [27]. A dark matter interpretation of these excesses, however, has been met with considerable skepticism (see, for instance, [6]). Experiments must demonstrate that

an observed excess nuclear recoil rate has the characteristics expected of true WIMP interactions. Therefore, additional information is required beyond simply an excess in count rate.

In particular, the differential scattering rate as a function of nuclear recoil energy for WIMP scatters is predicted to be roughly exponential in shape with typical recoil energies spanning 1 keV to 100 keV for a 10 GeV to 10 TeV WIMP [6]. Figure 1-2 shows the expected differential WIMP- ^{19}F spin-dependent scattering rate as a function of ^{19}F recoil energy for a variety of WIMP masses. Confidence in a positive dark matter detection could be derived from a confirmation that the dependence of the energy spectrum and total scattering rate scales as expected across a range of different nuclei for the hypothesized WIMP. In the literature, this has been referred to as the “materials signal” [16].

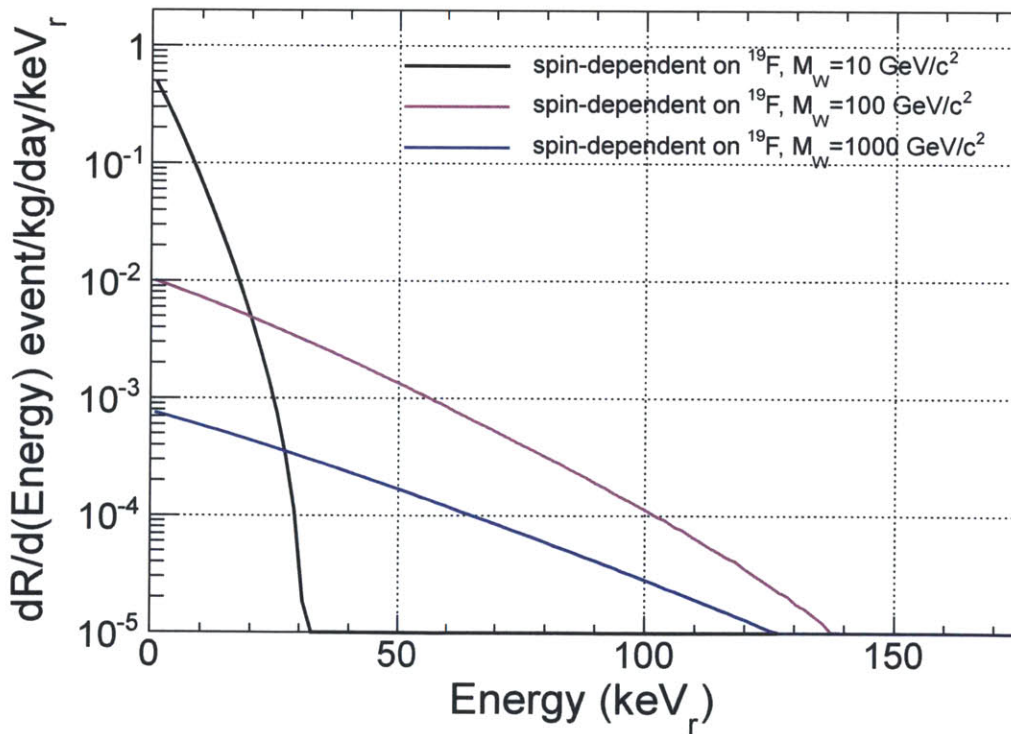


Figure 1-2: The predicted differential rate of WIMP- ^{19}F recoils per kg per day in the energy of the fluorine recoils, assuming a total spin-dependent WIMP- ^{19}F interaction cross-section of 1 picobarn. The differential rate is shown for three hypothetical WIMP masses, 10 GeV/c², 100 GeV/c², and 1000 GeV/c². The details of how these curves are computed are given at the beginning of Chapter 6.

The predicted relative motion of the Earth with respect to the dark matter halo affords distinct signatures that if measured can be exploited by experiments to bolster a WIMP detection claim. The nuclear recoil rate due to WIMPs above a fixed energy threshold varies over the course of the year on the Earth as the Earth moves alternately with and then against the motion of the Sun about the center of the Galaxy [28]. A claimed detection of a temporal modulation in nuclear recoil rate with a (0.999 ± 0.002) yr period and the correct phase has been reported by the DAMA/LIBRA experiment using NaI(Tl) crystal scintillators at a confidence level of 8.9σ [29]. The DAMA/LIBRA detection claim is in direct tension with standing null results from the CDMS and XENON collaborations [30]. Work is presently underway by the DAMA/LIBRA collaboration and others to confirm this result and to understand how a dark matter interpretation of these results could evade stringent bounds placed on the WIMP-nuclear scattering amplitude by other groups [6].

A third signature is that the directions of WIMP-induced nuclear recoils are predicted to be preferentially opposed to the direction of the Sun’s motion about the center of the galaxy [31]. For all positions on the surface of the Earth, this direction varies considerably over each 24 hour rotation of the Earth. This WIMP signature, and the prospects for its detection, will be discussed in the next section.

1.2 Directional direct detection

A statistically significant observation of the anti-correlation of the direction of nuclear recoils with the Sun’s motion would provide nearly irrefutable evidence of a galactic origin for the recoil progenitors. The rate of recoils anti-correlated with the Solar motion can be as much as $100\times$ that of the recoil rate in the opposite direction [14]. Figure 1-3 shows the differential scattering rate as a function of the angle between the nuclear recoil direction and the vector anti-parallel to the Sun’s motion for ^{19}F recoils for a $100 \text{ GeV}/c^2$ WIMP and a range of detector energy thresholds.

If the full 3D vector of nuclear recoils could be measured in the $1 - 20 \text{ keV}$ recoil energy range, a WIMP signal could be distinguished from an isotropic source of background with only $\mathcal{O}(10)$ recoils for a $100 \text{ GeV}/c^2$ WIMP [32], even in the presence

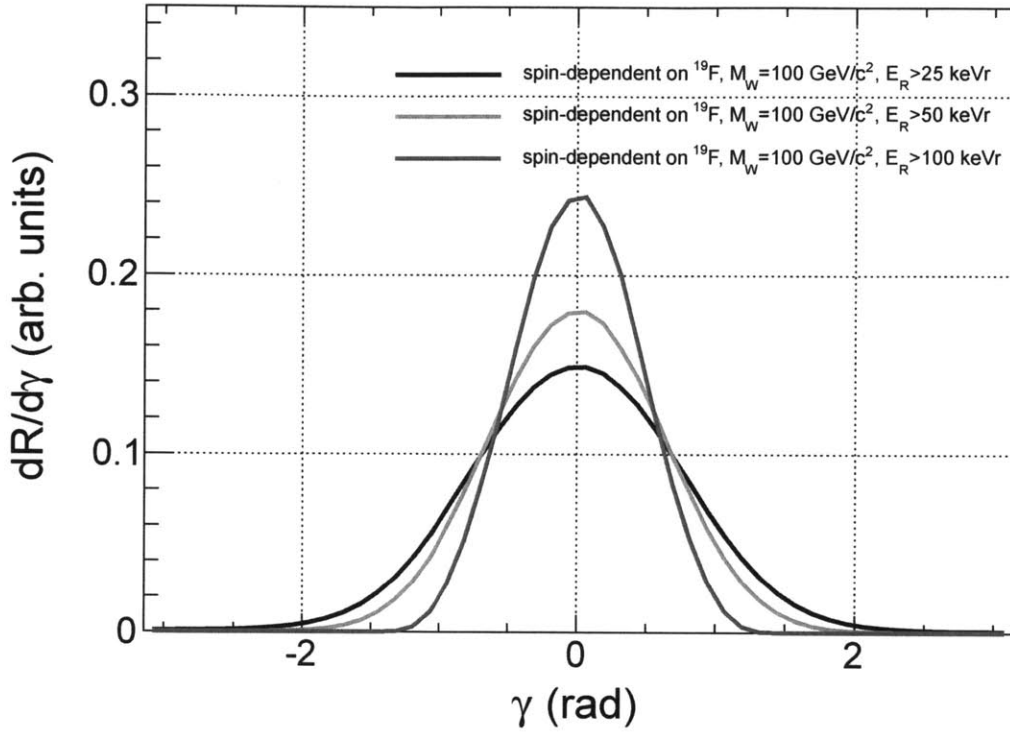


Figure 1-3: The predicted differential rate of WIMP- ^{19}F recoils per kg per day in the angle γ of fluorine recoil directions from the mean WIMP-wind direction. The differential rate is shown for a $100 \text{ GeV}/c^2$ hypothetical WIMP mass, for fluorine recoil energy detection thresholds of 25 keV, 50 keV, and 100 keV. The differential rates for each threshold have been scaled to have unit normalization. The method used to compute these curves is given at the beginning of Chapter 6. A strong preference for the fluorine recoils to scatter along the WIMP-wind direction is evident, particularly for recoils with large energies.

of a comparable number of background events [33, 34]. The directional signature offers considerable advantages over the materials signature, which would require many WIMP detections across several detectors [35], and the annual modulation signature, which can be more easily mimicked by non-WIMP interactions or instrumental effects [36].

In practice, however, the reconstruction of the direction of recoils with energies below 100 keV is very challenging due to a variety of factors including the extremely short range of $< 100 \text{ keV}$ nuclear recoils in liquids and solids ($< 100 \text{ nm}$) [37] and multiple scattering. A world-wide effort is currently underway to develop detectors capable of tackling these and other related challenges (see, for instance, [35] and [38]).

At present, the most promising experimental approach is thought to be gaseous, low pressure time projection chambers [37]. Other ideas being actively pursued include detectors based on DNA [39], columnar recombination in high-pressure Xenon gas [40], nuclear emulsion optical microscopy [41], and roton-anisotropy in liquid Helium [42].

In 1994 Buckland *et al.* [43] set the first limits on neutralino dark matter scattering using a low-pressure gas TPC with a CCD-imaged multi-stage parallel plate avalanche chamber (PPAC [44]). Groups actively pursuing the low pressure gas TPC approach today include the **D**irectional **R**ecoil **I**dentification **F**rom **T**racks¹ (DRIFT) [46], **D**ark **M**atter **T**ime **P**rojection **C**hamber (DMTPC) [47], **N**EW generation WIMP-search with an **A**dvanced **G**aseous tracking device **E**xperiment (NEWAGE) [48], **M**icro-tpc **M**Atrix of Chambers (MIMAC) [49], and the **D**irectional **D**ark **M**atter **D**etector (D³) [50] collaborations. Each group differs mainly in the method chosen to amplify and detect the primary ionization generated by nuclear recoils in their TPCs. DRIFT uses Multi-Wire Proportional Chambers (MWPCs) [51], NEWAGE uses μ -PICs [52], MIMAC uses MICROMEAS [53], and D³ uses Gas Electron Multipliers (GEMs) [54] with silicon pixel chip readout [55].

The Dark Matter Time Projection Chamber (DMTPC) collaboration seeks to optically image the direction of WIMP-¹⁹F recoils in low pressure CF₄ gas by improving upon the approach pioneered by Buckland *et al.* [43]. A single-stage PPAC coupled to a TPC is imaged through the semi-transparent mesh electrodes of the TPC by CCDs. Trails of ionization electrons left by low energy ¹⁹F WIMP recoils are drifted into the PPAC where approximately one photon is produced for every three electrons in the resulting avalanches in CF₄ [56, 57]. These photons are subsequently imaged in the plane of the PPAC by CCDs. Because the mean length of the ionization trail from a 50 keV (10 keV) ¹⁹F nucleus in 100 Torr of CF₄ gas is only 560 μ m (50 μ m) [58], it is a formidable experimental challenge to achieve the spatial resolution necessary to observe the low energy ionization trails expected from WIMP-induced nuclear recoils.

¹Unlike the other groups working with low pressure gas TPCs listed here, the DRIFT collaboration drifts negative CS₂⁻ ions instead of electrons, in a so-called negative ion TPC (NI-TPC) configuration [45].

Each experiment’s sensitivity to the full 3D direction of recoils degrades considerably with decreasing recoil energy, and most have better sensitivity to the direction of recoils which occur along certain preferred axes or planes relative to their detectors. As examples, the spatial resolution of the DRIFT-II detector is $10\times$ worse along one direction than along the other two [37] and DMTPC detectors possess negligible sensitivity to the component of low energy recoils perpendicular to the plane of the PPAC if only the CCD readout is used.² Experiments seek to measure not only the dimensions of ionization trails left by nuclear recoils, but also the vector sense of the recoils. Limited sensitivity to the sense, or “head-tail,” of low energy nuclear recoils (< 150 keV) has been reported by DRIFT [59] for ^{16}S recoils, and by DMTPC [60], NEWAGE [61], and MIMAC [62] for ^{19}F recoils. Strong sense determination at low energies reduces the number of detections required before isotropy can be confidently rejected by an order of magnitude [63] to the extent that sense-less, “axial” 3D angular reconstruction of tracks actually requires more detections in order to reject isotropy than 2D angular reconstruction with sense [34].

Figure 1-4 shows limits that have been set on σ_{xp}^{SD} by direction-sensitive experiments, compared with the world’s best direct detection experiments’ limits on σ_{xp}^{SD} . For large WIMP masses, recent results obtained by DRIFT with the DRIFT-II-d [67] detector are only two orders of magnitude less competitive than the COUPP [17] and SIMPLE [23] limits.

The DMTPC limit curve in Figure 1-4 was set with two back-to-back 10 liter TPCs operating in a basement laboratory at MIT [65]. 108 nuclear recoils were detected with energies between 80 keV and 200 keV. This detector was subsequently deployed underground at the Waste Isolation Pilot Plant (WIPP) outside Carlsbad, NM in October 2010. The first limits set using data taken at WIPP are less restrictive than the surface result, due to the presence of a previously unencountered background [70]. The majority of the excess counts are attributable to substantial changes made to the data analysis and instrument between the surface run at MIT [65] and the data

²In principle, the perpendicular component of tracks may be inferred from the measured two-dimensional range compared to the expected full three-dimensional range given the measured track energy, if the particle that produced the track can be identified based on its range and energy [37].

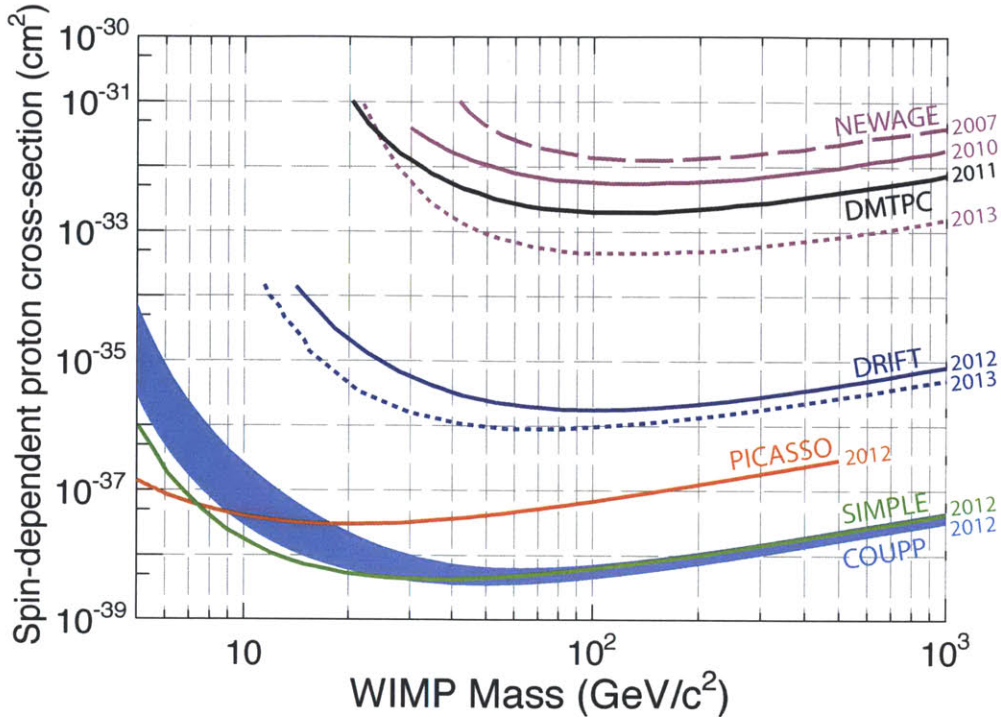


Figure 1-4: All known limits set on the spin-dependent WIMP-proton interaction cross-section $\sigma_{\chi p}^{\text{SD}}$ by dark matter direct detection experiments with some sensitivity to the direction of nuclear recoils. Limits set on the Earth's surface include those by NEWAGE (2007) [64] and DMTPC (2011) [65]. Limits have been set underground by DRIFT-IIId (2012) [46] and NEWAGE (2010) [48]. Unpublished underground limits presented at CYGNUS2013 [66] are shown from DRIFT-IIId (2013) [67, 68] and NEWAGE (2013) [66]. Also shown are the best limits on $\sigma_{\chi p}^{\text{SD}}$ obtained to date by direct detection experiments without directional sensitivity [69], including results from the PICASSO (2012) [24], SIMPLE (2012) [23], and COUPP (2012) [17] experiments.

taken at WIPP. Work is in progress to better understand the origin of these excess counts and eliminate them.

Beginning in 2008, the DMTPC collaboration began the construction of a new detector, designed to incorporate the lessons learned from previous DMTPC prototypes [71, 72, 73, 60, 74, 75], including the 10-liter detector currently at WIPP [65]. Chapters 3, 4, 5 and 6 of this thesis detail the design, construction, testing, and physics reach of this new detector. The scientific purpose of this effort is not to set a competitive limit on $\sigma_{\chi p}^{\text{SD}}$, but to test technologies that could make the construction of much larger detectors (with active volumes in excess of 1 m³) feasible.

Neutrons are a dangerous background to direct dark matter detection searches

because they can mimic closely the signal signature in non-directional direct dark matter detectors [76]. For this reason, it is desirable to measure the neutron flux directly at underground sites where dark matter experiments are active. Chapter 2 describes a liquid scintillator-based neutron detector designed for this purpose, which is currently underground and taking data at WIPP. Before being commissioned underground, the response of this detector to neutrons with kinetic energies from 50 MeV to 800 MeV was determined in a beam test at the Los Alamos Neutron Science Center (LANSCE) in NM.

Chapter 2

High Energy Neutron Backgrounds : The Neutron Veto

Neutrons are a worrisome background for direct dark matter direct detection searches because their interactions with matter can mimic closely the expected signature of a Weakly interacting massive particle (WIMP) scattering on matter [76]. The DMTPC collaboration presently operates a dark matter detector at the Waste Isolation Pilot Plant (WIPP) and further plans to install the dark matter detector described in Chapters 3, 4, 5, and 6 at WIPP in the near future. The WIPP site is a salt mine with an overburden of 1.585 km.w.e. [77], providing protection for the DMTPC detectors from cosmic rays. It is extremely important to the DMTPC effort and other on-going scientific efforts at the WIPP to measure the ambient neutron backgrounds at the experimental operating depth.

Section 2.1 of this chapter describes a neutron detector built at MIT with high sensitivity to very high energy neutrons (> 50 MeV) for this purpose. Section 2.2 discusses a direct measurement of the neutron sensitivity of this detector as a function of neutron energy that was undertaken at the Los Alamos Neutron Science Center in late 2008. Section 2.3 presents an estimate of the non-muon interaction rate measured with the detector at WIPP where the detector was deployed underground from late 2010 to early 2013.

Dark matter direct detection experiments typically operate their detectors within large passive water or polyethylene shields designed to absorb neutrons from the surrounding environment before they can generate a signal in the detectors that might

be misconstrued as a dark matter direct detection. Properly instrumented, these shields can be utilized to attenuate the neutron flux around an instrument while actively measuring its properties. In particular, the energy spectrum of neutrons underground is not well measured [78], especially for neutrons with energies in excess of 100 MeV [79]. The detector described in this chapter was designed to be deployed as an individual module in a larger array of identical detectors that could be arranged around a direct dark matter detector for this purpose. Such an array would be capable not only of attenuating the ambient neutron flux while measuring its total intensity and energy spectrum, but also of providing a coincidence “veto” to reject false dark matter candidate events associated in time with terrestrial or cosmic ray activity (neutron or otherwise).

2.1 The Neutron Veto Detector

The detector is a stainless-steel rectangular tank 15" wide, 10" tall, and 97.5" long. The ends of the rectangular tank are capped by pyramidal frustra which are matched to the 15" by 10" rectangular cross-section of the tank and taper to squares with 4.515" sides. Welded to the centers of the smaller, square ends of the frustra are 5" long cylindrical 304 stainless-steel flanges¹ whose axes are parallel to and centered on the long axis of the rectangular tank. These flanges have a 3.917" circular bore and are coupled to 5" Photonis XP4500B PMTs through 0.5" thick 7740 Pyrex optical glass windows. The walls of the frustra and rectangular tank are 1/8" thick and the walls of the cylindrical flanges are 0.083" thick.

2.1.1 Liquid scintillator

The detector, when full, contains approximately 71 US gallons of BC-517L² liquid scintillator. The properties of BC-517L most relevant to this work are reproduced in Table 2.1. BC-517L is composed of 85% mineral oil, 15% pseudocumene, 1 gm/liter PPO and 0.001 gm/liter Bis-MSB [82]. Energy transferred by neutrons to hydrogen

¹MDC Vacuum Products, Part #450010.

²Saint-Gobain Crystals.

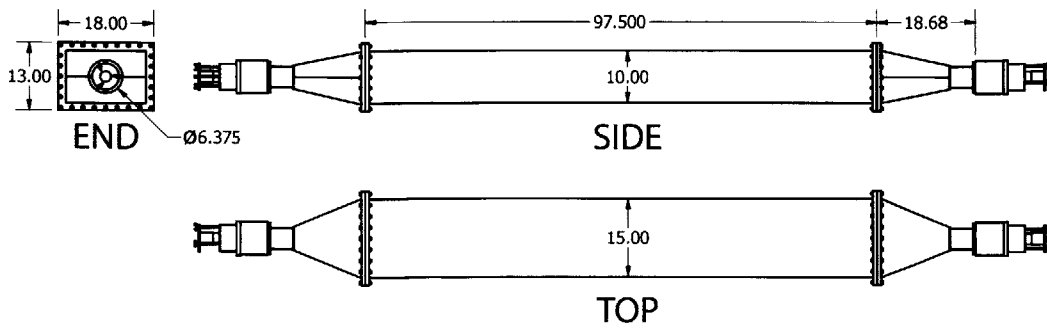


Figure 2-1: A CAD drawing of the neutron detector. Given dimensions are in inches.

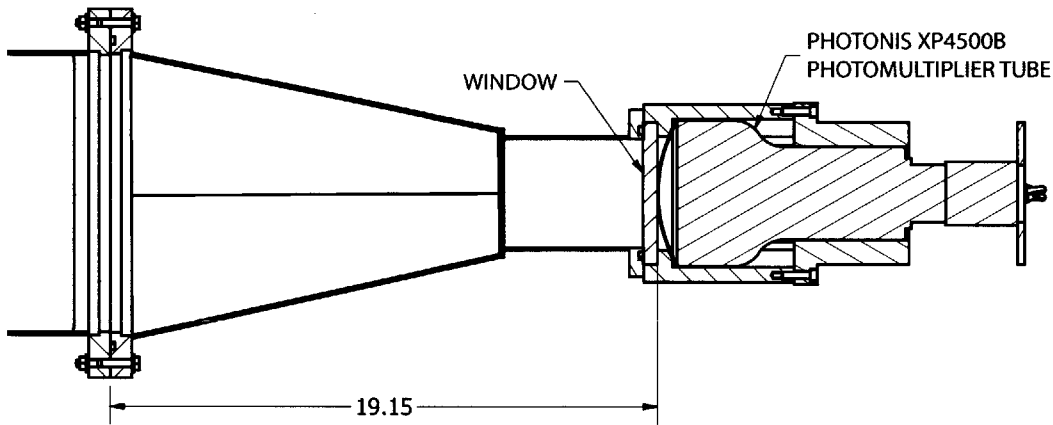


Figure 2-2: A close-up of one of the two neutron detector PMTs showing how it is coupled to the active liquid scintillator volume.

BC-517L Liquid Scintillator [80]							
Light Output (% Anthracene)	Decay Constant (ns)	H:C Ratio	Density (g/cm ³)	Refractive Index	No. H Atoms per cc	No. C Atoms per cc	
39	2	2.01	0.86	1.471	7.40×10^{22}	3.68×10^{22}	

Table 2.1: The physical properties of BC-517L liquid scintillator most relevant to this detector's design and performance. The light yield of anthracene is 1 blue photon per 65 eV of deposited energy [81].

and carbon nuclei through neutron scattering is re-absorbed by the PPO and Bis-MSB scintillation fluors, which subsequently deexcite via fluorescence which can be detected by PMTs. The nominal brightness of BC-517L when saturated with air (nitrogen) is 30% (39%) the light output of anthracene [80], implying a fluorescence yield of 4,600 fluorescence photons/MeV deposited (6,000 fluorescence photons/MeV deposited).³ In order to enhance the absolute light yield, each time the detector was filled with liquid scintillator nitrogen was bubbled through the BC-517L with an ultra-fine bubble diffuser for an extended period of time before the detector was sealed.

Figure 2-3 shows, as a function of neutron kinetic energy, the interaction cross-section of neutrons with hydrogen and carbon atoms. In BC-517L, for kinetic energies below 1 MeV, neutrons predominantly scatter elastically on hydrogen. Scattering on carbon becomes comparable in strength to scattering on hydrogen for kinetic energies above 30 MeV, and dominates neutron interactions with the detector for kinetic energies above 50 MeV despite BC-517L's 2.01:1 ratio of hydrogens to carbons. Elastic scattering is the predominant neutron-hydrogen scattering channel from 1 MeV to 1 GeV, while in that energy range only approximately 1/3 of neutron scatters on carbon are elastic.

2.1.2 Optics

To be detected, fluorescence photons generated by neutron interactions in the liquid scintillator must pass from where they are created in the BC-517L to the photocathode of one of the two detector PMTs. At minimum, each photon must pass through additional liquid scintillator, one of the two detector viewports' 0.5" thick Pyrex 7740 windows, the air gap between these windows and the curved PMT front faces, and the glass of a PMT face in order to reach the PMT photocathode and have a chance of photoconverting, producing a signal in the PMT. The photoconversion probability, or quantum efficiency, of the XP4500B is a function of photon wavelength

³This estimate for the expected fluorescence yield of BC-517L assumes that the light yield of anthracene is 1 blue photon per 65 eV of deposited energy [81].

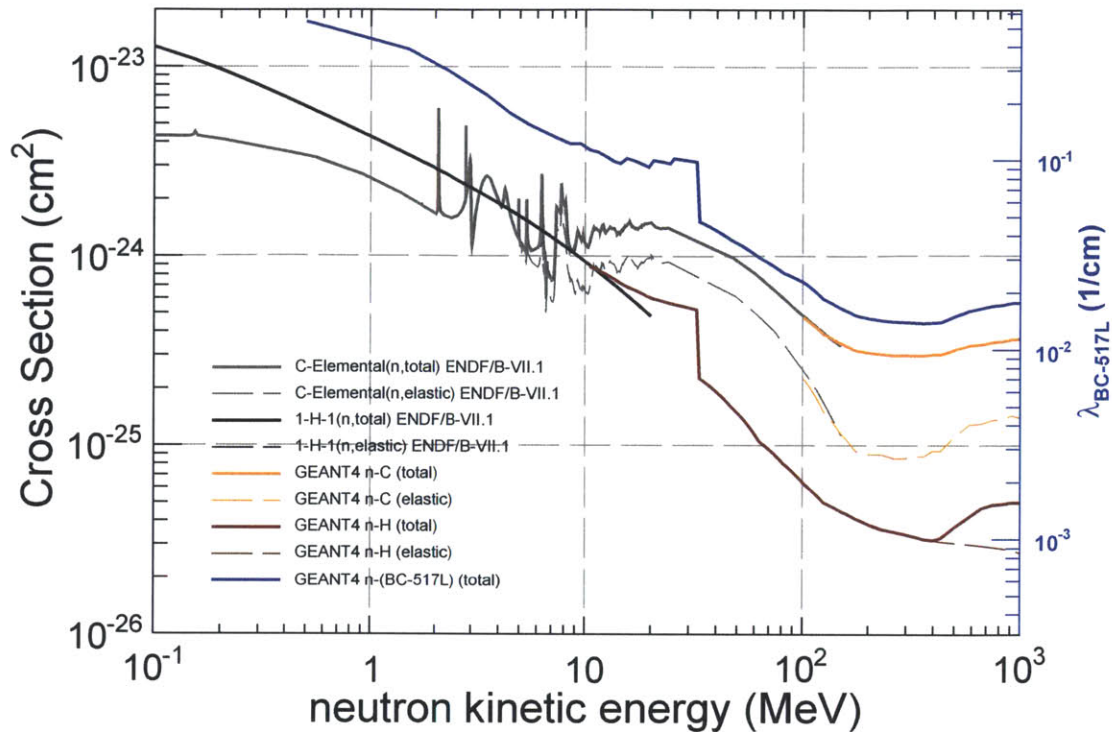


Figure 2-3: The neutron interaction cross-section as a function of neutron kinetic energy for elemental hydrogen and carbon, taken from the ENDF/B-VII.1 database [83], both elastic and total. Also shown are the elemental hydrogen, carbon and BC-517L liquid scintillator neutron interaction cross-sections in the GEANT4 LHEP_BERT_HP physics list. On the right, the neutron on BC-517L interaction cross-section has been converted into the corresponding neutron interaction length. The blue axis only applies to the blue curve.

and is well matched with BC-517L’s emission spectrum, as shown in Figure 2-4.

Photons may be lost due to absorption in the liquid scintillator or the materials which couple the PMTs to the liquid scintillator. The absorption in air, the viewport windows, and the PMT glass is expected to be negligible.⁴ Bulk absorption of photons is expected to occur primarily in the BC-517L itself, if only because it is present in much larger quantities than any of the other materials. The absorption length in BC-517L for 400 – 500 nm light is > 5 m [80], implying a transmission of $\gtrsim 50\%$ for a photon transversing the 3.43 m long detector once.

⁴The viewport windows are made of Pyrex 7740, which readily transmits photons with wavelengths greater than 400 nm [84]. The PMT entrance window is listed in the datasheet nondescriptly as “UV glass,” [85] and likely has an even lower wavelength cut-off than Pyrex 7740.

The fluorescence photons are produced isotropically and only 2% of the internal detector surfaces are photosensitive. To enhance the chance that photons not emitted with initial directions pointed directly at the PMT faces have a chance of contributing to the detected signal, the internal stainless-steel surfaces of the detector are layered with highly reflective aluminized mylar foil. Likewise, the inner surfaces of the PMT mounting hardware are made of diffusely reflective Teflon PTFE.

Parasitic reflections can also occur at the boundaries separating distinct materials in the detector lengthening the time a given photon spends in the detector and increasing its chances of being absorbed or arriving too late to be associated with the event that created it. The liquid scintillator is optically well matched to the Pyrex 7740 viewport windows⁵ but non-negligible reflections are expected in the air gap between these windows and the PMT faces.

2.1.3 Electronics and readout

The PMTs are biased through a Photonis VD105K voltage divider assembly [86] with a N1130 4-channel Wenzel Elektronik Nuclear NIM High Voltage Power Supply [87]. The VD105K supplies a dedicated BNC signal output which is connected through co-axial cables to two input channels of a 4-channel LeCroy WaveRunner 104MXi 1 GHz Oscilloscope [88], with one channel dedicated to reading out each PMT. In typical running, each signal line is split at the scope input with a BNC tee, splitting the signal across the oscilloscope and NIM logic modules used to form a trigger based on the signals.

2.2 LANSCE Weapons Neutron Research Facility

The Weapons Neutron Research Facility (WNR) at the Los Alamos Neutron Science Center (LANSCE) [89] operates a high-energy neutron beam with a broad range of energies, presenting an ideal opportunity for characterizing this detector's sensitivity to high energy neutrons. At the facility, an 800 MeV pulsed proton beam is driven

⁵Pyrex 7740 has an index of refraction $n_{\text{Pyrex 7740}} = 1.474$ [84] which is very well matched to BC-517L's index of refraction, $n_{\text{BC-517L}} = 1.471$ [80].

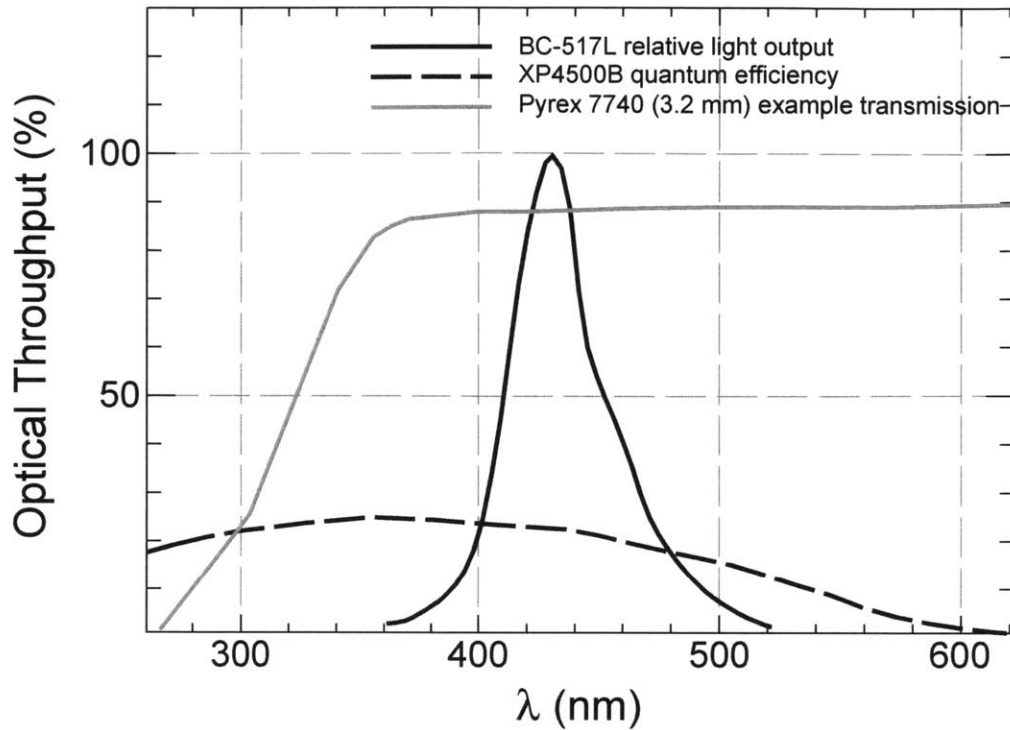


Figure 2-4: An overlay of the XP4500B PMT quantum efficiency [85] and the emission spectrum of BC-517L liquid scintillator [80] versus photon wavelength. Also shown is a reference curve for the optical transmission versus photon wavelength of 7740 Pyrex [84], although the curve shown is for 3.2 mm thick glass.

into a tungsten cylinder, producing neutrons with energies up to 800 MeV through spallation reactions. The spallation neutrons spray out of the tungsten target in all directions but channels cut into shielding surrounding the tungsten target form beam-lines along which users may perform experiments. This section describes a beam test of the neutron detector on one of these beam-lines spanning November 26, 2008 to December 6, 2008. Figure 2-5 shows the neutron flux versus energy on beam-line 4FP15L, where the detector was tested.

2.2.1 Purpose

The purpose of the beam test was to determine the absolute neutron detection efficiency of the detector for neutrons with kinetic energies between 10 MeV and 800 MeV. This measured efficiency could then be used to convert measured event rates at sites

like WIPP where the high-energy neutron flux is not known into measurements of the neutron flux.

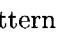
2.2.2 Experimental configuration

The beam test was carried out on WNR beam-line 4FP15L approximately 90 m away from the tungsten spallation target. Protons impinge on the tungsten cylinder in short 1-ns width “micropulses” separated by 1.8 μ sec per micropulse. Trains of these proton micropulses 625 μ sec long (macropulses) strike the tungsten target at 40 Hz.⁶ The expected neutron yield per proton micropulse at the 4FP15L beam-line is shown in Figure 2-5. Also shown is the neutron transmission spectrum for 4" of polyethylene (CH₂), which was placed in the beam upstream of the detector to eliminate low energy neutrons from the beam.

The transverse cross-section of the neutron beam was shaped into a circle by a long cylindrical brass and stainless-steel collimator. The diameter of the collimated beam was directly measured to be 1 cm using storage-phosphor imaging plates upstream and downstream of the detector.

Due to the size of the experimental area at 90 m on the 4FP15L beam-line, the detector had to be angled at 40.5° with respect to the neutron beam as shown in Figure 2-6. 32 cm of steel shielding was stacked between the neutron beam collimator and the detector on either side of the beam in order to keep unwanted secondary particles produced by interactions of the beam with the collimator from reaching the detector. The forward (with respect to the collimator) detector PMT was biased at -1700V⁷ and the backward detector PMT was biased at -2200V. At LANL, one of the detector windows was not one 0.5" thick Pyrex 7740 window but two 0.25" thick BOROFLOAT™ windows⁸ with a thin layer of optical grease connecting them.

Four other detectors were operated synchronously with the neutron detector in the neutron beam. A plastic scintillator detector was utilized upstream of the detector to

⁶ Actually, the macropulses are generated at 60 Hz in a repeating  pattern.

⁷ Excessive noise in the forward PMT at larger biases made it impossible to bias it at a lower voltage than -1700V at Los Alamos. This behavior was not present during previous testing at MIT.

⁸ 125 mm \varnothing , 6.5 mm thick, BOROFLOAT™ windows, uncoated, made by Edmund Optics Inc., part #NT45-685.

veto high energy charged particles in the beam. A second plastic scintillator detector was utilized downstream of the detector to monitor charged particles escaping the detector. The other two detectors were fission ionization chambers [90] provided and operated by the WNR facility.

The plastic scintillator detectors consisted of 16" long by 3.5" wide by 0.5" thick slabs of plastic scintillator optically coupled to PMTs. These detectors were salvaged from a previous experiment at MIT and none of their technical specifications were known.

The fission ionization chamber detectors consist of back-to-back stacks of cylindrical ionization chambers whose electrodes are thin stainless-steel foils with either ^{238}U or ^{235}U deposited on their surfaces [90]. These detectors are sensitive to neutrons through the charged by-products of neutron-induced uranium fission. The ionization chambers' response to neutrons is well understood and these detectors provide a non-destructive measurement of the integrated neutron flux. A ^{238}U fission ionization chamber was placed directly upstream of the detector in the beam and a ^{235}U fission ionization chamber was placed directly downstream of the detector in the beam.

The first two channels of the oscilloscope were connected to the detector PMTs and the second two were connected to the plastic scintillator detectors' PMTs. The PMTs were connected through long coax lines (>50 ft) to the oscilloscope in a nearby counting house.⁹

A logic pulse derived from a proton beam pick-off signal (T0) was provided at the counting house by the accelerator for each proton micropulse delivered to the spallation target by the accelerator. This T0 signal was used to trigger the digitization of the PMT signals via the external input of the oscilloscope.

2.2.3 Data sets

Data was acquired using a Python script running on the oscilloscope. The detector was exposed to the neutron beam and the trigger was the accelerator T0 pulse. For each T0, the two detector PMTs and the two plastic scintillator detector PMTs were

⁹Building MPF-17 in TA53.

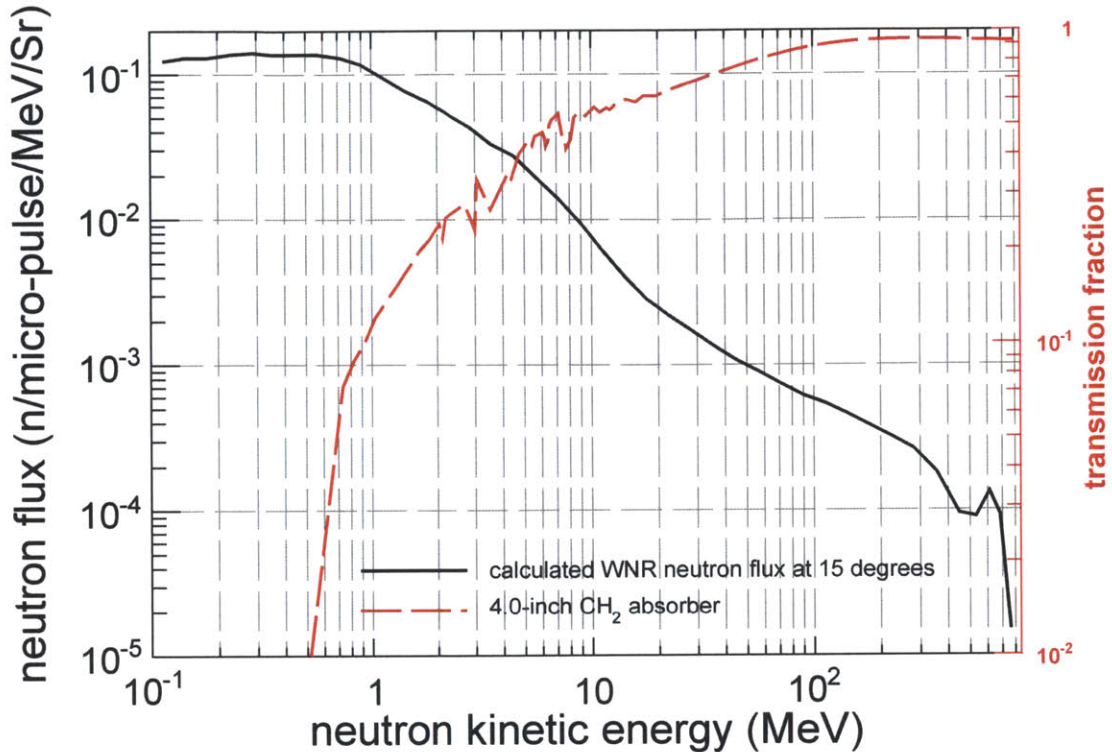


Figure 2-5: The neutron flux at the LANL WNR [91] versus neutron kinetic energy with the neutron transmission probability through 4" of polyethylene versus neutron kinetic energy overlaid in red. 4" of polyethylene was placed in the beam between the neutron source and the detector to absorb low energy neutrons. The left, black axis corresponds to the black curve while the right, red axis corresponds to the red curve.

sampled every 2 ns 1002 times with a -0.388 μsec trigger time offset. The detector PMTs were voltage sampled at 0.5 V/division (with a 1.9V offset) and the plastic scintillator detectors were sampled at 0.2 V/division (with a 0.6 V offset). In total, 7.47×10^6 raw triggers were written to disk in this mode over the course of 5 days. Simultaneously, the forward ^{238}U fission ionization chamber recorded 3876 raw triggers. Unfortunately the ^{235}U fission ionization chamber downstream of the detector was inoperational for these runs. The neutron beam datasets are broken down by day and detector in Table 2.2. The simple trigger logic for this dataset is illustrated in Figure 2-7. An example event from this dataset is shown in Figure 2-8.

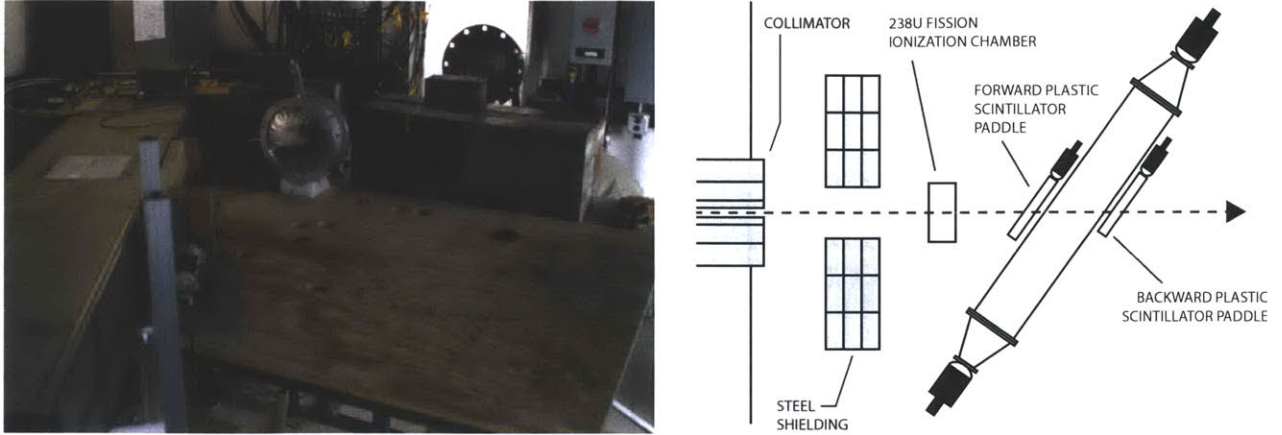


Figure 2-6: Left, a photograph of the configuration of the neutron detector for the calibration at LANL. The detector is on the left, a LANL fission ionization chamber is shown in the center of the image, and the stainless-steel beam collimator is shown in the upper right. Right, a schematic of the configuration of the neutron detector at LANL, as viewed from above.

2.2.4 Event selection

The following describes the off-line analysis used to reduce the raw data described in Section 2.2.3 into a manageable set of physically meaningful quantities.

Fission chamber neutron selection

The analysis of the ^{238}U fission ionization chamber data closely follows the analysis procedures described in [90]. For each neutron trigger, the fission ionization chamber reports a time relative to the accelerator T0 and an ADC count proportional to the energy released in the neutron-induced fission event. Figure 2-9 shows the raw ADC spectrum for the combined runs listed in Table 2.2. Two gaussian peaks are evident. The peak at lower ADC values is not due to neutron-induced ^{238}U fissions, but the spontaneous α decay of ^{238}U . As in [90] a hard cut is imposed on the fission ionization chamber ADC spectrum in order to select events that are likely to be neutron-induced fissions. The cut value was chosen to be 198 ADC units.

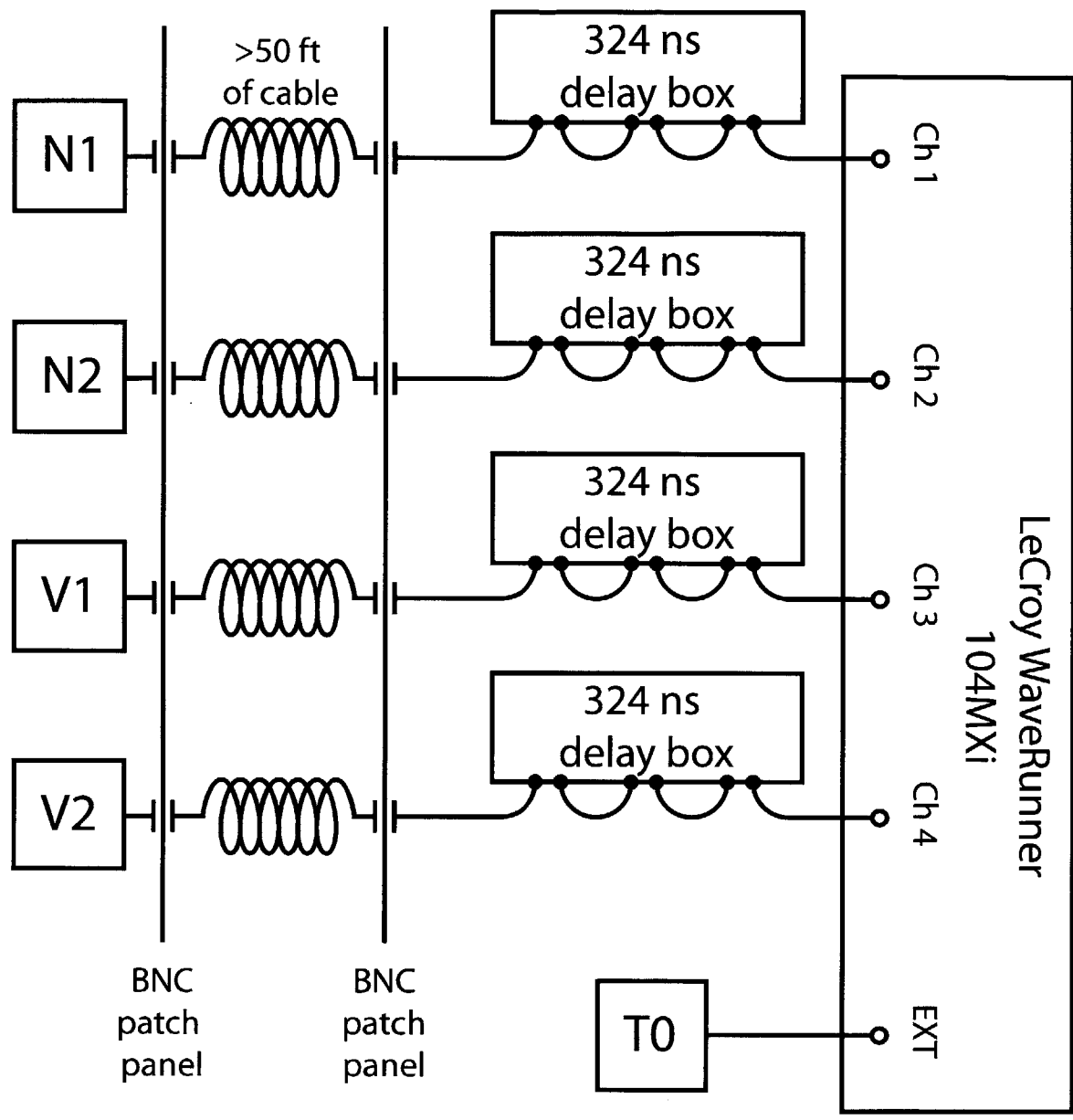


Figure 2-7: A block diagram of the triggering logic at LANL for neutron data-taking. N1 and N2 correspond to the two PMTs coupled to the detector. V1 and V2 correspond to the two plastic scintillator veto paddles. The T0 logic signal derived from the proton beam is used to trigger readout of the detector.

N_{T0}	Neutron Veto Dataset	$N_{triggers}^{NV}$	D^{NV}	Fission Chamber Dataset	$N_{triggers}^{FC}$	D^{FM}
5.09×10^8	11/27/08 AM	1.08×10^6	471.6	762	488	1.000
6.67×10^8	11/27/08 PM	1.44×10^6	463.1	763	656	0.997
3.27×10^8	11/28/08	0.53×10^6	616.1	764	312	1.000
5.42×10^8	11/29/08 AM	1.18×10^6	459.2	765	487	1.000
8.65×10^8	11/29/08 PM	1.7×10^6	508.8	766	839	1.000
5.03×10^8	11/30/08 AM	1.13×10^6	445.3	767	433	1.000
2.14×10^8	11/30/08 PM	0.48×10^6	446.8	768	212	1.002
4.67×10^8	12/02/08	1.01×10^6	462.7	771	449	0.998

Table 2.2: A list of all datasets taken at LANL. The datasets taken with the neutron detector are labeled by the date on which a run was started, while the fission ionization chamber datasets are labeled by a unique run number. N_{T0} is the number of micro-pulses delivered to the detectors during each run and $N_{triggers}^{NV}$ ($N_{triggers}^{FC}$) is the number of triggers the detector (fission ionization chamber) recorded during each run. D^{NV} (D^{FM}) is the average detector (fission ionization chamber) dead-time over the course of the run.

Neutron event selection and analysis

The majority of triggers recorded by the neutron detector do not contain a neutron interaction, due to the fact that the detector was triggered on the accelerator T0. The identification of probable neutron interactions in the PMT waveforms¹⁰ is performed in software off-line. The off-line analysis consists of three steps for each raw event:

1. **Waveform preparation.** For each PMT independently, every measured voltage is baseline-subtracted. The baseline is estimated from the first 10 bins for each channel, and is estimated independently for each event. The baseline-

¹⁰Each event's 4 "waveforms" are the lists of time voltage points (t, V) digitized for each PMT (the two coupled to the detector and the two coupled to the plastic scintillator veto paddles).

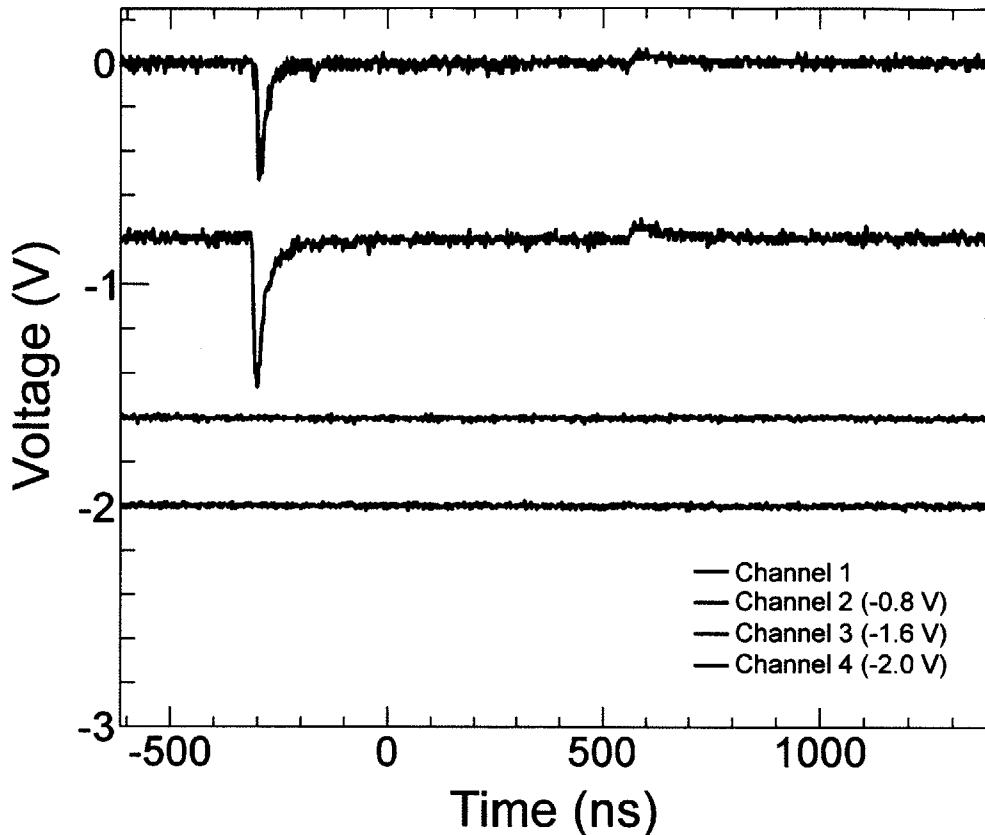


Figure 2-8: A typical LANL neutron event on the four neutron detector channels. Channels 1 and 2 are the detector PMTs. Channels 3 and 4 are the plastic scintillator veto paddles. Channels 2, 3 and 4 have been offset from 0V by -0.8V, -1.6V and -2.0V, respectively, so that all channels are simultaneously visible.

subtracted waveforms are then polarity reversed ($V \rightarrow -V$) so that light-induced pulses on the PMTs are positive-going.

2. **Peak finding.** For each PMT independently, a list of “peaks” is compiled. Peaks are local voltage maxima above a pre-defined voltage threshold. Two peaks are “connected” if the PMT waveform does not return to baseline in the time between them. If two peaks are connected, the smallest of the two is discarded, resulting in a list of disconnected peaks for each PMT.
3. **Peak matching.** Coincidence matching is only performed for the two detector PMTs. Peaks on the two PMTs are either “matched” or not. On each PMT separately, peaks are discarded if their maximum is smaller than and occurs

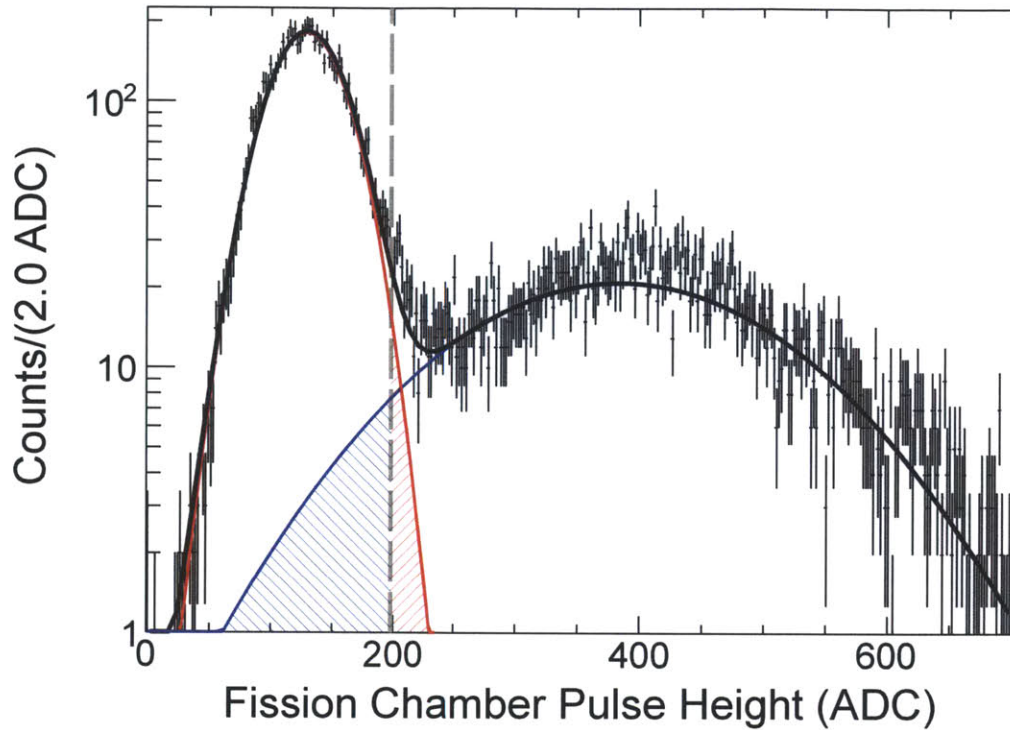


Figure 2-9: Fission ionization chamber raw ADC spectrum showing the neutron selection cut and the fits used to estimate alpha contamination. Events above 198 ADC units are selected as good neutron candidates. The majority of events below 198 ADC units are due to the spontaneous α decay of ^{238}U . The red and blue curves are gaussian fits to the α and neutron distributions used to estimate the number of α particles which leak into the signal region (the red hatched region) and the number of neutrons which leak out of the signal region (the blue hatched region).

within 40 ns of another peak's maximum on the same PMT. Within this subset of peaks, matches are peaks on one of the PMTs whose maximum occurs within 40 ns of a peak on the other PMT. If there are multiple peaks that satisfy this criterion on an individual PMT, then the peak with the smaller amplitude is discarded. In this way a list of matches of size N_{matches} is generated for each event.

For the LANL WNR neutron beam dataset, the peak-finding threshold was chosen to be 70 mV for the detector PMTs and 40 mV for the plastic scintillator PMTs. The following criteria are then required for an event to be identified as a neutron interaction:

LANL-I: At least one peak found on any channel. At least one peak must be found on one of the channels (including the forward and backward plastic scintillator veto paddles).

LANL-II: The PMT signals are within the digitizer's dynamic range. The peak height on the detector PMTs must be less than 3.85V and less than 1.4V on the plastic scintillator detector PMTs. Peaks higher than this saturate the digitizer bounds.

LANL-III: No signal in the forward and backward veto paddles. The peak heights on the plastic scintillator detector PMTs must be less than 40 mV, consistent with no charged particles entering or exiting the detector.

LANL-IV: Event timing consistent with the trigger beam-spill. The start (end) of a peak is the first time the waveform crosses baseline before (after) it. The start and end of matched peaks must be within 1.8 μ sec of the first digitized (t, V) point. This cut ensures that the peak is not a neutron interaction from a subsequent micro-pulse.

LANL-V: There is only one coincident signal on the two PMTs. The event must have 1 and only 1 matched peak. This eliminates events with multiple neutron interactions.

LANL-VI: Detector PMT pulses are coincident in time. The start of peaks matched on the first and second detector PMTs must be within 20 ns of their average start time.

LANL-VII: Detector PMT pulses must have non-negligible integrals. The integral of a peak is the sum of all voltages between its start and end (see LANL-IV), multiplied by the 2 ns digitization time spacing. Peaks on the detector PMT biased at $-1700V$ are required to have an integral above $1.4 V \times ns$ and peaks on the detector PMT biased at $-2200V$ are required to have an integral above $1.0 V \times ns$.

LANL-VIII: Inferred speed of interacting particle less than c . The neutron speed as determined from time-of-flight (TOF), must be less than $0.9c$. This cut eliminates γ -rays that are produced at the spallation target and subsequently interact with the detector. The next section describes how the neutron speed is determined from TOF.

Table 2.3 contains the numbers of events after each of these cuts. 1,001,198 events are found to pass all selection criteria.

Neutron kinetic energy from TOF

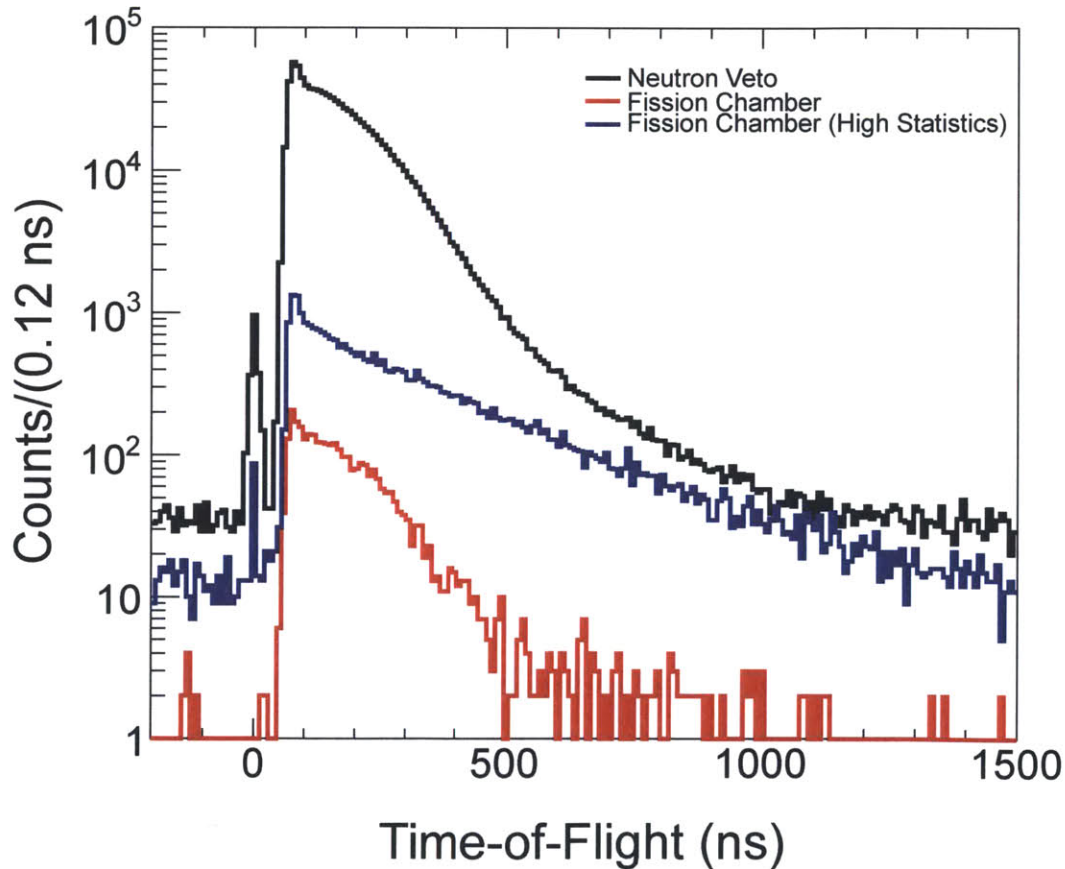


Figure 2-10: The time-of-flight (TOF) spectra in the fission ionization chamber and the neutron detector, after all selection cuts have been applied. Two datasets for the fission ionization chamber are shown. The high statistics (blue) fission ionization chamber run was taken with less restrictive collimation of the neutron beam in order to precisely determine the position of the γ -flash in the fission ionization chamber TOF spectrum.

The energy of neutron candidates in the neutron detector and fission ionization chamber is determined using the measured target-detector distances and neutron times-of-flight from the spallation target to detector. Figure 2-10 shows counts in the fission ionization chamber and neutron detector versus time for events that pass all non-TOF derived cuts outlined in Section 2.2.4. For the neutron detector, the event time is computed as the average start time of the two matched PMT pulses. These distributions have been shifted so that the first prominent feature, a sharp gaussian peak, is centered at time equals zero. This peak is due to γ -rays produced at the spallation target which arrive at the detectors first. The broad distribution following this “ γ -flash” are the beam neutrons that arrive later in time, with the highest energy neutrons arriving first. For the fission ionization chamber, a dedicated high statistics run¹¹ with less restrictive collimation was required to resolve the position of the γ -flash due to this detector’s much lower intrinsic event rate.

With the TOF relative to the time position of the γ -flash for each detector in hand, the kinetic energy KE_n of the neutrons can be determined from the following system of equations:

$$\beta_n = \frac{v_n}{c} = \frac{L}{(c \times \text{TOF}) + L} \quad (2.1)$$

$$\gamma_n = \frac{1}{\sqrt{1 - \beta_n^2}} \quad (2.2)$$

$$KE_n = m_n(\gamma_n - 1) \quad (2.3)$$

where v_n is the neutron velocity, c is the speed of light, L is the spallation target-detector separation, and m_n is the neutron mass. The spallation target-fission ionization chamber distance was known to be $L = (87 \pm 0.3)$ m. The spallation target-neutron detector distance was measured to be (88.6 ± 1.7) m.¹²

Neutron candidates detected more than 1.6 μ sec after the γ -flash were not considered in either the fission ionization chamber or neutron detector analyses, imposing a low energy neutron cut-off (ignoring neutrons arriving from a previous micro-pulse)

¹¹The fission ionization chamber run number of this high statistics run was 782.

¹²This distance is based on the relative center-to-center distance of 1.13 m measured between the neutron detector and fission ionization chamber.

of 12 MeV for both datasets. Candidates with inferred energies greater than 800 MeV were discarded. Figure 2-11 shows counts versus neutron kinetic energy from TOF for both detectors.

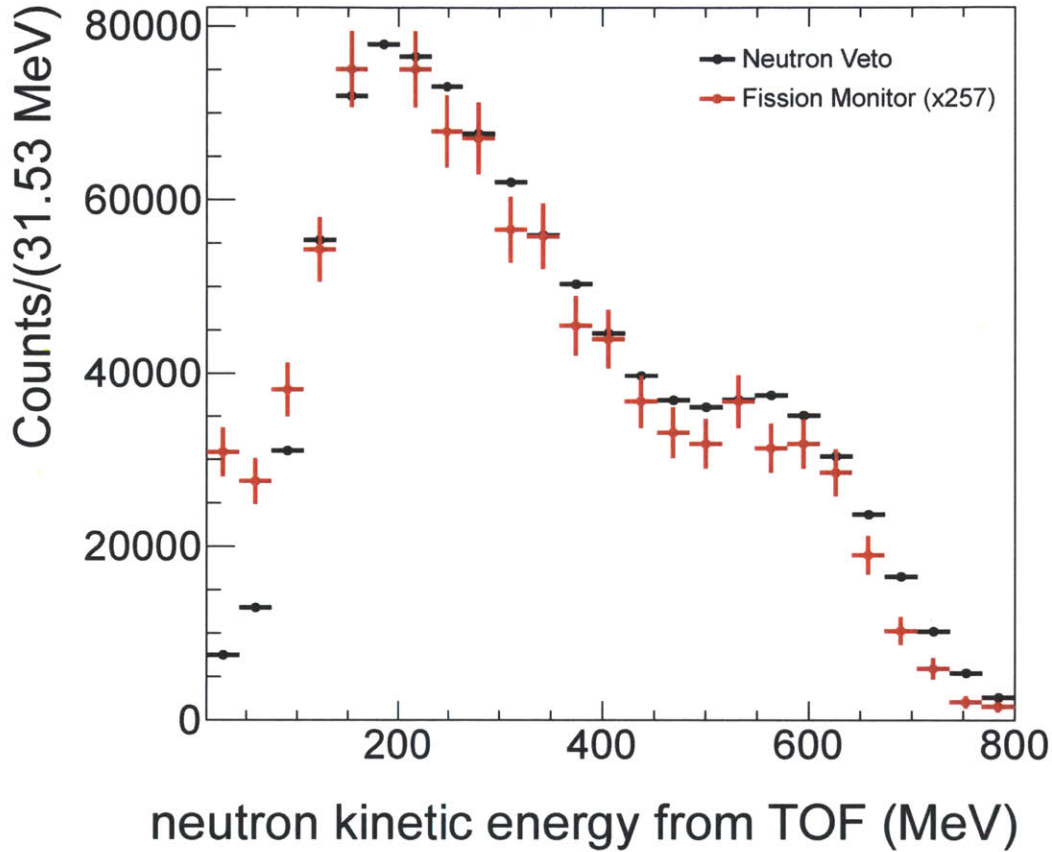


Figure 2-11: Counts versus kinetic energy for the neutron detector and fission ionization chamber datasets, after all selections. The fission ionization chamber spectrum has been scaled by a factor of 257, roughly the difference in neutron interaction cross-section between the two detectors, so that their features may be more easily compared.

2.2.5 Results

Absolute neutron detection efficiency measurement

The absolute detector neutron detection efficiency ϵ_n is defined to be

$$\epsilon_n(T_n^i) = \frac{N_n^{NV}(T_n^i) \times D^{NV}}{N_n^{LANL}(T_n^i)} \quad (2.4)$$

where T_n^i is the neutron kinetic energy bin indexed by i in which the efficiency is measured, $N_n^{\text{NV}}(T_n^i)$ is the number of neutrons observed by the detector in kinetic energy bin i (see Figure 2-11), and $N_n^{\text{LANL}}(T_n^i)$ is the number of neutrons delivered to the detector by the accelerator in bin i . The data is binned in 25 neutron kinetic energy bins of width 31.5 MeV from 11.68 MeV to 800 MeV.

The neutron detector dead-time D^{NV} is, over the course of the run, the ratio of the amount of time the detector is insensitive to neutrons to the amount of time it is capable of recording triggers. Although the average rate of neutron micropulses striking the detector was 12,926 Hz over the course of the run, the raw average trigger rate was only 27 Hz. D^{NV} was computed for each run from the ratio of the measured T0 rate to the raw neutron detector trigger rate, and is listed for every run in Table 2.2.

$N_n^{\text{LANL}}(T_n^i)$ is derived from the fission ionization chamber measured neutron flux as

$$N_n^{\text{LANL}}(T_n^i) = \left(\frac{N_n^{\text{FM}}(T_n^i) \times D^{\text{FM}}}{\epsilon^{\text{FM}}(T_n^i) \times \sigma_{n-238\text{U}}(T_n^i) \times (N_{238\text{U}}/\text{cm}^2)^{\text{FM}}} \right) \quad (2.5)$$

where $N_n^{\text{FM}}(T_n^i)$ is the number of neutron counts in neutron kinetic energy bin i , D^{NV} is the fission ionization chamber dead-time, $\epsilon^{\text{FM}}(T_n^i)$ is the known fission ionization chamber neutron detection efficiency, $\sigma_{n-238\text{U}}(T_n^i)$ is the ^{238}U neutron-induced fission cross-section, and $(N_{238\text{U}}/\text{cm}^2)^{\text{FM}}$ is the areal density of ^{238}U on the fission chamber foils.

The fission ionization chamber neutron detection efficiency ϵ^{FM} is taken to be 98%, independent of neutron energy as reported in Wender *et al.* [90]. The areal density $(N_{238\text{U}}/\text{cm}^2)^{\text{FM}}$ was 1.716×10^{18} ^{238}U atoms deposited on the foil per cm^2 . Figure 2-12 shows the ^{238}U neutron-induced fission cross-section as a function of neutron energy and is evaluated at the center of each bin in Equation 2.5. The fission ionization chamber dead-time is listed for each run in Table 2.2 and deviates from 1 only at the $\pm 0.3\%$ level. Because of this, the fission ionization chambers are treated as deadtime-free.

Figure 2-13 shows the numerator and denominator of the absolute neutron detection efficiency, Equation 2.4. Figure 2-14 shows the resulting efficiency measurement

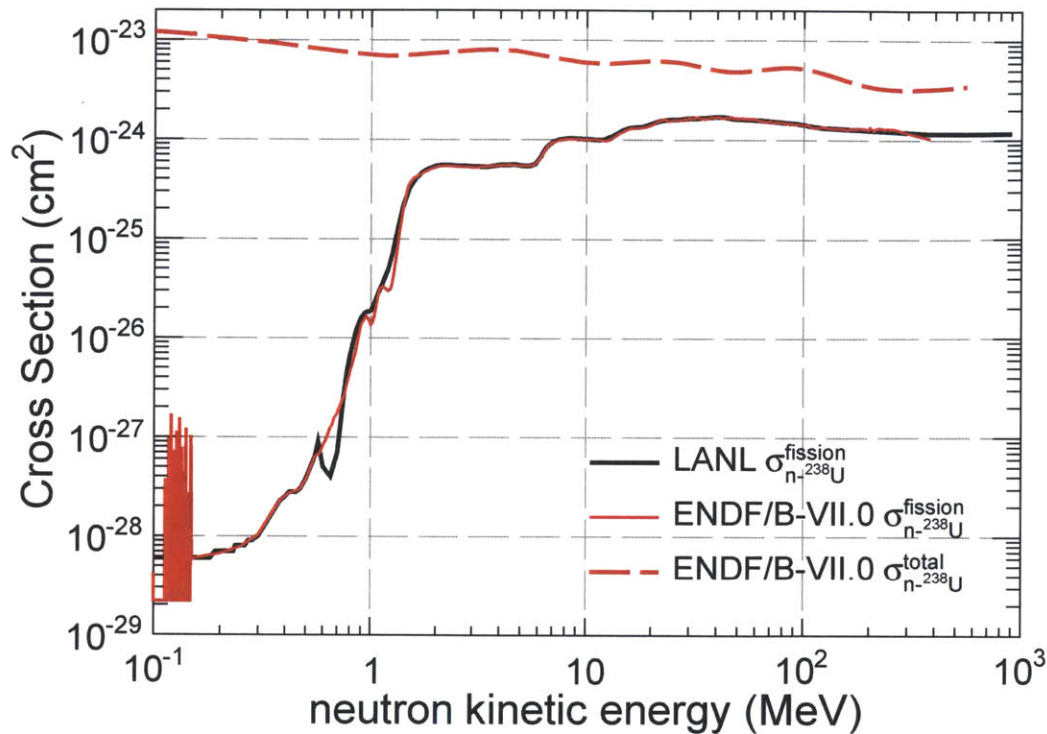


Figure 2-12: The neutron interaction cross-section as a function of neutron kinetic energy for neutron-induced fission on ^{238}U in the fission ionization chamber. Data taken from ENDF [83] and unpublished LANL measurements [92].

with statistical and systematic errors assessed. The next section describes how these errors are computed.

Errors on the absolute neutron detection efficiency measurement

The statistical errors on the number of counts in each kinetic energy bin for the neutron detector and the fission ionization chamber are computed as the square root of the number of counts in each bin.

Systematic errors are assessed from the following eight sources. These, and the values assessed, are:

LANLSYS-I: Fission ionization chamber areal density. The areal density of the fission ionization chambers is obtained by directly measuring the α yield of the ^{238}U atoms on the foil with a surface barrier detector [90]. An unpublished LANL report estimates the uncertainty on the measurement of the areal density

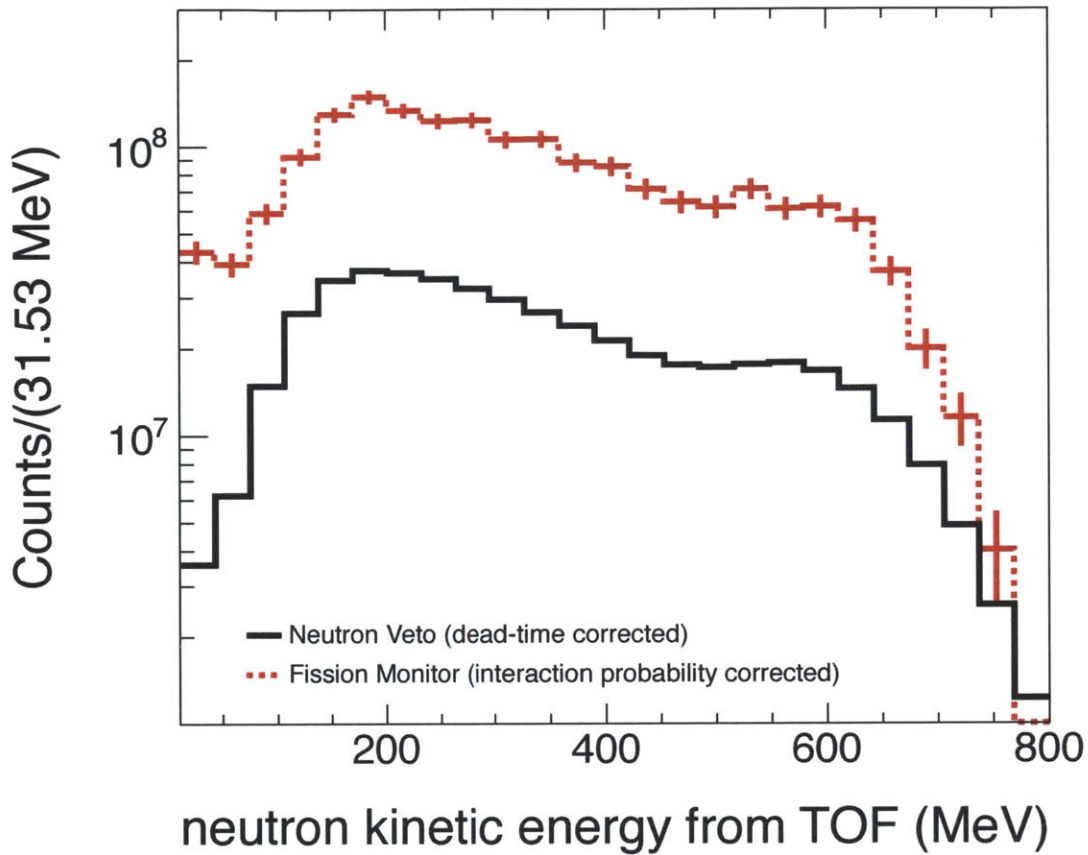


Figure 2-13: The denominator in red (the neutron interaction cross-section-corrected fission ionization chamber neutron energy spectrum) and numerator in black (the dead-time-corrected neutron detector neutron energy spectrum) of the detector neutron efficiency measurement (see Figure 2-14).

to be between 5% and 10% [93]. A 5% systematic uncertainty is assigned to the areal density.

LANLSYS-II: ^{238}U neutron-induced fission cross-section. Figure 2-12 shows the ^{238}U neutron-induced fission cross-section measured at LANL [92] and the same from the ENDF/B-VII.0 [83] database. Unfortunately there are no measurements of this cross-section in the ENDF/B-VII.0 database above 200 MeV to compare with the unpublished LANL measurements. Data below 200 MeV in the database differs from the LANL measurements by 0.5 – 5%. A 5% systematic uncertainty is therefore assigned to this cross-section, independent of neutron kinetic energy.

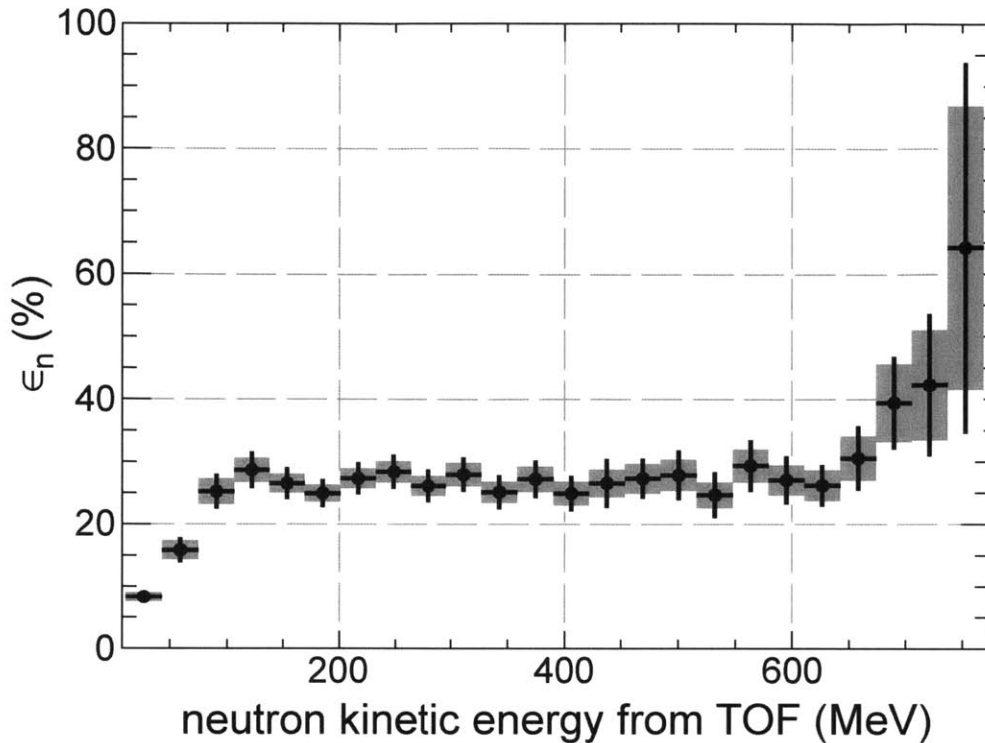


Figure 2-14: The neutron detection efficiency measured at LANL as a function of neutron kinetic energy with statistical and systematic errors. The gray bars indicate the statistical errors in each bin alone.

LANLSYS-III: Neutron detector dead-time. The estimated error on the neutron detector livetime is 1%, from the difference in the deadtime obtained from comparing the T0 rate averaged over all running to the raw neutron detector trigger rate averaged over all running and the deadtime obtained from comparing the number of raw neutron detector triggers to the number of T0s recorded over all runs.

LANLSYS-IV: Tungsten target-fission ionization chamber separation. The fission monitor-spallation target separation was measured by LANL using the positions of known carbon resonances in an absorber to within ± 0.3 m. A 0.2% systematic uncertainty was assigned to this distance.

LANLSYS-V: Tungsten target-neutron detector separation. The neutron detector-fission ionization chamber center-to-center distance was measured to

be (159 ± 3) cm. Given that the fission ionization chamber-spallation target distance was measured to be (87 ± 0.3) m by LANL, the spallation target-neutron detector separation was (88.6 ± 1.7) m, a systematic error of 1.9%.

LANLSYS-VI: Fission ionization chamber TAC-to-time conversion. The fission chamber records event times in digital TAC units, which must then be converted to ns using calibration constants measured by LANL. LANL calibrated the TAC-to-ns scale during the run and found it to be -1.133 ns/TAC.¹³ LANL estimates the error on this calibration constant is 0.001 ns/TAC [94].

LANLSYS-VII: Fission ionization chamber γ -flash position. The position of the γ -flash in the fission chamber data is determined by fitting it to a gaussian. The fit is on the digital TAC values reported by the fission ionization chamber before they have been converted into ns. The unshifted, fitted γ -flash position in TAC units in the fission ionization chamber high statistics dataset is (1382 ± 0.05) TAC. This 0.004% error is the fit error on the mean of the gaussian fit to the γ -flash and is taken as the systematic error on the fission ionization chamber γ -flash position.

LANLSYS-VIII: Neutron detector γ -flash position. The position of the γ -flash in the neutron detector data is also determined from a gaussian fit. The unshifted γ -flash position in the neutron detector data occurs at (207.1 ± 0.2) ns, where 0.2 ns is the fit error on the gaussian fit to the mean γ -flash position. This 0.1% error is taken as the systematic error on the fission ionization chamber γ -flash position.

Systematic errors LANLSYS-I through LANLSYS-III are propagated to the efficiency measurement by adding them directly in quadrature with the statistical errors of each bin of the efficiency measurement. Systematic errors LANLSYS-IV through LANLSYS-VIII are propagated to the efficiency measurement by varying each parameter assigned a systematic independently within the bounds of its systematic uncertainty and calculating the maximum resulting shift in the neutron detection

¹³The polarity of the TAC values is opposite the flow of time.

efficiency. This maximum shift is then assigned as the systematic uncertainty for each of the error sources LANLSYS-IV through LANLSYS-VIII. Table 2.4 lists the systematic uncertainties from each of the above sources averaged over all neutron kinetic energies and for a representative bin centered at 350 MeV.

2.3 Waste Isolation Pilot Plant

The Waste Isolation Pilot Plant, or WIPP, is a Department of Energy (DOE) facility approximately 26 miles south-east of Carlsbad, New Mexico. Its primary mission is the permanent, safe sequestration of hazardous transuranic waste in thick salt deposits 2,150 feet (1.585 km.w.e. [77]) underground [95]. The neutron detector was deployed at the WIPP site in the DMTPC underground laboratory on August 15, 2010. The DMTPC laboratory is located in an underground alcove at the intersection of the E-300 and N-1100 drifts. The laboratory itself is a 30 foot long steel storage container¹⁴ with approximately $\frac{1}{4}$ " thick steel walls. Data-taking with the neutron detector at WIPP began in late October, 2010.

2.3.1 Purpose

The WIPP underground site hosts several scientific efforts that require very low radioactive backgrounds, including DMTPC, the MAJORANA project [96], and the EXO-200 neutrino-less double-beta decay search [97]. Direct measurements of the fluxes of background particles at the WIPP are vital inputs to background predictions for these experiments and future experiments. Underground measurements at WIPP have been published of the total cosmic ray muon flux [98, 99], the total and thermal neutron fluxes [100, 101, 99], the amount of ^{222}Rn [102, 103], and the gamma flux [103, 99]. The purpose of this work is to measure the flux of high energy radiation underground at WIPP (> 1 MeV) as a function of energy, particularly the non-cosmic ray muon component of the flux. At very high energies, the flux is expected to be dominated by high energy neutrons [77], to which the detector has significant demonstrated sensitivity.

¹⁴From Maloy Mobile Storage, Albuquerque NM.

2.3.2 Experimental configuration

The detector was deployed in the WIPP underground DMTPC laboratory as shown in Figure 2-15. The detector is elevated several inches above the floor of the storage container and supported in the center by two car-jacks and on the ends by two 80/20 stands with 80/20 end guards for the two PMTs. To eliminate light leaks, the PMTs and their semi-translucent teflon holders were covered in several layers of black electrical tape, black plastic trash bags, and thick black felt.

Data acquisition was controlled remotely on the LeCroy WaveRunner oscilloscope by means of a web page administered by an Apache2 server running directly on the oscilloscope. The trigger decision was accomplished by means of NIM logic units. The trigger logic is shown schematically in Figure 2-16.

The signal from the two PMTs must travel through identical lengths of RG-58/U coaxial cable (≈ 10 ft long) and then through a $10\times$ attenuator¹⁵ followed by a tee that splits the signals between separate oscilloscope channels and NIM discriminators,¹⁶ which form the first step of the trigger logic. The discriminator thresholds were set at -30 mV and the discriminator pulse widths were 30 ns wide. The output of a NIM coincidence unit¹⁷ forms the trigger for recording the PMT signals on the oscilloscope.

The long axes of both the underground laboratory and the detector are aligned east-west. At WIPP, the northern-most PMT was connected to channel 2 on the oscilloscope and the southern-most PMT was connected to channel 1. The PMT-base hardware pairings at WIPP were identical to the pairings at the Los Alamos beam test, although the PMT-base combination connected to channel 1 of the oscilloscope at WIPP was connected to channel 2 of the oscilloscope at the Los Alamos beam test (and vice versa). The PMTs were both biased at -1700 V at WIPP due to excessive high frequency noise that developed on the PMT that was biased at -2200 V at Los Alamos. The PMT high voltage bias is remotely controlled for both PMTs with the oscilloscope using a USB controlled analogue output device¹⁸ coupled into

¹⁵TestPath Inc. 4 GHz bandwidth, $50\ \Omega$ attenuator, part #123-245.

¹⁶A NIM Model 623B Octal Updating Discriminator.

¹⁷A NIM Model 622 Quad 2-Fold Logic Unit.

¹⁸A LabJack U3-LV.

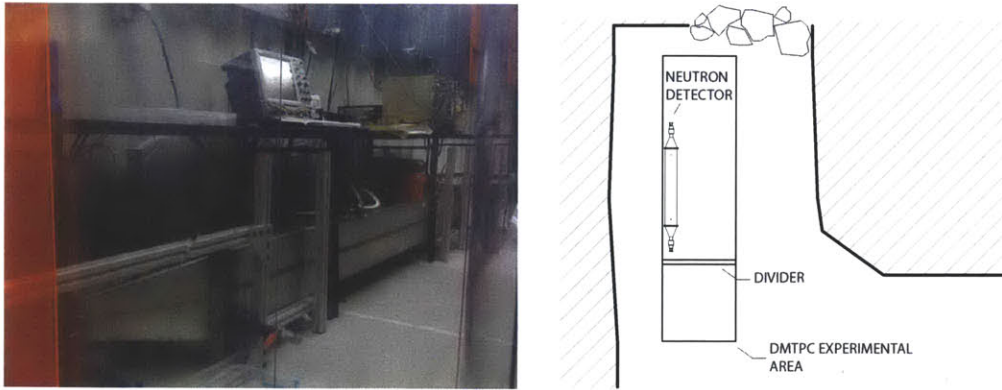


Figure 2-15: Left, a photograph of the configuration of the neutron detector at WIPP. The detector is at the bottom of the image, about a foot above the floor of the DMTPC underground laboratory. Right, a schematic of the configuration of the neutron detector at WIPP, as viewed from above.

the analogue output control of the Wenzel N1130 power supply. Because the USB controller is only capable of positive analogue output and the N1130 takes a negative reference when supplying negative voltages, a simple makeshift NIM-powered low voltage inverter module was built with operational amplifiers¹⁹ to interface between them.

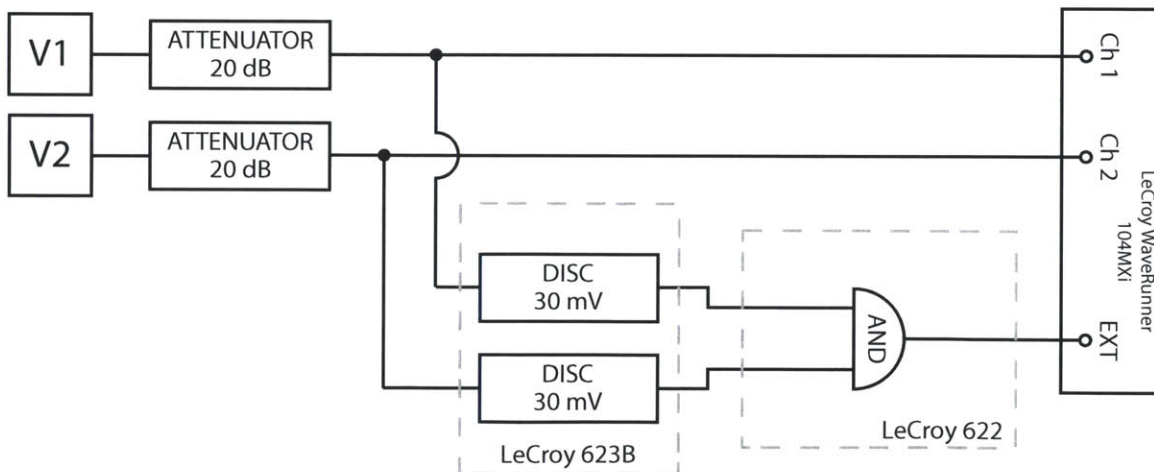


Figure 2-16: A block diagram of the triggering scheme at WIPP. V1 and V2 are the two detector PMTs. The trigger at WIPP was formed from the coincidence of the two detector PMT outputs using NIM logic units.

¹⁹Texas Instruments, LF411 Low Offset, Low Drift JFET Input Operational Amplifier.

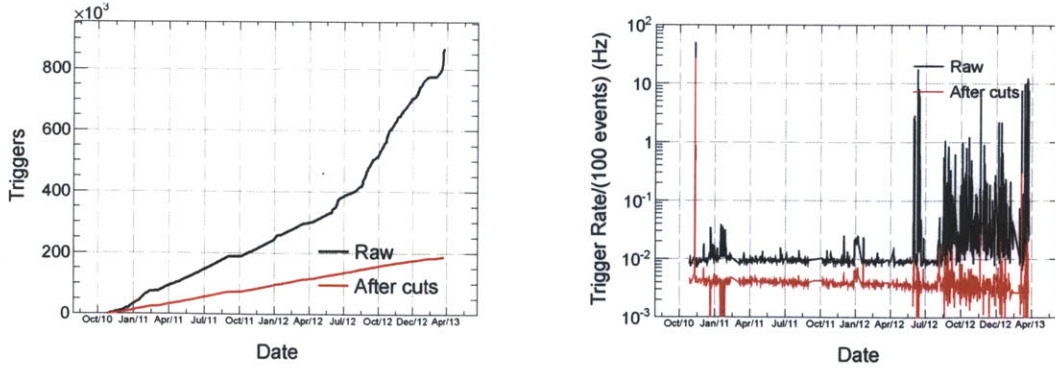


Figure 2-17: The number of events recorded by the detector at WIPP versus time and the trigger rate per each 100 events versus time, with and without the selection cuts described in Section 2.3.4.

2.3.3 Data sets

868,400 coincidence triggers were recorded with the detector from October 26, 2010 to March 26, 2013. Data was taken in sets of “runs” of 6x100 events. Each run is compressed and transferred to a computer at MIT for processing immediately after it completes. Figure 2-17 shows the raw number of triggers versus time and the event rate versus time. Table 2.5 lists all WIPP datasets between October 26, 2010 and March 26, 2013 organized by month and year. The datasets are labeled by the calendar day they were initiated. Typically data was requested in blocks of 100 runs, but datasets rarely met this goal due to power outages, network outages, oscilloscope crashes, oscilloscope auto-updates, data acquisition software crashes, and other factors. The total livetime was 59,909,056 seconds, 79% of the total time the detector was at WIPP after October 26, 2010.

The detector integrated data with little interruption, except for a set of *in situ* PMT gain calibrations performed between February 14, 2011 and March 3, 2011. A typical event is shown in Figure 2-18.

2.3.4 Analysis and event selection

WIPP *in situ* single-photoelectron calibration

The time integral of voltage pulses on each PMT (in units of $V \times ns$) is directly proportional to the number of photoelectrons (PE) detected. The mean $V \times ns$ corresponding

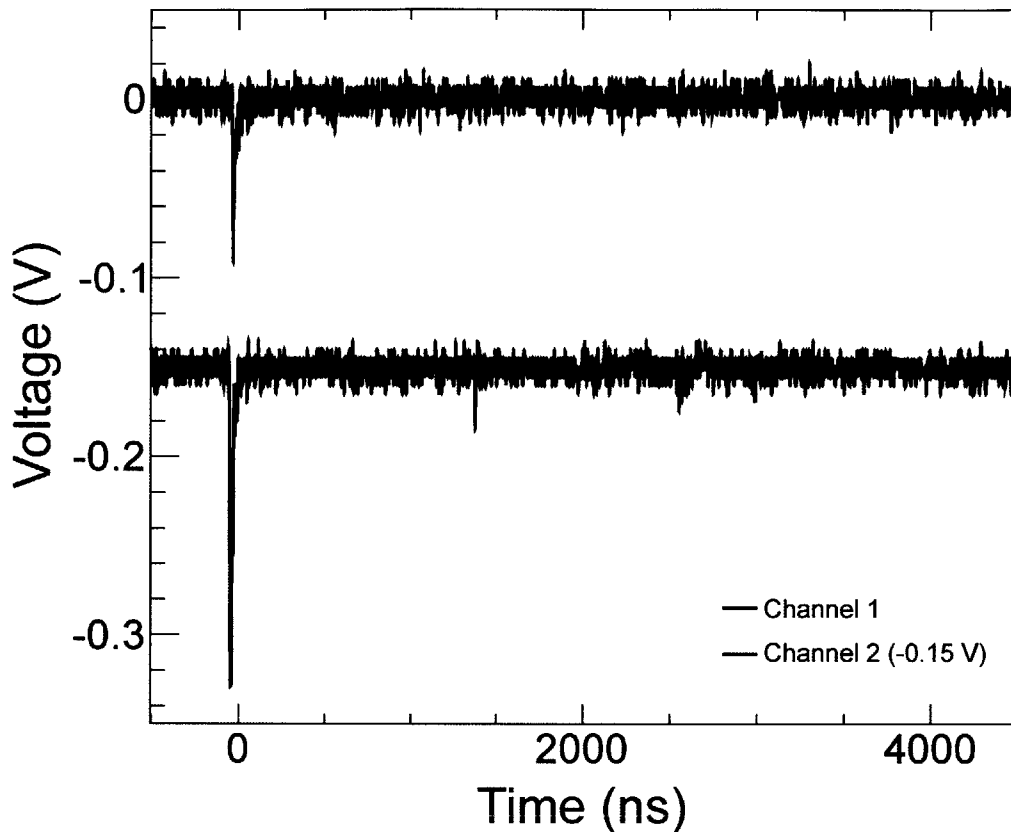


Figure 2-18: A typical WIPP coincidence event which passes the analysis cuts of Section 2.3.4. Channels 1 and 2 are the two detector PMTs. Channel 2 has been offset from 0V by -1.5V so that both channels are simultaneously visible

to a single PE is a unique property of each PMT that must be determined empirically. The $V \times ns/PE$ of each PMT at WIPP was determined with low-intensity LED pulses, with the PMTs in the exact same physical configuration as in standard data-taking.

Light from a blue LED²⁰ was coupled into the detector through the walls of a short length of semi-clear Teflon PTFE tubing in the plumbing that was originally used to fill the detector with liquid scintillator. Light was injected into the detector by pulsing the LED with a voltage pulse generator.²¹ The intensity of the light reaching the PMTs was controlled by limiting the voltage pulse height and width in time.

Data was taken, pulsing the LED, in the configuration shown in Figure 2-20.

²⁰Mouser part #638-MV5B6440, chosen because they emit light at 430 nm, almost exactly at BC-517L's wavelength of maximum emission, which is 425 nm [80].

²¹Berkeley Nucleonics Corporation (BNC) Low Jitter Digital Delay & Pulse Generator Model 565.

Every pulse delivered to the LED triggered digitization of the PMT signals, but the voltage pulse width and height were chosen such that only approximately 10% of triggers contained a PMT pulse consistent with one or more detected PE, implying that fewer than 0.5% of events with detected PE contained more than one PE.

Figure 2-19 shows the single-PE integral spectra measured for the detector PMTs at WIPP. Modeling the noise pedestal as a falling exponential and the single-PE response as gaussian, the channel 1 fitted mean $V \times ns$ per PE was $(0.0166 \pm 0.0008) V \times ns/PE$ with a fitted resolution of $(0.0061 \pm 0.0006) V \times ns$, and the Channel 2 fitted mean $V \times ns$ per PE was $(0.015 \pm 0.002) V \times ns/PE$ with a fitted resolution of $(0.0121 \pm 0.0009) V \times ns$.

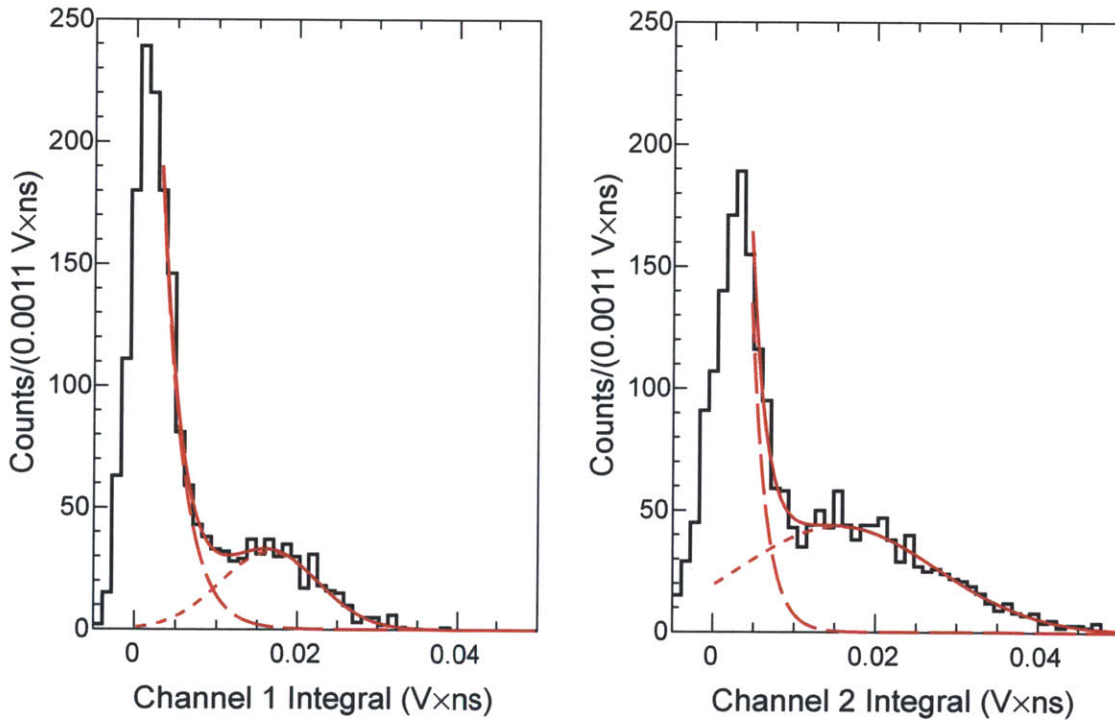


Figure 2-19: Single-PE spectra from both PMTs measured *in situ* at WIPP in the exact same detector configuration as normal data-taking. Also shown are gaussian fits to these spectra used to extract the mean charge corresponding to 1 PE in each PMT. The upper edge of the noise pedestal is simultaneously fit by an exponential.

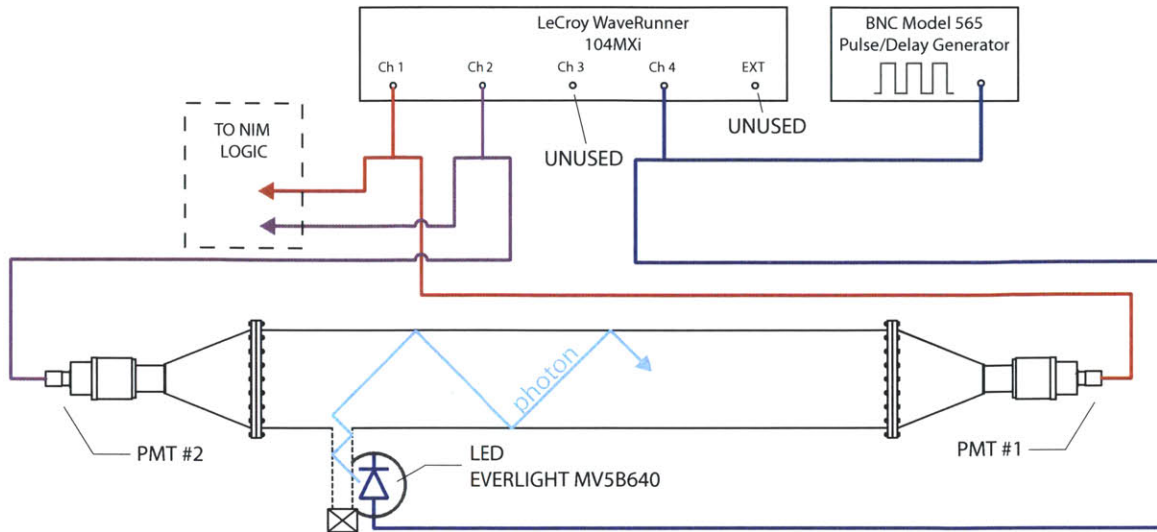


Figure 2-20: A schematic illustrating the setup for the single-PE characterization measurements at WIPP. A LED was driven with the same square voltage pulse used to trigger readout of the two detector PMTs. The amplitude of the voltage pulse was adjusted until many fewer than one photon arrived at each PMT per pulse, allowing a measurement of each PMT's *in situ* single photo-electron response.

WIPP event selection

The analysis described in Section 2.2.4 was applied to the WIPP dataset with a peak-finding threshold of 30 mV for both detector PMTs. The following criteria are then required for an event to be identified as a particle interaction with the detector:

WIPP-I: The PMT signals are within the digitizer's dynamic range. The peak height on the detector PMTs must be smaller than 0.98V. Peaks higher than this saturate the digitizer bounds.

WIPP-II: There is only one coincident signal on the two PMTs. The event must have 1 and only 1 matched peak, consistent with a single interaction.

WIPP-III: The PMT baselines are reasonable. The baseline of both PMTs must be within 5σ of the mean of a gaussian fitted to the distribution of all event baselines. This means channel 1's baseline must be within 11.00 mV of 0.68 mV and channel 2's baseline must be within 11.49 mV of 1.90 mV.

WIPP-IV: The timing of the PMT signals is reasonable. The start of matched

peaks on both channels must occur between 350 ns and 550 ns after the first time-point. The end of matched peaks on both channels must occur between 420 ns and 580 ns after the first time-point. The difference between the end and start of matched peaks must be smaller than 150 ns. This ensures that the reconstructed peak is properly associated with the event trigger, which arrives at the scope approximately 504 ns after the first time-point.

WIPP-V: PE-asymmetry cut. An event occurring close to one PMT will appear brighter to that PMT than the other detector PMT. The PE-asymmetry, defined as

$$A_{PE} = \left(\frac{N_{PE,1} - N_{PE,2}}{N_{PE,1} + N_{PE,2}} \right) \quad (2.6)$$

where $N_{PE,1}$ is the number of PE measured on channel 1 and $N_{PE,2}$ is the number of PE measured on channel 2, is thus a measure of where in the detector energy was deposited in a light-producing event. Events are required to have $|A_{PE}| < 0.5$ consistent with the energy deposition occurring in the central half of the detector. The exact relationship between event position and $|A_{PE}|$ is discussed in more detail below.

Table 2.6 contains the numbers of events after each of these cuts. 190,782 events are found to pass all selection criteria. Figure 2-21 shows the PE spectra for both PMTs for events that pass the above cuts, and A_{PE} . For events with $|A_{PE}| < 0.5$, the PE spectra on the two PMTs are nearly identical.

WIPP energy spectrum

Figure 2-22 shows the total PE spectrum from events that pass all selections. The broad peak that dominates the spectrum is due to through-going muons. The most probable expected energy loss for muons in the detector at WIPP has been estimated to be (52.5 ± 0.3) MeV using a GEANT4 [104] simulation of the detector and the parameterizations for the muon energy and angular intensity spectra at WIPP provided in [77]. The most probable number of PE created in the detector by a through-going muon is estimated from the data by fitting the total PE spectrum to a Landau dis-

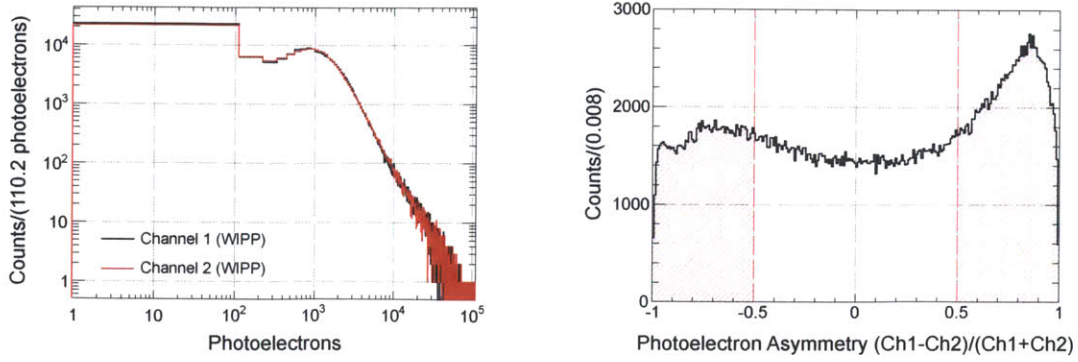


Figure 2-21: Right, the PE-asymmetry A_{PE} for data taken at WIPP. Events in the red hatched regions are cut by selection WIPP-V. The PE-asymmetry is plotted only for events with fewer than 50,000 PE on both PMTs. Left, the PMT PE spectra in both detector PMTs, after all selection cuts, including $|A_{PE}| < 0.5$.

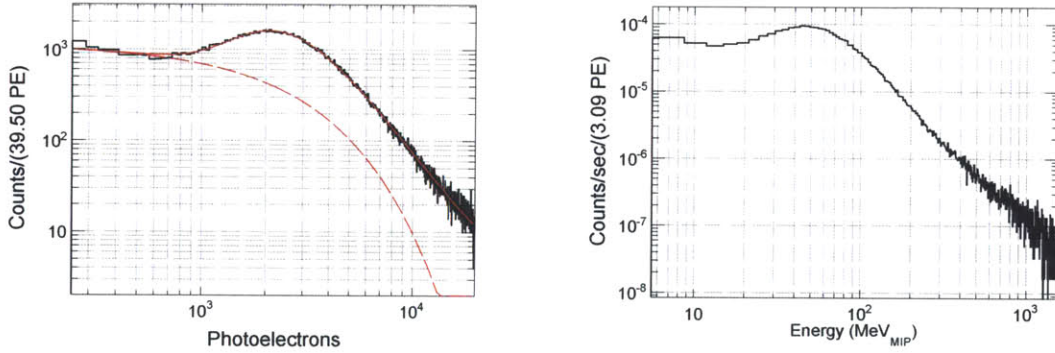


Figure 2-22: Left, the total detector PE spectrum with a Landau and exponential background fit to extract the energy scale. The energy calibration is obtained by comparing the most probable value of the fitted data Landau distribution to the expected most probable energy loss of muons in the detector from a GEANT4 Monte Carlo model. Right, the energy spectrum obtained after applying this calibration.

tribution with an exponential background, as shown in Figure 2-22. From this fit, the most probable number of PE created in the detector by a through-going muon is estimated to be (2378 ± 8) PE, implying (45.3 ± 0.3) PE are detected for every MeV deposited in the detector by a vertical-going minimum ionizing muon. The energy spectrum obtained at WIPP using this energy calibration is shown in Figure 2-22, normalized by the total detector livetime. Events are observed with deposited energy in excess of 1 GeV.

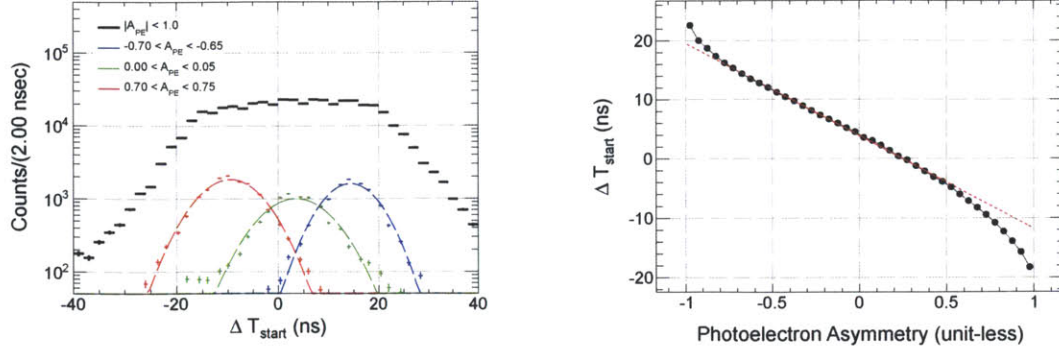


Figure 2-23: Left, the difference in reconstructed start time for the pulses on the two detector PMTs, $\Delta T_{\text{start}} = T_1^{\text{start}} - T_2^{\text{start}}$, for events that pass all selection cuts. Shown in blue, red and green are gaussian fits to ΔT_{start} for narrow slices of PE-asymmetry, $|A_{PE}|$. Right, the fitted mean gaussian ΔT_{start} for narrow slices of $|A_{PE}|$. For $|A_{PE}| < 0.5$ the relationship is linear and given by Equation 2.7.

WIPP detector area

Although the full active detector area is $(11306 \pm 89) \text{ cm}^2$,²² the PE-asymmetry cut excludes events that occur close to the detector PMTs. For $|A_{PE}| < 0.5$, the relationship between the difference in reconstructed pulse start times $\Delta T_{\text{start}} = T_1^{\text{start}} - T_2^{\text{start}}$ for coincident pulses on the two PMTs and A_{PE} is empirically found to be linear, as shown in Figure 2-23. A line fit to A_{PE} versus ΔT_{start} yields

$$\begin{aligned} \Delta T_{\text{start}}(A_{PE}) &= \left(T_1^{\text{start}} - T_2^{\text{start}} \right) (A_{PE}) \\ &= (3.89 \pm 0.02) \text{ ns} + (-15.68 \pm 0.05 \text{ ns}) \times A_{PE} \end{aligned} \quad (2.7)$$

where A_{PE} is unit-less. From geometrical considerations,

$$|\Delta T_{\text{start}}(0.5) - \Delta T_{\text{start}}(-0.5)| = \frac{2L}{(c/n_{\text{BC-517L}})} \quad (2.8)$$

where L is the active length in cm of the detector not removed by the $|A_{PE}| < 0.5$ cut, and $c/n_{\text{BC-517L}} = 20.38 \text{ cm/ns}$ is the speed of light in BC-517L. Equation 2.7 and Equation 2.8 imply that $L = (160 \pm 1) \text{ cm}$. The active area of the detector at WIPP is thus calculated to be $A = (160 \pm 1 \text{ cm}) \times (37.465 \text{ cm}) = (5990 \pm 40) \text{ cm}^2$.²³

²²Based on the fraction of vertical rays that intersect the liquid scintillator in a GEANT4 Monte Carlo model of the detector.

²³The active width of the detector is 14.75", or 37.465 cm.

2.3.5 The flux at WIPP not due to muons

The total rate of events observed at WIPP with deposited energies above 10 MeV²⁴ was (7.35 ± 0.01) mHz. Assuming all events in the detector are due to through-going muons, the muon flux implied by this rate is $(10.8 \pm 0.2) \times 10^{-7}$ Hz/cm², where corrections have been applied to take into account the expected number of muons that interacted with the detector but deposited less than 10 MeV and to remove the contribution of muons that entered the sides of the detector instead of the top.²⁵

The muon flux has been measured by Esch *et al.* at WIPP to be $(4.77_{-0.10}^{+0.08}) \times 10^{-7}$ Hz/cm² [98]. Naively subtracting the previously measured muon-only rate from the total event rate measured in this work implies that the rate of non-muon events in the detector at WIPP is (4.1 ± 0.1) mHz for events that deposit more than 10 MeV in the detector.

The total neutron flux through a surface at WIPP has been measured by Balbes *et al.* to be (332 ± 148) neutrons/(m² day) [100], while the thermal and epi-thermal neutron flux alone has been measured by Hime *et al.* to be (115 ± 22) neutrons/(m² day) [100]. Assuming that the detector is insensitive to thermal and epithermal neutrons, this implies the rate of neutrons entering each surface of the detector at WIPP is (217 ± 105) neutrons/(m² day), or a raw expected neutron event rate of (5.0 ± 2.5) mHz.²⁶ Assuming that the detector's neutron detection efficiency is $(26.6 \pm 0.5)\%$ independent of neutron energy (as measured at LANL above 100 MeV, see Figure 2-14), the expected rate of detected non-thermal neutrons at WIPP is estimated to be (1.3 ± 0.7) mHz, although the specific geometry of the detector, its immediate surroundings, and the cavern in which it is situated are estimated to affect the total neutron flux incident on the detector by factors of $(2 - 3) \times$ due to neutron

²⁴A 10 MeV cut-off was chosen because this is roughly the transition point between the exponential background and the Landau muon signal distribution assumed in Figure 2-22.

²⁵The same GEANT4-based Monte Carlo used to calculate the effective area was used to estimate that $(89.2 \pm 0.8)\%$ of through-going muons that deposit energy in the detector deposit less than 10 MeV, neglecting detector resolution, and that $(78.4 \pm 1.1)\%$ of through-going muons that deposit more than 10 MeV in the detector enter through the sides of detector instead of the top.

²⁶The active area of the detector used in this calculation was (1.98 ± 0.19) m², where any contribution from the area of the ends of the active volume in the detector has been neglected but subsumed into the error.

backscattering [105, 77]. The fact that this estimate is of the same order of magnitude as the observed excess rate of detected events in the detector at WIPP is encouraging, but the errors on this measurement are purely statistical, and more quantitative studies are needed to estimate the systematic errors on the measurement in order to establish the significance of the observed excess.

2.4 Conclusions

This chapter presents the results of operating a large, monolithic liquid scintillator detector that could be deployed as a module in a larger array of veto detectors around a dark matter direct detection experiment. The detector's sensitivity to high energy neutrons is significant and has been directly measured as a function of neutron energy at a spallation neutron source at the Los Alamos Neutron Scattering Center. The detector's size and modular design makes it ideal for moderating neutrons with energies below 10 MeV which could mimic the physical signature of a dark matter interaction in direct dark matter detectors. Its large detection efficiency for neutrons with energies in excess of 100 MeV additionally makes it well suited to actively measure the poorly constrained flux of high energy neutrons [79], which are nearly impossible to passively absorb [101]. The detector has been successfully operated in an underground site continuously for almost two years, and observes a significant excess rate of events with deposited energies greater than 10 MeV over the rate expected from through-going cosmic ray muons alone. The origin of this excess event rate is unknown, but consistent with the expected rate from high energy neutrons arising from cosmic muon spallation, although the uncertainties on this estimated rate are significant.

Cut	Number of Events
Raw number of triggers	8,550,000
A peak found on any channel (LANL-I)	3,283,980
Peak-heights within digitizer dynamic range (LANL-II)	3,283,707
No forward/backward veto signal (LANL-III)	3,120,290
Event in trigger beam-spill (LANL-IV)	2,917,057
One and only one coincidence in event (LANL-V)	1,034,202
Detector pulses coincident in time (LANL-VI)	1,010,281
Non-negligible detector pulse integrals (LANL-VII)	1,004,211
$\beta < 0.9c$ (LANL-VIII)	1,001,198
Total	1,001,198

Table 2.3: LANL neutron detector data selection cuts, with the number events that passes each cut, as the cuts are sequentially applied. Each cut is described in Section 2.2.4.

Error Source	Efficiency Averaged Error (%)	Efficiency Error at $KE_n = 350$ MeV (%)
Statistical	12.0	6.8
$(N_{238U}/\text{cm}^2)^{\text{FM}}$	5.0	5.0
σ_{n-238U}	5.0	5.0
D^{NV}	1.0	1.0
Tungsten target-fission chamber distance	0.2	0.1
Tungsten target-neutron detector distance	4.0	0.2
Fission chamber γ -flash position	3.9	4.2
Fission chamber digital-to-time conversion	3.8	1.4
Neutron detector γ -flash position	1.8	0.1
Systematic	10.0	8.4
Total	15.6	10.8

Table 2.4: Systematic and statistical errors assessed on the LANL neutron detection efficiency measurement. Each contribution to the total systematic error is described in detail in Section 2.2.5. The total error is assessed by combining each of the individual sources in quadrature. The efficiency averaged error is given by $\sum_i \sigma(KE_i)\epsilon(KE_i)/\sum_j \epsilon(KE_j)$, where the sums are over bins of neutron kinetic energy KE, and is provided to give a sense of the average error.

WIPP Datasets			
Month	Dataset(s)	$N_{triggers}^{NV}$	Livetime (d HH:MM:SS)
2010			
October	10-26-10, 10-28-10, 10-29-10, 10-30-10	1,500	2d 19:46:03
November	11-01-10, 11-02-10, 11-03-10, 11-04-10, 11-08-10, 11-09-10, 11-10-10, 11-10-10_2, 11-11-10, 11-12-10, 11-13-10, 11-14-10, 11-16-10, 11-20-10, 11-23-10, 11-26-10	9,500	15d 10:55:08
December	12-02-10, 12-17-10	30,600	36d 02:55:37
2011			
January	01-12-11	33,000	31d 22:03:31
March	03-04-11, 03-29-11, 03-31-11	22,800	23d 16:54:02
April	04-13-11, 04-27-11	19,200	26d 22:25:26
May	05-16-11, 05-19-11, 05-27-11	14,400	20d 23:09:54
June	06-09-11	16,800	23d 15:46:58
July	07-05-11	40,200	58d 00:35:51
September	09-14-11	600	0d 20:10:52
October	10-06-11	15,600	22d 06:31:34
November	11-01-11	19,800	29d 03:35:14
December	12-02-11, 12-13-11	34,200	36d 17:58:12
2012			
January	01-17-12	15,600	22d 18:13:53
February	02-11-12	22,800	33d 15:30:24
March	03-26-12, 03-31-12	4,200	6d 05:52:32
April	04-09-12	18,600	27d 18:14:48
May	05-08-12, 05-29-12	24,000	20d 10:37:31
June	06-02-12, 06-04-12, 06-16-12, 06-17-12, 06-18-12, 06-19-12, 06-23-12	49,800	38d 05:59:01
July	07-17-12	23,400	27d 10:50:00
August	08-16-12, 08-30-12	78,600	25d 10:31:16
September	09-12-12, 09-18-12	60,600	30d 22:33:50
October	10-16-12, 10-18-12, 10-19-12, 10-23-12	49,800	16d 20:47:38
September	11-03-12, 11-26-12, 11-26-12_2, 11-30-12	68,400	31d 17:04:36
December	12-12-12, 12-24-12	30,600	13d 08:29:28
2013			
January	01-02-13, 01-04-13, 01-25-13	68,400	33d 11:51:15
February	02-06-13, 02-11-13, 02-28-13	22,200	15d 17:15:05
March	03-15-13, 03-18-13, 03-23-13, 03-24-13, 03-25-13	73,200	11d 05:43:32
Total		868,400	693d 09:24:16

Table 2.5: A list of all datasets taken at WIPP. Datasets are labeled by the date on which a run was started. $N_{triggers}^{NV}$ is the number of triggers recorded by the detector during the course of each run.

Cut	Number of Events
Raw number of triggers	868,400
Peak-heights within digitizer dynamic range (WIPP-I)	862,032
One and only one coincidence in event (WIPP-II)	442,838
Baselines reasonable (WIPP-III)	442,131
Signals aligned in time with trigger (WIPP-IV)	440,035
PE asymmetry cut (WIPP-V)	190,782
Total	190,782

Table 2.6: WIPP neutron detector data selection cuts, with the number events that pass each cut, as the cuts are sequentially applied. Each cut is described in Section 2.3.4.

Chapter 3

The 4-shooter detector

This chapter describes the design and functionality of a new detector with sensitivity to the direction of dark matter-induced nuclear recoils that was constructed and commissioned at MIT between 2008 and 2013. The detector is named the “4-shooter” because it measures the direction of nuclear recoils using four scientific charged-coupled devices (CCDs). The detector is a low-pressure TPC with CCDs, photomultiplier-tubes (PMTs), and charge-sensing readout. This detector builds on knowledge and experience gleaned by the DMTPC collaboration from building and operating a similar detector, the “10L” [70, 65]. TPCs with optical readout were first suggested as a means for measuring the direction of dark matter-induced nuclear recoils by Buckland *et al.* in 1994 [43]. Figure 3-1 shows the opened detector in a surface laboratory at MIT.

Sections 3.1 and 3.2 describe the detector hardware. Section 3.3 describes the detector readout channels and detector operation in the context of an actual event. Section 3.4 describes the software tools used to monitor the detector’s health and operation, and to perform the data analysis and simulation.

3.1 Detector internals

Figure 3-2 shows the heart of the 4-shooter; the TPC which converts nuclear recoils into detectable signals. The TPC consists of two back-to-back concentric cylindrical stages, the drift stage and the amplification stage. The two stages have the same



Figure 3-1: An image of the 4-shooter detector in Building 24, Room 036 at MIT. The vacuum vessel is open, showing the TPC. The four blue CCD cameras are visible at the top of the image.

diameter and are separated by a mesh which is 77% optically transparent.¹ The cylindrical symmetry axis of the setup is vertical and the amplification stage is directly below the drift stage.

The mesh separating the drift and amplification stages is composed of 304 stainless-steel 0.0012" \varnothing wires woven in a square pattern such that there are 100 lines per square inch in both directions.² This mesh forms the top boundary of the amplification stage and is epoxied³ to the outer perimeter of the bottom boundary of the amplification stage, which is a circular, 1/4" thick copper-clad FR-4 plate.⁴ Three electrically separated electrodes are machined in the copper on the surface of this plate, as shown in Figure 3-4 and 3-5. The amplification stage mesh is only in electrical contact with the outer-most electrode. The innermost two electrodes serve as the TPC anode.

The amplification stage mesh is kept out of electrical contact with the inner two anode electrodes by non-conducting fused silica capillary tubes of diameter (435 ± 10) μm fixed between the mesh and anode plate.⁵ The spacing between the amplification stage mesh and anode plate is set by the thickness of these tubes. 13 of these tubes are arranged parallel to each other on a 1" pitch. Although the spacer end-points are fixed in place by epoxy, the spacers are not sufficiently rigid to remain fixed in shape, and their shape as a function of time must be carefully monitored. In practice, this is done by direct imaging with the CCDs.

The bottom of the TPC drift stage is the amplification stage mesh. The top boundary of the drift stage is another mesh, pressed between two copper retaining rings that serves as the TPC cathode. The distance between the cathode of the drift stage and the anode of the amplification stage was measured to be 26.7 ± 0.1 cm. Stacked between the amplification stage and the drift stage cathode are 26, 3 mm thick copper field shaping rings. The field shaping rings and cathode are aligned above

¹This optical transparency estimate is based entirely on the geometric fill factor of the wire strands composing the mesh.

²Made by G. Bopp USA Inc., article #11523.

³DP460EG Scotch-Weld Epoxy Adhesive, made by 3M.

⁴Copper clad FR-4 (2 oz of copper on the top)/(2 oz of copper on the bottom), made by Current Industrial Composites.

⁵Flexible fused silica capillary tubing with a standard polyimide coating, part #TSP320450, made by Polymicro Technologies.

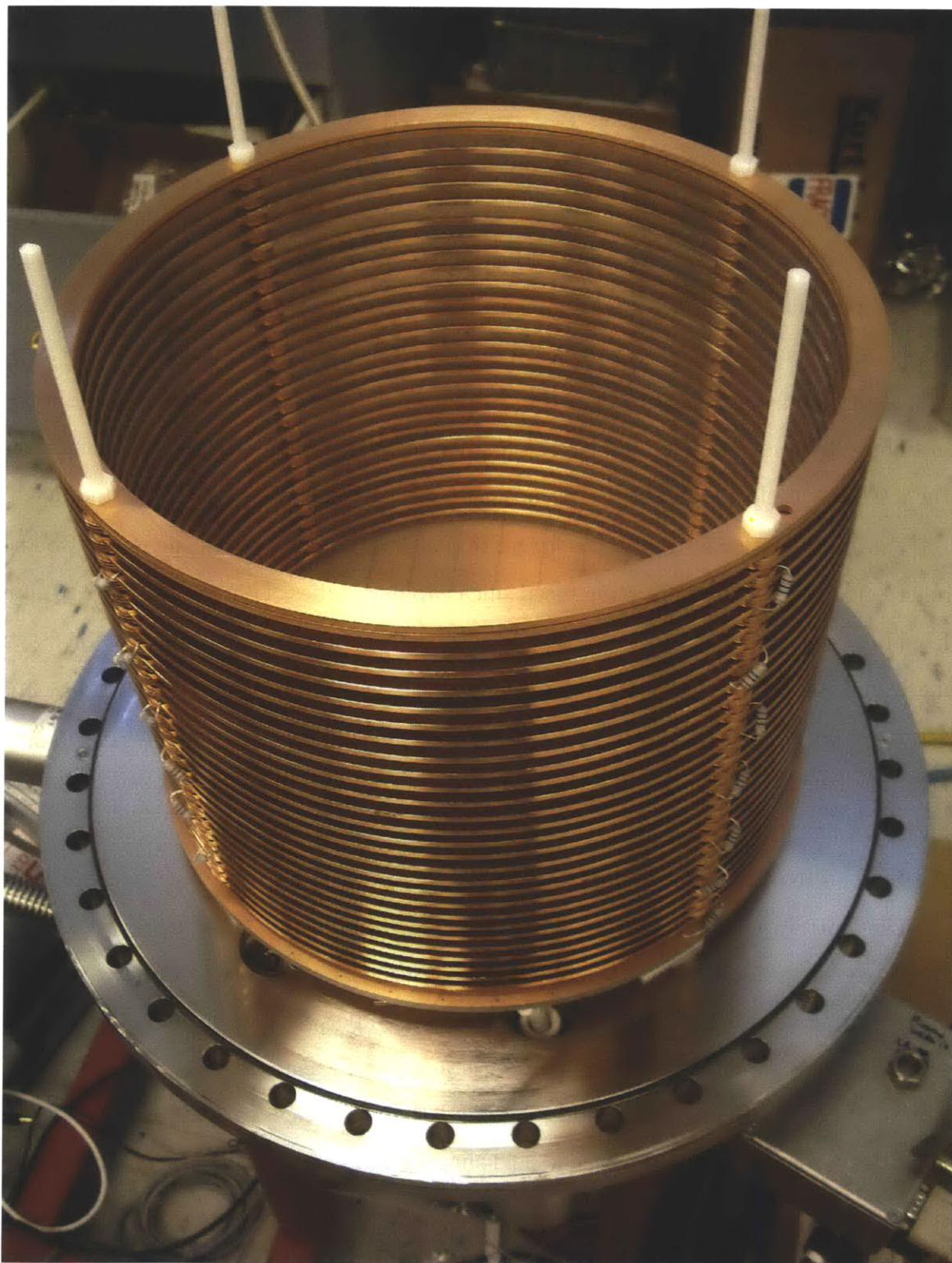


Figure 3-2: a close-up image of the field cage with the vacuum bell-jar removed. The resistor chain which distributes voltage over the TPC field cage rings is visible on the left and the right, running along the white delrin field cage support posts.

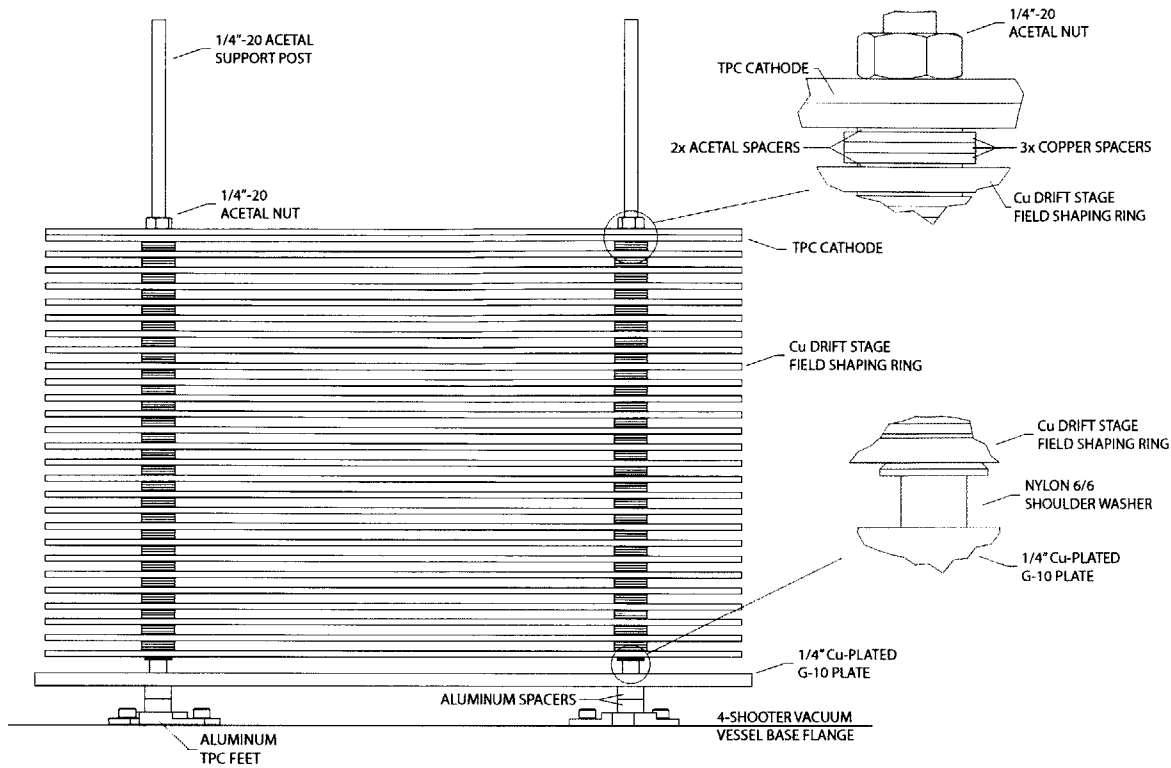


Figure 3-3: A CAD drawing of the field cage as seen from the side.

the amplification stage by four acetal 1/4-20 posts. The lowest field shaping ring is electrically separated from the amplification stage by a 1/4" thick nylon-6/6 shoulder washer. The other field shaping rings are separated by stacks of copper washers⁶ and acetal washers⁷ in an acetal-Cu-Cu-Cu-acetal pattern. This field shaping ring spacing scheme was chosen to limit the amount of acetal-outgassing in the chamber. The acetal and copper washers vary considerably in thickness even from washer to washer. According to their specifications, the field cage spacer stacks are expected to be between 0.19" and 0.32" thick in total. In practice, the spacer stacks are measured to be between 0.25" and 0.27". Figure 3-3 shows a picture and schematic of the TPC drift and amplification stages.

The cathode is electrically connected to the highest field shaping ring through a 1 MΩ resistor, and each subsequent field shaping ring is electrically connected to the

⁶Electrically Conductive Copper Flat Washer 1/4" Screw Size, 5/8" OD, .05"- .08" Thick, McMaster-Carr part #93744A130

⁷Wear-Resistant Delrin (Acetal) Flat Washer 1/4" Screw Size, 0.5" OD, .02"- .04" Thick, McMaster-Carr part #95647A125

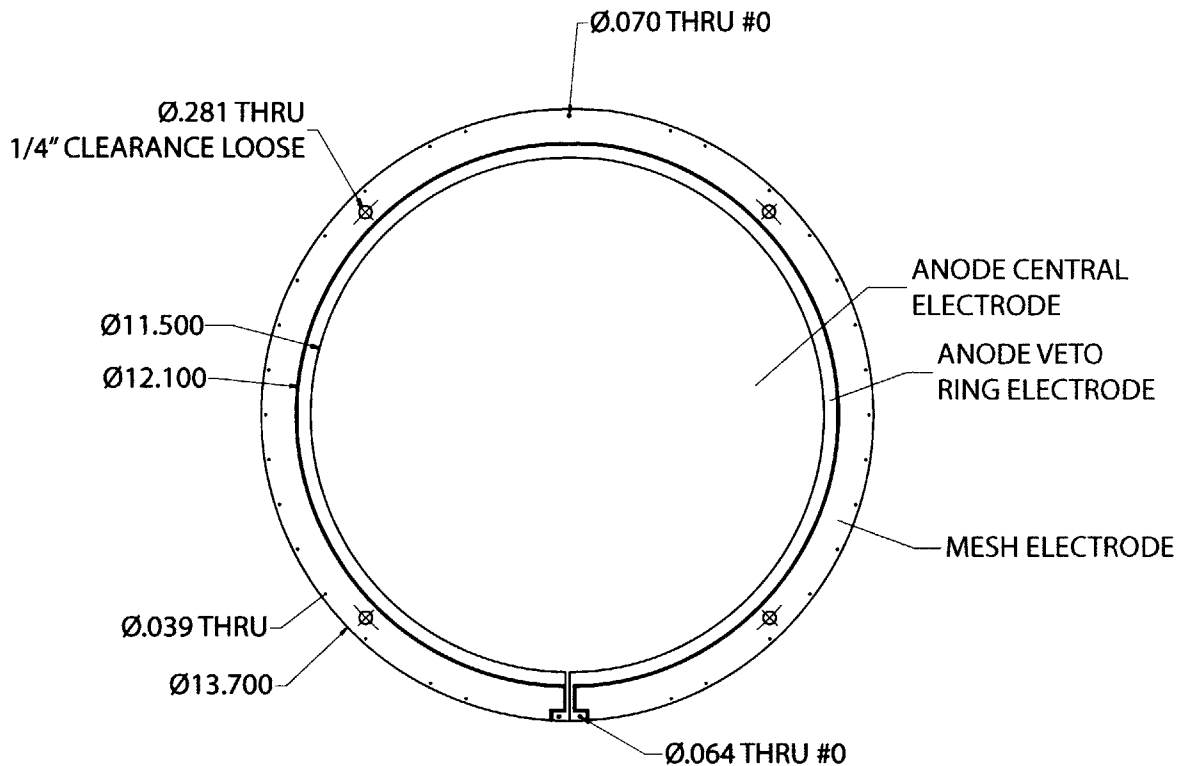


Figure 3-4: A CAD drawing of the anode plate with dimensions and electrodes labeled. All given dimensions are in inches.

ring directly above it through an identical $1\text{ M}\Omega$ resistor. The bottom field shaping ring is connected to the copper under-side of the amplification stage anode plate with a $1\text{ M}\Omega$ resistor. The copper under-side of the amplification stage anode plate is in turn electrically connected to the vacuum vessel chassis (ground) through four $\frac{3}{4}$ " tall metal feet that support the TPC on the chamber base flange. This means that there is a resistance of $27\text{ M}\Omega$ between the cathode and ground. The electrical connections between the field shaping rings and resistors are formed by folding the resistor leads around one of the acetal field cage support rods between the ring and delrin spacer immediately below or above it. Good electrical contact is achieved due to the weight of the field cage and $\frac{1}{4}$ -20 acetal nuts on the field cage support rods above the cathode which provide additional compression. Field cage spacers facilitating resistor connections are between 0.04" and 0.05" thicker than those without. For this reason, the resistor connections between field cage levels spiral around the field cage in 90° increments to avoid introducing a systematic tilt in the field cage.

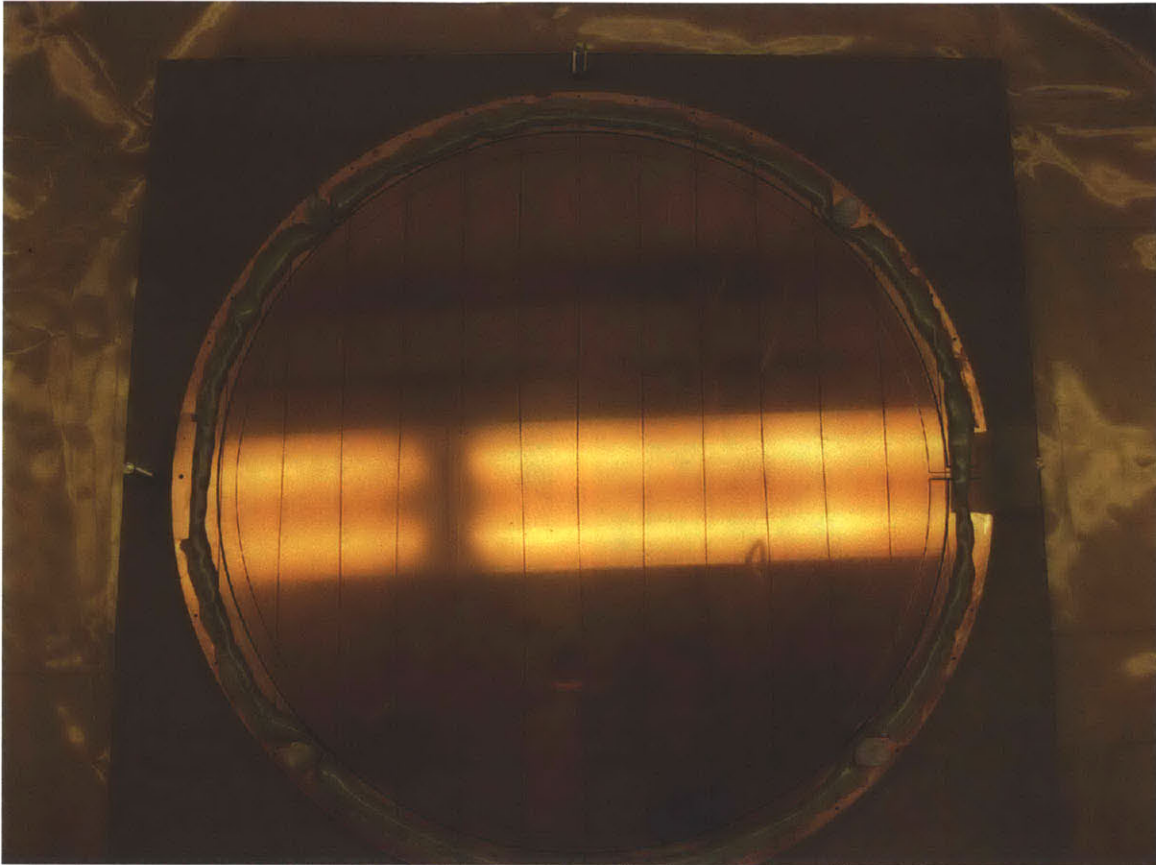


Figure 3-5: A close-up image of the fully assembled amplification stage showing the amplification stage mesh and spacers (the vertical lines) epoxied to the anode plate. Unlike the 4-shooter's anode, this anode has been polished to enhance light collection.

The cathode is powered through a single-pin ConFlat (CF) non-isolated high voltage feedthrough rated at 20 kV in vacuum.⁸ Early testing revealed that this feedthrough's alumina ceramic insulating core allowed an unacceptable amount of light into the detector, and a custom-machined light-tight aluminum housing was devised to provide a light tight cover for the air side of feedthrough. The cathode feedthrough with and without its cover is shown in Figure 3-6. Voltage is delivered to the cathode through this feedthrough by means of vacuum-compatible kapton insulated wire⁹ which runs directly from the stainless-steel feedthrough conducting pin to the copper cathode retaining ring.

⁸MDC part #9442001.

⁹Accu-Glass Products, Inc., 26 AWG, Kapton Insulated High Voltage Wire, 3kVAC / 10kVDC, part #100726.

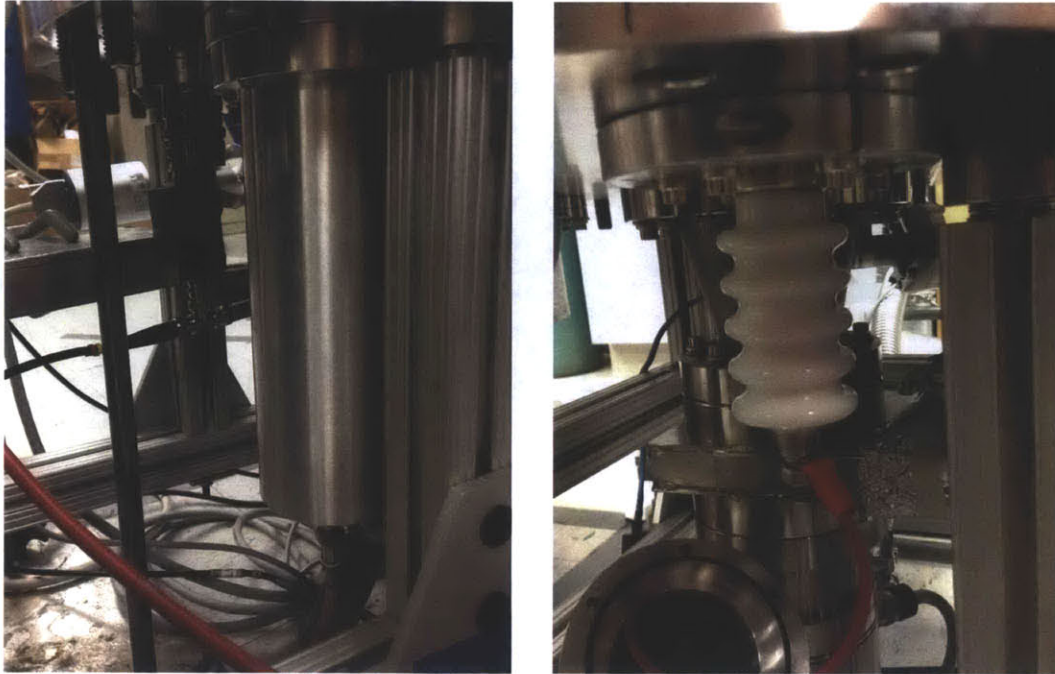


Figure 3-6: Left, the high-voltage feedthrough used to power the 4-shooter's cathode, inside of its custom light-tight cover, on the underside of the baseplate of the 4-shooter vacuum vessel. The red cable delivers voltage to the feedthrough. Right, the same feedthrough but with its custom light-tight cover removed. The inside of the cover and its Buna-N o-ring are shown in the lower left.

The central two anode electrodes are powered through an SHV-5 dual high voltage single-ended CF non-isolated exposed feedthrough,¹⁰ with one channel for each electrode. Insulated high voltage wire carries the voltage from the feedthrough to the electrodes on the anode plate inside the detector. The connections to the central anode electrodes inside the 4-shooter are shown in Figure 3-7.

One last electrical feedthrough provides a connection to the outer electrode of the anode plate, which is in electrical contact with the amplification mesh. The feedthrough is a 4-channel BNC single-ended CF non-isolated recessed feedthrough.¹¹ Only one of the 4 channels is used, to connect to the amplification stage mesh. The other three are terminated into 50Ω . Insulated high voltage wire connects the vacuum-side pin of the BNC feedthrough to the anode electrode in contact with the amplification stage mesh. The connection to the mesh inside the 4-shooter is

¹⁰Lesker, part #IFTSE021033.

¹¹Lesker, part #IFTBG042033.



Figure 3-7: Left, the vacuum-side electrical connection to the two central anode electrodes. The vacuum-side of the feedthrough is visible on the lower right of the image. The insulated high-voltage wires connect to the vacuum-side of the feedthrough with beryllium copper set-screw connectors, and to the anode through eyelet connectors held in place with #0-80 nylon screws. The nylon screws are secured on the underside of the anode by a shared rectangular G-10 washer and stainless-steel nuts. Right, the vacuum-side electrical connection to the amplification mesh. The connection scheme is identical to the other two anode connections excepting a rectangular copper washer on the top of the anode which holds a small patch of mesh captive against the outer annular electrode of the anode, ensuring electrical contact with the mesh.

shown in Figure 3-7.

Careful attention was paid during the construction and design of the 4-shooter TPC and its vacuum vessel to their materials composition and cleanliness. Cleaning and handling procedures were adapted from procedures and methods developed by the EXO [106, 107], KamLAND [108], Borexino [109] and SNO experiments [110]. All vessel and TPC materials were chosen based on their high vacuum compatibility (with particular attention paid to outgassing properties) and low expected intrinsic radioactive surface and bulk contaminants.

Additionally, all of the vacuum vessel welds were made with non-thoriated tungsten, and the interior surfaces of the stainless-steel vacuum vessel were electropolished. Where cost-effective, all vacuum seals were made with metal-to-metal CF oxygen-free high thermal conductivity (OFHC) copper gaskets, as opposed to elastomer o-rings. The only non-metal seals in persistent contact with the detector fill gas are a viton gasket used to seal the vacuum bell-jar¹², a viton seal in the gate valve used to separate the vacuum vessel containing the detector from the gas system, and a viton seal

¹²A&N Corporation part #WF1900-VG.

in the solenoidal valve¹³ used to feed gas into the detector.

The primary TPC conductor was chosen to be copper and the primary TPC insulator was chosen to be acetal plastic. The particular copper out of which the TPC field shaping rings were machined was electrolytically formed by the Aurubis Group in Germany.

A strict cleaning and handling procedure was adopted for all parts placed into the vacuum vessel. The following surface treatment was followed for all parts, always while wearing powder-free, nitrile gloves.

1. Scrub part surface with very hot tap water and liquid dish washing detergent.
2. Scrub part with acetone¹⁴ until lint-free KimWipes rubbed on the part surfaces yields no visible discoloration.
3. Rinse part surfaces in acetone.
4. Small parts underwent ultrasonic cleaning¹⁵ for approximately 15 minutes, first in acetone and then in isopropanol.¹⁶ The field shaping rings were also ultrasonically cleaned, but in a larger capacity sonic agitator.¹⁷
5. Rinse part surfaces in isopropanol.
6. Rinse part surfaces in de-ionized water.¹⁸
7. Dry part with lint-free KimWipes.
8. Allow part to air-dry for > 12 hours on a stainless-steel rack inside of a closed cabinet.

After surface cleaning, parts were only handled with powder-free nitrile gloves. Parts not immediately deployed in the detector after air drying are wrapped in lint-free KimWipes and stored in polyethylene bags until needed.

¹³MKS Instruments part #CV25-C3C3-ECNVV-24DC.

¹⁴99.5% Acetone, AR (ACS) for histological use, Mallinckrodt Baker Inc. part #2440-16.

¹⁵In a 1.7L capacity Aquasonic Model 75HT (VWR part #21811-810).

¹⁶99% Isopropyl Alcohol, McMaster-Carr part #3190K822.

¹⁷A 19L capacity Aquasonic Model 750D (VWR part #21811-836).

¹⁸100% Deionized Water, McMaster-Carr part #3190K741.

3.2 Vacuum and gas

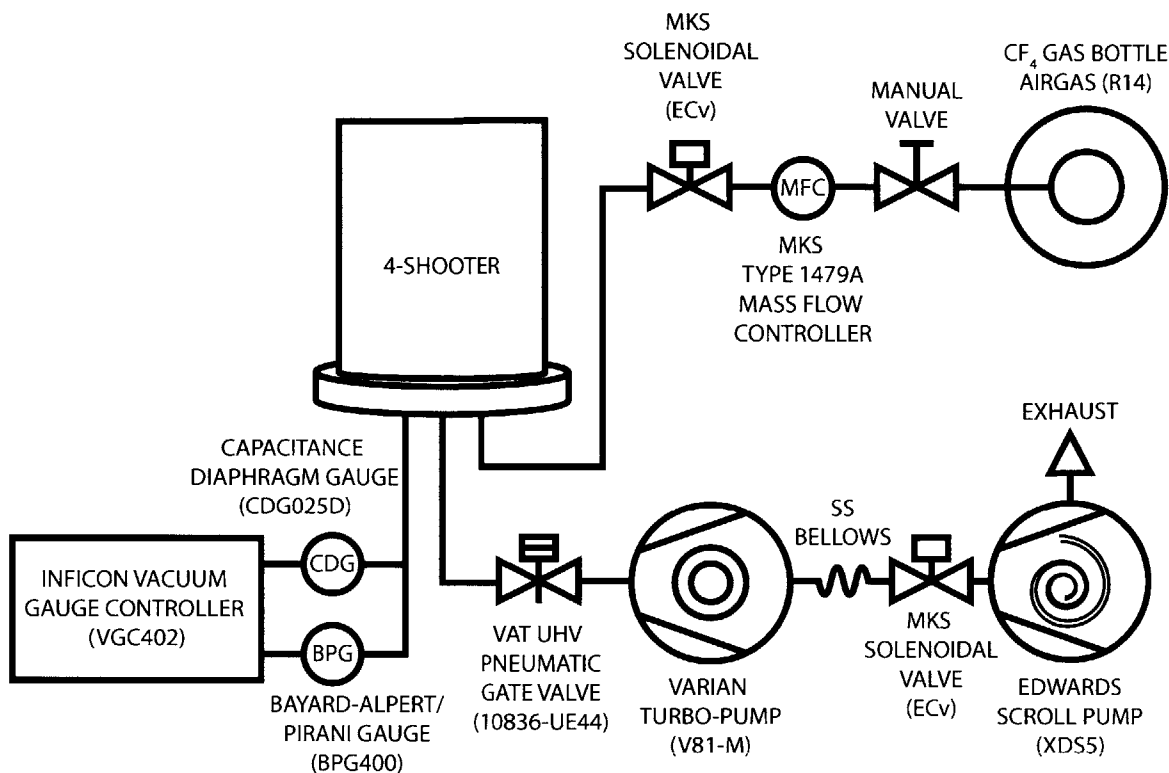


Figure 3-8: A schematic of the 4-shooter gas and vacuum system.

Figure 3-8 shows a schematic of the 4-shooter gas and vacuum system. Two pressure gauges are connected to the chamber through a 2 3/4" CF tee. One, a combination Bayard-Alpert and Pirani gauge,¹⁹ is gas-dependent and used to measure the chamber pressure below 0.1 Torr. The other, a capacitance diaphragm gauge,²⁰ is gas independent and is used to measure the chamber pressure from 0.1 Torr to 200 Torr.

To evacuate the chamber, a lubricant-free scroll rough pump²¹ is used to back a turbo-molecular pump.²² The turbo-molecular pump has a 4 1/2" CF inlet and connects to a 6" CF port on the detector chamber through a zero-length 4 1/2" CF-to-6 1/2" CF reducer. The lowest pressure achieved thus far with the fully assembled detector was 8.7×10^{-7} Torr on the Bayard-Alpert Pirani pressure gauge, after several

¹⁹The Inficon Bayard-Alpert Pirani Gauge BPG400.

²⁰The Inficon SKY® CDG025D Capacitance Diaphragm Gauge.

²¹The Edwards Vacuum XDS5 Scroll Pump.

²²The Varian Vacuum Turbo V81-M.

days of continuous pumping.

A remote-actuated metal-sealed mass flow controller²³ is used to fill the detector. Figure 3-9 shows the measured pressure over a typical pump-down and fill cycle. During normal operation, the detector is evacuated and back-filled with fresh CF₄ gas every 24 hours. The manufacturer quoted purity of the CF₄ gas is 99.99% (100 ppm total impurities).²⁴

From the ideal gas law and the 88 g molar mass of CF₄ [111], the total mass of carbon m_C and fluorine m_F in the sensitive volume of the TPC²⁵ is [111, 112]

$$m_C = 0.705 \left(\frac{P_{\text{CF}_4}}{60 \text{ Torr}} \right) \left(\frac{T_{\text{CF}_4}}{288 \text{ K}} \right)^{-1} \text{ g} \quad m_F = 4.46 \left(\frac{P_{\text{CF}_4}}{60 \text{ Torr}} \right) \left(\frac{T_{\text{CF}_4}}{288 \text{ K}} \right)^{-1} \text{ g} \quad (3.1)$$

where P_{CF_4} and T_{CF_4} are the CF₄ pressure and temperature in Torr and Kelvin, respectively.

3.3 The proto-typical event

A discussion of the readout channels of the 4-shooter is most clearly described in the context of a proto-typical nuclear recoil event.

In a proto-typical event, a dark matter particle χ (or exceedingly more likely, a neutron) striking a carbon or fluorine nucleus in a CF₄ molecule of the detector will transfer enough energy to it to free it from its CF₄ parent molecule. Once liberated, if the carbon or fluorine has non-zero residual kinetic energy, it will move through the gas, shedding kinetic energy partially through the ionization of nearby CF₄ molecules. If the resulting trail of freed electrons is generated in the drift stage of the TPC, the electrons will drift downwards until they pass through the amplification stage mesh. In the high electric field of the amplification stage, the electrons gain enough energy between collisions with the CF₄ gas to further ionize the gas, resulting in an amplification of the total number of electrons drifting in the amplification stage. In CF₄, electron amplification in high electric fields is accompanied by the creation of

²³The MKS Type 1479A Mass-Flo[®] Controller.

²⁴Airgas R14 Tetrafluoromethane Ultra High Purity Grade, part #REFR14U70.

²⁵The cylinder of gas bounded below by the anode plate, above by the cathode mesh, and in radius by the 292.1 mm \varnothing central anode electrode.

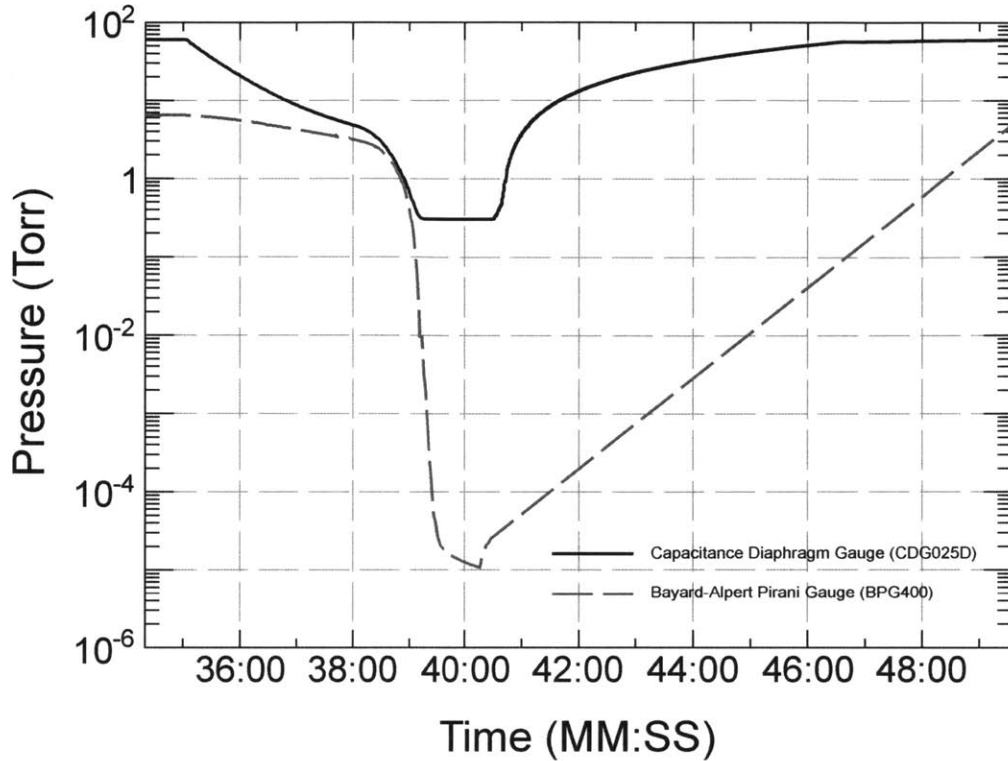


Figure 3-9: A typical curve showing the pressure in the 4-shooter over the course of an evacuation and CF_4 refill. The capacitance diaphragm gauge bottoms out at approximately 0.3 Torr, and the Bayard-Alpert Pirani (BAP) combination gauge is used to measure very low pressures in the detector. Note the discrepancy between the two gauges above 1 Torr due to the gas dependence of the BAP gauge.

large numbers of scintillation photons [56, 57]. Therefore, dark matter interactions in the TPC can be detected either via observation of these secondary scintillation photons or the drifting charges.

Figure 3-10 shows an actual $417 \text{ keV}_{ee}^{26}$ fluorine or carbon recoil²⁷ produced by a neutron interaction as seen by the 4-shooter. Each of the ten panels of Figure 3-10 correspond to the recorded output of a distinct 4-shooter sensor, each responding to the same 417 keV_{ee} nuclear recoil. Section 3.3.1 will explain how data is taken with

²⁶Only a fraction of the energy deposited in the detector by a nuclear recoil leads to ionization resulting in a visible signal. Experiments report the energy of recoils in terms of their visible energy in units of keV_{ee} , whereas the total deposited energy, which is greater, is reported in units of keV_t . This is discussed further in Section 3.4.3.

²⁷The detector is incapable of discriminating fluorine recoils from carbon recoils at these energies. However, CF_4 contains four times as many fluorine atoms as carbon atoms, making it more likely for a given nuclear recoil to be a fluorine recoil.

the 4-shooter. Section 3.3.2 will then discuss the CCD and PMT sensors which detect the secondary scintillation, while Section 3.3.3 will discuss the sensors which detect the secondary avalanche electrons drifting in the TPC amplification stage.

3.3.1 Trigger

4-shooter data is recorded in runs, where a run is a sequence of events. Every event contains four CCD images, as in Figure 3-10. During the course of each simultaneous exposure of the four CCDs, three synchronized 2-channel digitizers²⁸ sample and record the analog voltage output of 6 independent sensors over a pre-specified time window. The outputs of the 6 analog channels (the three PMTs and the anode, veto and amplification stage mesh) are digitized and recorded if a trigger condition is met. Generally, the trigger is a threshold voltage applied to one channel, but the digitizer boards can accommodate trigger criteria involving two channels. In general, the CCD exposure time (seconds) is much longer than the time window over which the digitizer samples and records (tens of microseconds), meaning each event often has multiple sets of 6 analog traces corresponding to the same simultaneous four-CCD exposure. From top to bottom in Figure 3-10, the 4-shooter analog channels are:

1. A high-bandwidth current-to-voltage transducer coupled to the amplification stage mesh, to be discussed in Section 3.3.3.
2. A charge-integrating pre-amplifier coupled to the central anode electrode, to be discussed in Section 3.3.3.
3. A charge-integrating pre-amplifier coupled to the inner-most anode ring electrode, to be discussed in Section 3.3.3.
- 4-6. Three PMTs, to be discussed in 3.3.2.

3.3.2 Optical sensors

Secondary scintillation produced in the TPC amplification stage is simultaneously sensed by 4 CCDs and 3 PMTs mounted on top of the detector vacuum vessel. The

²⁸The AlazarTech ATS860 with 250 MHz sampling and 100 MHz analog bandwidth.

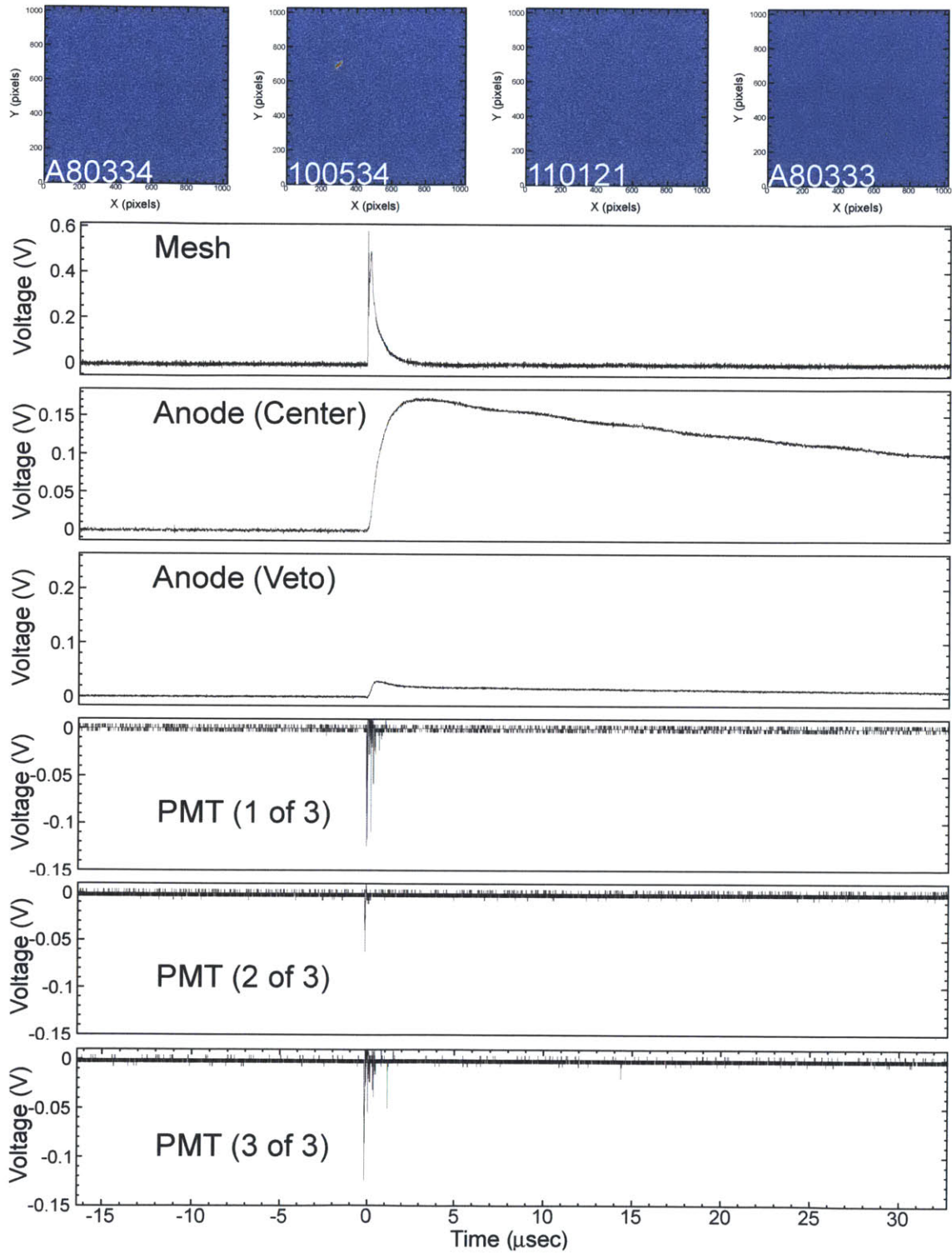


Figure 3-10: Data from Run 07723, event 953, scope trigger #7. Zooms of the charge waveforms are given in Figures 3-14, 3-17, and 3-19. A nuclear recoil is present in CCD 100534 at $(X, Y) \approx (300 \text{ px}, 700 \text{ px})$. A close-up of this recoil is shown in Figure 3-20.

CCDs and PMTs couple to the detector through five CF flanged optical viewports and are not in direct contact with the CF₄ gas. Figure 3-11 shows the layout of the optical viewports on the top flange of the 4-shooter. The following two sections describe the specific CCD and PMT sensor configurations in the 4-shooter.

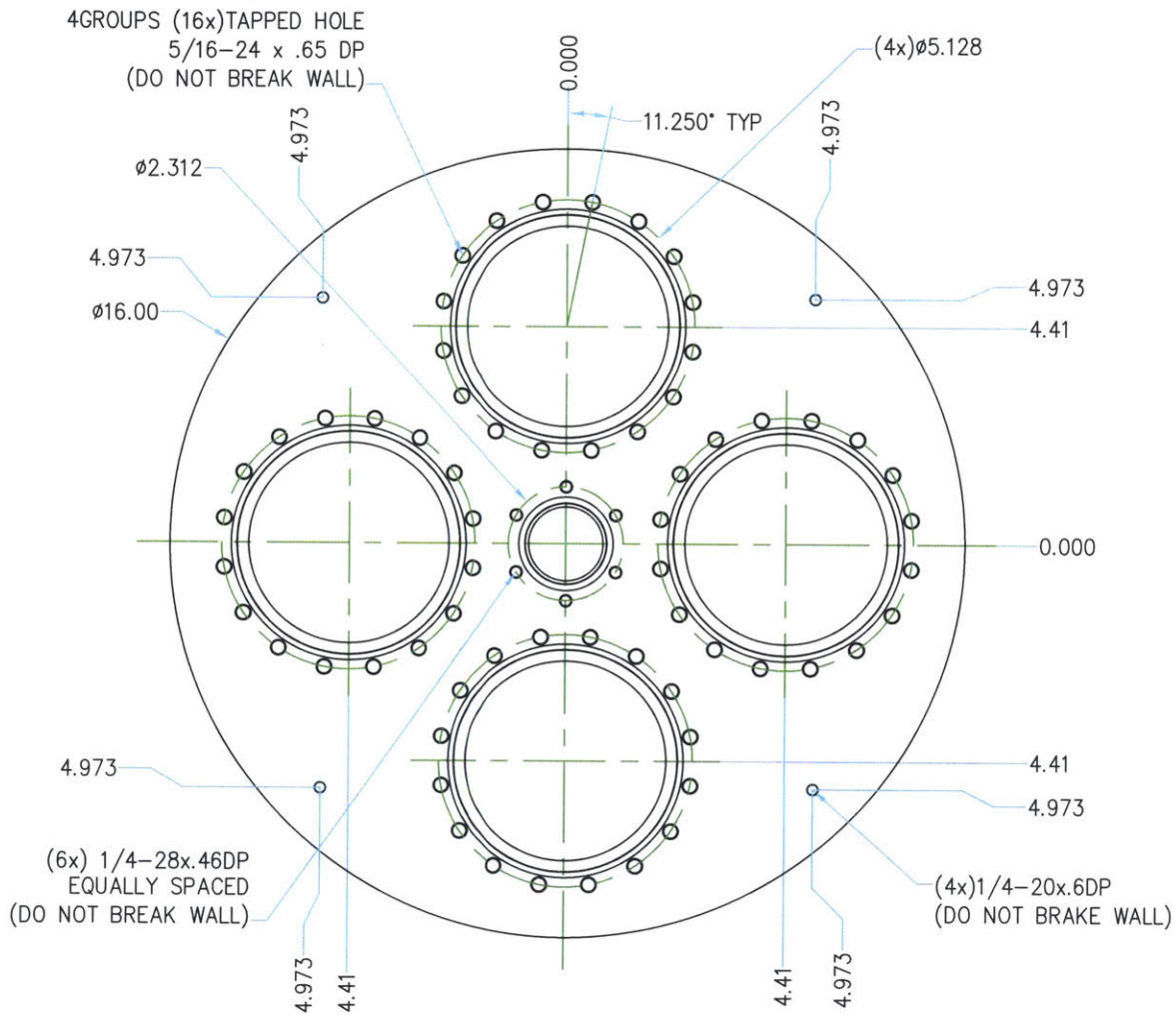


Figure 3-11: Schematic of the top flange of the 4-shooter showing the layout of the four 6" CF ports for the CCDs and the center 2³/₄" CF port for the PMTs. Dimensions are in inches.

Charge-coupled devices

Four Apogee Alta U6 scientific CCDs image the amplification stage in a 2 × 2 square pattern. The four CCDs are identifiable by their unique 6-digit manufacturer serial numbers, A80334, 100534, 110121, and A80333. Each U6 couples optically to

the detector vacuum vessel through its own 6" CF optical viewport,²⁹ as shown in Figure 3-11. The U6 houses the front-illuminated Kodak KAF-1001E CCD sensor, a 1024×1024 array of $24 \times 24 \mu\text{m}^2$ pixels. Light from the TPC amplification stage is focused onto each of the $24.576 \times 24.576 \text{ mm}^2$ CCD chips by Canon FD 85mm f/1.2 L telephoto lenses. The distance between the anode stage and the CCD chips is 71.5 cm and each Canon lens focuses a 164.25 mm square patch of the amplification stage onto its CCD's chip. Each CCD and lens assembly is coupled to its optical viewport through a custom-machined, light-tight mount. Light is prevented from leaking into the CCD mounting assembly by elastomer gaskets. The entire CCD, lens and mount assembly is shown in Figure 3-12. In early testing it was discovered that the CCD mounts were light-tight but that the U6 housing itself was not, particularly its unused electronic ports. During data-taking, these ports are covered liberally in duct-tape and thick black felt.

In order to be detected, light generated in the amplification stage must pass through both TPC meshes, the Kodial glass CCD optical viewport, the Canon lens, the U6 CCD's fused silica window, and then be absorbed by the CCD chip and produce a detectable electron-hole pair. Figure 3-15 shows the optical throughput as a function of photon wavelength of the CCD and CCD optical viewport, with the secondary scintillation spectrum of CF_4 overlaid for comparison.

Photomultiplier tubes

Three Hamamatsu R7400U-20 PMTs share the top flange's central $2 \frac{3}{4}$ " CF optical viewport³⁰ in a close-packed three leaf clover pattern. The PMTs are mechanically mounted to their optical viewport through a custom, light-tight mount. Elastomer gasket seals keep light from leaking into the PMT mount assembly. The entire PMT assembly is shown schematically in Figure 3-13. The photocathode of each PMT is approximately 495 mm from the amplification stage and has an 8 mm minimum diameter, and so each PMT photocathode subtends approximately 2×10^{-4} sr as seen from the center of the anode.

²⁹Lesker part #VPZL-600.

³⁰Lesker, part #VPZL-275Q.

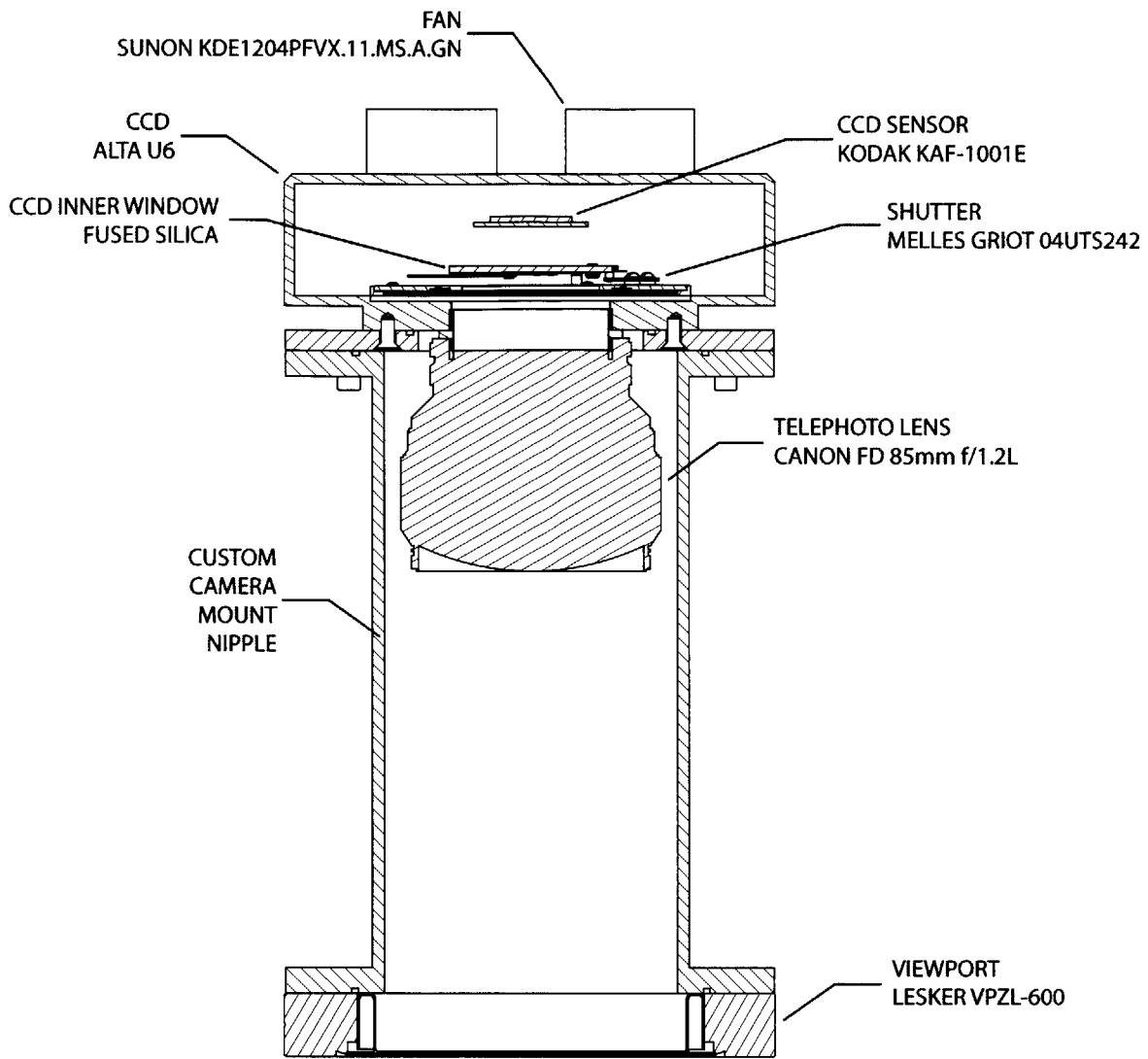


Figure 3-12: Cut-away of the assembled 6" CF optical feedthrough and mount for the 4-shooter CCDs.

All three PMTs are biased at -925 V via three Hamamatsu E5780 voltage divider assemblies. The first of the three PMTs is biased with the second channel of a NIM Bertan 380N MWPC high voltage power supply. The other two PMTs are biased with the first and second channels of a NIM Bertan 375N MWPC high voltage power supply.

Figure 3-14 shows the signal on all three PMTs for the proto-typical event of Section 3.3. Although the PMT-pulses are expected to be negative-going, large positive excursions from the baseline are evident. These positive after-pulses are not seen on a digitizer with higher bandwidth and are thought to be due to a bandwidth mismatch

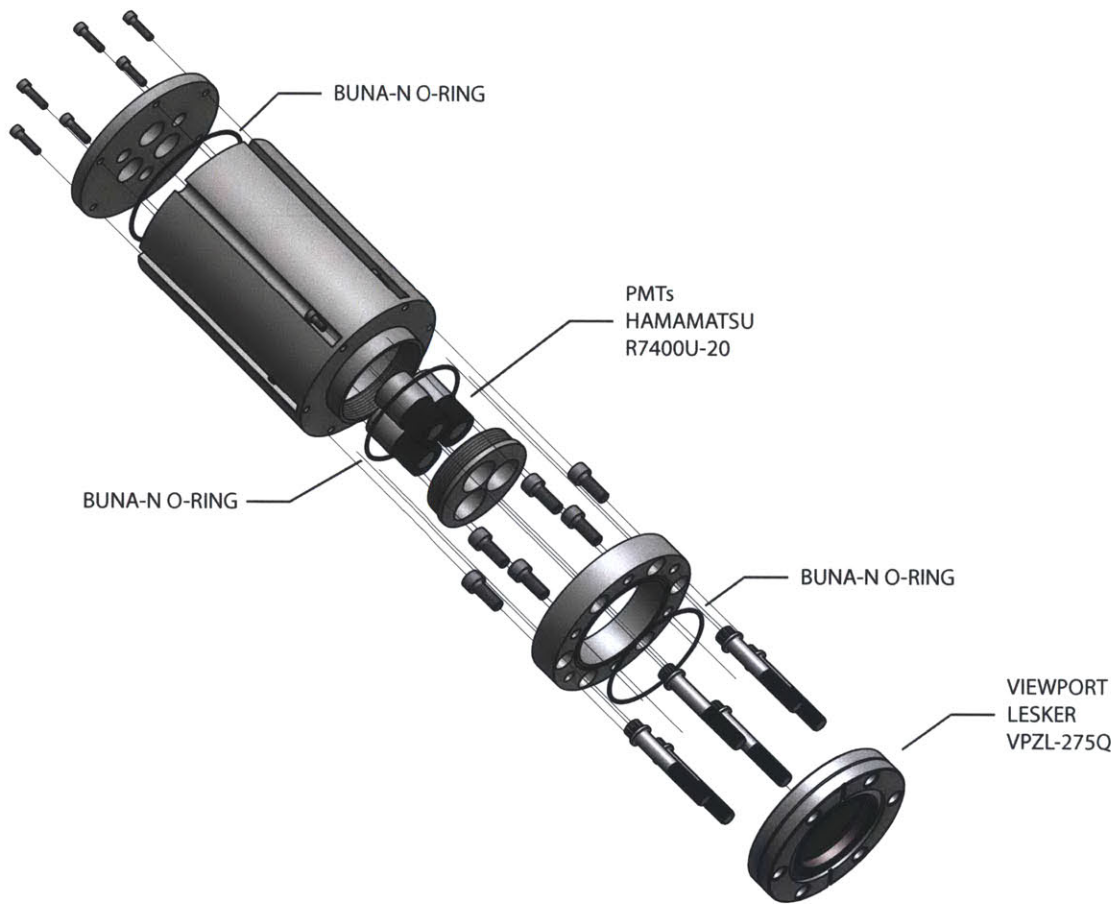


Figure 3-13: Exploded view of PMT coupling parts with labels. At the lower right is the $2\frac{3}{4}$ " CF optical feedthrough that couples the PMT assembly to the 4-shooter. Electrical connections to the PMTs (not shown) are made through the holes in the circular plate in the upper left.

between the PMTs and the Alazar ATS860 digitizer. Unfortunately, because of this bandwidth mismatch, data taken to date with the PMTs has been of limited use.

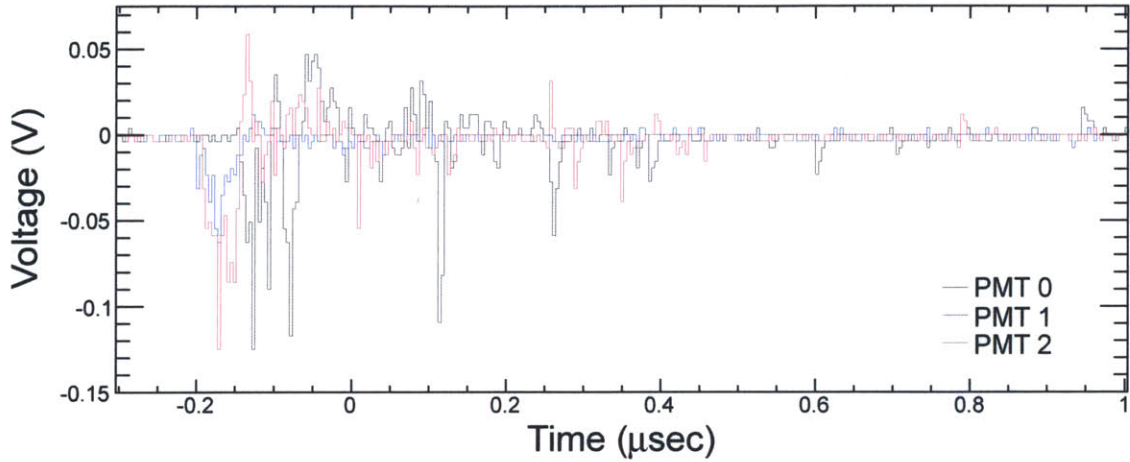


Figure 3-14: The three PMT signals from the nuclear recoil event in Figure 3-10 overlaid in black, red and blue. A bandwidth mismatch between the PMTs and the digitizer generates considerable parasitic after-pulsing.

Figure 3-15 shows the optical throughput as a function of photon wavelength of the PMTs and PMT optical viewport, with the secondary scintillation spectrum of CF_4 overlaid for comparison.

3.3.3 Charge sensors

Figure 3-16 is an equivalent circuit diagram of the 4-shooter. Three elements of the circuit as shown are capable of transducing the motion of the secondary charges produced in the TPC amplification stage by an ionization event into an analog voltage signal. The following three sections describe the specific configuration of the charge sensors in the 4-shooter detector. The charge sensors are not in direct contact with the CF_4 gas and connect to TPC electrodes through electrical feedthroughs on the bottom of the vacuum vessel.

Fast current-to-voltage mesh amplifier

As secondary avalanche electrons drift in the amplification stage towards the anode electrode, they induce an image current in the amplification stage mesh. A

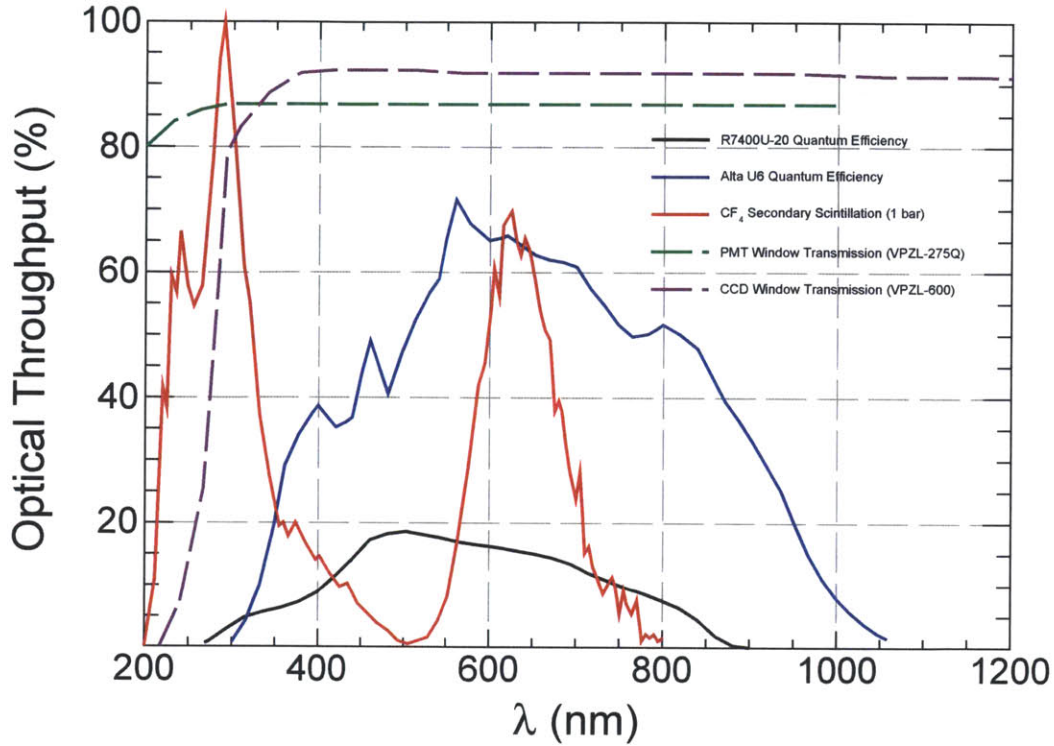


Figure 3-15: Overlay of the Hamamatsu R7400U-20 PMT's quantum efficiency, the Apogee U6 CCD's quantum efficiency, the CF_4 transmission spectrum, [113] and the PMT and CCD window light transmission versus wavelength.

Route2Electronics HS-AMP-CF current-to-voltage fast timing amplifier with 50Ω input impedance connected to the amplification stage mesh provides an instantaneous measurement of this induced current versus time with a bandwidth reaching from DC to 350 MHz.

Figure 3-17 shows the current versus time on the mesh for the prototypical event of Section 3.3, over a narrow, $2.5 \mu\text{sec}$ time window. A very sharp peak with $\sim 10 \text{ ns}$ width is observed, followed by a much broader peak that decays to baseline over the course of several micro-seconds. The first peak corresponds to the induced current due to the drift of the secondary avalanche electrons in the amplification gap and is very sharp in time because 1) the majority of avalanche electrons are produced in close proximity to the amplification stage anode and 2) the electron drift speed in the amplification stage in low-pressure CF_4 is very fast, greater than $20 \text{ cm}/\mu\text{s}$ [115]. The second peak corresponds to the induced current due to the drift of the

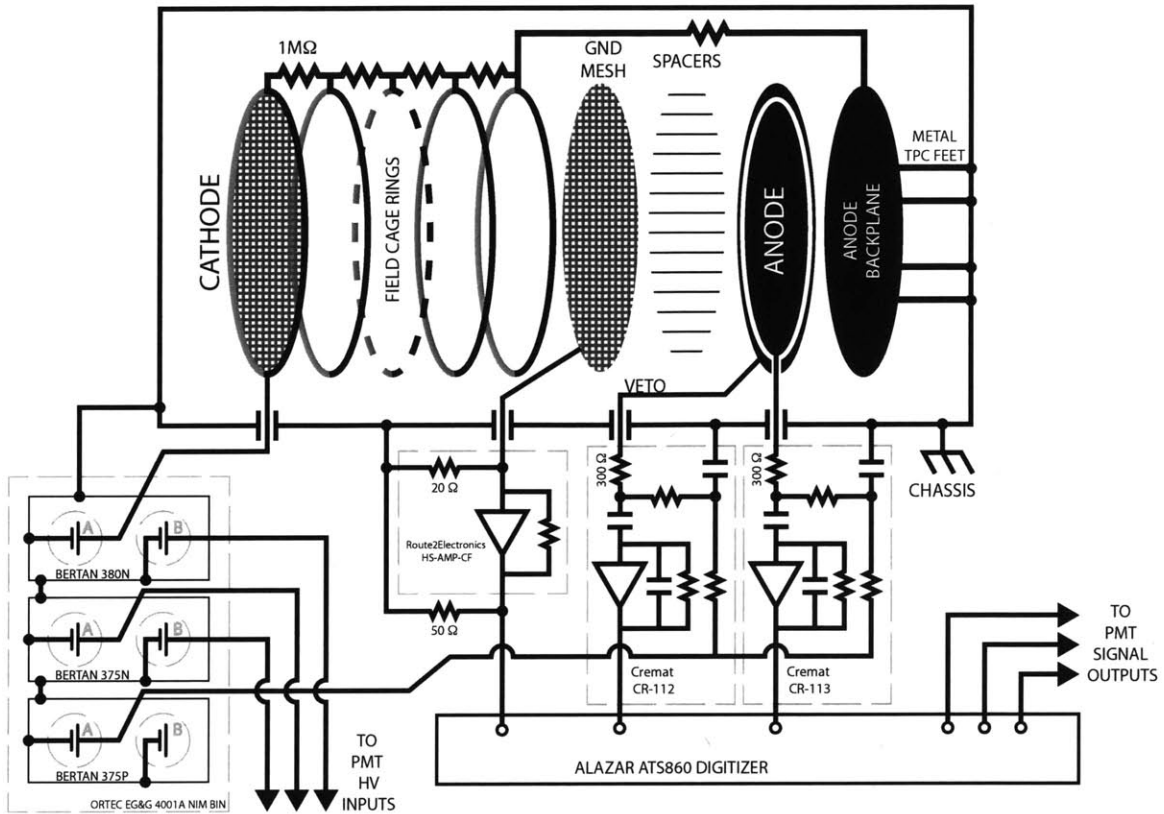


Figure 3-16: Simplified equivalent circuit of the 4-shooter detector including the TPC electrodes and charge readout channels. In the bottom right, from left to right, are the amplifiers connected to the grounded amplification stage mesh, the outer veto ring electrode on the anode of the amplification stage, and the central electrode on the anode of the amplification stage. Also shown, in the bottom left, are the high voltage supplies used to bias the TPC electrodes. Solid black lines denote electrical connections.

secondary avalanche ions in the amplification gap. This peak is much broader in time because 1) ions must drift much further than electrons before they are collected on the amplification stage mesh and 2) ions drift much more slowly than electrons in low pressure CF_4 , by a factor of over 200 [116].

The high gain ($80\times$ voltage gain) and wide bandwidth of the HS-AMP-CF amplifier makes it particularly susceptible to electromagnetic interference (EMI) and electronic noise on its two power input lines. The HS-AMP-CF is powered with $\pm 12\text{V}$ broken out from the voltage bus of an EG&G Ortec 4001A NIM bin. To mitigate electronic noise on the amplifier input power line, the NIM bin input wall AC

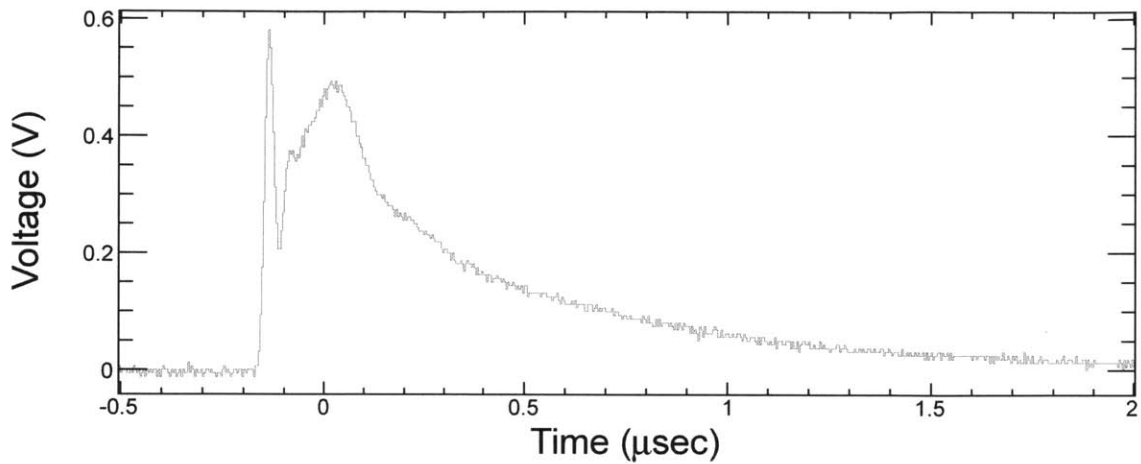


Figure 3-17: The fast amplifier mesh signal from the nuclear recoil event in Figure 3-10. The two-peaked shape of this pulse is characteristic of nuclear recoils, and is exploited to discriminate between nuclear recoils and energy depositions due to other particles interacting in the detector like electrons or γ -rays [71, 114].

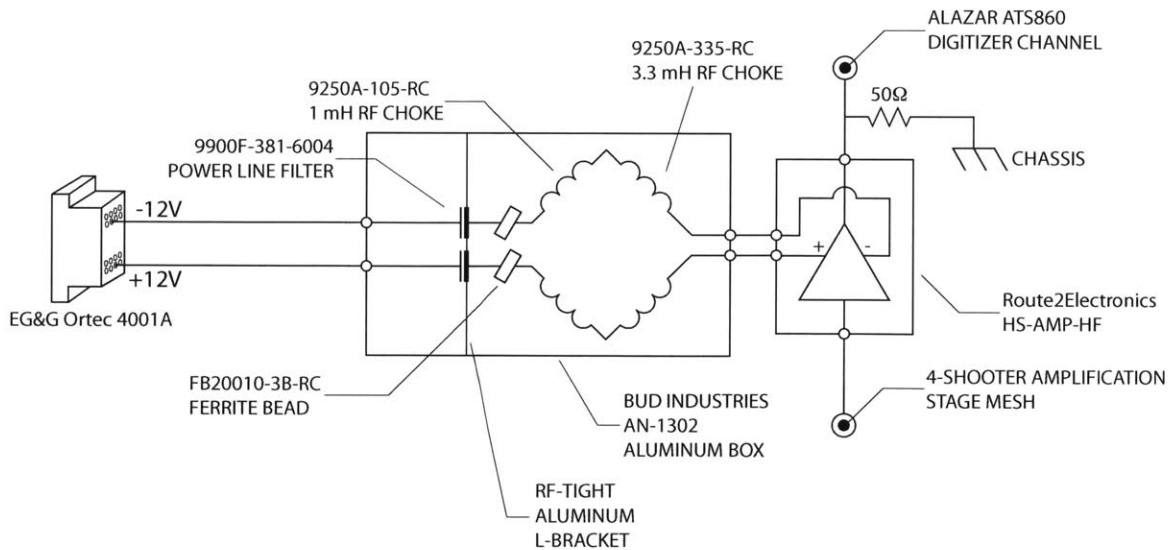


Figure 3-18: Filter used for the $\pm 12V$ power inputs of the mesh HS-AMP-CF amplifier. The filter is designed to eliminate high frequency noise from low frequency signal lines.

power is filtered with an isolation transformer³¹ and the filter³² in Figure 3-18 is used to further filter the input power just before it is delivered to the amplifier. A small, troublesome DC offset was observed in the bare amplifier output when coupled directly into the Alazar ATS860 digitizer, and the offset level was observed to change randomly in discrete steps over long time-scales. The offset was eliminated by teeing a 50 Ω BNC terminator with the output of the amplifier directly on the amplifier output.

Charge integrating central anode amplifier

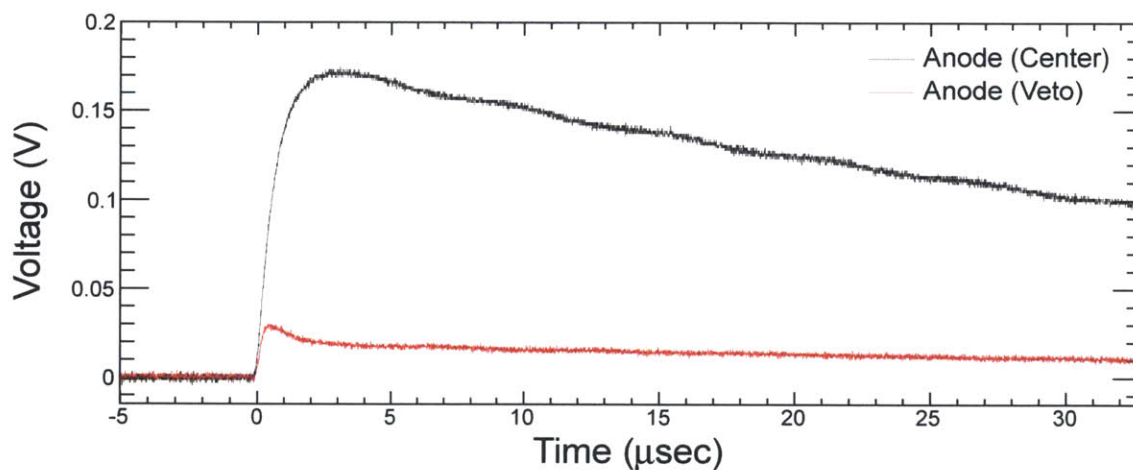


Figure 3-19: The anode and veto signals from the nuclear recoil event in Figure 3-10. Even though the nuclear recoil did not occur over the veto electrode, a small signal is present on the veto channel due to cross-talk between the two electrodes.

A Cremat CR-113 charge sensitive pre-amplifier is connected to the central, circular anode electrode in Figure 3-4. This amplifier integrates the total induced current due to the drift of the avalanche electrons in the central 292.1 mm \varnothing of the amplification stage. The CR-113 is interfaced with the detector through a Cremat CR-150 evaluation board which is housed in a custom aluminum Radio Frequency (RF)-tight box. The amplifier connects to the anode electrode through a 300 Ω resistor which provides protection for the amplifier if the amplification stage discharges. The central anode electrode is biased through the CR-150 board on the first channel of a NIM

³¹The Tripp Lite IS-500 500W Isolation Transformer.

³²Filter designed by Brian D'Urso.

Bertan 375P MWPC high voltage power supply. The central anode electrode and anode veto ring electrodes are both biased on the same high voltage power supply channel. The CR-113 chip is powered with $\pm 12\text{V}$ broken out from the voltage bus of an EG&G Ortec 4001A NIM bin.

Figure 3-19 shows the signal on the central anode electrode for the proto-typical event of Section 3.3. The nominal gain of the CR-113 is 1.5 mV per picoCoulomb of integrated charge. The height of the pulse provides a measurement of the integrated current in the amplification stage, which is proportional to the total energy deposited by an ionization event if the event occurs directly above the central anode electrode. The long-time behavior of the pulse is dominated by the 50 μsec RC time constant of the amplifier circuit.

Charge integrating anode veto ring amplifier

A Cremat CR-112 charge sensitive pre-amplifier is connected to the inner-most annular anode electrode in Figure 3-4. This high-gain amplifier preferentially integrates current induced by the drift of secondary avalanche electrons in the amplification stage produced between a radius of 5.765" and 6.05" off the cylindrical symmetry axis of the TPC. The maximum radius at which an ionization event can occur and produce a detectable signal in the TPC is restricted by the 6.05" inner radius of the TPC field shaping rings. The total charge integrated on the CR-112 amplifier output can be used to veto ionization events that begin on or outside of the TPC and cross into the TPC active volume or vice versa. This allows the detector to be fiducialized in the (X, Y) plane.

The CR-112 is connected to the anode veto ring electrode in exactly the same configuration as the CR-113 is connected to the central anode electrode. The nominal gain of the CR-112 is 13 mV per picoCoulomb of integrated charge.

Figure 3-19 shows the signal on the anode veto ring electrode for the proto-typical event of Section 3.3. Although the ionization event occurs well inside the 5.765" inner radius of the veto ring electrode, a small "cross-talk" current is nevertheless induced on the veto electrode and subsequently integrated on the high gain CR-112.

Ionization occurring directly over the veto electrode can be identified by comparing the total charge induced in the veto electrode to the total charge induced in the central anode electrode, as in Lopez *et al.* [71].

3.4 Software

A large body of custom software has been developed by the DMTPC collaboration for the 4-shooter. Section 3.4.1 will describe the software that has been developed to control and monitor the 4-shooter during data-taking operations. Data analysis is performed off-line, independent of data-taking, and is described in Section 3.4.2. Section 3.4.3 sketches the framework that has been developed to model the full response of the 4-shooter detector to ionization events.

3.4.1 Data acquisition and slow control

Data acquisition is accomplished on a dedicated Linux machine with C++ macros written in the ROOT analysis data framework [117] which interact with the CCDs and digitizer boards through their manufacturer provided Application Programming Interfaces (APIs). The 4-shooter's three 2-channel Alazar ATS860 digitizer Peripheral Component Interconnect (PCI) cards are housed in the data acquisition machine. CCD images (16-bit) and digitizer traces (8-bit) are stored directly as native ROOT data types in the ROOT file format on the data acquisition machine (as TH2S and TH1C ROOT data-types, for images and traces, respectively).

A second Linux, "slow control" machine is dedicated to persistent monitoring of the 4-shooter detector state. A C++ executable linked to the ROOT libraries constantly running on the slow control machine continuously monitors a subset of the 32 16-bit analog inputs of a National Instruments (NI) 6229 PCI card, which are connected to an array of sensors monitoring different aspects of 4-shooter operations. These sensors interface with the NI cards via two BNC break-out boxes.³³ The slow control monitoring script samples and records the sensor outputs at approximately 1 Hz³⁴ and

³³The NI BNC-2090A shielded rack-mount BNC connector block.

³⁴Standard MySQL timestamps have 1 second precision.

records them in a local MySQL³⁵ database administered by the slow control machine. The following sensors are continuously monitored using the NI 6229 board:

1. Two temperature sensors.³⁶ Both sensors are outside of the TPC vacuum vessel. One is near ground-level, taped to one of the four 4-shooter stand support legs. The other is taped on the outside of the vacuum vessel half-way between the top of the vacuum vessel and the vessel base-plate.
2. The high voltage being supplied and current drawn by each channel of the three Bertan MWPC high voltage power supplies used to bias the TPC electrodes and the 3 PMTs. +1 V on the voltage monitoring lines corresponds to 1 kV of bias voltage and +1 V on the current monitoring lines corresponds to 100 μ A [118].
3. The instantaneous mass flow controller CF₄ flow rate. The mass flow controller provides a 0 to 5 VDC output which is proportional to the rate the controller flows CF₄ into the detector vessel [119].

The pressure in the vacuum vessel is monitored by the slow control machine through a serial connection to a 2-channel vacuum gauge controller³⁷ connected to the two detector pressure gauges. During data-taking, through the data acquisition machine, the slow control machine also logs the CCD sensor temperatures and raw average measured intensities for each exposure.

Four analog outputs on the NI 6229 allow computer-control of the CF₄ flow rate through the mass flow controller, and the TPC anode and cathode voltages. Remote control of these analogue outputs is accomplished through CGI scripts accessible via an Apache2 HTTP server³⁸ running on the slow control machine. Perl³⁹ CGI scripts accessible through this Apache2 server produce real-time plots of all of the sensor measurements monitored by the slow control.

³⁵<http://www.mysql.com/>

³⁶National Semiconductor LM35 Precision Integrated-Circuit Centigrade Temperature Sensors.

³⁷The Inficon VGC402 vacuum gauge controller.

³⁸<http://httpd.apache.org/>

³⁹<http://www.perl.org/>

3.4.2 Off-line analysis

Once data has been taken and saved in ROOT files on the data acquisition machine, the data files are transferred to computers at MIT for off-line analysis. Information about interactions in the detector is extracted from both the saved lists of voltages versus time, or “waveforms,” from the 6 digitizer channels, and the 4 CCD images recorded for each event.

Image analysis

Image analysis is performed with the DMTPC `cleanSkim` analysis package.⁴⁰ `cleanSkim` identifies clusters of pixels likely to be associated with an energy deposition in the TPC, and estimates physically meaningful parameters associated with the putative track that deposited the energy.

Dark frame and overscan cleaning. Preceding each sequence of images taken in a data run,⁴¹ a series of 100 back-to-back dark (shutter-closed) frames is taken. These images are then averaged and used as an estimate of the baseline, source-free intensity of each pixel, for each CCD.

The Alta U6 Kodak-1001E CCD chip has 12 extra 1024-pixel columns (4 at the left of the chip and 8 at the right) of masked, “overscan” pixels that provide a low-statistics image dark reference, even when the shutter is open for an exposure. The overscan pixel-to-pixel baseline level is also estimated from the dark-frames preceding each data run, by averaging the dark-frame associated overscans to form an average overscan image.

Large, intermittent fluctuations in pixel intensity can systematically bias both the overscan and dark frame image averages, and occur frequently. The contribution of these high intensity “outlier” pixels is removed from the average by replacing the intensity of pixels whose measured intensity is $1.25\times$ the dark frame or overscan mean intensity with the average measured intensity of the

⁴⁰DMTPC software version v4.

⁴¹Typical 4-shooter data runs consist of 100 dark frames, followed by 1000 exposures.

outlier pixel's 8 nearest neighbors. This outlier removal process is repeated 3 times for both the dark frame and overscan averages.

Image-based spark identification. Discharges between the TPC amplification stage electrodes generate light, and exposures in which a discharge occurs must be identified and discarded. An exposure is identified as containing a discharge if 1) the mean of the exposure divided by the previous non-spark image mean is less than a pre-determined, CCD-specific value⁴² and 2) if the image mean minus the overscan mean is less than a pre-determined CCD-specific value. Because the overscan pixels are not directly exposed, the mean of the exposed pixels in an exposure containing a discharge will be systematically enhanced over the mean of the non-exposed overscan pixels.

If there are more than 4 pixels in an image with measured intensities greater than 55,000 ADU, the positions of these “saturated” pixels are flagged and stored as likely Residual Image (RI) [120, 70] precursors which could be later misidentified as physical energy depositions in the TPC.

Image and overscan cleaning. For each exposure not identified as a spark, individual pixels with anomalously large measured intensities must be removed before track finding is performed on the image. Pixels with measured intensities greater than $1.25\times$ the image (overscan) mean and no neighboring pixels with measured intensities greater than 95% of $1.25\times$ the image (overscan) mean are replaced with the average intensity of their nearest 8 neighboring pixels.

Average dark frame/overscan subtraction. The outlier-scrubbed average dark frame and overscan are subtracted from each outlier-scrubbed image and overscan.

Image pedestal drift correction. A sizeable drift in the baseline, source-free intensity of each CCD pixel has been observed as a function of time, making the average dark frame and overscan computed at the beginning of each se-

⁴²Typically the $(\text{image mean})/(\text{previous non-spark image mean})$ is required to be < 1.01 .

ries of exposures an increasingly poor estimate of pixels' source-free intensities. To compensate for this time-dependent effect, for each image the difference between the average dark frame overscan intensity and the average image overscan intensity is subtracted from each pixel.

Track finding. Track finding is performed on non-spark, dark frame-subtracted, pedestal drift-corrected images using a hysteresis threshold-based image segmentation algorithm⁴³, as in [70]. The algorithm returns a list of clusters of pixels, or “tracks,” likely to be associated with an energy deposition in the TPC.

For each track found in each image, a small number of physically meaningful parameters are computed and stored, including the most likely 2D axis of the track in the plane of the CCD, the track's reconstructed direction of travel along that axis or “sense,” its projected range,⁴⁴ energy, mean position, and others, as described in Section 5.3.3 of [70]. The lengths and orientations of the major and minor axes of each track are determined by means of a principal component analysis, and the major axis is taken to be the two-dimensional axis of the track. The sense of the track is assigned by splitting the track in half along its reconstructed major axis and comparing the track intensity in either half. The brightest half of the track is designated as its beginning. This technique relies on the theoretical prediction that low-energy nuclear recoils should produce greater ionization density at their beginnings than at their ends [121]. Figure 3-20 shows a close-up of the nuclear recoil CCD candidate identified in the proto-typical event of Section 3.3. The yellow halo shows the boundaries of the cluster of pixels identified as composing the track by the track-finding algorithm and the arrow shows the axis and direction along that axis which the track was reconstructed to have been traveling in the plane of the CCD image.

⁴³The “Seed Cluster Finder” algorithm, in DMTPC parlance.

⁴⁴A track's projected range is its full three-dimensional range projected into the two-dimensional read-out plane of the CCDs.

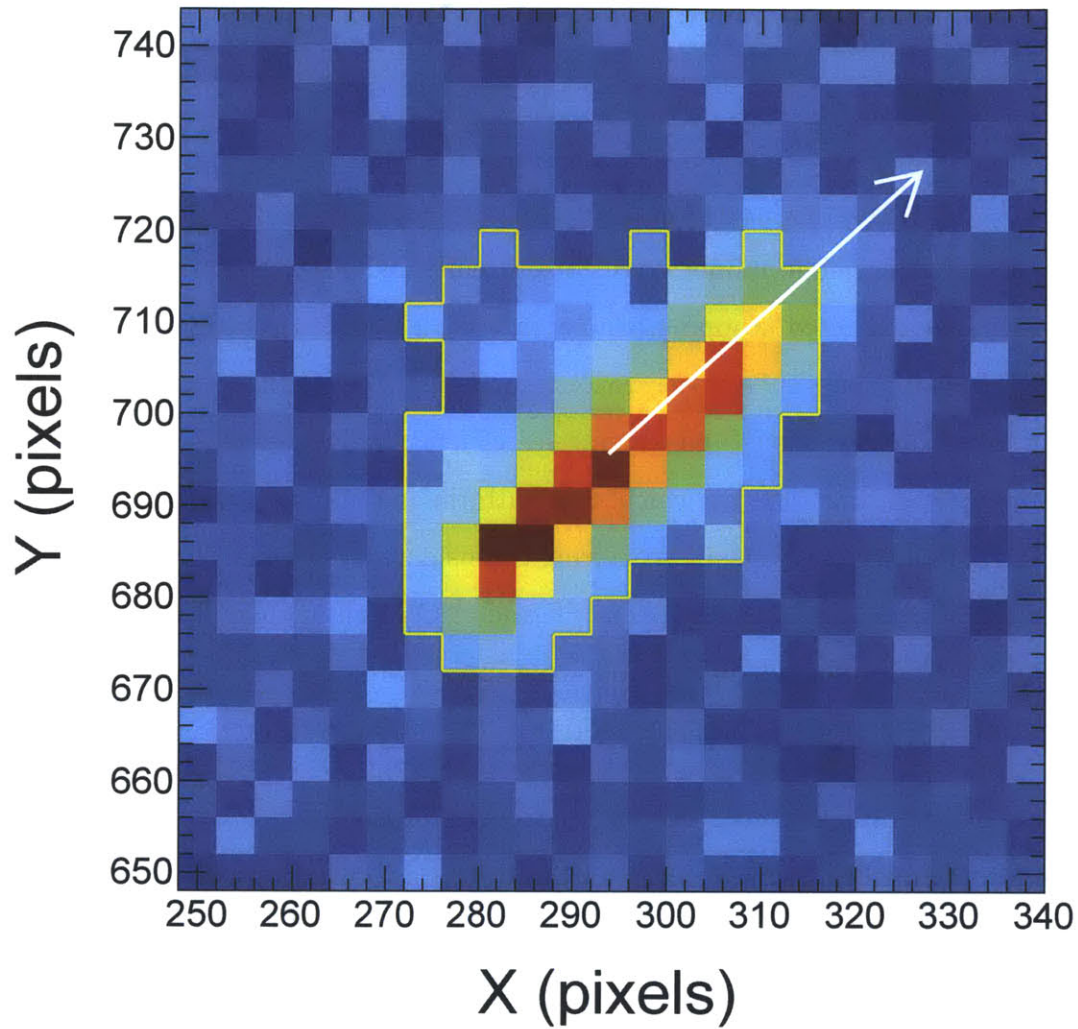


Figure 3-20: A close-up of the nuclear recoil event in Figure 3-10 in CCD 100534. The yellow halo shows the boundaries of the track as determined by the seed cluster track finding algorithm in `cleanSkim`. The white arrow shows the two-dimensional vector direction reconstructed for this track based on its principle axes and ionization profile. The subset of the CCD image shown is $14.436 \text{ mm} \times 14.436 \text{ mm}$, the track has a projected range of 8.36 mm , and the track has a total energy of 417 keV_{ee} .

Waveform analysis

The extraction of physically meaningful parameters from the waveforms digitized from the output of the amplifiers connected to the 3 electrodes of the TPC amplification stage is performed as described in Lopez *et al.* [71]. No PMT waveform analysis is carried out for this work.

3.4.3 Monte Carlo

The parametrized Monte Carlo described in [70] is used to model the 4-shooter's response to radiation. The model does not currently include the digitizers. In the Monte Carlo, the expected stopping of ions in the TPC CF_4 is calculated with the aid of SRIM-2006⁴⁵ [58] energy-loss tables, including longitudinal and lateral ion straggling. The cross-sections and kinematics of neutron interactions with fluorine and carbon nuclei in the TPC are calculated with the aid of Evaluated Nuclear Data Files (ENDFs) [83], and only elastic scattering is considered, for which there are ENDF parametrization available of the neutron- ^{19}F and ^{12}C recoil angular distributions.

The Monte Carlo depends on the following input parameters⁴⁶ that must be obtained empirically from measurements as described in Chapter 4:

Electron diffusion. Detected energy depositions in the TPC active volume take the form of trails of ionized electrons. As these signal electrons are drifted in the TPC field cage to the amplification stage for read-out, they spread out transversely and longitudinally to the drift field direction through multiple collisions with CF_4 molecules, a process called diffusion [122]. For the two-dimensional CCD read-out, only the transverse diffusion is relevant. The transverse electron diffusion as a function of drift length z is parametrized as gaussian with a standard deviation σ_T given by [72]

$$\sigma_T(z) = \sqrt{\sigma_{T,0}^2 + z \cdot \sigma_{T,z}} \quad (3.2)$$

⁴⁵SRIM version SRIM-2006.02, <http://www.srim.org/>.

⁴⁶Besides obvious inputs like the TPC geometry, TPC electrode biases, source of interactions and its details, etc..

where $\sigma_{T,0}$ and $\sigma_{T,z}$ are CCD-specific input parameters that must be determined empirically as described in Section 4.1.3.

Quenching. Only the fraction of the total energy lost via ionizing electrons by ions stopping in the TPC active volume is detected. This fraction is far from unity for low energy ions, and depends on the initial energy of the stopping ion. By convention, the energy deposited in the detector through ionization alone is typically reported in units of keV_{ee} , whereas the total deposited energy is reported in units of keV_r . The quenching is defined as the ratio of the ionization energy to the total deposited energy. Following the notation of [121], the visible, electronic energy deposited per unit length, LET_{el} , by ^{19}F ions in CF_4 is parametrized as [73]

$$\text{LET}_{el}(E_r) = S_e(E_r) + \frac{1}{3} \cdot S_n(E_r) \quad (3.3)$$

where S_e and S_n are the electronic and nuclear stopping, respectively, predicted by SRIM-2006, and E_r is the total energy of the ^{19}F ion in keV_r . This parametrization is in agreement with the quenching predicted by Hitachi [121] to within 5% for fluorine ions with energies between 50 keV_r and 200 keV_r . This parametrization of the quenching is $\sim 10\%$ higher than a recent, albeit preliminary, measurement in CF_4 at 50 mbar by Guillaudin *et al.* [123] for ^{19}F ions with energies less than 200 keV_r .

Pixel-to-mm conversion. The conversion factor between pixels and physical mm on the amplification stage must be specified. The determination of the pixel-to-mm conversion factor is described in Section 4.1.4.

Camera noise. The total CCD ADU noise in each pixel is parametrized by a gaussian distribution. The standard deviation is assumed to be the same for every pixel in a given CCD and must be specified. The determination of the total CCD noise for each 4-shooter CCD is described in Section 4.1.1.

Camera gain. The conversion factor between CCD measured pixel intensity in

ADU and visible deposited energy in that pixel in keV_{ee} must be specified for each pixel. The determination of the total $\text{ADU}/\text{keV}_{ee}$ gain for each 4-shooter CCD is described in Section 4.1.3.

Chapter 4

Detector calibration

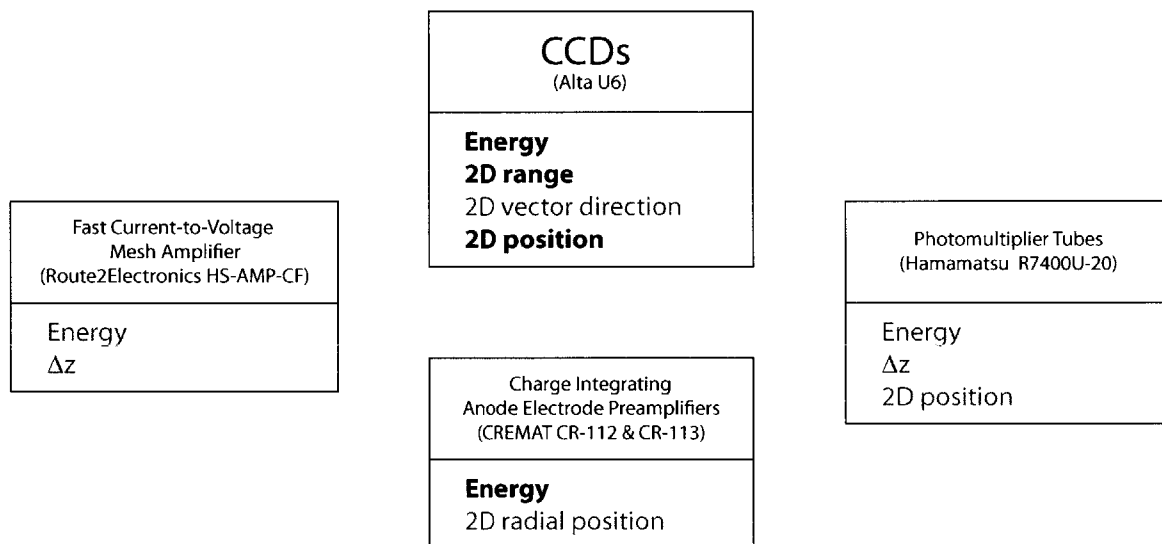


Figure 4-1: For each 4-shooter sensor, a list of the characteristics of tracks in the detector to which that sensor is known to have sensitivity. Only the calibration of the **bold** entries under each sensor heading will be discussed in this chapter.

Measurements are required to calibrate the relationships between voltages measured on the digitizer boards and digital counts integrated by the CCDs and the physical characteristics of the particle interactions taking place within the 4-shooter. Additional measurements are required to determine the values of the Monte Carlo input parameters necessary to accurately model the detector response listed in Section 3.4.3.

Figure 4-1 summarizes the known relationships between the 4-shooter's many

sensor channels and the properties of nuclear recoil tracks in the detector. This chapter will describe only the properties highlighted in bold typeface in Figure 4-1, because they are necessary inputs to the measurements presented in Chapter 5.

Sensitivity to the energy E , position in the detector (x, y, z) , and vertical extent of tracks, Δz , has been observed with the PMTs for very high energy nuclear recoils and ^{241}Am α particles [124], but a severe bandwidth mismatch between the PMTs and the digitizer cards used to read them out presently renders the PMTs unusable for the low energy nuclear recoils of interest to a dark matter search.

Work is underway to calibrate the relationship between pulses observed from nuclear recoils on the fast mesh amplifier and the energy and Δz of those tracks. The fast amplifier's sensitivity to these track parameters is expected to be similar to the performance noted in Lopez *et al.* [71], as the detector used was nearly identical to the 4-shooter.¹ Work is also underway to better exploit the information encoded in pulses digitized on the anode veto ring charge preamplifier, beyond simply using the pulse height as a veto as was done in [71]. Recent studies have determined that ratio of the heights of pulses on the veto and central anode electrode preamplifiers is well correlated with the radius on the anode at which an event occurs [125], providing an independent means by which to fiducialize the detector in the plane of the CCDs.

4.1 Charge coupled devices

In order to be observed in the 4-shooter CCDs, signals must compete with fluctuations in intensity in each pixel which arise naturally from dark current, read noise, and photon shot noise. Even in the absence of photons, a dark current of thermally excited electrons charges up each CCD pixel [126] as time elapses in an exposure. The dark current's contribution to the total CCD noise is mitigated by cooling the CCD chips to -20°C and limiting exposures to 10 seconds or less. The act of reading out the charge accrued in each pixel and converting it to a machine-readable digital number also contributes to the per-pixel intensity noise, and is called the read-noise

¹However, although the amplification stage of the TPC in [71] was identical to the 4-shooter's, the drift stage was 10 cm, $\approx 1/3$ the length of the 4-shooter's drift stage.

[126]. This source of noise is mitigated in the 4-shooter by binning pixels into groups of 16 (4×4 squares) prior to digitization thereby only incurring readout noise once for each bin but $16 \times$ more signal. Section 4.1.1 presents measurements of the total CCD noise per pixel, from readout and dark current combined, as a function of exposure time for the 4-shooter CCDs.

The statistical fluctuation in detected intensity of photons per pixel generated by nuclear recoils in the 4-shooter is the photon shot noise, and increases with the square root of the detected light intensity [120]. The intensity fluctuations due to photon shot noise are comparable to the detected intensity for low numbers of detected photons, or very low energy recoils, which are of particular interest to a direct dark matter search. Section 4.1.3 presents measurements of the relationship between energy and detected signal intensity in the 4-shooter CCDs, while Section 4.1.2 presents measurements of the dependence of this relationship on the location of a pixel in its CCDs' image.

Sections 4.1.4 and 4.1.3 present additional measurements performed to determine the CCD-specific Monte Carlo inputs necessary to model the 4-shooter response.

4.1.1 Total CCD Noise Per-Pixel

The total noise in each CCD pixel is estimated by differencing two adjacent dark frames D_1 and D_2 , and fitting the distribution of pixel differences to a gaussian for the standard deviation, $\sigma_{D_1-D_2}$. The total noise in each pixel, assumed to be uniform across the entire CCD chip, is a function of exposure length, and is given by [126]

$$\sigma_N(T_{\text{exposure}}) = \frac{\sigma_{D_1-D_2}(T_{\text{exposure}})}{\sqrt{2}} \quad (4.1)$$

where σ_N is the total noise in each pixel for a T_{exposure} length exposure. Figure 4-2 shows the total CCD noise for the four 4-shooter cameras as a function of exposure length, for exposures less than 10 seconds. For exposures much greater than 10 seconds, the total CCD noise per pixel increases considerably due to thermal noise. Although the DC level of the measured total noise in ADU varies from camera to camera, the total gain (see Section 4.1.3) for each camera varies in kind² yielding

²*i.e.* the camera with the lowest total noise, A80334, also has the lowest total ADU/keV_{ee} gain.

similar S/N for tracks in each of the four cameras.

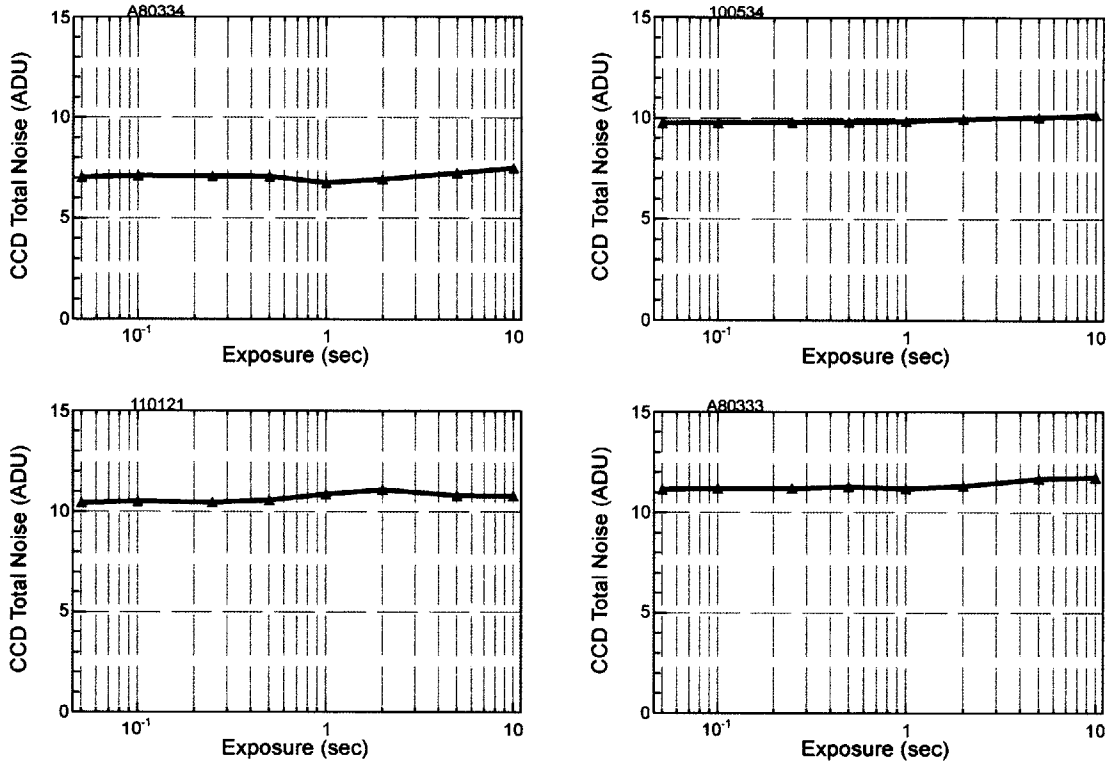


Figure 4-2: The total noise in ADU per pixel in each CCD, as a function of exposure time, as determined from differencing dark frames as described in Section 4.1.1. The fit error on the total noise is less than 0.3% and is smaller than the data points. For exposures of length 10 sec or less with the Alta U6 CCD, the total noise is dominated by the CCD read-noise. Each plot is labeled by its corresponding CCD in the upper left.

4.1.2 Gain spatial dependence

Pixel-to-pixel variations in gain are measured by flooding the chamber with low-energy X-rays from a ⁵⁷Co source, as in [70]. The 192 m interaction length [127] of the 122.1 keV X-rays [128] from the ⁵⁷Co in CF₄ at ≈ 0.1 atm is much greater than the drift length and diameter of the TPC,³ filling the drift stage of the detector approximately uniformly with ionization electrons (primarily ionized by electrons Compton scattered by the X-rays), resulting in a nearly uniform, albeit dim, glow

³To reach the CF₄, however, the ⁵⁷Co X-rays must penetrate through the top, 0.75" thick stainless-steel of the detector vacuum vessel. The attenuation length of 122.1 keV X-rays in stainless-steel is ~ 0.2 " [127].

in the amplification stage. Averaging hours of back-to-back exposures with the ^{57}Co source present produces the equivalent of a flat field image in astronomy that can be used to correct for spatial non-uniformities due to pixel-to-pixel differences in optical throughput, the physical gas gain in the amplification stage as a function of position, or the CCD quantum efficiency.

For this measurement, the ^{57}Co source is placed above the TPC on the outside of the vacuum vessel, as close as possible to the central axis of the TPC.⁴ The X-rays must penetrate the 3/4" thick SS circular top-plate of the vacuum vessel to reach the drift stage of the TPC. 18 sequences of 1000 10-second exposures were taken back-to-back, and analyzed as described in Section 3.4.2. These images are converted into a map of the relative pixel-to-pixel gain as follows:

Image averaging. For each CCD, all 18,000 images from the runs are averaged to make a single image. Images are not included in the average if a discharge is identified in the event by `cleanSkim`, or if a discharge was identified in either of the two preceding events. For each event, individual pixels are not allowed to contribute to the average if:

1. They are part of a `cleanSkim`-identified track.
2. The pixel saturated previously in the run or in the preceding run. The latter criterion is not applied to the first run of 1000 exposures. Pixel saturation is defined in Section 3.4.2.

Baseline subtraction. In the 4-shooter, unlike in previous DMTPC detectors, approximately 50% of each image is inactive providing a convenient running dark reference for each event (in addition to the overscan). The distribution of yields of all pixels with centers >200 pixels (32.08 mm) outside of the amplification stage is fit to a gaussian, and the fitted gaussian mean is subtracted from every pixel of the average image for each camera.

⁴For the measurement described here, the source was placed between cameras 100534 and A80334, approximately 1.375" from the center of the TPC, as close as the PMT mounting hardware would allow.

Cold pixel removal. A small number of pixels in the baseline-subtracted average images are negative, due to outliers and excessively hot pixels in the dark frames subtracted from the images that are averaged. All negative pixels are set equal to the median of their positive, non-zero bordering neighbors.

Hot pixel removal. A larger number of pixels in the baseline-subtracted average images are much brighter than expected from the ^{57}Co exposure alone, due to a variety of sources including tracks and cosmic ray interactions with the CCD not identified as such by `cleanSkim` (see Section 5.3) and defective, intermittently flickering pixels. Unusually bright pixels are identified by applying a bilateral filter [129] to the averaged images and computing the difference between each pixel's value post-filter and the median value of the pixel's bordering neighbors in the filtered image.⁵ If the difference is greater than 0.5 ADU, the pixel is flagged as "hot." Hot pixels in the unfiltered image are replaced with the unfiltered average of the nearest 2 bracketing pixels in the hot pixel's row.

Smoothing. The hot and cold pixel scrubbed average images are smoothed with a gaussian bilateral filter [129] with a spatial spread of 3 pixels and a pixel value spread of 3 ADU.

Normalization. The smoothed average images are normalized by dividing every pixel by the average yield of all pixels whose center is > 10 pixels (1.604 mm) inside the circular TPC active region in each image, and at a > 20 pixels (3.208 mm) minimum distance from the known positions of the spacers based on the anode illuminations described in Section 4.1.4.

Figure 4-3 shows the resulting map of the relative pixel-to-pixel gain. The observed spatial gain variation in each CCD is radially symmetric with respect to each lens' symmetry axis, and thus likely attributable to the radial dependence of the optical throughput. Good qualitative agreement is found between measurements of the total optical vignetting with radius [130] and the radial dependence of the relative

⁵The gaussian bilateral filter used for hot pixel identification uses a spatial (geometric) spread of 3 pixels and a pixel value (photometric) spread of 0.5 ADU.

gain measured with the ^{57}Co source, as shown in Figure 4-4. Vignetting refers to a host of similar effects (mechanical vignetting, optical vignetting, and natural vignetting) which result in tracks with identical intrinsic intensities appearing dimmer in proportion to how far off the axis of the optical system they are detected [131].

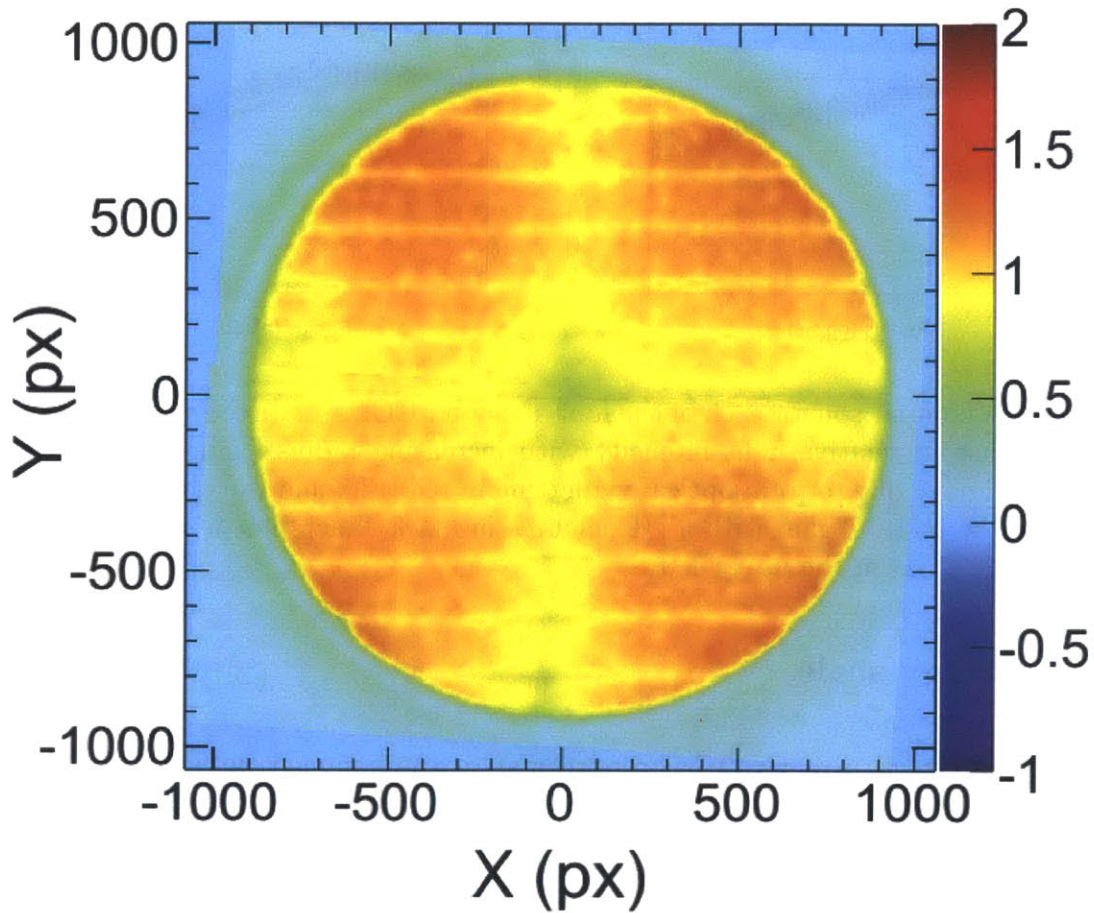


Figure 4-3: A map of the relative pixel-to-pixel gain variations in the 4-shooter CCDs, obtained with a radioactive ^{57}Co source as described in Section 4.1.2. The spacers are clearly visible as locations of reduced gain. The exposures have been stitched together to form a composite mosaic image, based on the known relative positioning of the four 4-shooter cameras. The intensity scale is arbitrary, although red areas correspond to high gain zones, and blue to low gain zones.

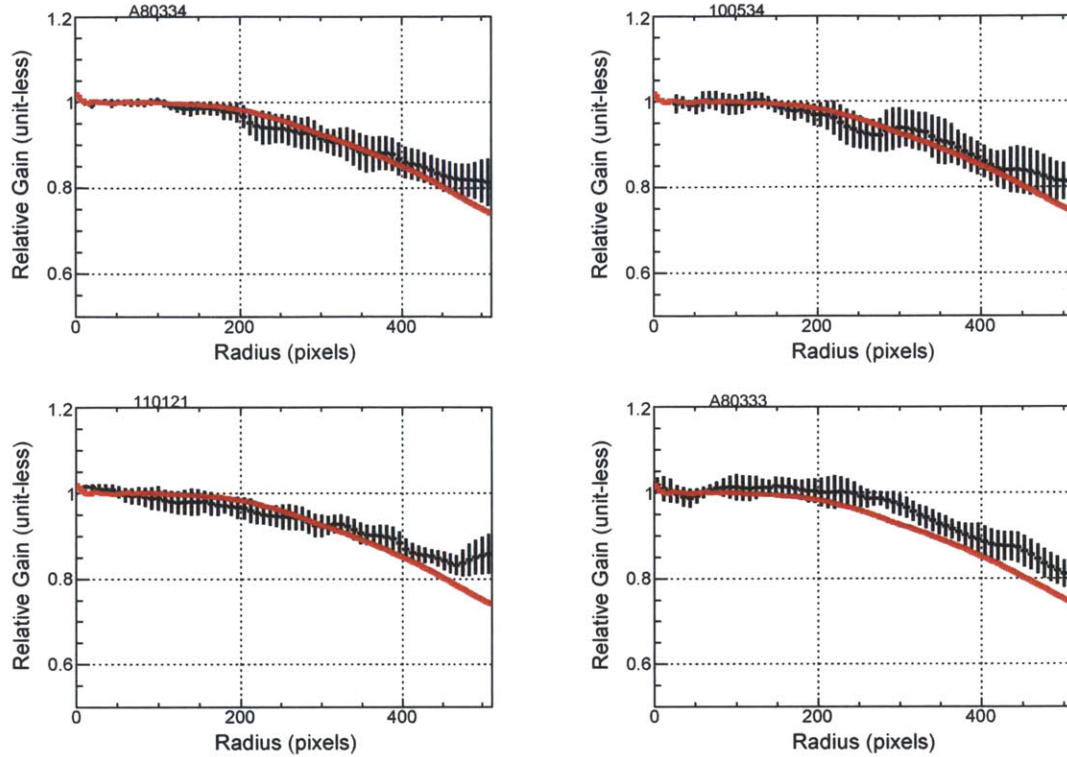


Figure 4-4: A comparison for each of the four 4-shooter CCDs, of direct measurements of the decrease in relative light intensity with increasing radius from the center of each CCD’s image due to total optical vignetting in red [130] and the observed radial decrease in the relative gain with a ^{57}Co source in black. Each plot is labeled by its corresponding CCD in the upper left.

4.1.3 Energy scale

The energy of track in a CCD is proportional to the summed intensity of all of the pixels in the track. The CCD measures intensity in arbitrary, analog-to-digital units, or ADU. The corresponding physical energy in keV is determined by placing radioactive ^{241}Am sources at predetermined positions in the detector. ^{241}Am decays predominantly to ^{237}Np and an α particle. The dominant α energies are 5485.56 keV (84.8% of the time), 5442.80 keV (13.1% of the time), and 5388 keV (1.7% of the time) [132]. These α energies are too close together to be individually resolved in the 4-shooter.

For 5 MeV α particles, keV_{ee} and keV_{r} differ by less than 1% [58], while for low energy nuclear recoils (<1 MeV keV_{r}) keV_{ee} is only a fraction of keV_{r} and is

particle- and keV_r-dependent [123, 121]. For this reason high-energy α 's only provide a measurement of the conversion factor from ADU to keV_{ee} and additional corrections must be applied for low energy nuclear recoils to convert an energy measured in ADU to keV_r [121].

The ²⁴¹Am sources used to calibrate the CCD energy scale are obtained from ionization smoke detectors.⁶ The ²⁴¹Am is packaged in the source behind a thin foil of unknown composition and thickness. The energies of the α particles emitted by the four sources used in these studies were measured in vacuum with a surface barrier detector⁷ to be (4.76 ± 0.17) MeV, (4.59 ± 0.18) MeV, (4.514 ± 0.21) MeV and (4.51 ± 0.15) MeV, respectively, where the errors are the fitted gaussian standard deviation of the energy distributions of each source. The sources were press fitted into custom-machined acrylic collimators with 1" long, #79 (0.01449 inch \varnothing) collimating channels. An aluminum alignment jig was custom-machined to guide the placement of the sources between pairs of field shaping rings to ensure that they were aligned in-between and parallel to the amplification stage spacers. Figure 4-5 shows an example image taken with one source placed in each camera field of view. The ADU/keV_{ee} conversion constant for each CCD is measured by fitting the normalization of the longitudinal intensity projection of α tracks averaged over many events in data to the same projection in Monte Carlo, where the Monte Carlo has been closely tuned to match the data in all other respects. This measurement proceeds in the following three stages:

α track selection. Good α tracks are identified in data and the average longitudinal intensity projection of these tracks is computed. An α track candidate is selected to be included in the average longitudinal intensity projection if:

²⁴¹Am-I: Non-zero reconstructed projected range, energy, etc.. The α candidate must have a non-zero cleanSkim reconstructed energy, projected range, number of pixels, number of neighboring pixels, maximum pixel value, mean pixel value, and pixel RMS.

⁶The Kidde FIREX basic smoke detector 0915E (i9050).

⁷The Ortec ULTRA BU-014-050-100 ion-implanted-silicon detector.

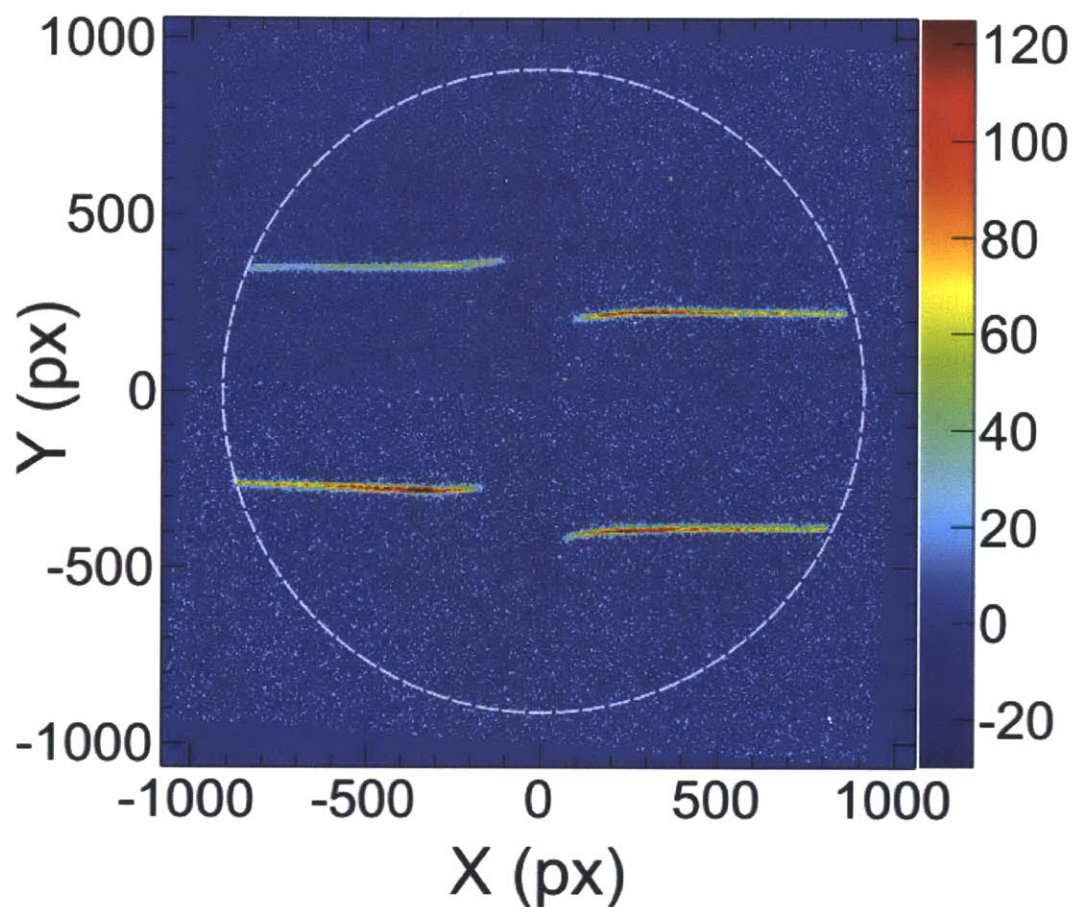


Figure 4-5: Four ^{241}Am α tracks emitted by sources in each of the four cameras during a typical α energy calibration described in Section 4.1.3. The exposures have been stitched together to form a composite image, based on the known relative positioning of the four 4-shooter cameras. The images are actually from different events, but the same run. The dashed white circle shows the circular boundary of the central anode electrode of the amplification stage.

²⁴¹Am-II: No spark in image. The α -containing image must not contain a spark, where the presence of a spark in the image is determined as described in Section 3.4.2.

²⁴¹Am-III: Not recently preceded by a spark. The α -containing image must be preceded by at least 4 spark-free exposures.⁸ The time-stamp of the image must additionally be 15 (5) seconds after (before) the last (next) spark, based on the anode bias high voltage supply current, as described in Section 5.3.

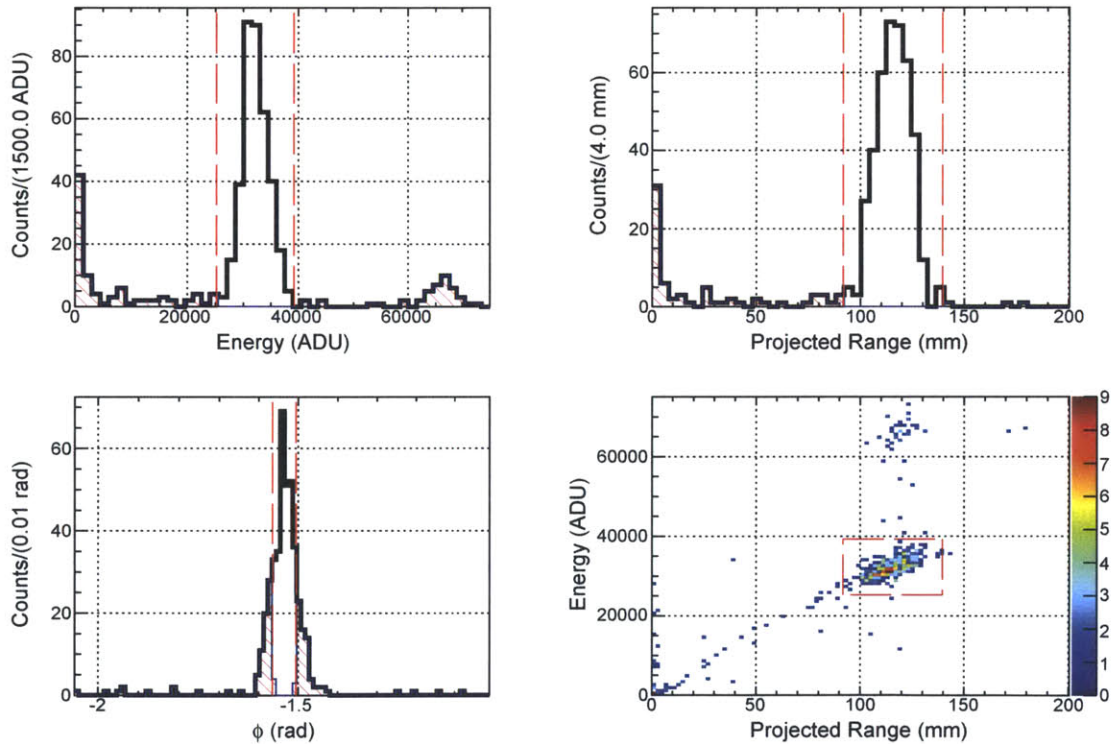


Figure 4-6: Typical spectra from a ²⁴¹Am α calibration dataset in one CCD with the cuts in Section 4.1.3 shown as dashed red lines. Upper left, the energy spectrum and cut ²⁴¹Am-V. The second peak just above 60,000 ADU corresponds to pile-up events where two α tracks are emitted on top of one another in the same exposure and are reconstructed as one track. Upper right, the projected range distribution and cut ²⁴¹Am-IV. Lower left, the two-dimensional angle ϕ distribution and cut ²⁴¹Am-VII. Lower right, the α energy versus projected range with a box overlaid corresponding to cuts ²⁴¹Am-IV and ²⁴¹Am-V.

⁸Am-241 α -source exposures are 1 second long.

- ²⁴¹Am-IV: Projected range cut.** The reconstructed projected range of the α candidate must fall within ± 3 gaussian standard deviations of the mean of a gaussian fit to the projected range distribution of all of the α candidates in the run. A typical α projected range distribution demonstrating this cut is shown in Figure 4-6. This cut selects α particles that pass cleanly through the collimator and range out in the detector. In conjunction with cut ²⁴¹Am-V it also reduces contamination from non- α backgrounds.
- ²⁴¹Am-V: Energy cut.** The reconstructed energy of the α candidate must fall within ± 3 gaussian standard deviations of the mean of a gaussian fit to the energy distribution of all of the α candidates in the run. A typical α energy distribution demonstrating this cut is shown in Figure 4-6. This cut reduces non- α backgrounds and selects clean α interactions as discussed in ²⁴¹Am-IV.
- ²⁴¹Am-VI: Edge cut.** No pixel in the α candidate can fall within 10 pixels of the edges of the candidate's image.
- ²⁴¹Am-VII: ϕ cut.** The reconstructed two-dimensional angle, ϕ , of the α candidate must fall within 0.03 rad (1.7°) of the mean of a gaussian fit to the ϕ distribution of all of the α candidates in the run. A typical α particle ϕ distribution demonstrating this cut is shown in Figure 4-6.
- ²⁴¹Am-VIII: Position consistent with coming from the ²⁴¹Am source.** The α candidate must contain a pre-selected pixel (typically near the average Bragg peak position of the α 's over the entire run) consistent with the track having been emitted from the known position of the ²⁴¹Am source.
- ²⁴¹Am-IX: In active region.** The α candidate must not contain any pixels outside of the active region of the TPC. The active region is taken to be the inner 29.21 cm diameter of the anode, the diameter of the central anode electrode.
- ²⁴¹Am-X: Straightness cut.** No pixel in the α candidate with measured intensity greater than $3\times$ the RMS of the candidate's image may be at a

minimum distance greater than 3.208 mm (20 pixels) from the line parallel to the reconstructed ϕ of the α candidate which passes through the candidate's mean position in its image.

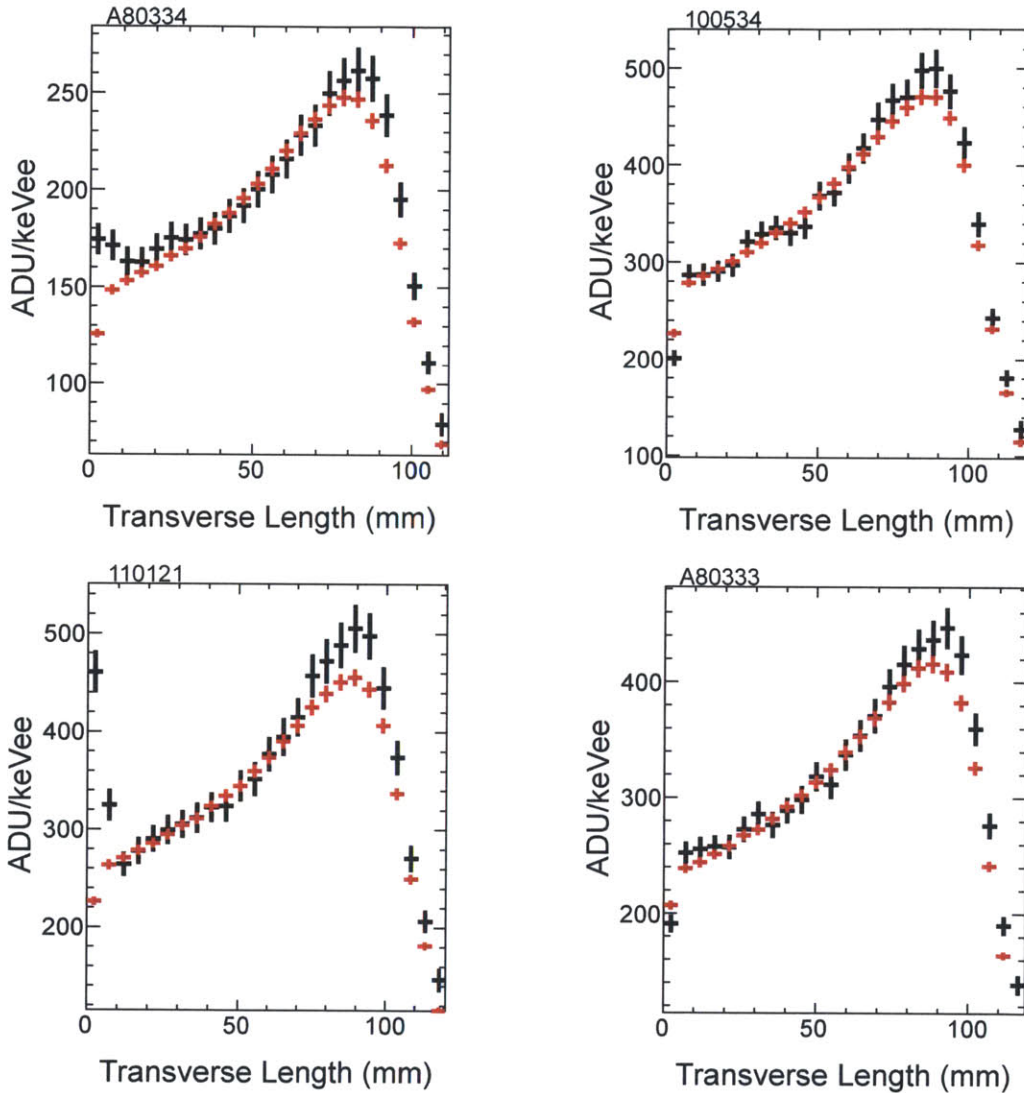


Figure 4-7: The average longitudinal projection of α tracks in a typical calibration dataset (black) compared with the tuned Monte Carlo prediction (red), for data taken in 60 Torr CF_4 . The normalization of the Monte Carlo curve has been fit to the data to extract the total CCD gain in $\text{ADU}/\text{keV}_{\text{ee}}$. Each plot is labeled by its corresponding CCD in the upper left.

Figure 4-7 shows the averaged longitudinal intensity projection of many α candidates passing all of these cuts for an example run.

Tuning Monte Carlo to match data. ^{241}Am α Monte Carlo datasets are generated and the input parameters are iteratively adjusted until the average longitudinal and transverse intensity profiles of the α particles are well-matched between the data and the Monte Carlo. The same analysis code used to detect and reconstruct good α tracks in data is applied to the Monte Carlo.

The five source-independent Monte Carlo input parameters are described in Section 3.4.3 and are the electron diffusion, the quenching, the pixel-to-mm conversion, the camera noise, and the camera gain. The quenching, pixel-to-mm conversion constant, and camera noise are fixed for all runs. The measurement of the pixel-to-mm conversion is described above in Section 4.1.4. The measurement of the camera noise is described below in Section 4.1.1. The quenching parametrization described in Section 3.4.3 is used, although the quenching is expected to be negligible.

The total input Monte Carlo electron diffusion is adjusted until the mean transverse width of the α candidates passing all cuts in data is consistent with the mean transverse width of the α candidates passing all cuts in the Monte Carlo. Figure 4-8 shows the total input Monte Carlo electron diffusion required to match the data for 5 independent datasets where the ^{241}Am sources were at varying heights. The total amount of diffusion increases with electron drift distance, as expected. These data can be fit for the electron diffusion parameters for each CCD in Equation 3.2, as in Caldwell *et al.* [72], yielding:

$$\begin{aligned}
 \sigma_{T,A80334}^2(z) &= (0.59 \pm 0.07 \text{ mm}^2) + z[\text{mm}] \cdot ((6.1 \pm 0.4) \times 10^{-3} \text{ mm}) \\
 \sigma_{T,100534}^2(z) &= (0.46 \pm 0.06 \text{ mm}^2) + z[\text{mm}] \cdot ((6.2 \pm 0.4) \times 10^{-3} \text{ mm}) \\
 \sigma_{T,110121}^2(z) &= (0.37 \pm 0.12 \text{ mm}^2) + z[\text{mm}] \cdot ((6.5 \pm 0.7) \times 10^{-3} \text{ mm}) \\
 \sigma_{T,A80333}^2(z) &= (0.49 \pm 0.08 \text{ mm}^2) + z[\text{mm}] \cdot ((6.2 \pm 0.5) \times 10^{-3} \text{ mm})
 \end{aligned} \tag{4.2}$$

where z is the distance the ionization electrons must drift. The z -coefficient in Equation 4.2 is linearly proportional to the lateral electron diffusion coefficient.

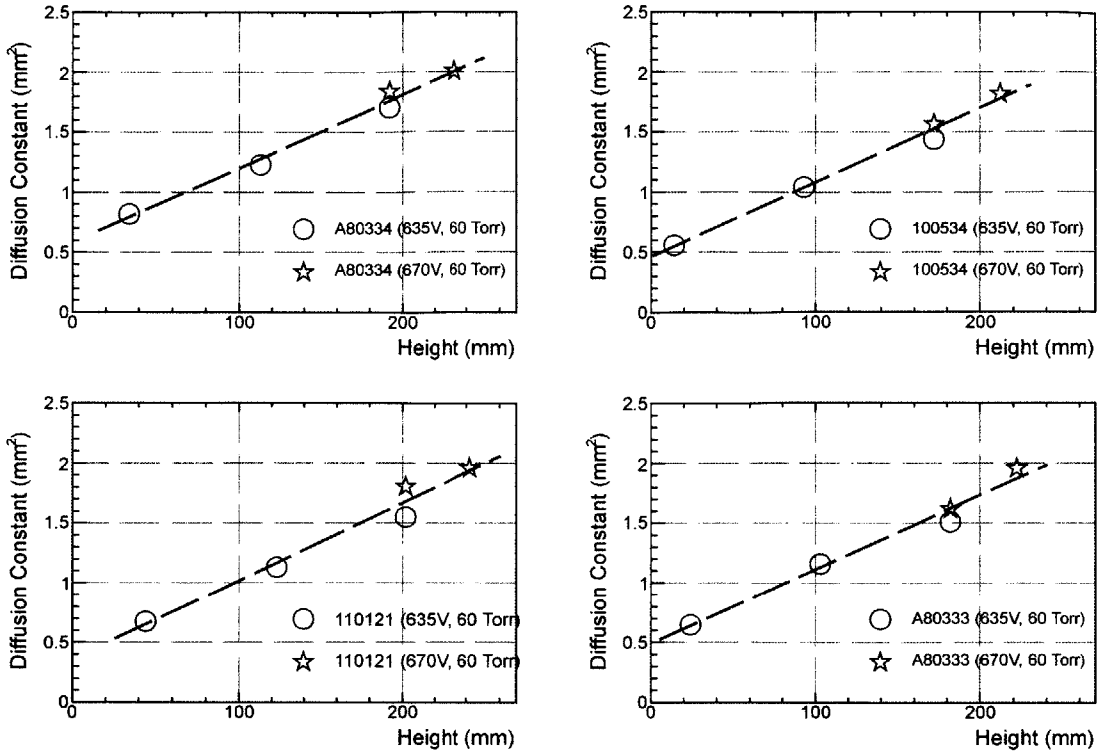


Figure 4-8: The lateral electron diffusion coefficient as a function of drift distance determined from the transverse width of α tracks in calibration datasets taken with ^{241}Am α sources at varying heights z above the amplification stage in the 4-shooter. The diffusion coefficient is determined by tuning its value in the Monte Carlo until agreement is obtained with the average transverse width of α tracks in the data. Determined in this way at a variety of heights, the z -dependence of the coefficient is extracted with the line fit shown. Each plot is labeled by its corresponding CCD in its legend.

Figure 4-9 compares this measurement of the lateral electron diffusion coefficient in CF_4 to the best fit value of Christophorou *et al.* [115] at the 4-shooter operating drift field of 187 V/cm. The values obtained here are systematically $\approx 20\%$ larger than the best fit value.

Measured electron diffusion parameters in hand, the Monte Carlo position of the ^{241}Am source in each camera must be optimized to match the data as closely as possible. The line along which the source falls is obtained from the reconstructed ϕ and mean α track pixel positions for candidates passing the above cuts, and the Monte Carlo alphas are constrained to lie along this line. Only pixels

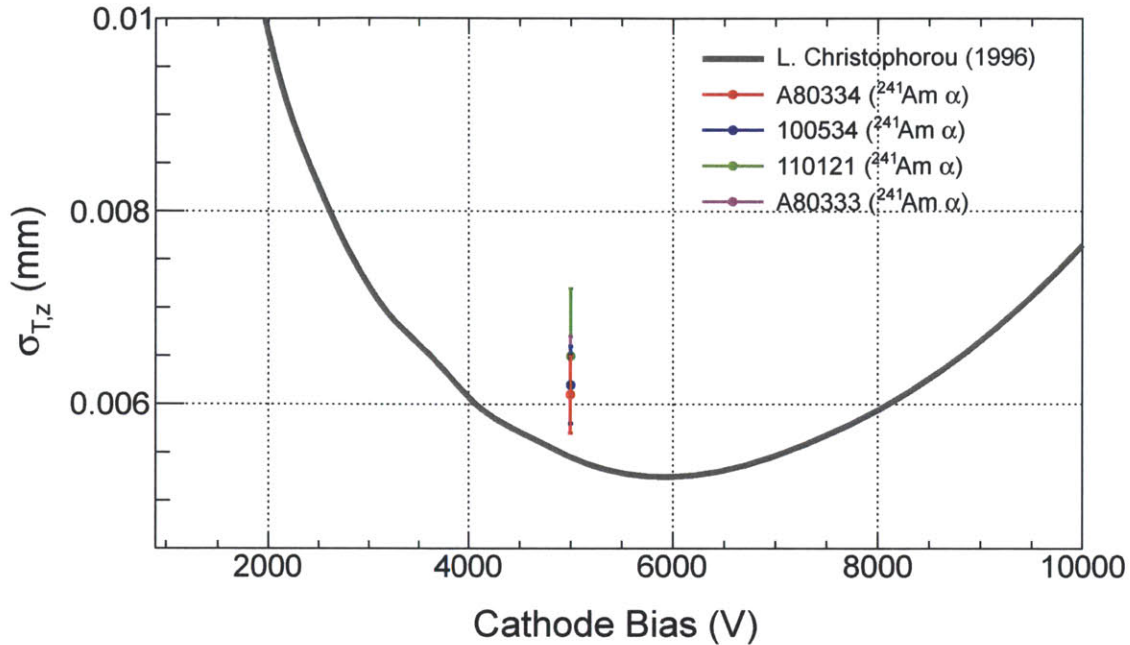


Figure 4-9: The measured CF_4 transverse electron diffusion coefficient $\sigma_{T,z}$ in mm (see Equation 3.2) for -5000 kV cathode bias with the four 4-shooter CCDs. Overlaid is the recommended transverse diffusion coefficient as a function of cathode bias from Christophorou *et al.* [115].

within the active region of each CCD's image are populated with counts in the Monte Carlo, where the active region is defined identically as in the data (see $^{241}\text{Am-IX}$ above). Data is taken with the bases of the α collimators pulled back approximately 1" from the TPC field cage so that ionization occurring just outside the collimator ends is blocked from reaching the amplification stage by the field shaping rings on which each collimator is supported. When the collimator ends are pushed fully into the TPC drift stage, the amplification stage discharge rate is observed to increase considerably, and the sparks have been localized using CCD exposures to be occurring at the collimator ends. Pulling the collimators back was observed to eliminate the increase in discharge rate, but at the cost of no longer precisely knowing the fraction of the ^{241}Am tracks over the amplification stage. The starting positions of the Monte Carlo α particles are thus adjusted along the line on which the source is reconstructed to be pointing until the mean projected range of the α candidates passing all

cuts in data is identical to the mean projected range of the α candidates passing all cuts in the Monte Carlo.

Extracting the ADU/keV_{ee} conversion constant. After adjusting the α starting position in the Monte Carlo as described above, the average longitudinal intensity projection of these Monte Carlo tracks is computed, and the ratio of the data to Monte Carlo is computed in coarse bins (≈ 5 mm wide) of longitudinal track length. The average of this ratio estimates the relative difference between the ADU/keV_{ee} gain in the data versus the Monte Carlo, and is used to update the Monte Carlo. Monte Carlo data is iteratively generated, updating the input Monte Carlo ADU/keV_{ee} gain until the ratio of the data to Monte Carlo average longitudinal α track projections is consistent with unity within the uncertainty on the ratio determination. The uncertainty on the ratio determination is estimated by adding the statistical error on each ratio bin contributing to the average in quadrature. The ratio is only averaged over a short sub-interval of the average longitudinal projection, typically beginning 150 pixels (24 mm) after the beginning of the tracks and ending 150 pixels (24 mm) before the average Bragg peak position.

Figure 4-10 shows the measured total ADU/keV_{ee} gain in 60 Torr CF₄ with the amplification stage biased at 635V and 670V, for all four 4-shooter CCDs, with the ²⁴¹Am sources at varying distances above the amplification stage. Even though the transverse diffusion varies by a factor of 2 depending on the height of the α particles above the amplification stage, the measured ADU/keV_{ee} gain is observed to be independent of height. Table 4.1 tabulates the measured CCD ADU/keV_{ee} constants for the four 4-shooter cameras in 60 Torr CF₄ with 635V and 670V bias on the amplification stage.

The measured ADU/keV_{ee} gains are comparable for CCDs 100534, 110121 and A80333, but A80334's gain is nearly half that of the other three. Preliminary measurements of the conversion gain (ADU/electron in the CCD) find similar values as quoted on the datasheets for the CCDs, except for A80334. The electron-to-ADU

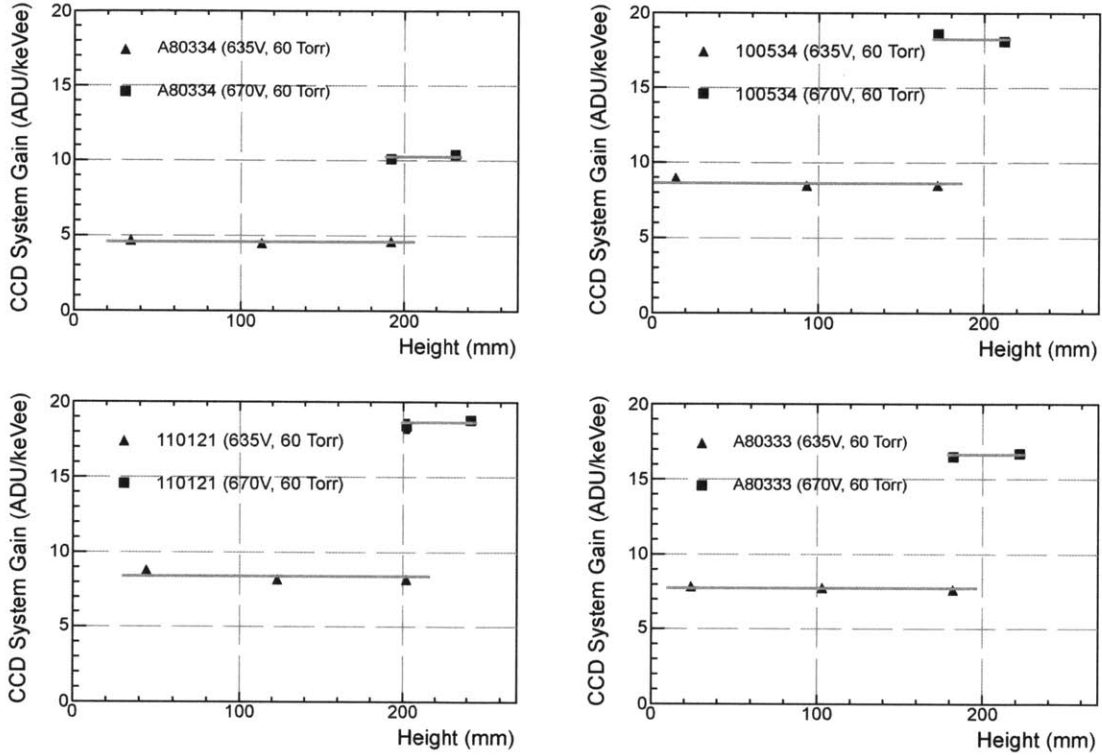


Figure 4-10: The CCD gain in ADU/keV_{ee} for the four 4-shooter cameras as a function of source height z above the amplification stage measured with ^{241}Am α tracks in 60 Torr CF₄. No systematic variation is observed with source height. Each plot is labeled by its corresponding CCD in its legend.

conversion gain in A80334 is observed to depend non-linearly on the intensity of light illuminating the CCD chip. The reason for this abnormal behavior is not understood, and although results are presented for this CCD alongside the others throughout this work, they may be atypical.

Measurements of the ADU/keV_{ee} gains were hindered by the fact that the spark rate was observed to increase dramatically as the vertical distance between the ^{241}Am sources and the amplification stage was decreased. Figure 4-11 shows the spark rate as a function of amplification stage bias with four ^{241}Am sources in the 4-shooter at progressively smaller distances above the amplification stage. Sparks were observed in the CCD images to occur at the location of the ^{241}Am α track Bragg peaks and just outside the ^{241}Am source collimators. At present, the best hypothesis for the observed increase in discharge rate at these positions is that the high ionization density

Setup	CCD	CCD Total Gain (ADU/keV _{ee})
60 Torr CF ₄ 635V	A80334	4.59 ± 0.03 ± 0.08
	100534	8.64 ± 0.05 ± 0.22
	110121	8.4 ± 0.06 ± 0.28
	A80333	7.75 ± 0.05 ± 0.09
60 Torr CF ₄ 670V	A80334	10.3 ± 0.2 ± 0.2
	100534	18.4 ± 0.2 ± 0.3
	110121	18.6 ± 0.2 ± 0.2
	A80333	16.6 ± 0.2 ± 0.1

Table 4.1: The CCD gain in ADU/keV_{ee} for the four 4-shooter cameras measured with ²⁴¹Am α tracks in 60 Torr CF₄ and averaged over the different heights in Figure 4-10. The first error is the fit error on the CCD gain from a degree-0 polynomial fit to the gain versus height in Figure 4-10, while the second error is the RMS deviation of the gain measurements at different heights. Data at lower heights was taken with lower bias on the amplification stage (635V instead of 670V) to counteract the higher spark rate due to the sources' proximity to the amplification stage.

at these points approaches the Raether limit [133, 134], inducing a discharge. The effect becomes more pronounced for short drift distances because the ionized charges undergo less transverse and longitudinal diffusion to reduce the ionization density. Nuclear recoils can also induce discharges if their ionization density is sufficiently high, and the discharge probability depends on the height in the detector at which the nuclear recoil occurs. This will be discussed further in Section 5.1.

4.1.4 Length Calibration

Every bin in a CCD image during normal data-taking is actually a super-pixel of 4x4 hardware pixels binned together on the Alta U6 CCD chip during readout, although images are still plotted in units of the original hardware pixels. The conversion factor between hardware pixels and physical mm was measured to be (0.1604 ± 0.0004)

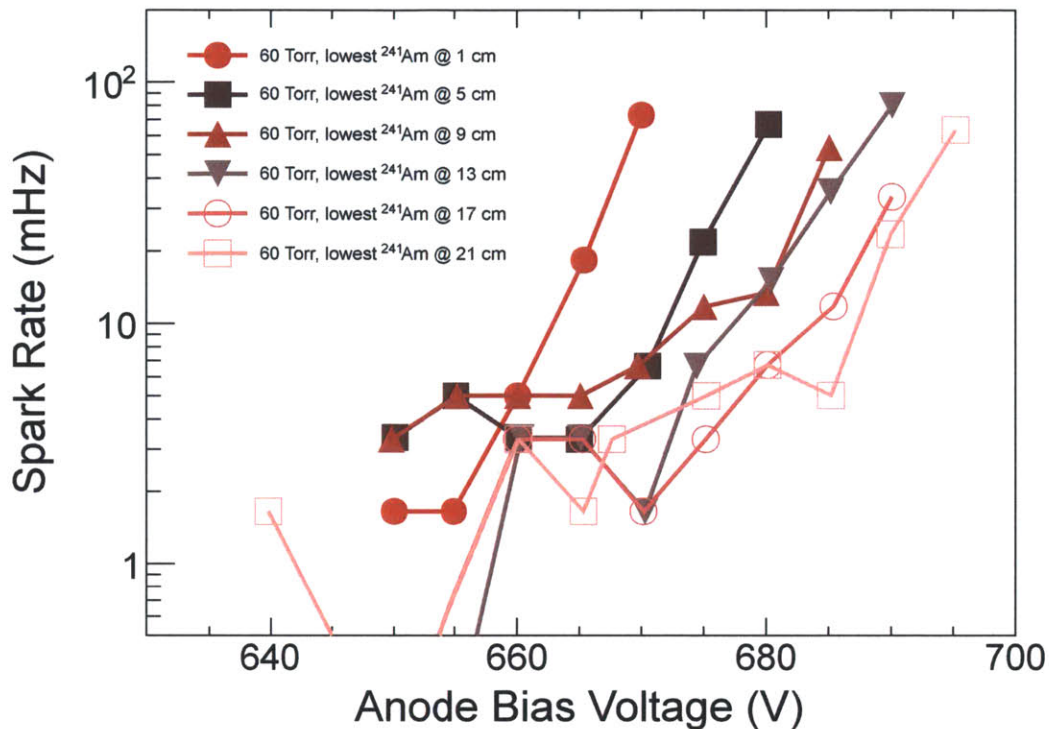


Figure 4-11: The amplification stage discharge rate versus amplification stage bias voltage with ^{241}Am α sources at different heights z above the amplification stage in 60 Torr CF_4 . As the sources are moved closer to the amplification stage, the discharge rate in the amplification stage is observed to systematically increase for a fixed bias voltage.

mm/pixel. This conversion factor was obtained by comparing the observed mean radius of the two inter-electrode channels machined into the copper on the top of the anode (see Figure 3-4) in LED-illuminated images⁹ to their known positions. The measurement is done using images binned 1x1 in CCD hardware pixels, to increase the accuracy of the length calibration. The root-mean-squared of all 8 of these determinations is 0.00025 mm/pixel, and the furthest measurement from the central value is different by +0.00035 mm/pixel in the positive direction and -0.00032 mm/pixel in the negative direction. The error is taken to be the maximum deviation of the 8 measurements from the mean.

⁹The 4-shooter run used to extract the mm/pixel conversion factor was run #03022.

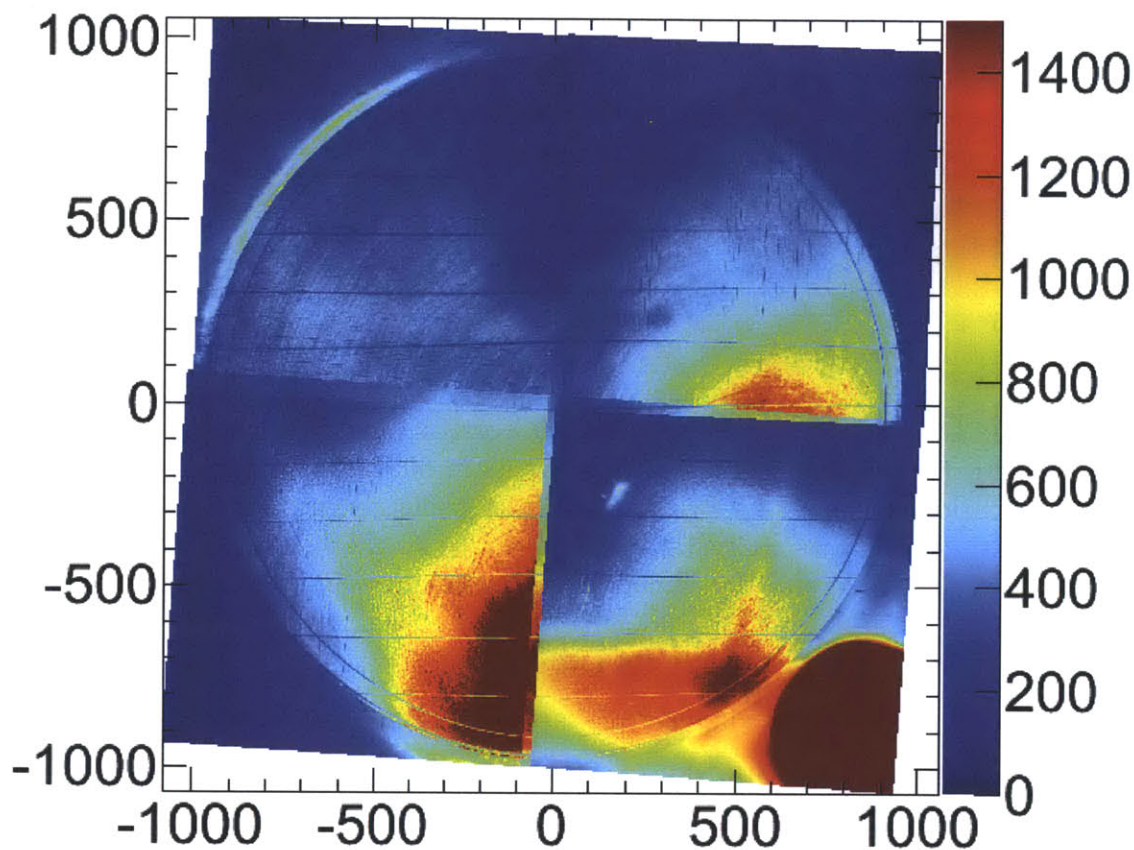


Figure 4-12: Images taken while the 4-shooter anode was under LED illumination. The exposures have been stitched together to form a composite image, based on the known relative positioning of the four 4-shooter cameras. Features with well known physical dimensions are clearly visible like the veto and anode electrode boundaries, the spacers, and the inner edges of the TPC field cage rings. The bright red spot in the lower right is a reflection of the LED used to illuminate the chamber.

4.2 Central anode electrode charge readout

This section describes measurements performed in order to calibrate the response of the 4-shooter central anode charge integrating pre-amplifier to energy deposition in the TPC. The peak voltage measured on the charge integrating pre-amplifier connected to the central anode plate electrode is proportional to the energy of the ionization event. The energy scale in keV_{ee} is determined by placing a $30 \mu\text{Ci } ^{55}\text{Fe}$ source¹⁰ directly on the the top surface of the 4-shooter cathode mesh, inside of the detector

¹⁰The source was counted to be $59 \mu\text{Ci}$ in November, 2010.

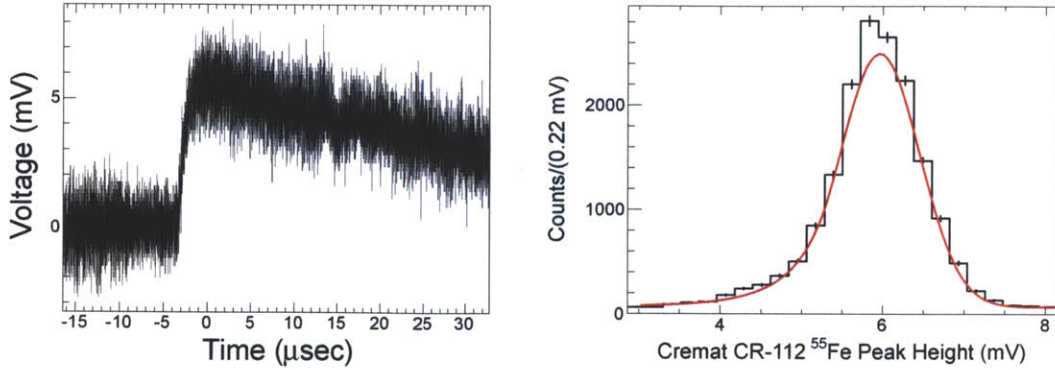


Figure 4-13: Left, a typical ^{55}Fe event in 60 Torr CF_4 corresponding to a $5.9 \text{ keV}_{\text{ee}}$ X-ray. Right, the spectrum of many ^{55}Fe events in 60 Torr CF_4 with 600 V bias on the amplification stage and -5 kV on the drift stage clearly showing a $5.9 \text{ keV}_{\text{ee}}$ X-ray line. The red curve shows a Crystal Ball function fit to the spectrum used to extract the energy scale. A Crystal Ball function is a gaussian with a low energy power law tail.

vacuum vessel. ^{55}Fe decays via electron capture to 5.895 keV X-rays which deposit their full energy in the detector through photoelectric absorption, the dominant process for X-rays with energies less than 10 keV in CF_4 [127]. Figure 4-13 shows a typical event taken with the higher gain Cremat CR-112 charge-integrating amplifier on the central anode electrode, and the spectrum of pulse heights from many events taken in 60 Torr CF_4 with 600V bias on the amplification stage. Figure 4-14 shows the ^{55}Fe peak height measured on the CR-112 as a function of amplification stage bias voltage and CF_4 pressure, where the peak height is obtained from fitting a Crystal Ball function [135] to the ^{55}Fe spectrum for many events at each pressure and bias. The fitted peak height versus anode bias in 45 Torr, 60 Torr, and 75 Torr CF_4 is measured to be:

$$\begin{aligned}
 V_{\text{CR-112}}^{55\text{Fe}, 45 \text{ Torr}}[\text{mV}] &= (7.60 \pm 0.09) \times 10^{-5} \exp\left(\frac{V_{\text{bias}} [\text{V}]}{51.26 \pm 0.05 \text{ V}}\right) \\
 V_{\text{CR-112}}^{55\text{Fe}, 60 \text{ Torr}}[\text{mV}] &= (3.06 \pm 0.02) \times 10^{-5} \exp\left(\frac{V_{\text{bias}} [\text{V}]}{49.28 \pm 0.03 \text{ V}}\right) \\
 V_{\text{CR-112}}^{55\text{Fe}, 75 \text{ Torr}}[\text{mV}] &= (8.91 \pm 0.07) \times 10^{-6} \exp\left(\frac{V_{\text{bias}} [\text{V}]}{47.08 \pm 0.02 \text{ V}}\right)
 \end{aligned} \tag{4.3}$$

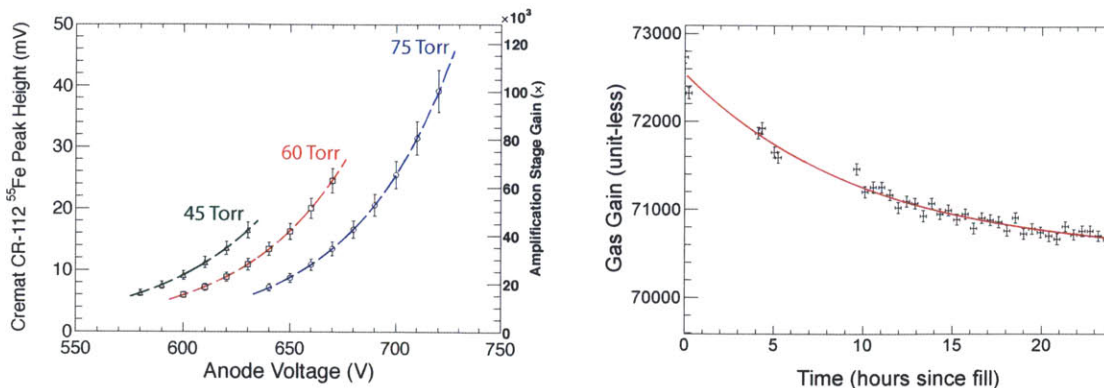


Figure 4-14: Left, from left to right in the figure, the ^{55}Fe -derived gas gain versus anode bias voltage for 45 Torr, 60 Torr, and 75 Torr. Right, the ^{55}Fe -derived gas gain as a function of time over a 24 hour period. This dataset was taken in 75 Torr CF_4 with 720 V bias on the amplification stage and -5 kV on the drift stage. The data on the right was taken without attenuating the ^{55}Fe source, resulting in a systematically lower measured gain than in the left figure, as discussed in the text.

where V_{bias} is the amplification stage bias voltage.

Given the W -value, or energy required to generate an electron-ion pair in the CF_4 gas, this measurement can be converted into a measurement of the gas gain as a function of pressure and anode voltage, or the number of secondary electrons produced in the TPC amplification stage for each primary electron that drifts into it. Unfortunately, there is disagreement in the literature about the W -value in CF_4 , with reported values ranging from 34.3 eV [136] to 54 eV [137, 121]. For this measurement, 34 eV is used, in line with a recent DMTPC measurement using α particles in a parallel plate ionization chamber which obtained 33.8 ± 0.4 eV [138].

The gain of the CR-112 was measured to be 14.06 mV/picoCoulomb, with negligible errors except for a 25% systematic uncertainty due to the nominal tolerance of the preamplifier's test capacitor's ¹¹ capacitance. The measured gain is 8% higher than the 13 mV/picoCoulomb gain reported on the amplifier's datasheet [139]. This implies that the amplification stage gain of the TPC is $2,564 \times$ the voltages measured on the CR-112 in Equation 4.3. Gas gains achieved in the 4-shooter TPC amplification stage range from $10^3 - 10^4$ secondary electrons per primary ionization electron

¹¹Digikey part #311-1089-1-ND.

entering the amplification stage, as shown in Figure 4-14.

In normal operation, the Cremat CR-113 charge-integrating pre-amplifier, not the higher gain CR-112 pre-amplifier, is connected to the central anode electrode. The gain of the CR-113 was measured to be $(0.100 \pm 0.002) \times$ the CR-112's gain, in perfect agreement with the expected gain ratio between the two amplifiers based on the manufacturer datasheets [139, 140], but implying the CR-113 gain is also 8% higher than the 1.3 mV/picoCoulomb expected datasheet gain [140]. Given that the measured signals correspond to 5.895 keV_{ee} of deposited energy, the conversion between the measured CR-113 peak height and energy can be obtained from the measured ⁵⁵Fe CR-112 peak heights in Equation 4.3 through

$$\begin{aligned} V_{\text{CR-113}}/E &= \left(\frac{V_{\text{CR-112}}^{55\text{Fe}}}{5.895 \text{ keV}_{\text{ee}}} \right) \times \left(\frac{G_{\text{CR-113}}}{G_{\text{CR-112}}} \right) \text{ mV/keV}_{\text{ee}} \\ &= (1.70 \pm 0.03) \times 10^{-2} \cdot V_{\text{CR-112}}^{55\text{Fe}} \text{ mV/keV}_{\text{ee}} \end{aligned} \quad (4.4)$$

where $V_{\text{CR-112}}^{55\text{Fe}}$ is in mV and $(G_{\text{CR-113}}/G_{\text{CR-112}})$ is the measured ratio of the CR-113 and CR-112 gains.

The measured ⁵⁵Fe X-ray response is observed to vary with the intensity of the ⁵⁵Fe source, an effect that has been observed by many other groups working with gaseous ionization detectors [134]. The gain measurements reported here were measured with the ⁵⁵Fe source wrapped in 8 layers of household aluminum foil, attenuating the source intensity by a factor of 100 according to Geiger counter measurements. The gain measured with the unattenuated source is $0.67 \times$ the gain with 8 layers of foil, although the measured gain is observed to plateau as the number of layers was increased from 0 to 10. Fits to the asymptotic behavior of the measured gain as a function of attenuation indicate that the measured gain with 8 layers is within 0.5% of the gain in the infinite attenuation limit.

Figure 4-14 shows the gas gain in 75 Torr CF₄ as a function of time, over the course of a day. The gain is observed to stabilize at a value 3% lower than the initial value with a $10.1_{-0.7}^{+0.8}$ hour exponential time constant.

Chapter 5

$^{241}\text{Am-Be}(\alpha,n)$ directionality study

A primary goal of this work is the quantitative exploration of the 4-shooter's ability to reconstruct the 2-dimensional vector direction of low-energy nuclear recoils. This chapter describes a direct measurement of the 4-shooter's sensitivity to the 2-dimensional "sense" of nuclear recoils as a function of the recoil energy. The recoils in this study are produced by neutrons emitted from an $^{241}\text{Am-Be}(\alpha,n)$ neutron source positioned near the detector. Nuclei struck by neutrons recoil nearly identically to ones struck by dark matter. Similar studies have been undertaken by other dark matter directional direct detection efforts [59, 141, 142, 143].

5.1 Detector operation and configuration

For this study, an $^{241}\text{Am-Be}(\alpha,n)$ neutron source¹ was placed near the detector as shown in Figures 5-1 and 5-2. The ^{241}Am activity of the source was 10 mCi in April 1985, implying an approximately 26,000 neutron/sec emission rate for the source used in this study [144]. The source is contained in an $11\frac{1}{4}" \times 6\frac{1}{4}" \times 6\frac{1}{4}"$ (LxHxW) lead box with a $1\frac{3}{4}"$ cylindrical bore in which the $^{241}\text{Am-Be}(\alpha,n)$ source sits at an unknown depth. The front of the rectangular source container was placed 82 cm from the outer wall of the 4-shooter, or 40.28" from the center of the 4-shooter amplification region. The distance between the floor and the bottom of the source container was 42.5 cm, implying that the centroid of the neutron beam was 1.11" above the top face of the 4-shooter amplification region. The source is recessed at least 1" into the

¹A Troxler Laboratories 3320 Series Depth Moisture Gauge.

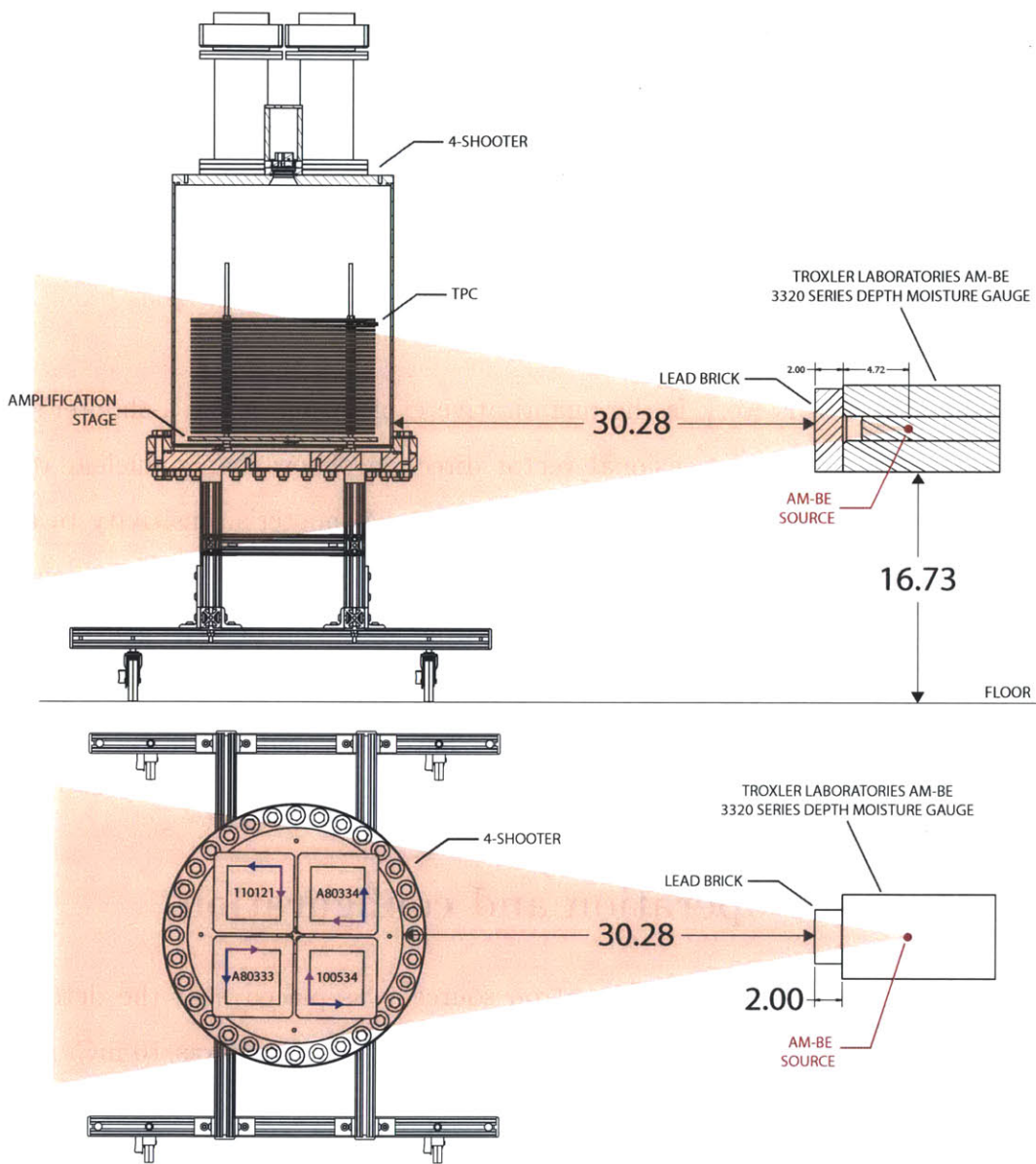


Figure 5-1: Schematic of the Am-Be source and 4-shooter setup as described in Section 5.1. These drawings are to scale. Top, a view of the setup from the side. Bottom, a view from above, with the source pointing to the left. The four 4-shooter cameras and their relative orientation to the source direction is illustrated by blue and magenta arrows. For each CCD, the blue arrow points in the $\phi = 0$ direction and the magenta arrow points in the $\phi = +\pi/2$ direction.



Figure 5-2: A photograph of the Am-Be setup sketched in Figure 5-1. The Am-Be source is in the center of the image, underneath a sheet of RICORAD, and behind a single lead brick, on the cart with wheels. The 4-shooter is on the right in the image, and the edge of the 4-shooter electronics rack is just visible on the far right.

source container, implying the neutrons are collimated to a cone with a half-angle of 40° or less. 2" of lead was placed between the source and the 4-shooter to reduce the copious γ - and X-rays also produced by the $^{241}\text{Am-Be}(\alpha,n)$ source. The source was pointed at the center of the detector. The expected neutron energy spectrum for a typical $^{241}\text{Am-Be}(\alpha,n)$ source with no shielding is shown in Figure 5-3, although the exact spectrum of the specific source used here may be considerably different [145]. The neutron energy spectrum of the $^{241}\text{Am-Be}(\alpha,n)$ source used in this study has not been previously measured.

Data was taken at MIT in building 24, room 036 in 24 hour long increments, each of which was preceded by evacuating the chamber with the turbo-molecular pump to 2×10^{-5} Torr or lower. The detector was then filled with 60 Torr of fresh CF_4

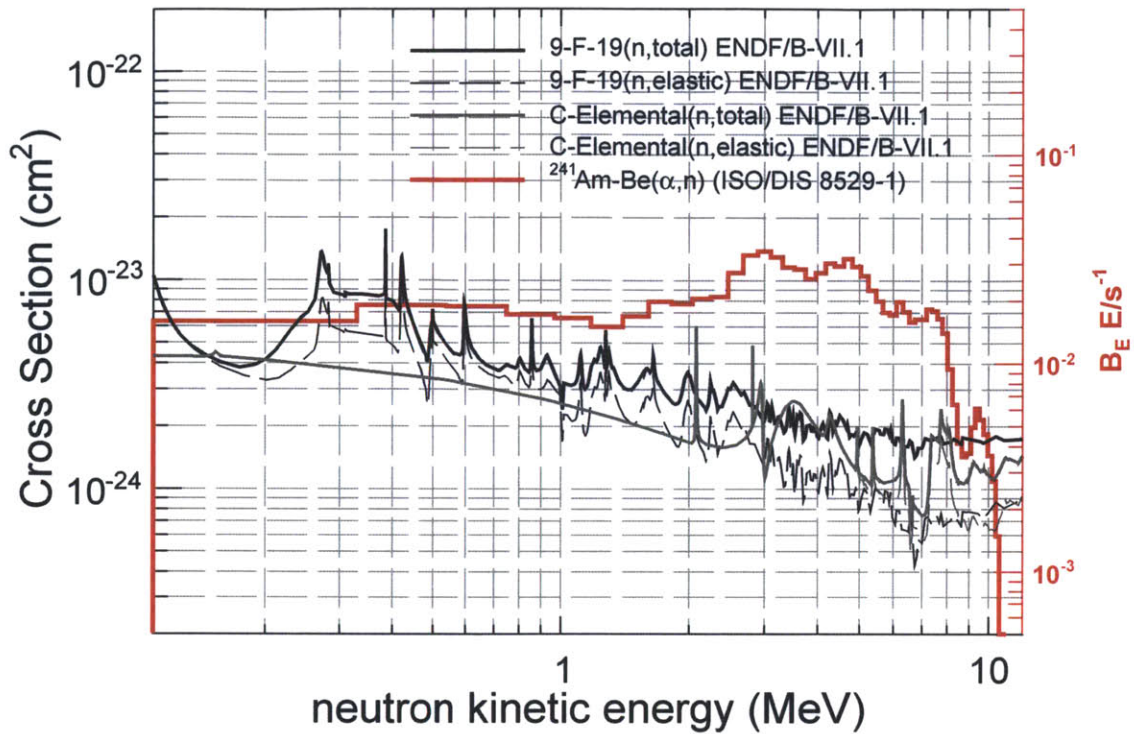


Figure 5-3: The red curve shows the neutron energy spectrum from a typical $^{241}\text{Am-Be}(\alpha,n)$ source [146]. Overlaid on the Am-Be spectrum are the neutron-carbon and neutron-fluorine total (solid curves) and elastic (dashed curves) interaction cross-sections spanning the Am-Be neutron energies. The cross-sections have been taken from ENDF [83]

gas. The amplification stage was biased with 670 V and the cathode was biased with -5000 V. The three photomultiplier tubes were biased at -925V .

The choice to run at 60 Torr CF_4 pressure was primarily motivated by the competing desires to 1) have long tracks even at very low energies to aid in the determination of their directions and 2) the need for a low energy threshold and high S/N for nuclear recoils in the CCDs. Monte Carlo studies indicate that directional reconstruction is optimal in 20 Torr pure CF_4 for a $100 \text{ GeV}/c^2$ WIMP, and at much lower pressures for lower WIMP masses [147]. However, higher gas gain is required at lower pressures to maintain a comparable S/N ratio due to the lower surface brightness of the nuclear recoils. Unfortunately the maximum achievable stable gas gain as a function of CF_4 pressure, shown in Figure 5-4, is observed to decrease as the CF_4 pressure is

decreased. Above this maximum achievable gain, the amplification stage is difficult to maintain at constant bias due to continual discharging. The choice of 670V for the

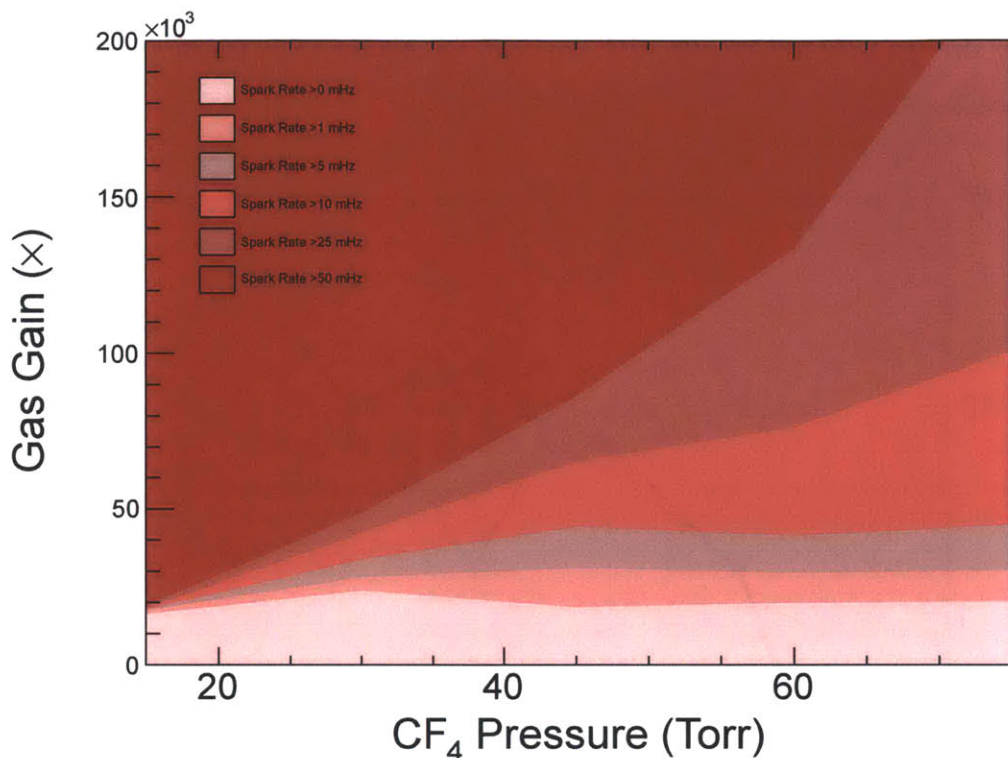


Figure 5-4: Spark rate contours in CF_4 pressure and gas gain, sampled at 15 Torr, 30 Torr, 45 Torr, 60 Torr and 75 Torr CF_4 pressure. The gas gain for the 15 Torr and 30 Torr pressure points are estimated based on linear fits to the pressure dependence of the parameters in Equation 4.3.

amplification stage bias was driven by two competing factors: 1) the desire for a low CCD energy threshold and 2) the desire to avoid nuclear recoil-induced discharges. The former requires as large a bias as stably achievable (see Figure 5-4). Meanwhile, Figure 5-5 shows the discharge rate in the amplification stage as a function of amplification stage bias with and without the ^{241}Am -Be neutron source present, and with 2" of lead between the 4-shooter and the ^{241}Am -Be source. The presence of the source, even with 2" of lead shielding, markedly increases the discharge rate. The increase in discharge rate is attributed to sparks induced by nuclear recoils² More work is necessary to determine if nuclear recoil-induced sparks pose a serious problem for a dark

²See the discussion of the Raether limit at the end of Section 4.1.3.

matter search. It is possible that the very low energy nuclear recoils ($< 100 \text{ keV}_r$) expected from WIMP recoils have ionization densities low enough to evade the Raether limit [133], and that the observed increase in discharge rate with the Am-Be source present is due to neutron recoils with energies far higher than those expected from WIMP scattering.

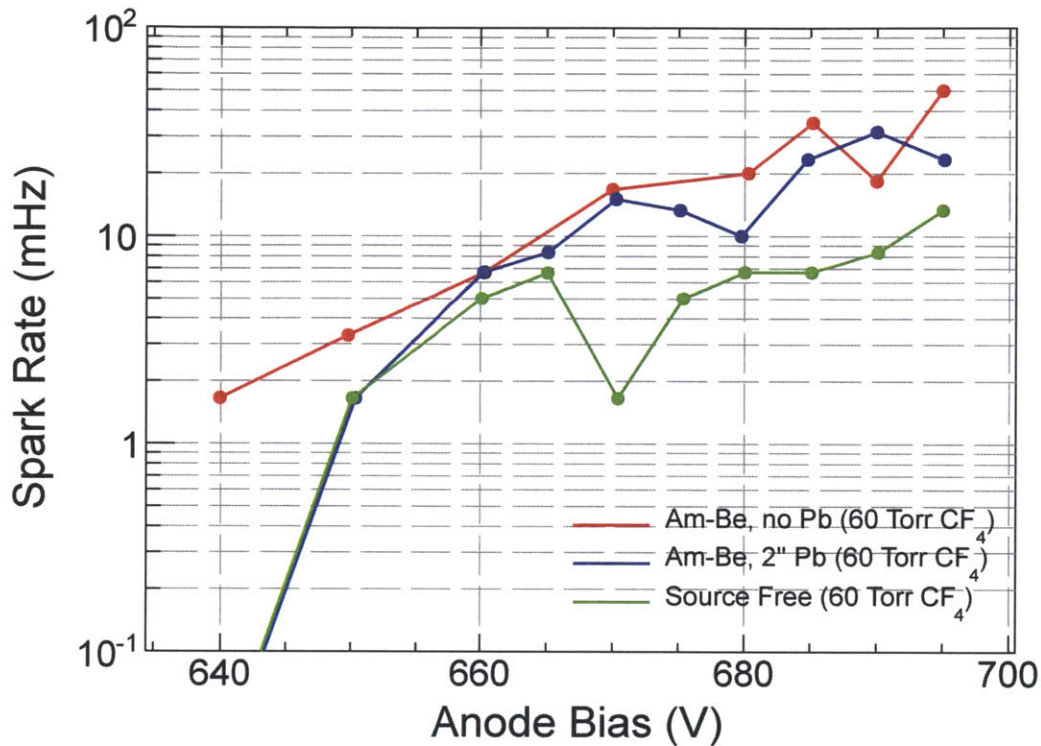


Figure 5-5: The amplification stage discharge rate versus amplification stage bias without the Am-Be source present, with the Am-Be source present and no shielding between the source and the 4-shooter, and with 2" of lead between the Am-Be source and the 4-shooter. Measurements in 60 Torr CF₄. The spark rate is noticeably higher in the presence of the Am-Be source, even after the detector has been shielded from the Am-Be source's γ and X-rays with 2" of lead.

For biases higher than $\approx -5500\text{V}$ on the drift stage, continual discharging was observed in 60 Torr CF₄ across the 3 cm separating the retaining rings of the TPC cathode or the leads of the field cage resistors and the stainless-steel inner walls of the vacuum vessel. The total transverse diffusion encountered by ionization electrons while drifting to readout in the amplification stage is dependent upon the electric field in the drift stage. The curve in Figure 4-9 shows the recommended transverse

diffusion in 60 Torr CF_4 as a function of cathode bias in the 4-shooter as estimated from [115]. Although the transverse diffusion minimum occurs at a bias of roughly -5160V (193 V/cm in the 4-shooter), the transverse diffusion constant at -5000V (187 V/cm) is $< 2\%$ larger, and further from the -5500V breakdown point.

5.2 Data sets

Data was taken in trigger-less, “witness” mode, repeatedly exposing the CCDs for 1 second, saving images between each exposure. Every set of 1000 1-second CCD exposures was preceded by 100 1-second “dark” frames, so-called because they are taken with the CCD shutter closed. In DMTPC parlance, 100 dark frames followed by 1000 exposures constitutes a “run.” The CCDs are binned 4×4 during readout (prior to digitization) so that each camera image has 256×256 bins.

Simultaneous with the CCD exposure, the waveform digitizer was armed to accept triggers. The charge channels were sampled every 4 ns over a 49 μsec window every time a pre-specified trigger condition was met. 4096 (8192) samples are stored before (after) the trigger condition is satisfied. This condition was met whenever the integrated charge on the anode exceeded 17.2 mV in runs 06999–07078 and 07548–07653 and whenever it exceeded 10.9 mV in runs 07654–07933. This corresponds to an energy threshold of 41 keV_{ee} and 26 keV_{ee} using the energy calibration of Section 4.2. Every time this simple trigger condition was met, the signals on the 3 PMTs, the 2 charge integrating amplifiers connected to the anode electrodes and the high-bandwidth current-to-voltage amplifier on the mesh were digitized and stored. On average, the trigger condition was satisfied (4.8 ± 2.2) times per 1-second CCD exposure with a 41 keV_{ee} threshold and (12.5 ± 3.5) times per 1-second CCD exposure with a 26 keV_{ee} threshold. The 41 keV_{ee} trigger threshold corresponds roughly to the energy threshold of the CCDs for detecting nuclear recoils. The threshold was lowered mid-run in order to study nuclear recoils with energies below the CCD threshold using the digitizer data alone, although only the joint CCD and digitizer analysis will be discussed here. Table 5.1 lists the configuration of each digitized channel.

1,864,000 total CCD images and 4,290,831 triggers were recorded with the 4-

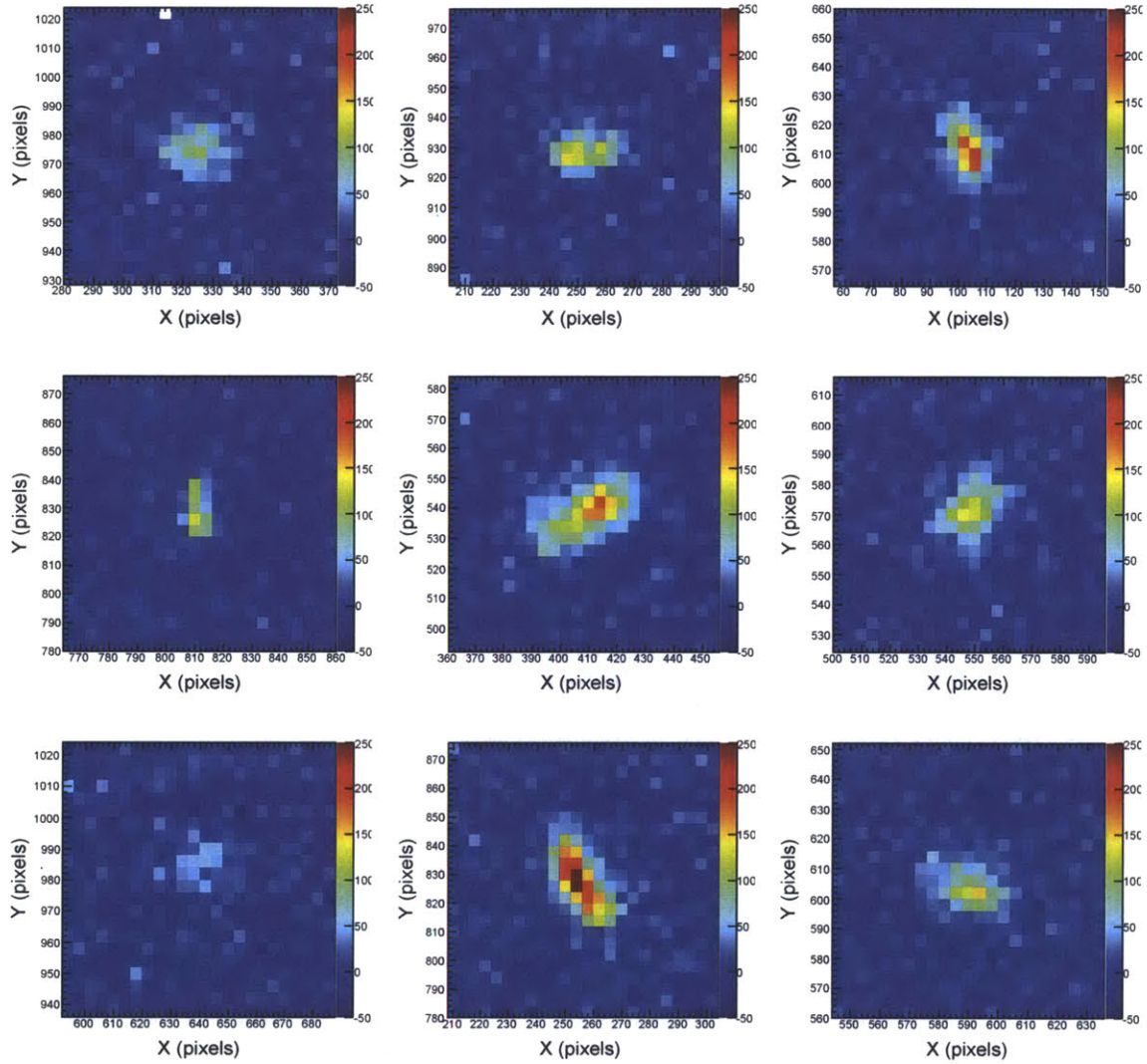


Figure 5-6: Am-Be nuclear recoil candidates, 60 Torr CF_4 , 670V bias on the amplification stage, and -5 kV on the drift stage. From left to right moving down the rows, a 105 keV_{ee} recoil in CCD 110121, a 148 keV_{ee} recoil in CCD 110121, a 171 keV_{ee} recoil in CCD A80333, a 116 keV_{ee} recoil in CCD A80334, a 243 keV_{ee} recoil in CCD 100534, a 168 keV_{ee} recoil in CCD A80333, a 65 keV_{ee} recoil in CCD A80333, a 303 keV_{ee} recoil in CCD A80333, and a 132 keV_{ee} recoil in CCD 100534. Each image is 14.44 mm on a side.

Channel	Scope Coupling	Dynamic Range
Mesh Current-to-Voltage (Route2Electronics HS-AMP-CF)	AC/1M Ω	± 800 mV
Anode Charge-to-Voltage (Cremat CR-113)	AC/1M Ω	± 200 mV
Veto Charge-to-Voltage (Cremat CR-113)	AC/1M Ω	± 100 mV
PMT #1	DC/50 Ω	± 500 mV
PMT #2	DC/50 Ω	± 500 mV
PMT #3	DC/50 Ω	± 500 mV

Table 5.1: The digitizer settings for the Am-Be runs listed in Table 5.2.

shooter over the course of 11 days. Data was taken over two separate periods of time in 2012, November 15 to November 17 for runs 06999–07078 and December 12 to December 19 for runs 07548–07933. The source was removed from the laboratory after run 07078, and brought back and positioned as closely as possible to the same position for runs 07548–07933. Table 5.2 summarizes the raw dataset. Runs 07548–07653 were identical to runs 07654–07933 except for the lower triggering threshold in the latter set of runs.

5.3 Event selection

The following describes the off-line analysis used to reduce the raw data listed in Table 5.2 to a set of likely nuclear recoil candidate events. Table 5.3 lists the number of events that passes each cut, in the same order as below.

AMBE-I: Track-candidate found in CCD image. The analysis begins with CCD track candidates identified by the `cleanSkim` analysis package. Candi-

Run Range	N_{images}	N_{triggers}	Scope Triggering Threshold (mV)	Energy Threshold (keV _{ee})	Start Time (MM-DD hh:mm)
06999–07040	168,000	210,576	17.2	41	11–15 19:07
07041–07078	152,000	192,083	17.2	41	11–16 19:56
07548–07598	204,000	250,648	17.2	41	12–11 10:53
07599–07647	196,000	232,633	17.2	41	12–12 12:04
07648–07653	24,000	28,924	17.2	41	12–13 14:18
07654–07689	144,000	430,286	10.9	26	12–13 17:22
07690–07737	192,000	577,255	10.9	26	12–14 11:47
07738–07785	192,000	567,633	10.9	26	12–15 11:54
07786–07830	180,000	531,133	10.9	26	12–16 12:09
07831–07882	208,000	630,590	10.9	26	12–17 11:01
07883–07933	204,000	639,070	10.9	26	12–18 13:06
Total	1,864,000	4,290,831	–	–	–

Table 5.2: Statistics relating to the Am-Be dataset. Each line represents approximately one day’s worth of back-to-back 1000 event runs, where each run is designated by a unique 5-digit number. N_{images} is the total number of images taken across all four cameras in each range of runs (so the number of exposures per CCD was $N_{\text{images}}/4$). The 4-shooter was evacuated and refilled with 60 Torr CF_4 between each series of runs, or lines in this table. The six 4-shooter digitizer channels were triggered on the central anode electrode preamplifier at the voltage thresholds listed. All data was taken in 2013.

dates identified by `cleanSkim` are required to have a non-zero reconstructed energy, projected range, number of pixels, number of neighboring pixels, maximum pixel value, mean pixel value and pixel root-mean-squared.

AMBE-II: CCD track-candidate not spatially near 110121 problem spot.

Raw images taken with CCD 110121 contain a strong bar-like feature parallel to the image X-axis, at approximately Y-pixel 748. The feature is mostly eliminated by dark-frame subtraction, but pixels near $(X, Y) = (18 \text{ px}, 748 \text{ px})$ are

often systematically high, even after dark-frame subtraction. For this reason, tracks in CCD 110121 with mean positions falling between 5 px $<X < 30$ px and 740 px $<Y < 755$ px are discarded. The other CCDs do not have analogous features in their images.

AMBE-III: Radial fiducialization. CCD track candidates cannot contain any pixels within 60 pixels, or 9.624 mm, of the anode central electrode-veto electrode separation channel.

AMBE-IV: Edge fiducialization. Analysis is done on a camera-by-camera basis (not on the composite mosaic image). CCD track candidates cannot contain any pixels within 20 pixels, or 3.208 mm, of a CCD image boundary.

AMBE-V: Spacer fiducialization. CCD track candidates cannot contain any pixels with a pixel-spacer distance of ≤ 8 pixels, or 1.283 mm. The spacer positions were mapped by eye based on their positions in the most recent LED anode illumination images.³ The spacers are not straight and are mapped as piecewise-continuous line segments. The minimum pixel-spacer distance is the minimum of the distances of every track pixel to all spacer line segments, for every spacer. Figure 5-7 shows the mean positions of all CCD tracks with and without the edge, radial and spacer fiducialization cuts.

AMBE-VI: Residual image rejection. A CCD track candidate is tagged as a likely residual image and discarded if either 1) more than 2 tracks are found in the track's run that are closely spaced in position to the track or 2) the track is less than 3 pixels distant from a pixel that saturated previously in the track's run. A pixel is deemed saturated if its value is greater than 55,000 ADU (out of a maximum possible 65,536 ADU) and if at least 5 other pixels have measured counts greater than 55,000 ADU in the same image. A typical spark followed by a residual image is shown in Figure 5-8.

³The most recent LED anode illumination to the Am-Be running was run 07363

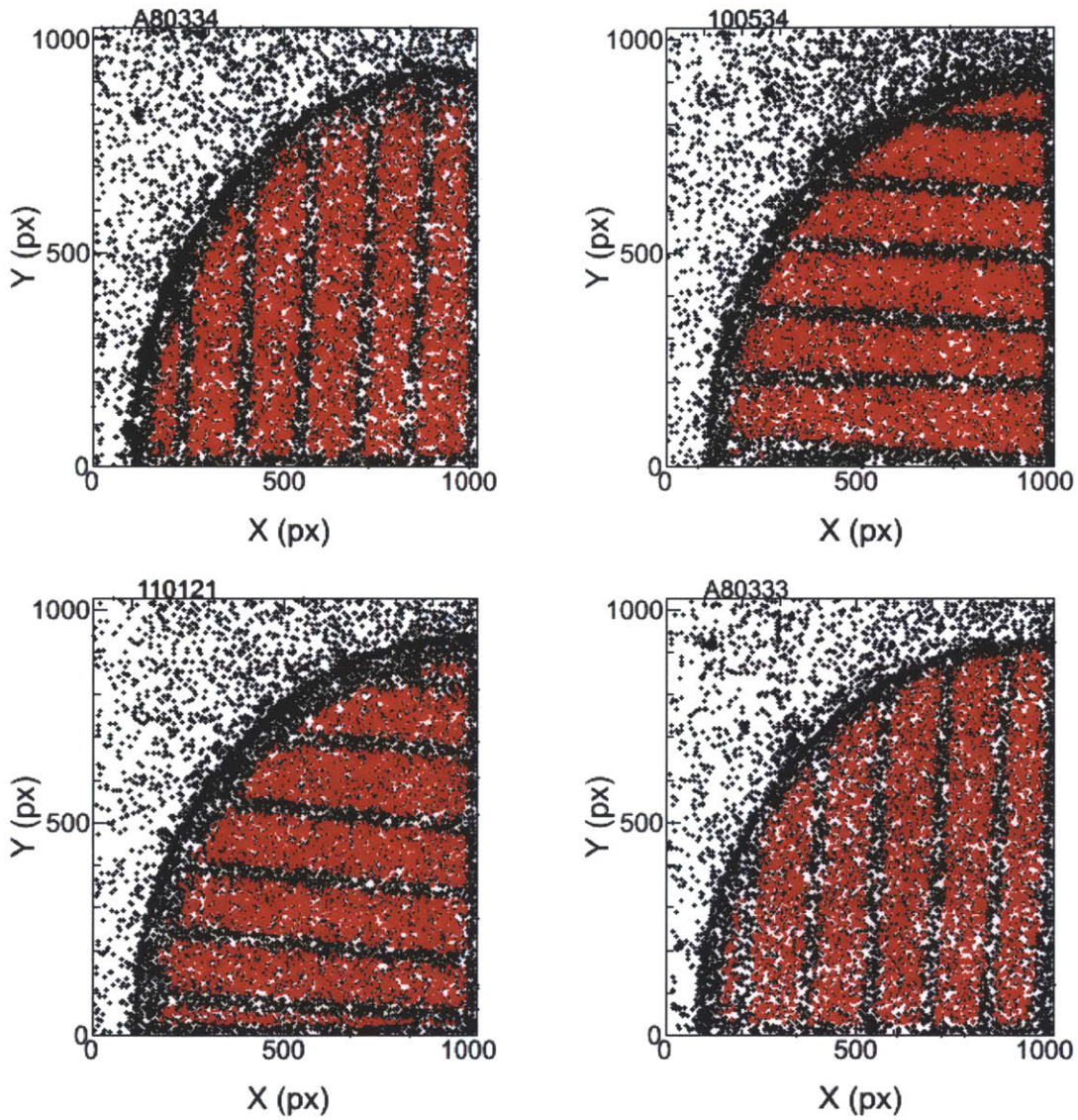


Figure 5-7: Nuclear recoil candidate locations (mean positions) in each camera for the Am-Be run. Scatter plot, for each 4-shooter CCD of the centroids of nuclear recoil candidates without fiducialization cuts AMBE-III, AMBE-IV and AMBE-V in black, and after these cuts in red. Each plot is labeled by its corresponding CCD in the upper left.

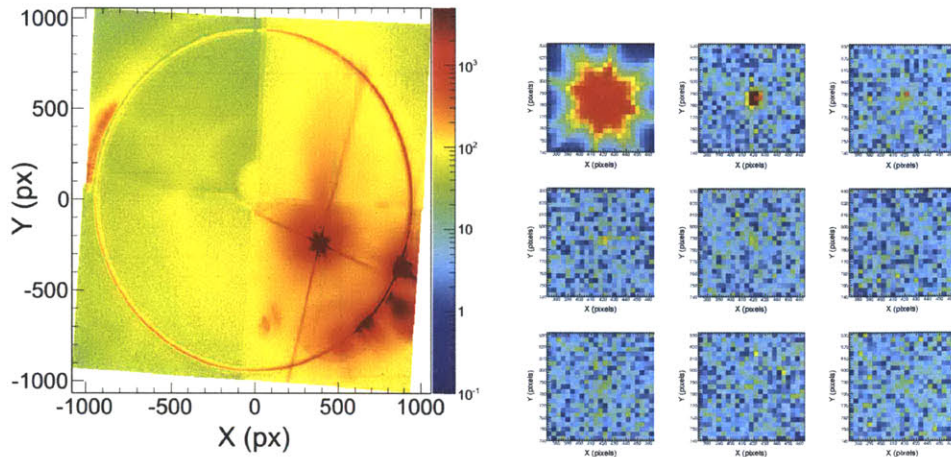


Figure 5-8: Left, a discharge in the amplification stage. The exposures have been stitched together to form a composite image, based on the known relative positioning of the four 4-shooter cameras. The discharge occurred in the bottom right CCD, near $(X, Y) = (400 \text{ px}, -200 \text{ px})$. The scale is in CCD ADU counts, and the log of the intensity is plotted in each pixel. Right, the upper left panel is a closeup of the spark on the left. From left to right moving down the rows, the 1-second exposures immediately following the anode discharge are shown, exhibiting a residual image in the CCD at the discharge position that fades gradually with time.

AMBE-VII: Maximum pixel < 500 ADU. CCD track candidates whose maximum pixel is greater than 500 ADU are discarded. This would correspond to an energy deposition of $\gtrsim 50 \text{ keV}_{ee}$ in one pixel in CCD A80334 and $\gtrsim 30 \text{ keV}_{ee}$ in one pixel in CCDs 100534, 110121, and A80333. Such a large implied ionization density is much more likely to be a CCD artifact than an actual nuclear recoil.

AMBE-VIII: $-5 \text{ sec} < (T - T_{\text{spark}}) < 15 \text{ sec}$ based on the anode current.

Any CCD track in an exposure occurring at a time T between -5 seconds before and 15 seconds after a spark occurring at time T_{spark} is discarded. Discharges in the chamber are accompanied by sharp pulses in the anode bias high voltage supply current, which is continuously monitored during data-taking at a sample rate of approximately 1 Hz. The specific cut times were chosen based on how long it took the detector gain to recover after discharging in ^{55}Fe gas gain measurements, as shown in Figure 5-9. The average discharge rate was measured using the anode bias supply current to be $(12 \pm 2) \text{ mHz}$ over the course of the

Am-Be run.

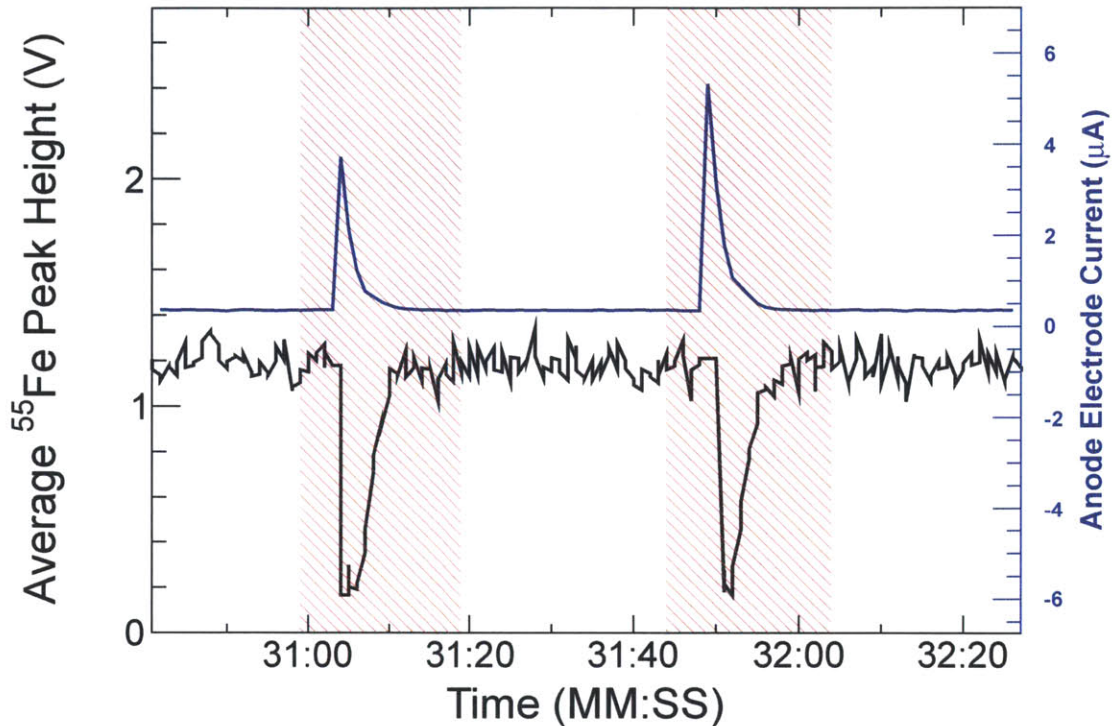


Figure 5-9: The black line shows the mean ^{55}Fe peak-height as a function of time on the central anode preamplifier, measured as described in Section 4.2. During the time period shown, the 4-shooter amplification stage discharged twice, leading to a loss of gain. Overlaid in blue is the current drawn by the anode bias high voltage supply, in which the discharges are detected as spikes in the current drawn by the supply. Nuclear recoil candidates occurring in the red hatched time intervals are cut by AMBE-VIII due to their proximity in time to the discharges sensed on the supply current monitor.

AMBE-IX: $N_{\text{triggers}} > 0$. The event with the CCD track must have at least 1 digitizer trigger. This cut has no teeth - only 0.007% of CCD tracks occur in events with no associated trigger.

AMBE-X: > 0 triggers passing basic cuts. The event with the CCD track must additionally have at least 1 digitizer trigger satisfying the following “basic” criteria⁴:

⁴Digitizer traces are smoothed with a gaussian discrete-time digital finite-impulse-response (FIR) filter before analysis quantities are computed on them.

1. *Quiet pre-trigger baseline:* The calculated pre-trigger baseline of the mesh and anode electrode waveforms must be consistent with zero. For the fast mesh waveform the baseline must be between -5.5 mV and -2.5 mV, for the central anode electrode waveform the baseline must be between -1.5 mV and 1.5 mV, and for the veto anode electrode waveform the baseline must be between -5.5 mV and -2.5 mV. The baseline of each waveform is computed as the average of the first 500 digitized voltages in the waveform.
2. *Reasonable pre-trigger RMS:* The RMS spread in the voltages used to calculate the baselines of the waveforms is required to be small for each channel, except for the PMTs. For the fast mesh waveform the RMS must be between 5 mV and 8 mV, for the central anode electrode waveform the RMS must be between 0.8 mV and 1.45 mV, and for the veto anode electrode waveform the RMS must be between 0.7 mV and 1.2 mV. The RMS spread of each waveform is computed as the RMS deviation of the first 500 digitized voltages in the waveform.
3. *No saturated channels:* The maximum recorded raw voltage on the channels must be within the digitizer channels' dynamic range. For the fast mesh waveform the maximum raw voltage measured must be less than 790 mV, for the central anode electrode waveform the maximum raw voltage measured must be less than 198 mV, and for the veto anode electrode waveform the maximum raw voltage measured must be less than 98 mV.

AMBE-XI: > 0 triggers passing nuclear recoil cuts. The event with the CCD track must additionally have at least 1 digitizer trigger satisfying the following criteria designed to select nuclear recoils based on charge information alone. The criteria seek to exploit the fact that pulses on the mesh caused by nuclear recoils have a characteristic two-peaked structure as discussed in [71], while pulses caused by other types of radiation do not. For nuclear recoils, the first very narrow (fast) peak occurs almost immediately while the second, broad (slow) peak typically lags the first by $\gtrsim 100$ ns.

1. *Fast mesh rise-time:* The 25%-75% rise-time⁵ of the pulse on the mesh must be less than 18 ns. If the signal height on the central anode electrode is less than 25 mV, then the 10%-90% rise-time must also be less than 25 ns.
2. *Fast veto rise-time:* The 25%-90% rise-time of the veto pulse must be less than 380 ns, and the 10%-90% rise-time must be less than 500 ns.
3. *Mesh & veto signals coincident:* The time at which the veto pulse peaks must be within 1.2 μ s of the first peak on the mesh.
4. *Veto less than anode:* The pulse height on the veto V_V must satisfy the following relationship with the pulse height on the central anode electrode V_A : $V_V[\text{mV}] < 2 \text{ mV} + 307.69 \times V_A[\text{mV}]$.
5. *Fast & slow mesh peaks well separated in time:* The second peak on the mesh must occur at least 80 ns after the minimum in the mesh pulse between the first and second peaks.
6. *Mesh fast-to-slow peak ratio:* If the peak height on the central anode electrode is greater than 20 mV, the ratio of the height of the first peak on the mesh to that of the second peak on the mesh must be greater than 0.94.
7. *Mesh-anode relative pulse heights:* If the peak height on the central anode electrode is greater than 40 mV, then the pulse height on the central anode electrode V_A must satisfy the following relationship with the first peak height on the mesh $V_{M,1}$: $V_{M,1}[\text{mV}] > -1 \text{ mV} + 2.8293 \times V_A[\text{mV}]$.

AMBE-XII: CCD & charge candidate matching by energy. The central anode charge energy E_{charge} and CCD energy E_{CCD} of the two charge and CCD candidates in an event with the closest energies in keV_{ee} must satisfy the following relationship: $|(E_{\text{charge}} - E_{\text{CCD}}) - 5.6 \text{ keV}_{ee}| < 33.7 \text{ keV}_{ee}$. The determination of E_{charge} , E_{CCD} , and this relationship are discussed in detail in Section 5.4.1.

⁵The X%-Y% rise-time of a waveform is the time it takes an identified pulse in that waveform to change in voltage from X% of its maximum voltage to Y% of its maximum voltage.

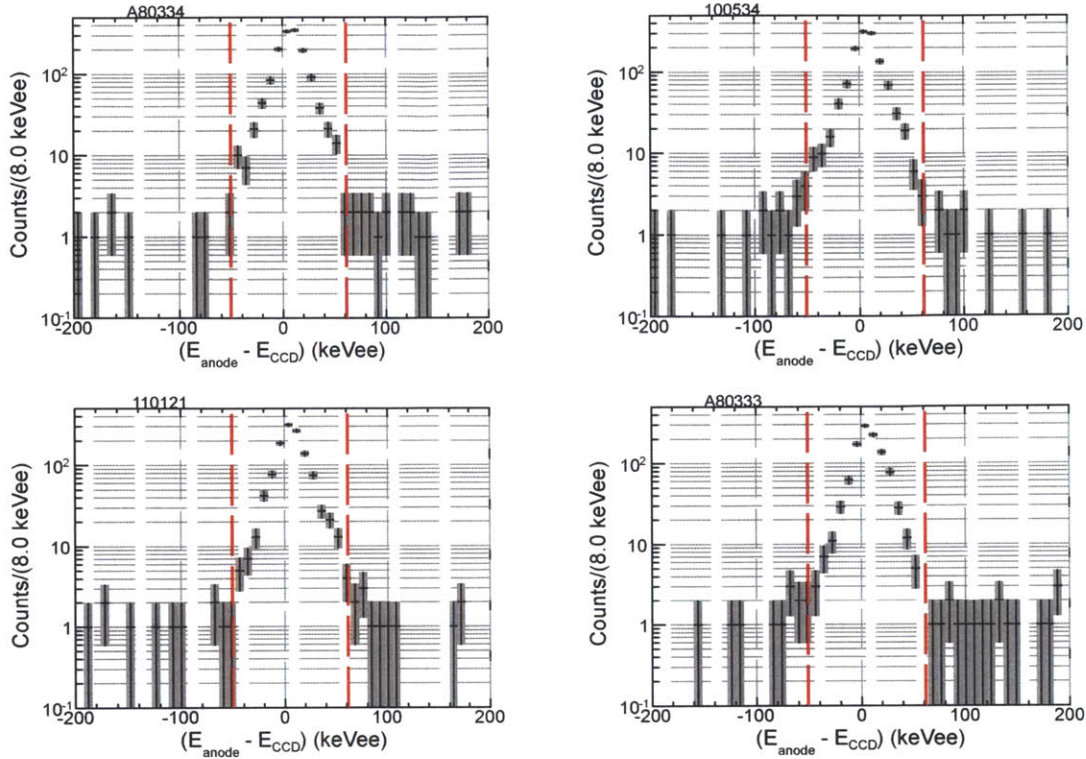


Figure 5-10: Am-Be nuclear recoil candidates, 60 Torr CF_4 , 670V bias on the amplification stage, and -5 kV on the drift stage. The difference between the energy of the recoils determined with the CCDs, E_{CCD} , and the energy determined with the charge integrating preamplifier, E_{anode} . The red dashed lines illustrate events cut by AMBE-XII. Each plot is labeled by its corresponding CCD in the upper left.

AMBE-XIII: Fisher discriminant cut. As in [70], a Fisher linear discriminant [148] is trained using the Toolkit for Multivariate Data Analysis [149] (TMVA⁶) in the ROOT framework [117] to classify events as more likely to be CCD instrumental artifacts or nuclear recoils. The classifier is trained using data taken with the TPC voltages off consisting only of CCD artifacts, and simulated Am-Be nuclear recoils. 855,000 voltages-off images were taken with each camera, and 21,000 Am-Be nuclear recoils were simulated for each camera. The same variables are used as inputs to the discriminant as in [70]. Figure 5-11 shows the distribution of the Fisher discriminant for the two training datasets. Figure 5-12 shows the distribution of the Fisher discriminant for the Am-Be neutron dataset, with and without any cuts that rely on the charge channel measurements. It

⁶TMVA version 4.1.2 was used for this analysis.

is clear that the dataset has a large CCD artifact contamination without any charge cuts (as in [70]), but the contamination is greatly reduced by the charge cuts in the 4-shooter alone. To increase the nuclear recoil purity of this data sample, the Fisher discriminant is required to be positive, corresponding to $> 98\%$ signal acceptance (CCD artifact rejection) for all four cameras.

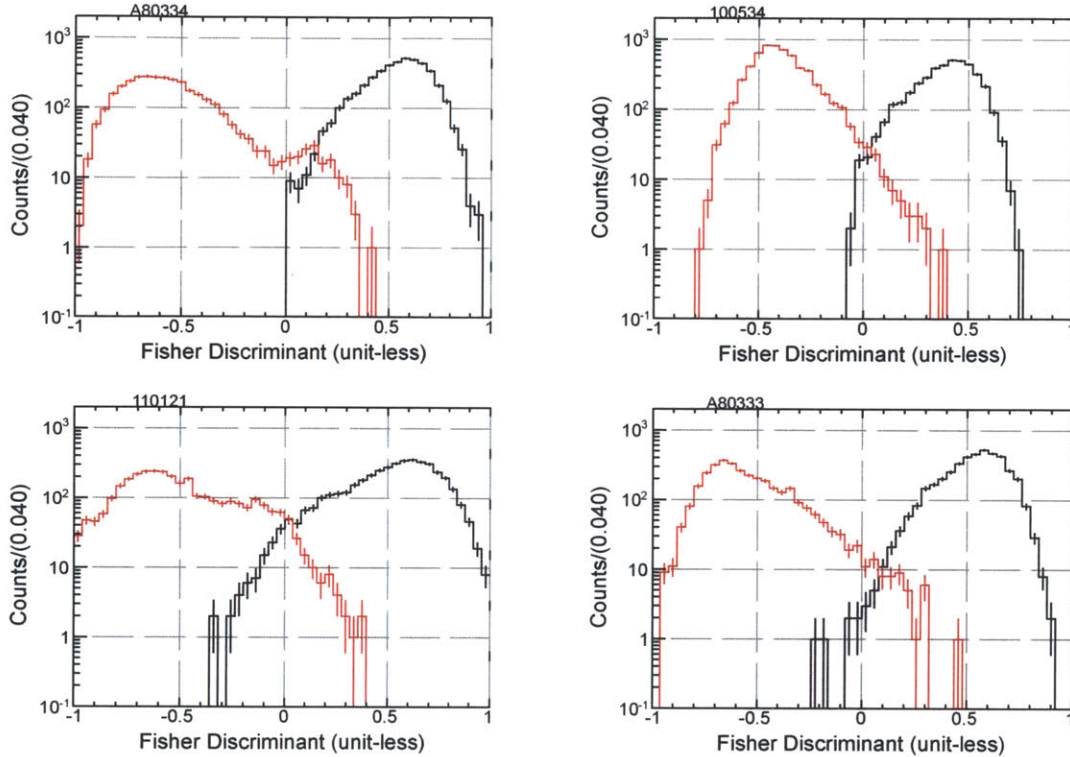


Figure 5-11: The fisher discriminant of cut AMBE-XIII applied to its training datasets, data taken with the TPC voltages off consisting entirely of CCD artifacts (red) and Monte Carlo nuclear recoils (black). Each plot is labeled by its corresponding CCD in the upper left. In the Am-Be analysis, events with Fisher discriminant less than 0 are discarded as likely CCD artifacts.

The numerical effect of these cuts on the Am-Be dataset are shown in Table 5.3. Cuts AMBE-X through AMBE-XII are based on techniques developed in [71].

An eye scan of approximately 30% of all events passing cuts AMBE-I through AMBE-XII found that over 98% of events were visually consistent in the CCDs and charge channels with nuclear recoil candidates. Less than 2% of events were clearly not nuclear recoils and were events where a valid nuclear recoil candidate in the

Cut	Port A (A80334)	Port B (100534)	Port C (110121)	Port D (A80333)
Raw # of images	466,000	466,000	466,000	466,000
# of CCD track candidates	21,168	18,306	33,948	14,460
Not in 110121 problem spot	–	–	17,837	–
Radial fiducialization	12,411	11,943	11,228	7,580
Edge fiducialization	10,848	10,276	9,167	6,226
Spacer fiducialization	8,006	7,437	6,510	4,558
Residual image rejection	3,901	6,692	5,324	4,051
Maximum pixel < 500 ADU	3,308	5,334	4,502	3,190
$-5 \text{ sec} < T - T_{\text{spark}} < 15 \text{ sec}$ from anode current	2,768	4,476	3,912	2,685
$N_{\text{triggers}} > 0$	2,768	4,476	3,912	2,685
> 0 triggers passing basic cuts	2,767	4,475	3,912	2,685
> 0 triggers passing nuclear recoil cuts	1,248	1,329	1,070	1,210
Charge-CCD matching	1,142	1,243	993	1,136
Fisher discriminant > 0	1,126	1,182	931	1,098
Total	1,126	1,182	931	1,098

Table 5.3: Cuts applied to the track candidates in the Am-Be dataset to select nuclear recoils, as described in Section 5.3. Line one in this table corresponds to AMBE-I in the text, line two to AMBE-II, etc.. For each camera, the number of track candidates surviving each cut is given. A total of 4,337 nuclear recoil candidates survive all selections across the four 4-shooter cameras.

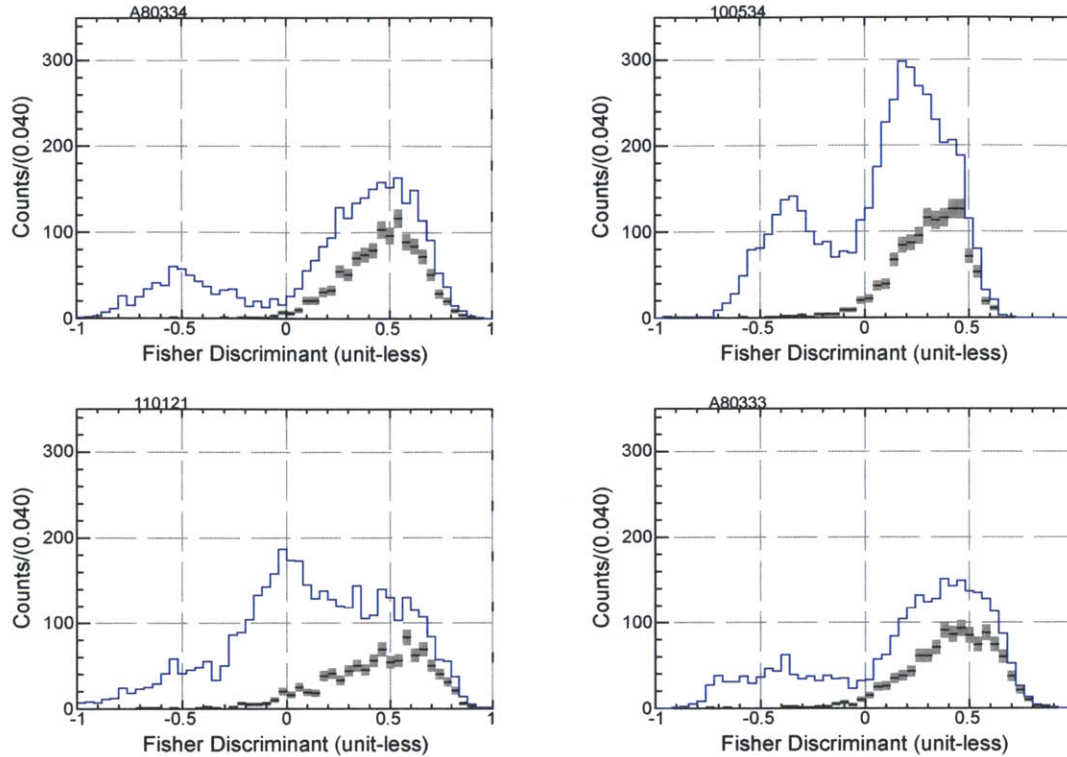


Figure 5-12: The fisher discriminant of cut AMBE-XIII applied to the Am-Be dataset, with the charge cuts AMBE-IX through AMBE-XII (in black and gray) and without them (in blue). Each plot is labeled by its corresponding CCD in the upper left. The charge cuts are observed to eliminate the majority of events independently determined to be CCD artifacts by the Fisher discriminant analysis.

charge channels was incorrectly associated with an obvious CCD artifact, in spite of the charge-CCD energy matching cut AMBE-XII. Cut AMBE-XIII was subsequently added to the analysis to reduce the dominant background of CCD artifact-charge nuclear recoil coincidences. Based on these eye scans and the addition of cut AMBE-XIII, the nuclear recoil purity of the full data sample after all analysis cuts is expected to be in excess of 98%.

5.4 Data-Monte Carlo comparisons

Direct comparison with data builds confidence in the Monte Carlo's ability to model the 4-shooter's actual performance. To this end, 84,000 Am-Be neutron fluorine recoils were generated in the Monte Carlo for each 4-shooter camera. The neutrons were

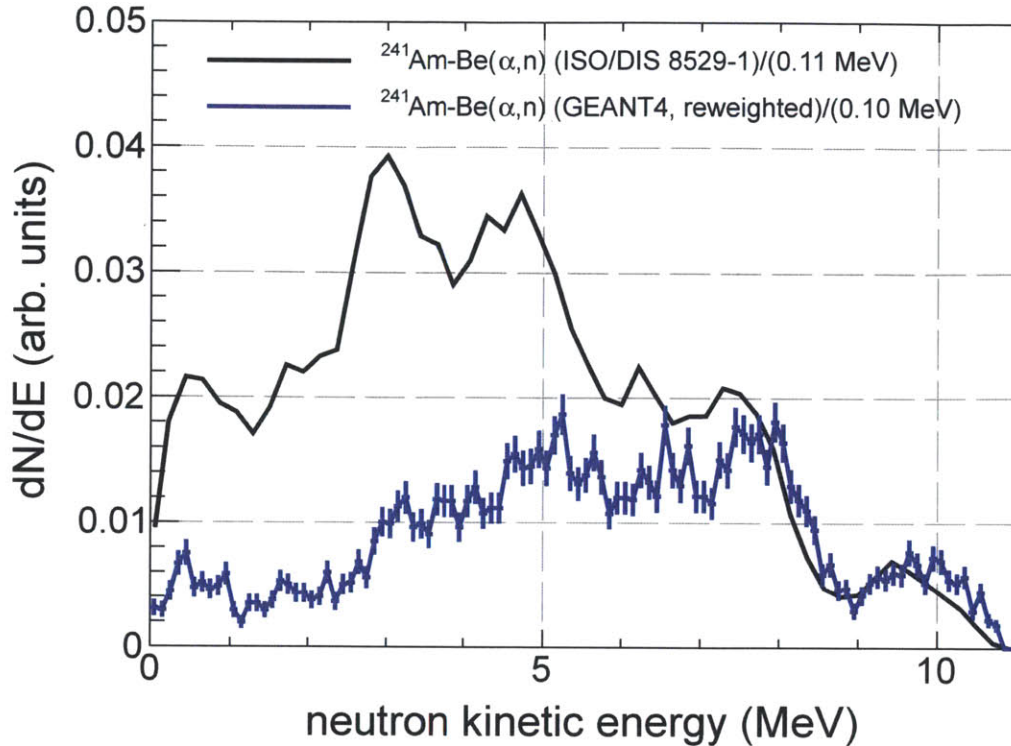


Figure 5-13: The neutron energy spectrum from a typical $^{241}\text{Am-Be}(\alpha,n)$ source [146] (black) and the energy spectrum predicted with GEANT4 for neutrons which make it into the TPC through the lead, air, stainless-steel, inactive CF_4 and copper in between the Am-Be source and the sensitive volume of the 4-shooter (blue) if the black curve is the Am-Be neutron energy spectrum at the source. Both histograms have been normalized such that the sum over all bins is equal to one.

generated with the energy spectrum in Figure 5-3, in the source-detector configuration described in Section 5.1, and collimated to a cone with a 40° half-angle. Before comparing the Monte Carlo results to the data, the Monte Carlo neutron energy spectrum is re-weighted to incorporate the energy-dependent attenuation expected for the neutrons by the 2" of lead shielding, the air outside the vacuum vessel, the inactive CF_4 outside of the TPC and the Cu rings of the TPC field cage. The 2" of lead shielding alone is expected to attenuate the neutron flux emitted from the source by a factor of 5 for neutrons with energies between 0.1 MeV to 10 MeV [83]. The spectrum before and after weighting is shown in Figure 5-13. The weighting function is determined from a GEANT4 [104] simulation with identical parameters to the Monte Carlo described here, using the high precision neutron package (NeutronHP

[150]) to model the neutron transport.

At present, the charge signals and their measurement are not simulated in the Monte Carlo. Implicit in the comparisons to follow is the assumption that the efficiency of the charge cuts in Section 5.3 is uniform across the full range of the parameters being compared. This important point is discussed further in Chapter 6.

5.4.1 Monte Carlo bias and resolution

The Monte Carlo is used to estimate the relationship between the measured intensity and size of track candidates in the CCD, in ADU and pixels, respectively, and the true energy and projected range of the recoil corresponding to the candidates, in keV_{ee} and mm. Figure 5-14 shows the measured CCD energy in ADU divided by the true energy in keV_{ee} as a function of true energy in keV_{ee} for simulated Monte Carlo Am-Be nuclear recoils. The Monte Carlo incorporates the measured pixel-to-pixel gain variations described in Section 4.1.2 in the generated signals, and the CCD energies here have been corrected to remove these variations as in the data. For low energy recoils, the difference between the input Monte Carlo CCD gain in $\text{ADU}/\text{keV}_{ee}$ and the ratio between the measured energy in ADU and the true recoil energy in keV_{ee} is substantial. The bias on the energy determination as a function of recoil energy is estimated by fitting the effective $\text{ADU}/\text{keV}_{ee}$ gain in the Monte Carlo to a rational polynomial. The ratio of two degree-1 polynomials is found to provide an adequate fit to the effective $\text{ADU}/\text{keV}_{ee}$ gain versus energy. In the infinite energy limit, this function is independent of energy, reflecting the expectation that there should be negligible bias in the determination of the energy of tracks with energies in excess of 1 MeV_{ee} . The fit results for the effective $\text{ADU}/\text{keV}_{ee}$ gain G versus energy are as

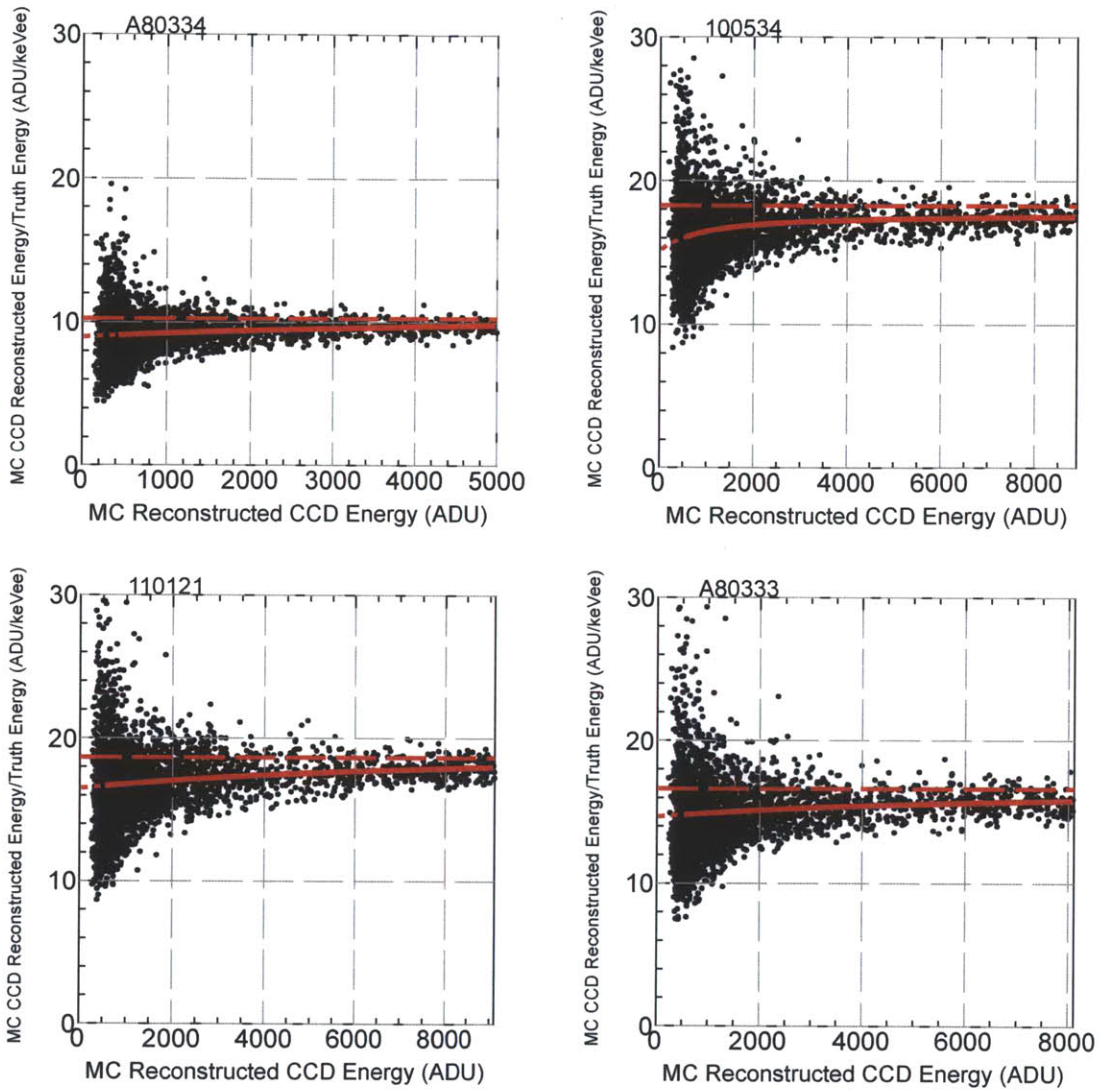


Figure 5-14: Am-Be nuclear recoil Monte Carlo. The black points are the reconstructed CCD energy in ADU divided by the true recoil energy in keV_{ee}, versus the reconstructed energy. The dashed red line shows the ADU/keV_{ee} gain specified in the Monte Carlo. The solid red line shows the rational polynomial fits used to estimate the energy reconstruction bias as a function of reconstructed energy as described in Section 5.4. The results of these fits are given in Equation 5.1. Each plot is labeled by its corresponding CCD in the upper left.

follows for each camera:

$$\begin{aligned}
G_{A80334}[E \text{ (ADU)}] &= \left(\frac{(5.0 \pm 2.6) \times 10^4 + (10.8 \pm 0.5) \times E}{(5.6 \pm 2.9) \times 10^3 + E} \right) \frac{\text{ADU}}{\text{keV}_{ee}} \\
G_{100534}[E \text{ (ADU)}] &= \left(\frac{(1.4 \pm 0.4) \times 10^4 + (17.7 \pm 0.1) \times E}{(9.0 \pm 3.0) \times 10^2 + E} \right) \frac{\text{ADU}}{\text{keV}_{ee}} \\
G_{110121}[E \text{ (ADU)}] &= \left(\frac{(1.3 \pm 0.3) \times 10^5 + (19.3 \pm 0.4) \times E}{(8.1 \pm 1.9) \times 10^3 + E} \right) \frac{\text{ADU}}{\text{keV}_{ee}} \\
G_{A80333}[E \text{ (ADU)}] &= \left(\frac{(1.0 \pm 0.3) \times 10^5 + (16.8 \pm 0.4) \times E}{(7.2 \pm 2.2) \times 10^3 + E} \right) \frac{\text{ADU}}{\text{keV}_{ee}}
\end{aligned} \tag{5.1}$$

These relationships are used to convert from intensity measured in the CCDs to true recoil energy in keV_{ee} in both the data and the Monte Carlo. As the Monte Carlo reconstructed CCD energy approaches infinity in Equations 5.1, the observed gain divided by the Monte Carlo input gain (see Table 4.1) approaches (1.05 ± 0.05) , (0.97 ± 0.01) , (1.04 ± 0.02) , and (1.01 ± 0.02) for CCDs A80334, 100534, 110121, and A80333, respectively. For Monte Carlo recoils, Figure 5-15 shows the estimated resolution on the energy determination computed using these relationships as a function of the recoil energy. For all four 4-shooter cameras, the estimated energy resolution degrades as the recoil energy decreases below 100 keV_{ee} , from 10% to 20%.

The energy of recoils as measured with the CCDs using Equations 5.1 can be directly compared to the energy of the same recoils measured independently using the charge integrating preamplifier on the central anode electrode (see Section 4.2). Figure 5-16 shows the CCD-derived energy plotted against the anode-derived energy for Am-Be recoils. The relationship is linear for energies considerably above the energy threshold of the CCDs. The asymptotic slope and energy offset between the CCD and anode energy determinations is fit for using the ratio of a degree-2 polynomial to a degree-1 polynomial, yielding asymptotic slopes of (1.08 ± 0.03) , (1.10 ± 0.02) , (1.04 ± 0.02) , and (1.07 ± 0.02) for CCDs A80334, 100534, 110121 and A80333, respectively. Gaussian fits to the global difference between the CCD and anode-determined energies ($E_{\text{CCD}} - E_{\text{charge}}$) yield offsets of $+(7.9 \pm 0.4) \text{ keV}_{ee}$, $+(6.6 \pm 0.4) \text{ keV}_{ee}$, $+(6.6 \pm 0.4) \text{ keV}_{ee}$, and $+(7.5 \pm 0.4) \text{ keV}_{ee}$. The CCD and charge-derived

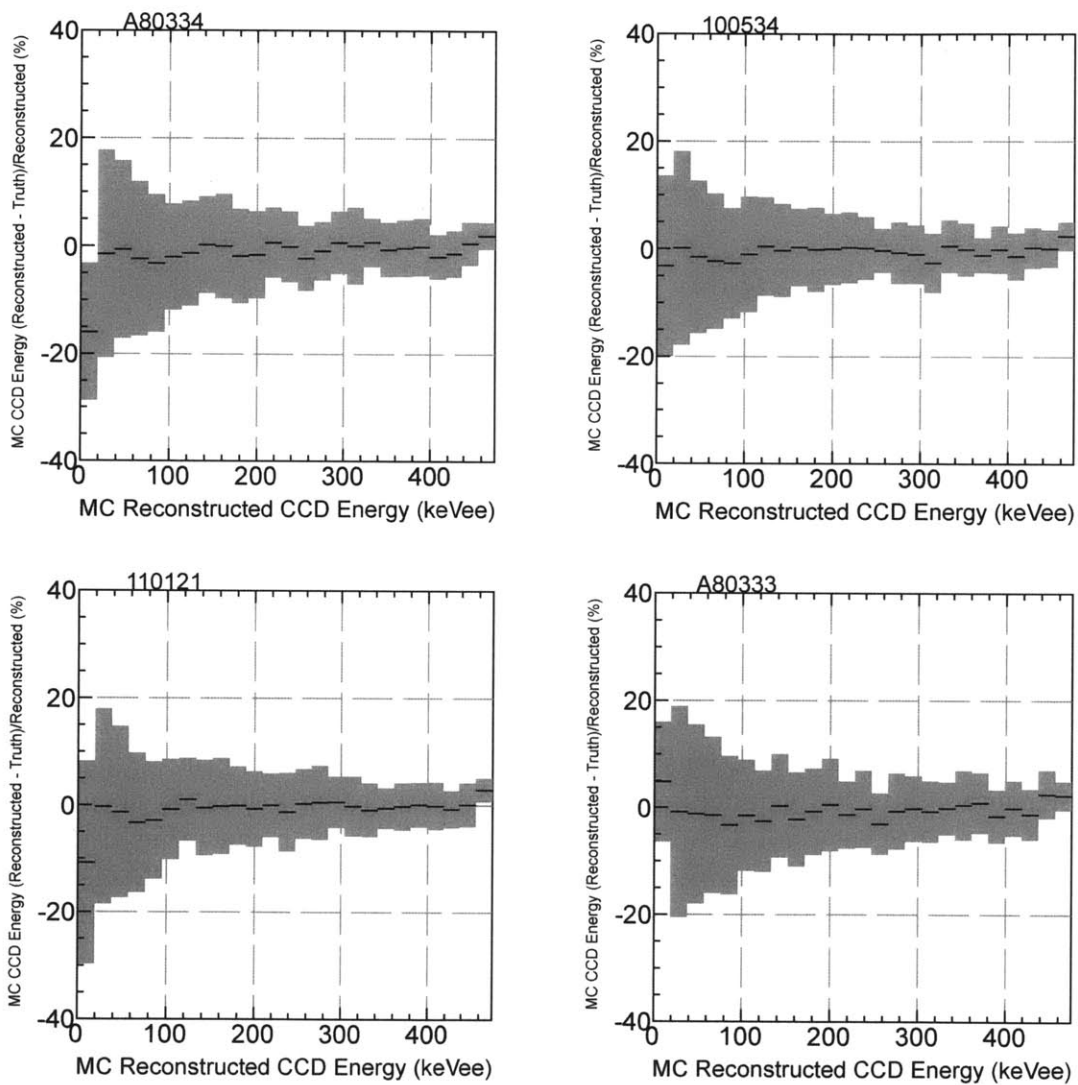


Figure 5-15: Am-Be nuclear recoil Monte Carlo. The residuals between the true energy of Monte Carlo nuclear recoils and the reconstructed CCD energy. The gray bars indicate the standard deviation of the residuals in each energy bin. Each plot is labeled by its corresponding CCD in the upper left.

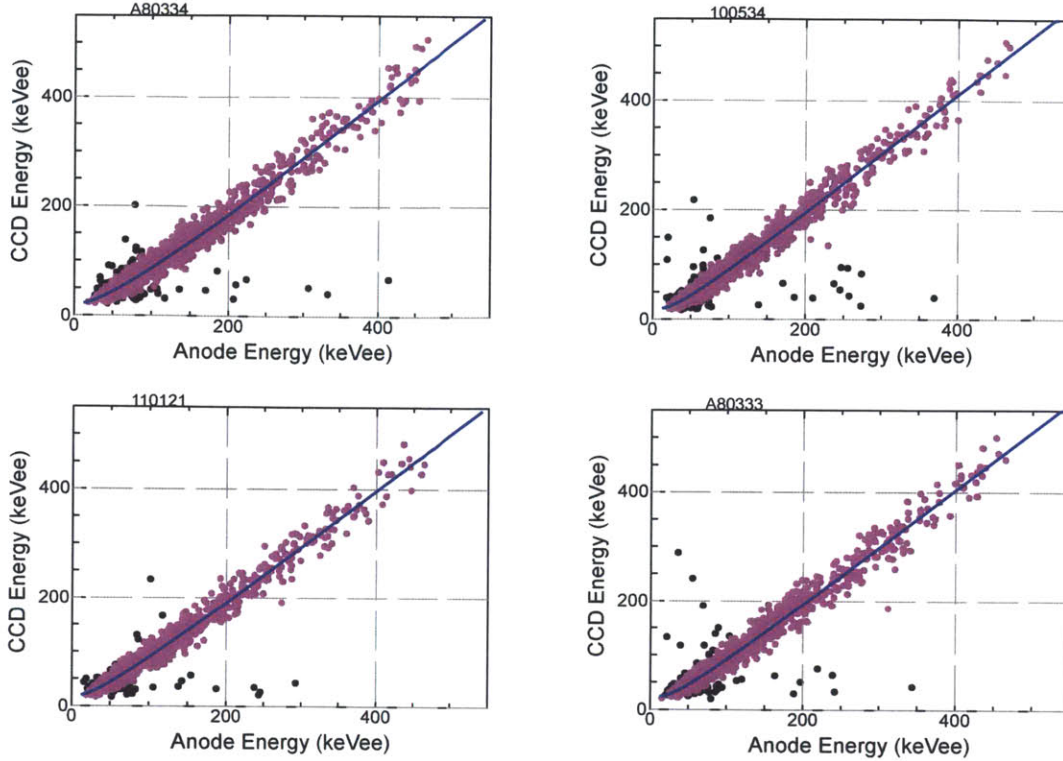


Figure 5-16: Am-Be nuclear recoil candidates, 60 Torr CF_4 , 670V bias on the amplification stage, and -5 kV on the drift stage. The recoil energy in keV_{ee} determined from the CCDs versus the recoil energy determined from the preamplifier on the amplification stage central electrode. The solid blue lines show the rational polynomial fits used to estimate the relationship between the two energy determinations. Only the magenta points are included in the fits. The black outlier points are not included in the fits because they fall 3 RMS deviations away from the mean value of the ratio of the CCD-derived energy to the charge-derived energy. Each plot is labeled by its corresponding CCD in the upper left.

recoil energy determinations are thus in agreement at the 20% level for energies above 50 keV_r , and approach the 5%-10% level of agreement for recoil energies in excess of 100 keV_r . The CCD-derived recoil energy determination favors systematically higher recoil energies than the charge. The origin of the small disagreement between the CCD and anode energy determinations is unknown, although the error quoted here on the asymptotic ratio is only the fit error and likely to be an underestimate of the total error.

Figure 5-17 shows the measured CCD track projected range in mm as a function of true projected range in mm for simulated Monte Carlo Am-Be nuclear recoils. The

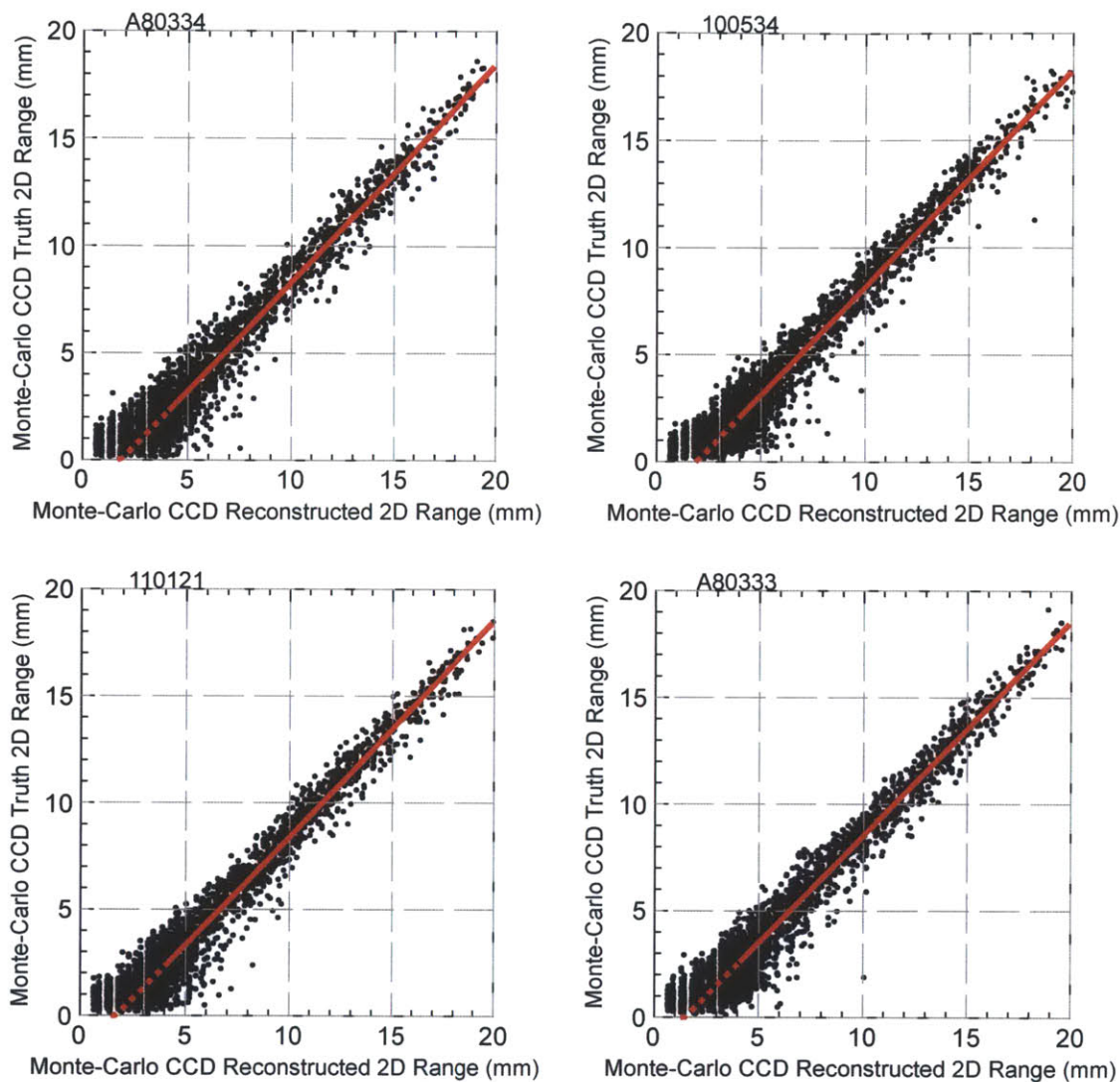


Figure 5-17: Am-Be nuclear recoil Monte Carlo. The black points are the reconstructed CCD projected range in mm versus the true recoil projected range in mm. The solid red lines show the line fits used to estimate the projected range reconstruction bias as a function of reconstructed projected range as described in Section 5.4. The dashed part of each red line is not included in the fits but is used to estimate the true projected range of recoils from the reconstructed projected range. The results of these fits are given in Equation 5.2. Each plot is labeled by its corresponding CCD in the upper left.

bias on the projected range determination as a function of reconstructed projected range is estimated by fitting the true projected range as a function of the reconstructed projected range to a line above 4 mm reconstructed projected range. The fit results for the true recoil projected range in mm versus the reconstructed projected range in mm are as follows for each camera:

$$\begin{aligned}
R_{A80334}^{2D}[R_{\text{reco}}^{2D} \text{ (mm)}] &= \left((-1.8 \pm 0.2) + (1.01 \pm 0.02) \times R_{\text{reco}}^{2D} \right) \text{ mm} \\
R_{100534}^{2D}[R_{\text{reco}}^{2D} \text{ (mm)}] &= \left((-1.9 \pm 0.2) + (1.01 \pm 0.02) \times R_{\text{reco}}^{2D} \right) \text{ mm} \\
R_{110121}^{2D}[R_{\text{reco}}^{2D} \text{ (mm)}] &= \left((-1.7 \pm 0.2) + (1.01 \pm 0.02) \times R_{\text{reco}}^{2D} \right) \text{ mm} \\
R_{A80333}^{2D}[R_{\text{reco}}^{2D} \text{ (mm)}] &= \left((-1.5 \pm 0.2) + (1.00 \pm 0.02) \times R_{\text{reco}}^{2D} \right) \text{ mm}
\end{aligned} \tag{5.2}$$

The true projected range is systematically lower than the measured projected range by approximately 2 mm for all four 4-shooter cameras. This behavior has been previously observed [70], and is expected as electron diffusion increases the measured projected range, and the track-finding algorithm has a tendency to pad tracks with extra pixels.

These relationships are used to convert from projected range measured in the CCDs to true projected range in mm in both the data and the Monte Carlo. For Monte Carlo recoils, Figure 5-18 shows the estimated resolution on the projected range determination computed using these relationships as a function of the reconstructed projected range. For all four 4-shooter cameras, the estimated projected range resolution degrades as the reconstructed projected range decreases below 5 mm, from 10% to 20%.

5.4.2 Data-Monte Carlo comparisons

Figure 5-19 shows the Am-Be energy spectrum in data versus Monte Carlo, where the energy is estimated in the data and the Monte Carlo using Equations 5.1 to convert from reconstructed energy in ADU to recoil energy in keV_{ee}. For this comparison and most of the following data-Monte Carlo comparisons, the Monte Carlo histograms have been normalized so that the Monte Carlo and data have the same number of

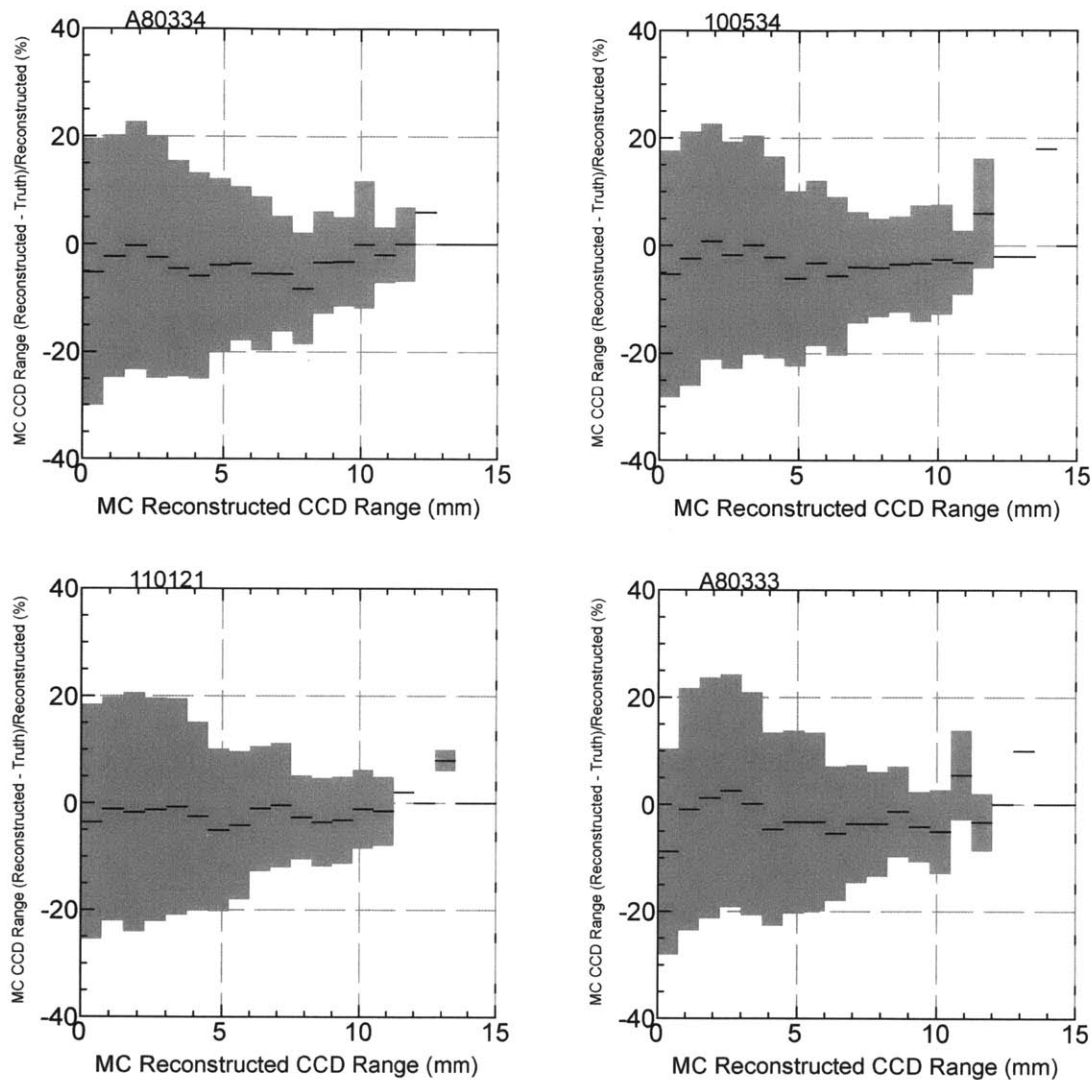


Figure 5-18: Am-Be nuclear recoil Monte Carlo. The residuals between the true projected range of Monte Carlo nuclear recoils and the reconstructed CCD projected range. The gray bars indicate the standard deviation of the residuals in each projected range bin. Each plot is labeled by its corresponding CCD in the upper left.

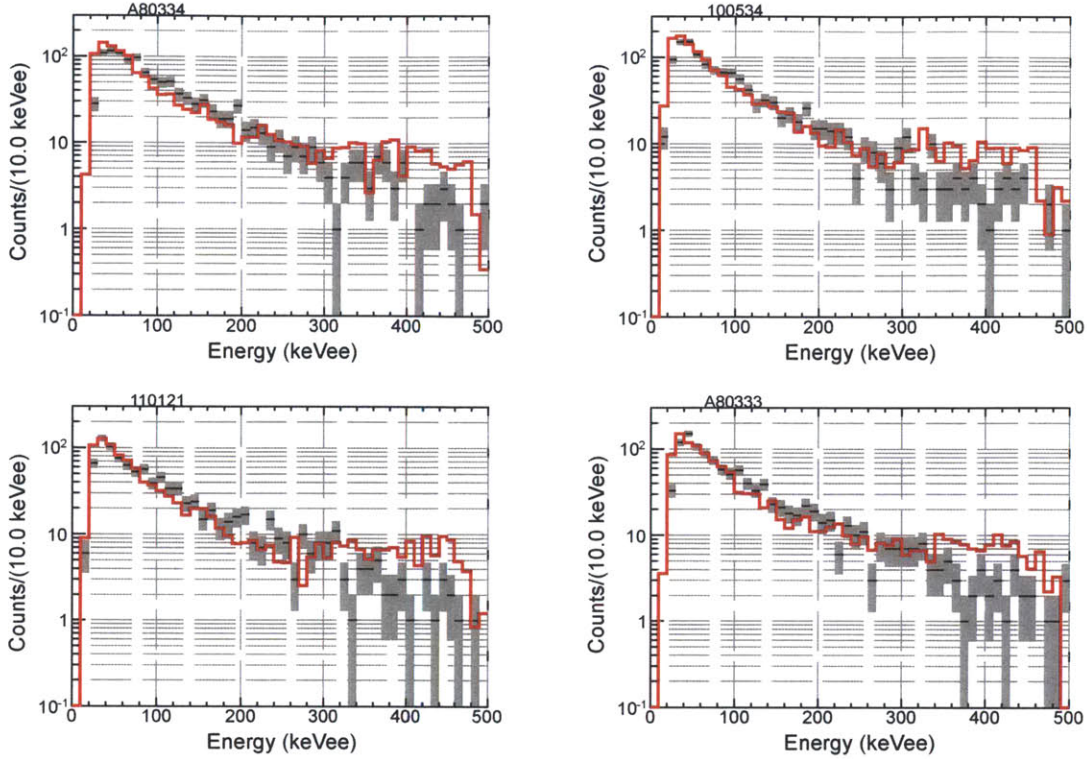


Figure 5-19: Am-Be nuclear recoil candidates, 60 Torr CF_4 , 670V bias on the amplification stage, and -5 kV on the drift stage. Data energy distribution (black and gray) versus Monte Carlo energy distribution (red). The normalization of the Monte Carlo has been adjusted so that the data and Monte Carlo have the same number of events between 0 keV_{ee} and 200 keV_{ee} . Each plot is labeled by its corresponding CCD in the upper left.

recoils with energies below 200 keV_{ee} . Only energies below 500 keV_{ee} are shown in 5-19 because tracks with energies in excess of 471 keV_{ee} fail the charge saturation cut AMBE-XI.3, above, for the central anode electrode. Figure 5-20 compares the Monte Carlo and data energy spectra for the low energies more relevant to a direct dark matter search. Fair agreement is found between the Monte Carlo and data recoil energy spectra, except at the highest recoil energies where the Monte Carlo has an excess of hard recoils relative to the data, and at the lowest recoil energies, near threshold. The Monte Carlo/data agreement near threshold could be improved if the Monte Carlo input CCD $\text{ADU}/\text{keV}_{\text{ee}}$ gain were systematically smaller by approximately 10% across all four 4-shooter CCDs. Unfortunately, smaller $\text{ADU}/\text{keV}_{\text{ee}}$ CCD gains would further increase the observed tension between the CCD and anode energy

determinations.

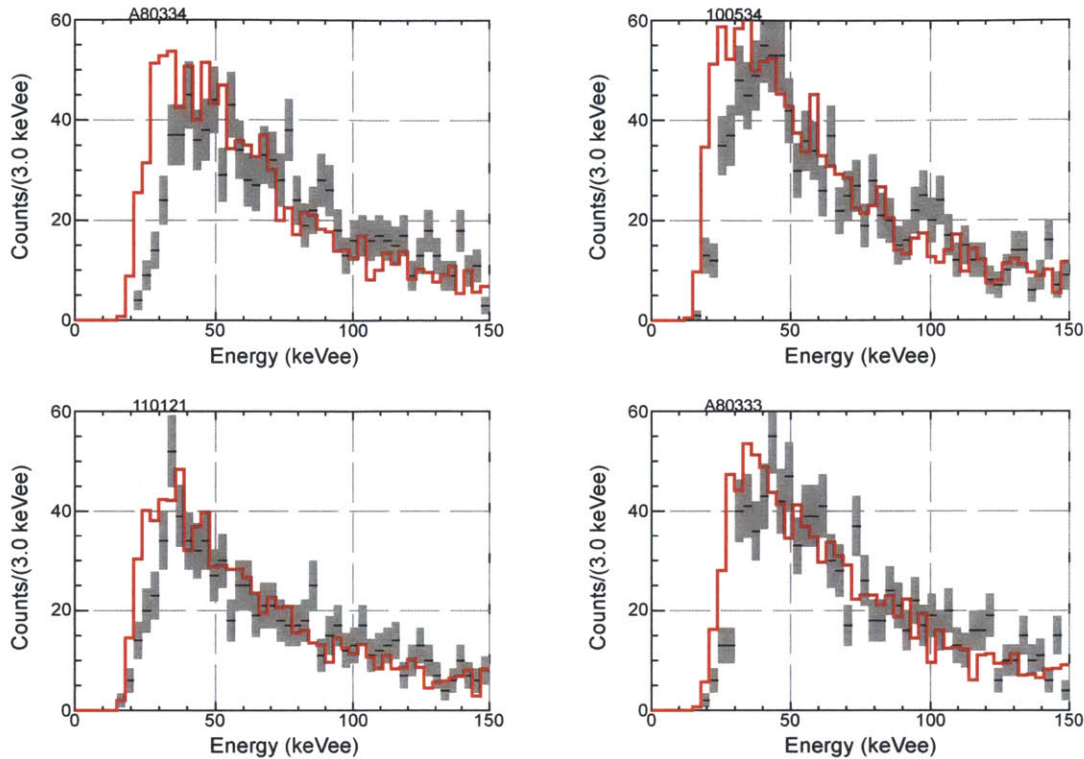


Figure 5-20: Am-Be nuclear recoil candidates, 60 Torr CF_4 , 670V bias on the amplification stage, and -5 kV on the drift stage. Data energy distribution (black and gray) versus Monte Carlo energy distribution (red) for energies less than 150 keV_{ee} . The normalization of the Monte Carlo has been adjusted so that the data and Monte Carlo have the same number of events between 0 keV_{ee} and 200 keV_{ee} . Each plot is labeled by its corresponding CCD in the upper left.

Figure 5-21 shows the inclusive Am-Be projected range spectrum in data versus Monte Carlo, where the projected range is estimated in the data and the Monte Carlo using Equations 5.2 to convert from reconstructed projected range to true recoil projected range in mm. As in the energy comparison, an excess of hard recoils is observed in the Monte Carlo relative to the data.

Figure 5-22 shows the width of Am-Be recoils transverse to their reconstructed directions in the data versus the Monte Carlo. The reconstructed transverse width of recoils in the Monte Carlo is systematically larger in the Monte Carlo versus the data by approximately 10% in all four CCDs.

It is tempting to adjust the CCD Monte Carlo $\text{ADU}/\text{keV}_{ee}$ gains and transverse

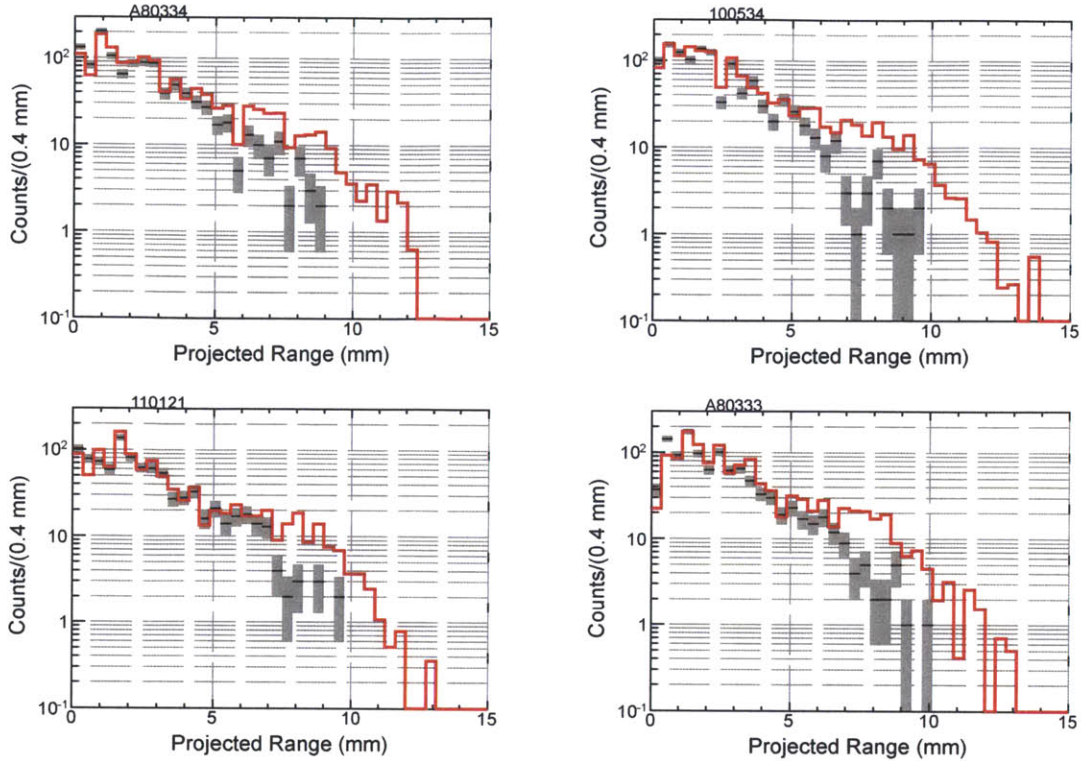


Figure 5-21: Am-Be nuclear recoil candidates, 60 Torr CF_4 , 670V bias on the amplification stage, and -5 kV on the drift stage. Data projected range distribution (black and gray) versus Monte Carlo projected range distribution (red). The normalization of the Monte Carlo has been adjusted so that the data and Monte Carlo have the same number of events between 0 keV_{ee} and 200 keV_{ee} . Each plot is labeled by its corresponding CCD in the upper left.

diffusion parameters as suggested above to obtain better data-Monte Carlo agreement in the energy and transverse width spectra. Lower values are in fact favored by data obtained by other groups [115] for the lateral electron diffusion constants. However, abandoning the independent measurements of these parameters from the ^{241}Am calibrations of Section 4.1.3 runs the risk of over-tuning the Monte Carlo to the Am-Be dataset, especially since the Am-Be energy spectrum employed in the Monte Carlo is little more than an educated guess. In part to address these concerns, work is presently underway to measure the neutron energy spectrum of the Am-Be source used in this study using a ^3He neutron capture detector [110, 151]. It is also operationally useful to see the level agreement achievable with only α -based calibrations, because they require much less time and effort than calibration with a neutron source.

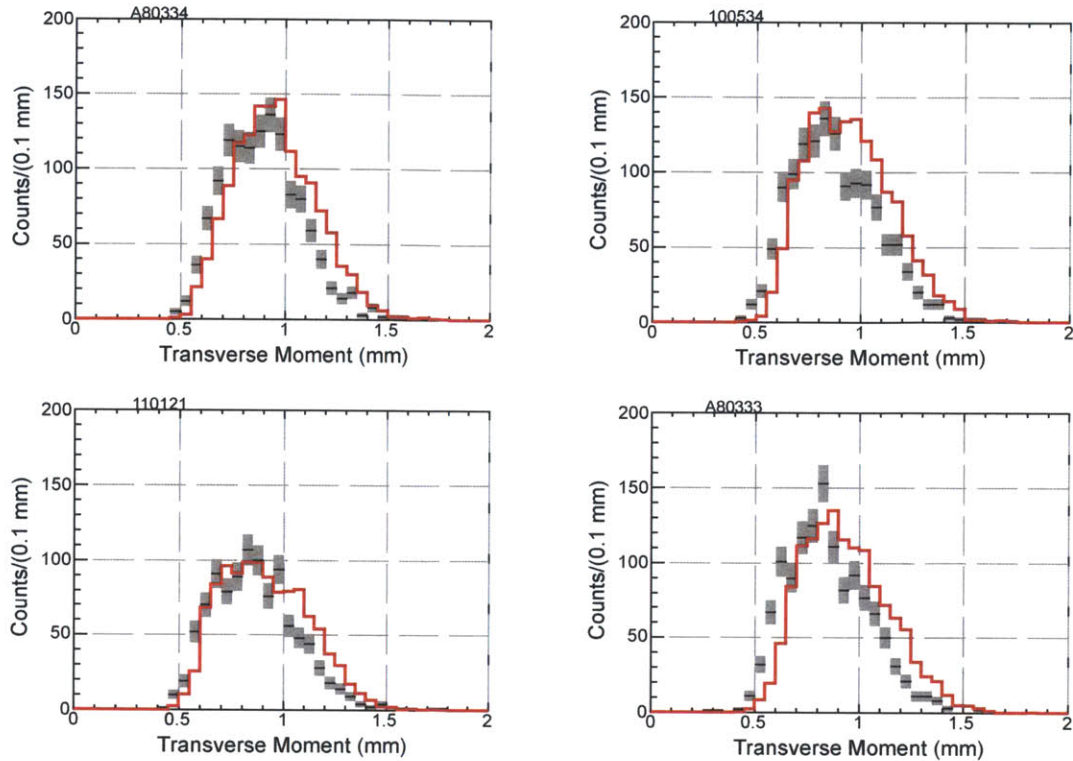


Figure 5-22: Am-Be nuclear recoil candidates, 60 Torr CF_4 , 670V bias on the amplification stage, and -5 kV on the drift stage. Data transverse width distribution (black and gray) versus Monte Carlo transverse width distribution (red). The normalization of the Monte Carlo has been adjusted so that the data and Monte Carlo have the same number of events between 0 keV_{ee} and 200 keV_{ee} . Each plot is labeled by its corresponding CCD in the upper left.

Figure 5-23 shows the data recoil energy versus two-dimensional projected range compared with the SRIM-2006 [58] prediction for the mean energy versus three-dimensional range for ^{19}F and ^{12}C recoils in 60 Torr of CF_4 . For a given energy, the majority of the recoils have projected two-dimensional ranges below the full SRIM-2006 three-dimensional ranges, as expected.

Figure 5-24 shows the recoil reconstructed angle, ϕ , in the plane of the CCD for recoils with energies greater than 250 keV_{ee} and projected ranges greater than 4 mm. Cuts AMBE-IX through AMBE-XIII have not been applied, allowing events with energies much greater than 471 keV_{ee} to contribute. The ϕ spectra for the four cameras peak at $+\pi/2$ rad, $+\pi$ rad, 0 rad, and $-\pi/2$ rad for CCDs A80334, 100534, 110121, and A80333, respectively. These directions in each CCDs' coordinates correspond

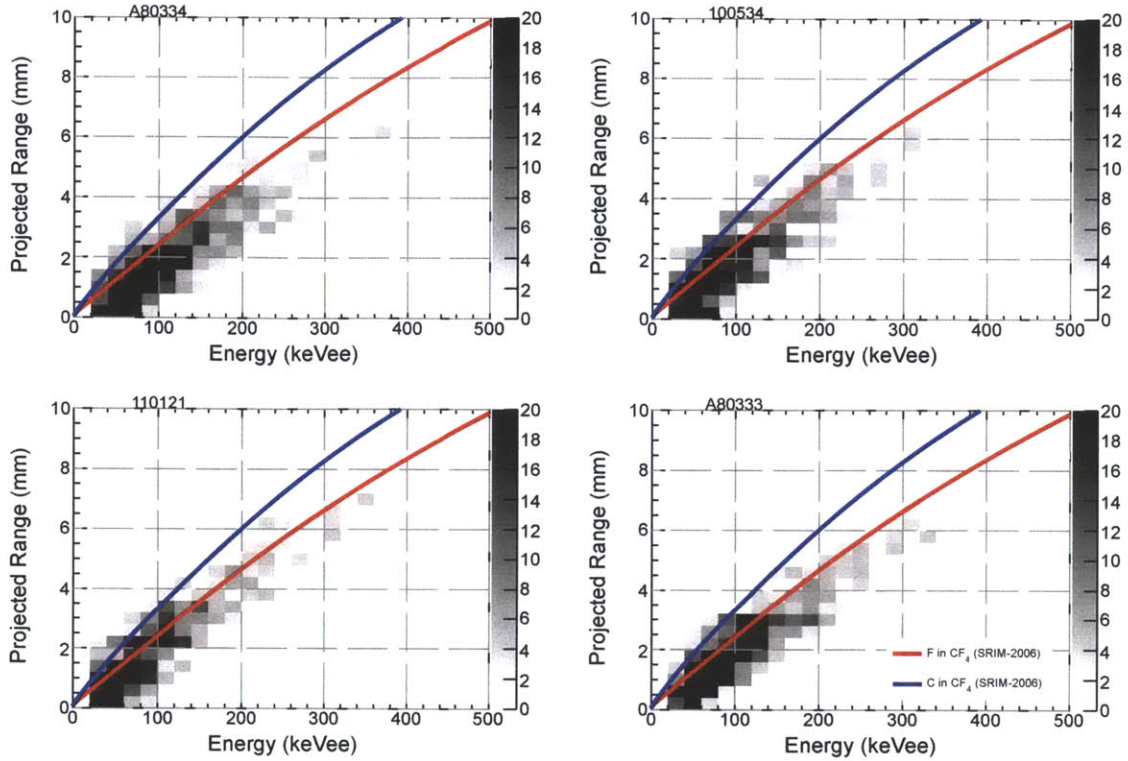


Figure 5-23: Am-Be nuclear recoil candidates, 60 Torr CF_4 , 670V bias on the amplification stage, and -5 kV on the drift stage. Recoil energy versus projected range. Overlaid are SRIM-2006 predictions for the mean full recoil range versus energy for carbon (blue) and fluorine (red) recoils. Each plot is labeled by its corresponding CCD in the upper left.

exactly to the most probable direction expected for the Am-Be neutrons based on the source position relative to the 4-shooter. For this comparison, the Monte Carlo histogram has been scaled to have the same normalization as the data.

Figure 5-25 shows the fraction of recoils whose reconstructed ϕ points away from the Am-Be source position as a function of recoil energy for data and Monte Carlo, in 20 keV_{ee} width bins, from the lowest measured energies up to 400 keV_{ee} . Before reconstruction in the Monte Carlo, less than 10% of nuclear recoils scatter greater than 90° from the mean direction of the Am-Be source beam. After reconstruction, however, 50% of recoils with energies less than 100 keV_{ee} are reconstructed in the data and Monte Carlo to be pointing 90° or more away from the mean direction of the Am-Be source beam. The 4-shooter's predicted and measured sensitivity to the forward backward asymmetry of the Am-Be flux is thus negligible for recoils with

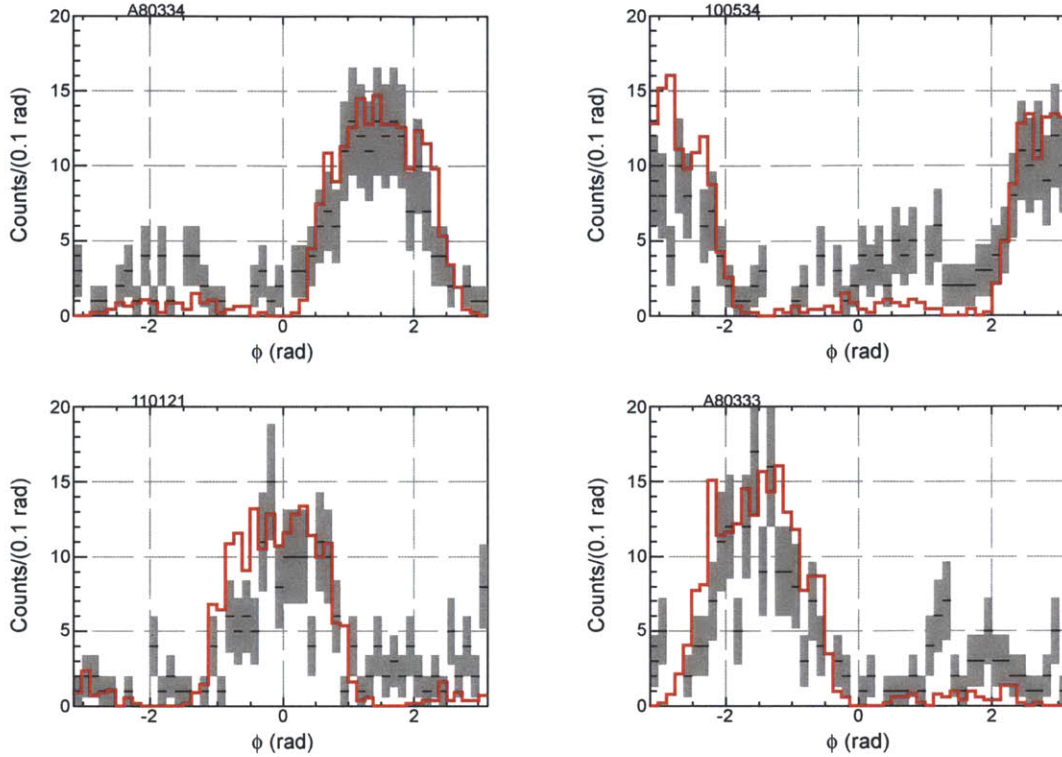


Figure 5-24: Am-Be nuclear recoil candidates, 60 Torr CF_4 , 670V bias on the amplification stage, and -5 kV on the drift stage. The reconstructed ϕ in the readout plane in data versus Monte Carlo, for recoils with energies greater than 250 keV_{ee} and projected ranges greater than 4 mm. Each plot is labeled by its corresponding CCD in the upper left.

energies lower than 100 keV_{ee} (148 keV_r).

Figure 5-26 shows the fraction of recoils whose reconstructed ϕ is within 45° of the Am-Be beam direction in the 4-shooter's read-out plane. Neutron-induced nuclear recoils scatter preferentially along the beam direction as the energy transferred to the nucleus increases, leading to an increase in this fraction with increasing recoil energy. Curiously, although fair agreement is found between the data and Monte Carlo for recoils with energies greater than 150 keV_{ee} , this fraction for CCDs A80333 and A80334 deviates considerably from the Monte Carlo prediction. Figures 5-27 and 5-28 show the reconstructed data and Monte Carlo ϕ spectra for recoils with energies between 0 keV_{ee} and 50 keV_{ee} , and 50 keV_{ee} and 100 keV_{ee} , respectively. The spectrum below 50 keV_{ee} exhibits no obvious ϕ -dependence. For recoils with energies between 50 keV_{ee} and 100 keV_{ee} , the Monte Carlo predicts that the reconstructed recoil

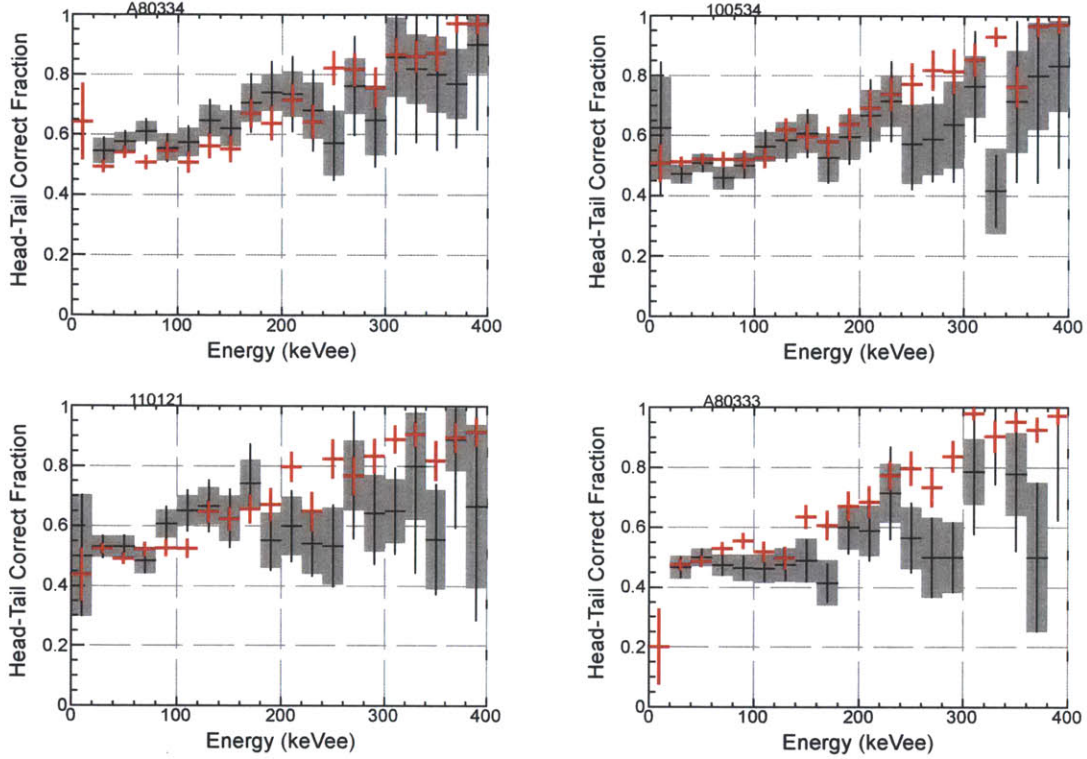


Figure 5-25: Am-Be nuclear recoil candidates, data versus Monte Carlo. 60 Torr CF_4 , 670V bias on the amplification stage, and -5 kV on the drift stage. The fraction of recoil candidates whose reconstructed angle ϕ in the 4-shooter readout plane is within 90° of the mean Am-Be neutron direction in the readout plane as a function of energy. Each plot is labeled by its corresponding CCD in the upper left.

directions prefer the axis *perpendicular* to the Am-Be beam direction. Qualitatively the data actually favors this predicted behavior for CCDs 100534 and 110121 in Figure 5-28, but the preferred axis in CCDs A80334 and A80333 is clearly still the Am-Be beam direction in the data.

In contrast, the ϕ spectra for the four 4-shooter CCDs at higher energies are clearly well correlated with the Am-Be beam direction. Figure 5-27 shows the recoil ϕ spectrum for $0 \text{ keV}_{ee} < E < 50 \text{ keV}_{ee}$ (0 keV_r to 84 keV_r), Figure 5-28 shows the recoil ϕ spectrum for $50 \text{ keV}_{ee} < E < 100 \text{ keV}_{ee}$ (84 keV_r to 148 keV_r), Figure 5-29 for $100 \text{ keV}_{ee} < E < 200 \text{ keV}_{ee}$ (148 keV_r to 263 keV_r), Figure 5-30 for $200 \text{ keV}_{ee} < E < 300 \text{ keV}_{ee}$ (263 keV_r to 367 keV_r), and Figure 5-31 for $300 \text{ keV}_{ee} < E < 400 \text{ keV}_{ee}$ (367 keV_r to 465 keV_r). A systematic bias in the ϕ reconstruction preferring the angles $\phi = \pi/2$ and $\phi = -\pi/2$ for very low energy recoils would provide an easy explanation

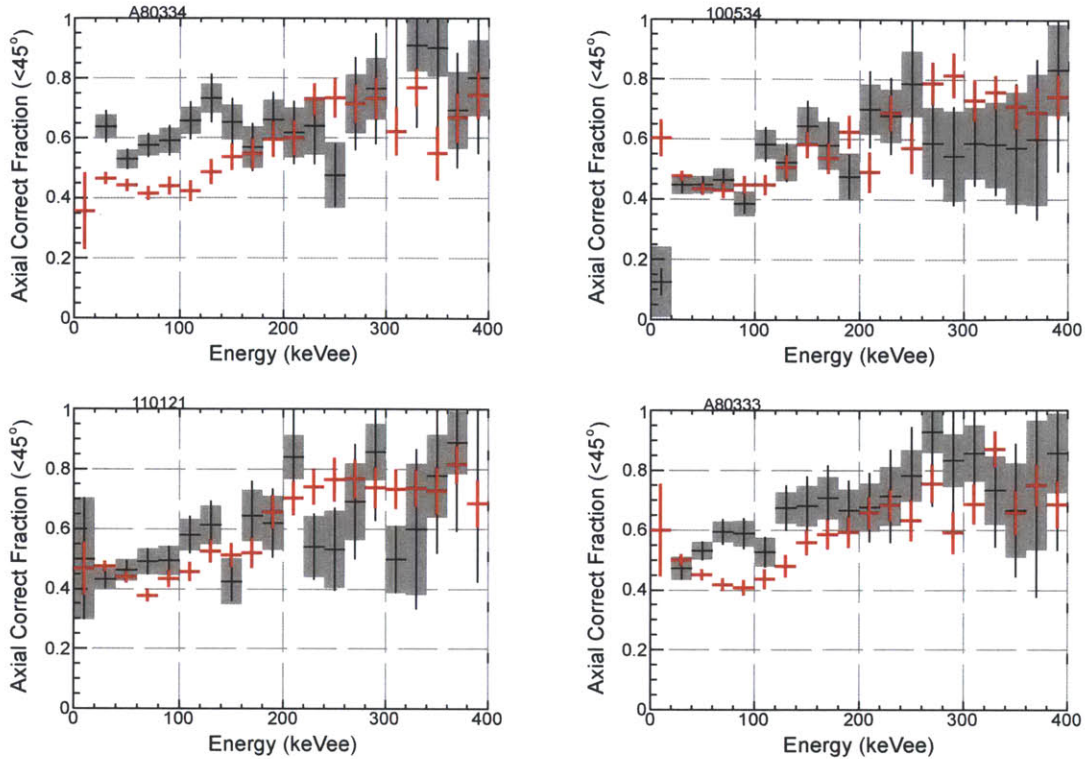


Figure 5-26: Am-Be nuclear recoil candidates, data versus Monte Carlo. 60 Torr CF_4 , 670V bias on the amplification stage, and -5 kV on the drift stage. The fraction of recoil candidates whose reconstructed angle ϕ in the 4-shooter readout plane is within 45° of the mean Am-Be neutron axis in the readout plane. Each plot is labeled by its corresponding CCD in the upper left.

for the data, and inconclusive hints of just such a bias have been observed in previous 4-shooter neutron exposure datasets. However, the Monte Carlo *predicted* $\pi/2$ shift in reconstructed ϕ for low energy recoils muddies the waters. In fact, a $\pi/2$ phase shift can be directly understood from the theory of elastic collisions. As the recoil energy approaches zero, the predicted recoil angle with respect to the neutron beam direction is expected to approach $\pi/2$ [152]. The recoil angle of a 50 keV_r recoil is greater than $\sim 60^\circ$ by the kinematics of elastic collisions for neutrons with kinetic energies in excess of 1 MeV, and the majority of the neutrons emitted by the Am-Be source have energies greater than 1 MeV. Given this theoretical expectation, it is puzzling that in the data only two of the four cameras exhibit a $\pi/2$ shift in the reconstructed ϕ of the recoils as the recoil energy approaches zero. The expected phase shift also calls into question the appropriateness of this method, which compares the number of recoils

with recoil angles greater than and less than 45° from the neutron beam direction, for quantifying the 4-shooter's axial reconstruction ability for low-energy neutron recoils.

The data-Monte Carlo agreement in Figures 5-25 and 5-26 is fair for nuclear recoils with energies in excess of $100 \text{ keV}_{\text{ee}}$, justifying the use of the Monte Carlo in the following chapter to estimate the sensitivity of the 4-shooter to WIMP-induced nuclear recoils and their directions. In fact, the level of agreement achieved is somewhat surprising given 1) the overly simplistic assumptions of the Monte Carlo (see Section 3.4.3), 2) that the neutrons are likely to scatter at least once before entering the field cage,⁷ which is not modeled, and 3) the fact that the model of the Am-Be source and its beam properties (opening angle, energy distribution, etc.) is only an educated guess.

⁷The neutrons can also scatter back into the detector, in the opposite direction as the neutron beam direction.

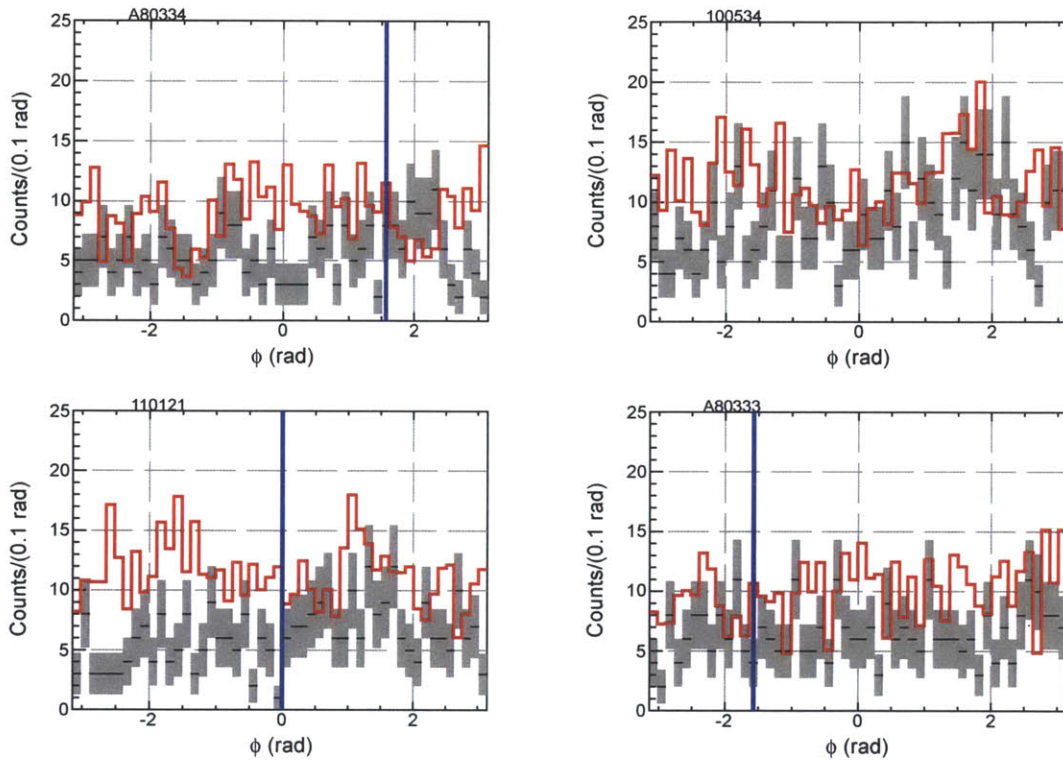


Figure 5-27: Am-Be nuclear recoil candidates, the reconstructed ϕ in the readout plane in data versus Monte Carlo, for recoils with energies between 0 keV_{ee} and 50 keV_{ee} (0 keV_r to 84 keV_r). 60 Torr CF₄, 670V bias on the amplification stage, and -5 kV on the drift stage. The solid blue line shows the expected mean ϕ of the Am-Be neutrons. Each plot is labeled by its corresponding CCD in the upper left.

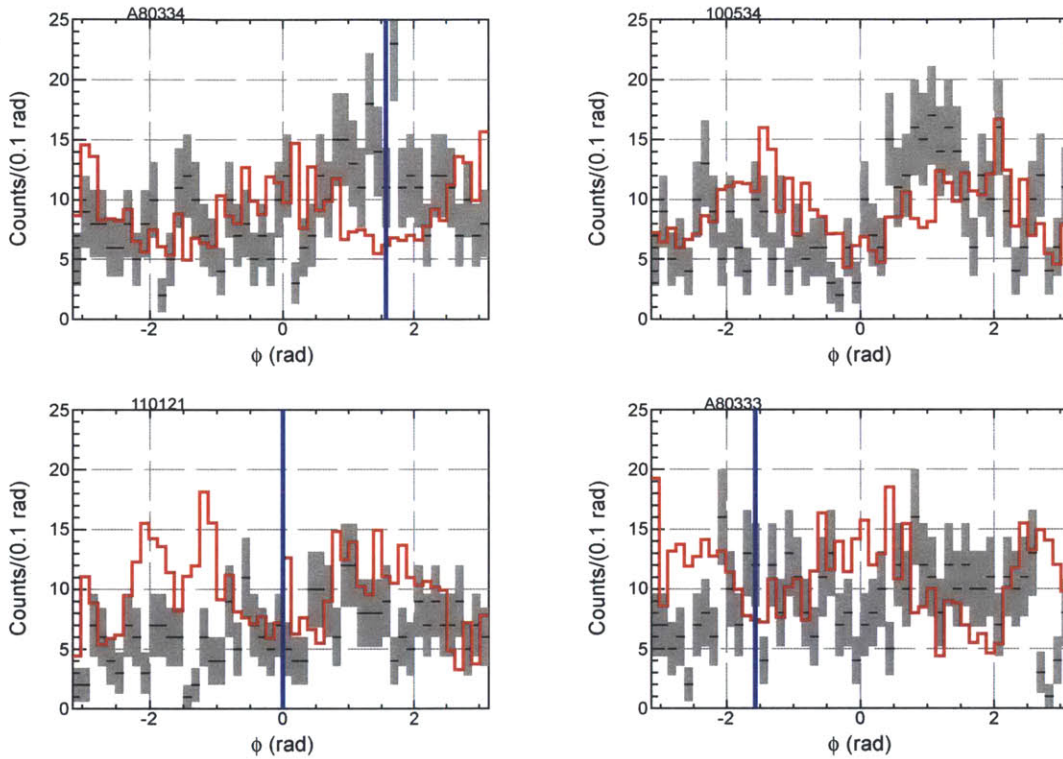


Figure 5-28: Am-Be nuclear recoil candidates, the reconstructed ϕ in the readout plane in data versus Monte Carlo, for recoils with energies between 50 keV_{ee} and 100 keV_{ee} (84 keV_r to 148 keV_r). 60 Torr CF_4 , 670V bias on the amplification stage, and -5 kV on the drift stage. The solid blue line shows the expected mean ϕ of the Am-Be neutrons. Each plot is labeled by its corresponding CCD in the upper left.

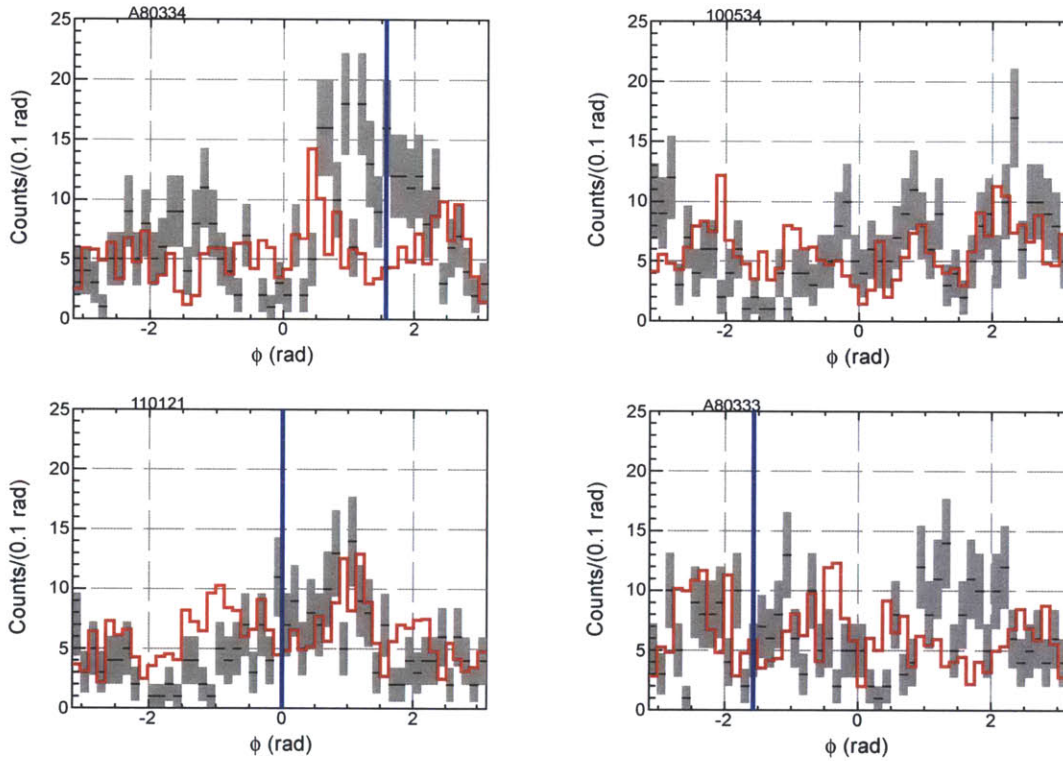


Figure 5-29: Am-Be nuclear recoil candidates, the reconstructed ϕ in the readout plane in data versus Monte Carlo, for recoils with energies between 100 keV_{ee} and 200 keV_{ee} (148 keV_r to 263 keV_r). 60 Torr CF_4 , 670V bias on the amplification stage, and -5 kV on the drift stage. The solid blue line shows the expected mean ϕ of the Am-Be neutrons. Each plot is labeled by its corresponding CCD in the upper left.

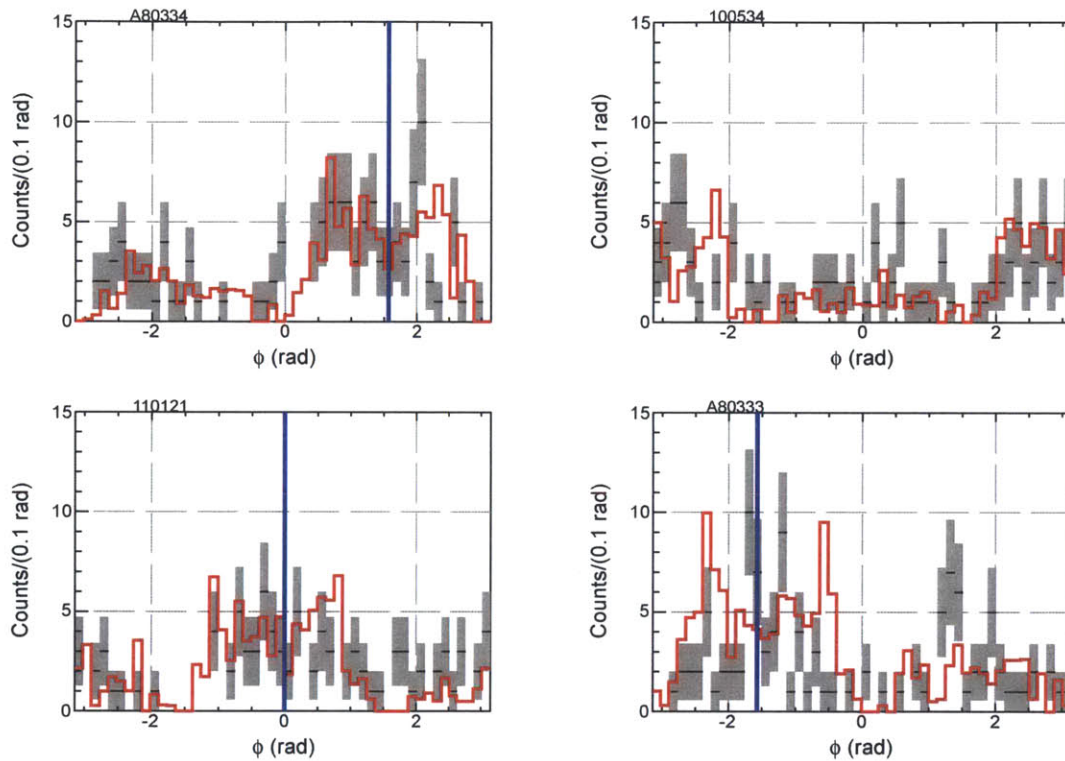


Figure 5-30: Am-Be nuclear recoil candidates, the reconstructed ϕ in the readout plane in data versus Monte Carlo, for recoils with energies between 200 keV_{ee} and 300 keV_{ee} (263 keV_r to 367 keV_r). 60 Torr CF_4 , 670V bias on the amplification stage, and -5 kV on the drift stage. The solid blue line shows the expected mean ϕ of the Am-Be neutrons. Each plot is labeled by its corresponding CCD in the upper left.

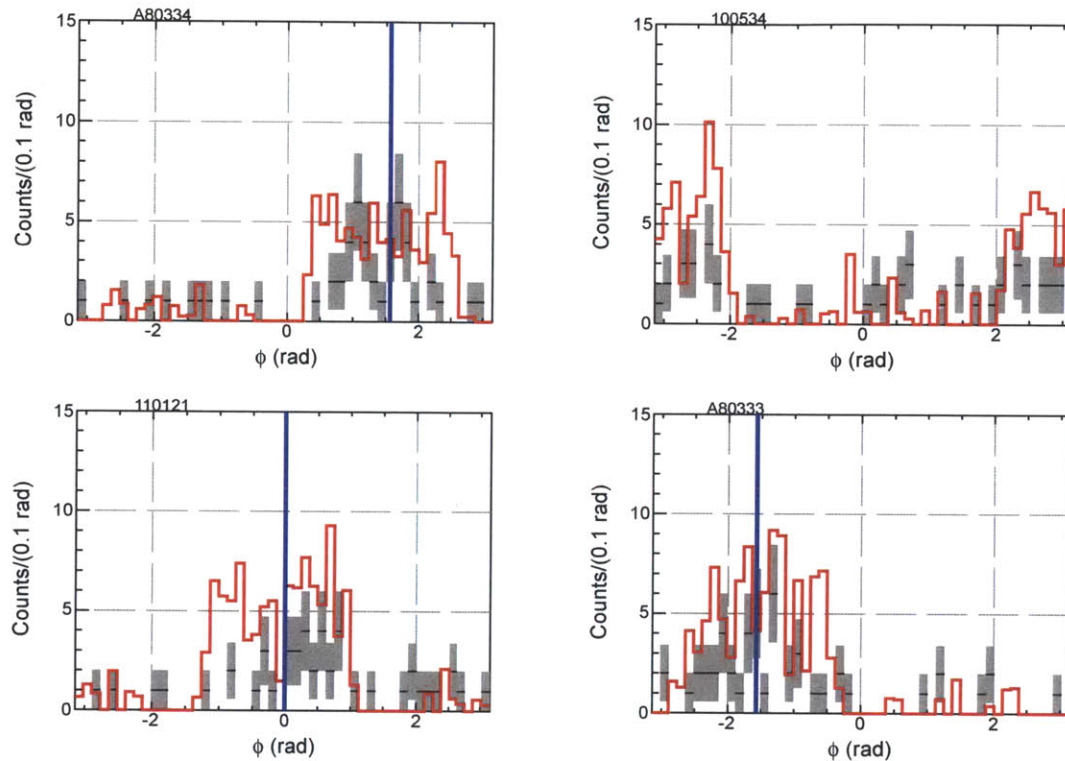


Figure 5-31: Am-Be nuclear recoil candidates, the reconstructed ϕ in the readout plane in data versus Monte Carlo, for recoils with energies between 300 keV_{ee} and 400 keV_{ee} (367 keV_r to 465 keV_r). 60 Torr CF₄, 670V bias on the amplification stage, and -5 kV on the drift stage. The solid blue line shows the expected mean ϕ of the Am-Be neutrons. Each plot is labeled by its corresponding CCD in the upper left.

Chapter 6

Conclusions and outlook

The purpose of this chapter is to predict the 4-shooter’s sensitivity to the direction and rate of WIMP-nucleus scatters. The Monte Carlo developed in Chapters 4 and 5 to model the 4-shooter response is used to predict the response of the 4-shooter to dark matter recoils.

For these studies, WIMP ^{19}F recoils are generated in the Monte Carlo following the procedure laid out in [14] and using the standard astrophysical parameter assumptions in Table 1.1. The spin-dependent WIMP- ^{19}F form factor is taken from Bednyakov *et al.* [153]. The predicted shape of the recoil rate as a function of recoil energy was validated by comparing the generator-level output of the 4-shooter Monte Carlo to the output of the MICROMEGAS¹ code [154], with which nearly perfect agreement is obtained.

6.1 Nuclear recoil detection efficiency

The nuclear recoil detection efficiency as a function of energy is determined by generating isotropic ^{19}F recoils flat in energy, and then taking the ratio, in bins of recoil energy, of the events that pass analysis cuts AMBE-I through AMBE-VII and AMBE-XIII from Section 5.3. The efficiency of cuts AMBE-VIII through AMBE-XII cannot be estimated in this way because the Monte Carlo does not presently simulate the response of the digitizer channels. Although only approximately half of each CCDs’ imaged area is active, for the purposes of this estimate, recoils are generated uniformly

¹MICROMEGAS version 3.0.24.

in position over the entire image for each CCD. The resulting efficiency estimate for each CCD is then divided by the fraction of pixels out of the total 1024×1024 that are not cut by fiducialization cuts AMBE-III through AMBE-V. This fraction is $(49.5 \pm 0.2)\%$, $(47.4 \pm 0.2)\%$, $(48.1 \pm 0.2)\%$, and $(49.0 \pm 0.2)\%$ for CCDs A80334, 100534, 110121, and A80333, respectively. Figure 6-1 shows the resulting, scaled, recoil detection efficiency as a function of recoil energy. The efficiency does not peak at 100% because a sizeable fraction of recoils with centroids outside of the fiducial cut regions are still cut, especially for high recoil energies, because they contain a pixel inside a fiducial cut region. Also shown are error function fits to the efficiency versus recoil energy, where the error functions have been constrained to asymptote to zero at low recoil energies. The results of these fits for each camera are as follows:

$$\begin{aligned}
\epsilon_{A80334}[E(\text{keV}_r)] &= (0.70 \pm 0.02) \times \left(1 + \text{erf} \left(\frac{E - (50 \pm 2 \text{ keV}_r)}{(21 \pm 4 \text{ keV}_r)} \right) \right) \\
\epsilon_{100534}[E(\text{keV}_r)] &= (0.70 \pm 0.02) \times \left(1 + \text{erf} \left(\frac{E - (41 \pm 2 \text{ keV}_r)}{(15 \pm 2 \text{ keV}_r)} \right) \right) \\
\epsilon_{110121}[E(\text{keV}_r)] &= (0.69 \pm 0.02) \times \left(1 + \text{erf} \left(\frac{E - (43 \pm 1 \text{ keV}_r)}{(12 \pm 2 \text{ keV}_r)} \right) \right) \\
\epsilon_{A80333}[E(\text{keV}_r)] &= (0.68 \pm 0.02) \times \left(1 + \text{erf} \left(\frac{E - (47 \pm 2 \text{ keV}_r)}{(15 \pm 2 \text{ keV}_r)} \right) \right)
\end{aligned} \tag{6.1}$$

To lowest order, because the charge based analysis cuts have a much lower energy threshold than the CCD analysis cuts, their effect on the efficiency is expected to be a flat, recoil energy independent factor. However, this heuristic argument may well break down for cuts like AMBE-XI, which cuts on details of the shape of the pulses on the amplification stage mesh electrode. If charge cuts AMBE-VIII through AMBE-XII are recoil energy independent, their main contribution to the efficiency should be due to the difference in the CCD and digitizer live-times. Because the CCD images are taken with the CCD shutters open, the total live-time of the CCDs is approximately equal to the total time over which data is being taken.² By contrast, the total

²Not including the time required to take dark frames and neglecting the time required to readout the CCDs during which time the CCDs are only partially exposing.

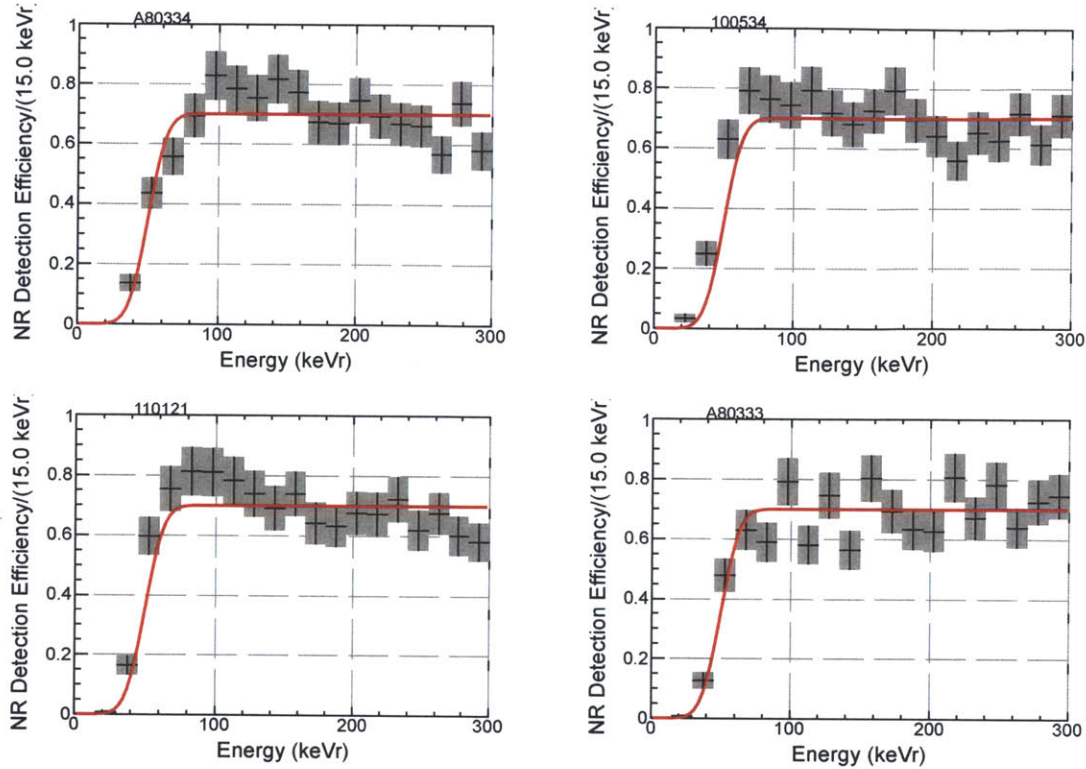


Figure 6-1: Isotropic Monte Carlo ^{19}F recoils, assuming 60 Torr CF_4 , 670V bias on the amplification stage, and -5 kV on the drift stage. The nuclear recoil detection efficiency for CCD cuts only versus keV_r expected for isotropic fluorine recoils. The solid red line shows the error function fits used to estimate the nuclear recoil detection efficiency as a function of recoil energy as described in Section 6.1. The results of these fits are given in Equation 6.1. Each plot is labeled by its corresponding CCD in the upper left.

exposure of the digitizer channels is always the exposure time requested multiplied by the number of exposures, by fiat. The ratio of the total exposure time requested to the total time over which data was taken for the Am-Be runs in Chapter 5 was $(64 \pm 1)\%$ for the high threshold runs 06999-07078 and 07548-07653, and $(63 \pm 1)\%$ for low threshold runs 07654-07933 (see Table 5.2).

If the charge cuts are eliminated, the dominant background by far are CCD artifacts which are present even when exposures are taken with the TPC voltages off (see Figure 5-12) In previous analyses [70], more restrictive cuts on the Fisher discriminant of cut AMBE-XIII were used to eliminate this background in the absence of charge information. Figure 6-2 shows the ratio of the energy spectra in the Am-Be dataset

with and without charge cuts AMBE-VIII through AMBE-XII, with a much harder cut on the Fisher discriminant for each CCD than cut AMBE-XIII. In Figure 6-2 the Fisher discriminant is required to be greater than 0.5 for CCDs A80334 and A80333, and greater than 0.4 for CCDs 100534 and 110121. These values were chosen because they eliminate every CCD artifact in the training data samples. The mean and RMS of these ratios across all energy bins are $(65 \pm 2)\%$, $(67 \pm 5)\%$, $(58 \pm 2)\%$, and $(65 \pm 6)\%$ for CCDs A80334, 100534, 110121, and A80333, consistent with the estimated live-time mismatch between the digitizer and CCD. Figure 6-2 provides weak evidence that the charge based cuts are independent of recoil energy, except possibly in the lowest energy bin for each CCD, although the behavior of this bin may be strongly affected by its proximity to the energy threshold of the CCD-based analysis cuts.

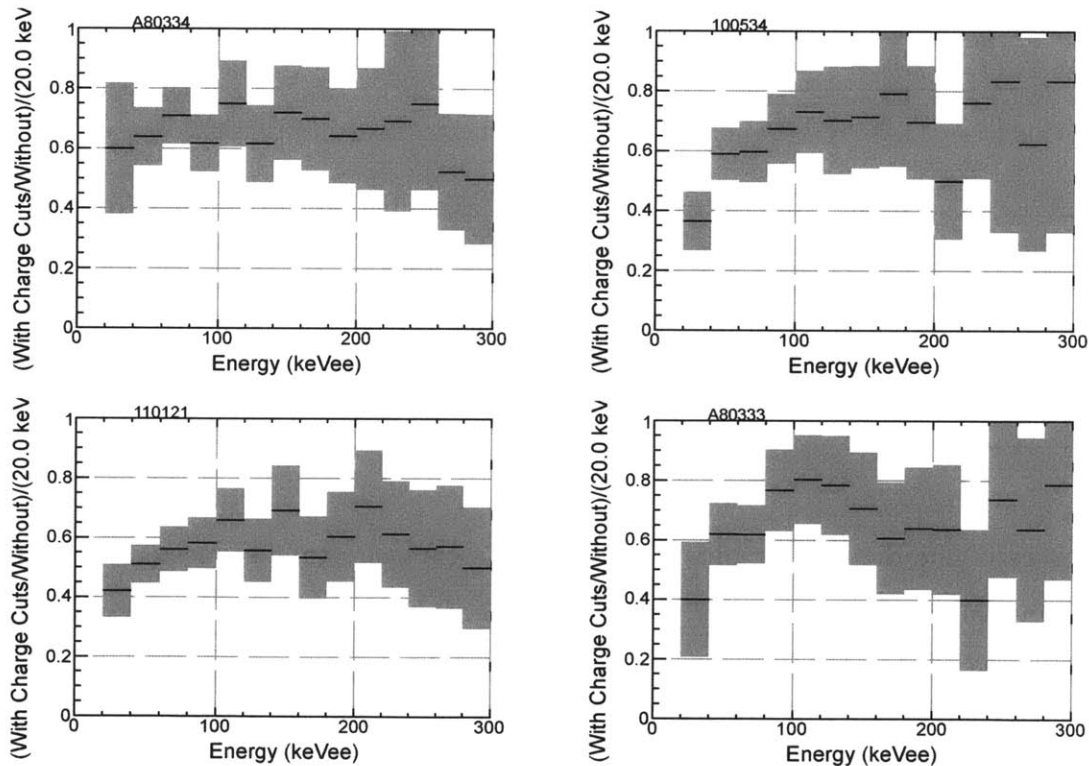


Figure 6-2: Am-Be nuclear recoil candidates, 60 Torr CF_4 , 670V bias on the amplification stage, and -5 kV on the drift stage. The ratio of the energy spectra with and without charge cuts AMBE-VIII through AMBE-XII, and with a very restrictive cut on the Fisher discriminant. Each plot is labeled by its corresponding CCD in the upper left.

Assuming perfect overlap between the CCD and digitizer live-times (*i.e.*, when

the CCD is exposing the digitizer is also exposing), the efficiency of the charge cuts is unity if the live-time is taken to be the requested exposure time. If the live-time is defined as the total data-taking time, the nuclear recoil efficiency must be degraded by the average ratios above to account for the charge cuts.

If the full CCD image were active, the total mass of ^{19}F viewed by each camera would be 1.797 grams in 60 Torr CF_4 . The proper active ^{19}F masses to use with the efficiency curves in Figure 6-1, however, are 0.891 grams, 0.857 grams, 0.873 grams, and 0.887 grams, for cameras A80334, 100534, 110121, and A80333, due to the geometric scaling factors applied to each CCD's efficiency to partially account for the fiducialization cuts as described above. These active masses and efficiencies are used in the WIMP sensitivity calculations below.

6.2 Sensitivity to the WIMP-induced nuclear recoil direction

In order to estimate the expected sensitivity of the 4-shooter to the direction of WIMP-induced nuclear recoils as a function of nuclear recoil energy and WIMP mass, large numbers of WIMP interactions were simulated with the Monte Carlo. For these studies, the WIMP wind's mean direction (opposite the solar motion) was fixed in the plane of the TPC and parallel to the serial register of the CCDs, in the $\phi = -\pi/2$ direction in each CCD's image coordinate system. Because the laboratory and CCD image coordinate systems are not identical, this means the WIMP wind is approximately aligned with the amplification stage spacers for cameras 100534 and 110121 in these studies, and anti-aligned for cameras A80334 and A80333.

^{19}F recoils were generated in large numbers at fixed energies with the correct WIMP-induced angular spectrum, for WIMPs with masses $100 \text{ GeV}/c^2$, $1,000 \text{ GeV}/c^2$, and $10,000 \text{ GeV}/c^2$. For each recoil energy sampled and WIMP mass, Figure 5-26 shows the fraction of nuclear recoils whose reconstructed two-dimensional angle ϕ fell within 45° of the direction of the WIMP wind, ϵ_{45° . This is the WIMP analogue of Figure 5-26. Each point in Figure 6-3 represents at least 2,000 simulated recoils. For recoils with energies in excess of 50 keV_r , Figure 6-3 exhibits a preference for the

reconstructed recoil ϕ to be within 45° of the axis parallel to the WIMP wind. Also shown in Figure 6-3 are error function fits to this “axial correct” fraction as a function of recoil energy, which are used below to estimate the 4-shooter’s sensitivity to the axial direction of the WIMP-wind. No points are shown for recoils with energies in excess of 170 keV_r , 225 keV_r , and 230 keV_r for WIMPs with masses $100 \text{ GeV}/c^2$, $1,000 \text{ GeV}/c^2$, and $10,000 \text{ GeV}/c^2$, because less than 0.001% of the total recoil rate occurs above these energies for each of these WIMP masses.

For all masses considered here, the 4-shooter’s axial sensitivity is negligible for recoil energies below 50 keV_r . Recoils with energies in excess of 50 keV_r make up only approximately 13%, 22%, and 23% of the total recoil rate for a $100 \text{ GeV}/c^2$, $1,000 \text{ GeV}/c^2$, and $10,000 \text{ GeV}/c^2$ WIMP, respectively. By contrast, $< 5 \times 10^{-6}\%$ of recoils have energies in excess of 50 keV_r for a $10 \text{ GeV}/c^2$ mass WIMP. It is clear that determining the axis of the WIMP wind to within 45° with the 4-shooter would only be feasible if the WIMP has a mass $\gtrsim 100 \text{ GeV}/c^2$.

Using the same simulated recoils, Figure 6-4 shows the fraction of nuclear recoils whose reconstructed two-dimensional angle ϕ is within 90° of the vector direction of the WIMP wind, ϵ_F (*i.e.* the fraction of recoils pointing into the same hemisphere as the WIMP-wind in the detector plane). This is the WIMP analogue of Figure 5-25. 50 keV_r recoils scatter into the same half of the read-out plane as the WIMP-wind points approximately 98%, 95%, and 95% of the time for a $100 \text{ GeV}/c^2$, $1,000 \text{ GeV}/c^2$, and $10,000 \text{ GeV}/c^2$ WIMP, respectively. The fact that the fraction of 50 keV_r recoils reconstructed to be pointing into the same hemisphere as the WIMP-wind is 50% indicates that the 4-shooter is no better at determining the sense of 50 keV_r recoils than random guessing.³ The Monte Carlo predicts the 4-shooter is blind to the forward/backward WIMP-recoil asymmetry for recoil energies less than 100 keV_r , and that the 4-shooter’s sensitivity to the asymmetry, even at recoil energies as high as 200 keV_r , will be very weak. Following the above discussion, Figure 6-4 indicates that a detection of a WIMP-induced forward/backward recoil asymmetry could only

³Care should be taken, however, in interpreting Figure 6-4 as purely the probability as a function of recoil energy that the sense of a recoil can be correctly determined, as the reconstructed recoil axis is an input to the sense reconstruction.

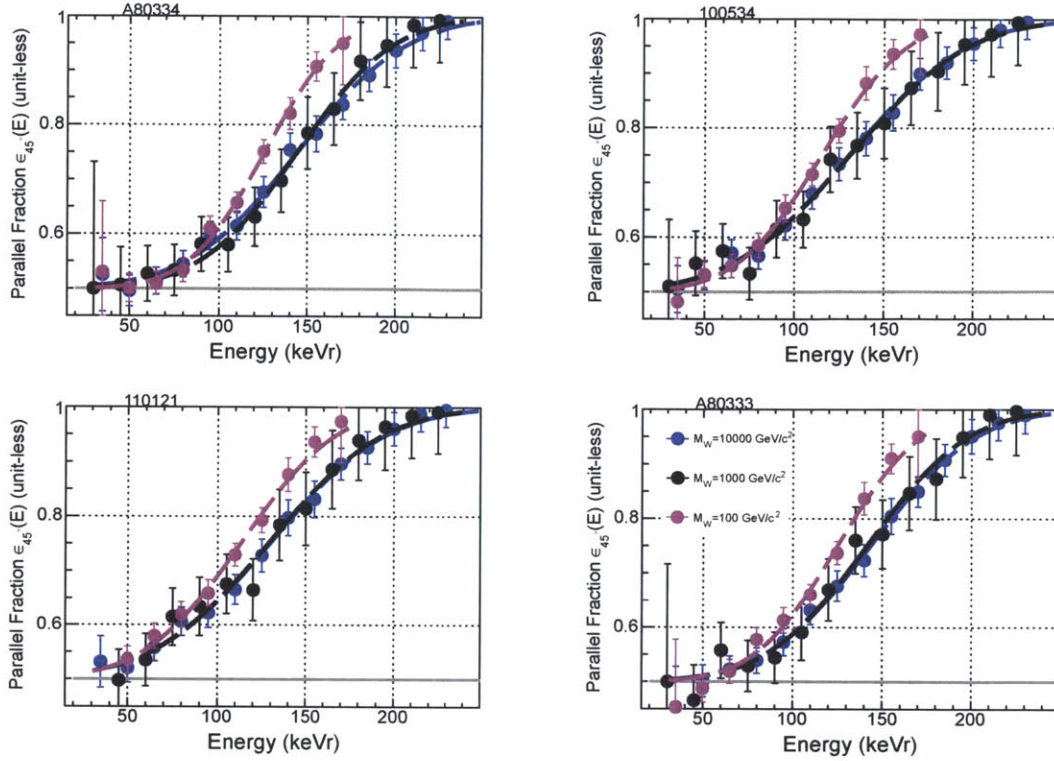


Figure 6-3: For a sample of fixed recoil energies, the probability that the WIMP recoil is reconstructed within 45° of the WIMP wind axis, for each 4-shooter CCD, as a function of recoil energy for a $100 \text{ GeV}/c^2$, $1,000 \text{ GeV}/c^2$, and $10,000 \text{ GeV}/c^2$ mass WIMP. The dashed lines show the error function fits used to estimate the reconstructed nuclear recoil axial asymmetry as a function of recoil energy. Each plot is labeled by its corresponding CCD in the upper left.

be feasible for WIMP masses far in excess of $100 \text{ GeV}/c^2$, in order to observe recoils with energies high enough that their sense could be determined. Unfortunately, even for very high mass WIMPs, the 4-shooter's sensitivity to a forward/backward asymmetry is predicted to be very modest, because the essentially 100% generator level asymmetry at the highest recoil energies in Figure 6-4 is only reconstructed by the 4-shooter as a 10%-20% effect.

6.3 Sensitivity to the WIMP-matter interaction cross-section

During the Am-Be runs in Chapter 5, the average number of 1 second exposures that could be reliably obtained with each camera per day was 46,875, or 0.542 days

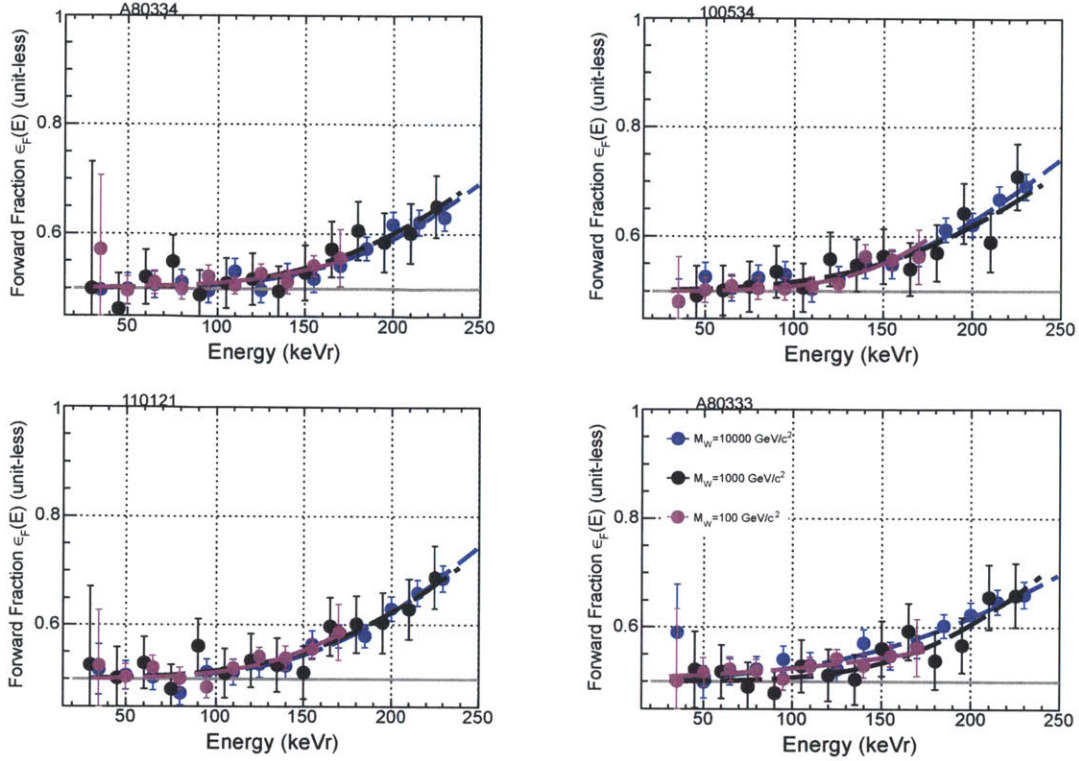


Figure 6-4: For a sample of fixed recoil energies, the probability that the WIMP recoil is reconstructed pointing in the same hemisphere as the WIMP wind direction, for each 4-shooter CCD, as a function of recoil energy for a 100 GeV/c², 1,000 GeV/c², and 10,000 GeV/c² mass WIMP. The dashed lines show the error function fits used to estimate the reconstructed nuclear recoil forward/backward asymmetry as a function of recoil energy. Each plot is labeled by its corresponding CCD in the upper left.

of exposure per day. If a year of data could be achieved under these conditions, it would correspond to a ¹⁹F exposure of 0.177 kg days, 0.170 kg days, 0.173 kg days, and 0.176 kg days in cameras A80334, 100534, 110121, and A80333 with the recoil detection efficiencies given in Figure 6-1⁴. If no nuclear recoil candidates were observed over the course of this exposure, it would lead to a 90% C.L. limit of 13.0 recoils/kg/day, 13.5 recoils/kg/day, 13.3 recoils/kg/day, and 13.1 recoils/kg/day for the detected WIMP-¹⁹F scattering rate in cameras A80334, 100534, 110121, and A80333 [6]. These limits on the detected recoil rate can be converted into a limit on the

⁴These livetimes are optimistic, because they do not include deadtime due to discharges. On the other hand, the spark rate in the Am-Be study discussed in Chapter 5 was systematically higher than the rate that should exist during source free operation, due to the presence of the Am-Be source. Pessimistically assuming that the discharge rate is the same as that encountered in the Am-Be dataset would reduce the expected total livetime for each camera by $\sim 20\%$.

WIMP- ^{19}F interaction cross-section $\sigma_{\chi F}^{SD}$ by dividing the limits by the expected detectable WIMP- ^{19}F scattering rate per picobarn. The expected detectable WIMP- ^{19}F scattering rate assuming $\sigma_{\chi F}^{SD} = 1$ picobarn is computed here by integrating the recoil rate predicted by the MICROMEAS code against the 4-shooter nuclear recoil efficiency for each camera, Equation 6.1. Figure 6-5 shows the resulting predicted recoil rate per kg per day per picobarn as a function of assumed WIMP mass. The predicted detected rate is very similar across the four 4-shooter cameras.

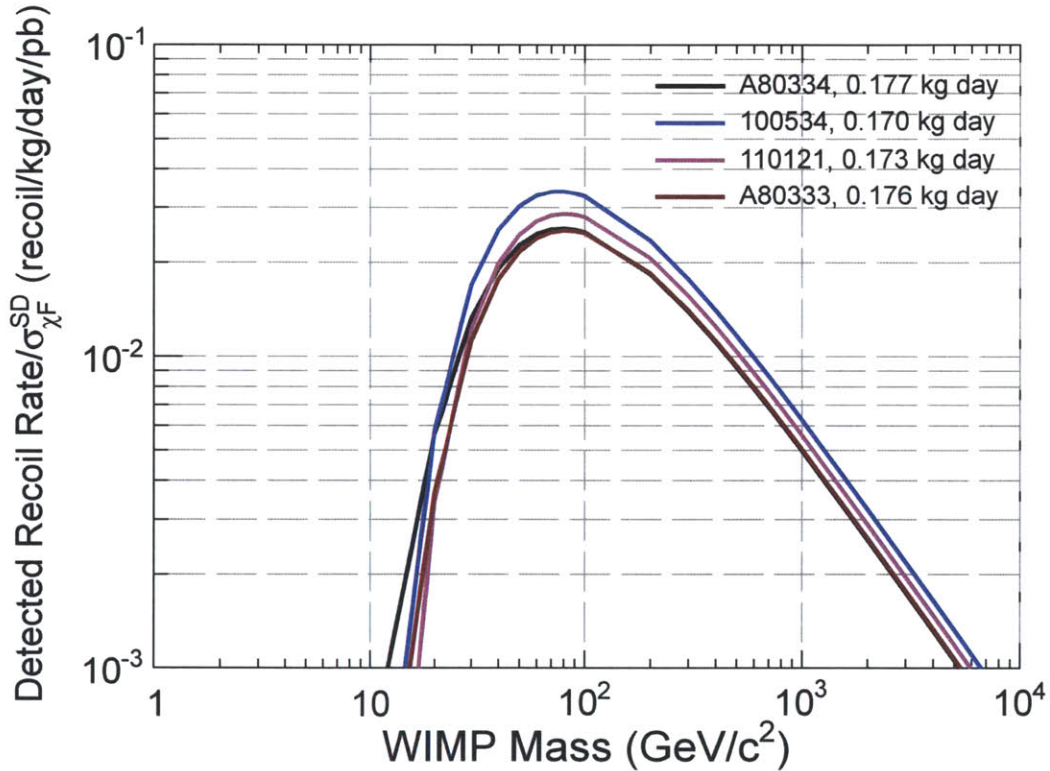


Figure 6-5: The predicted detected WIMP- ^{19}F recoil rate per kilogram per day in the 4-shooter assuming a 1 picobarn WIMP- ^{19}F spin-dependent interaction cross-section $\sigma_{\chi F}^{SD}$ as a function of hypothetical WIMP mass. These curves are generated by integrating the predicted dark matter recoil rate from the MICROMEAS [154] code against the 4-shooter nuclear recoil detection efficiencies for each CCD given in Equation 6.1.

Multiplying these curves by the above livetimes and then inverting them yields the projected limit that could be set with each 4-shooter camera after a year of continuous running, if no backgrounds are encountered. Figure 6-6 shows the 90% C.L. upper limit averaged over cameras 100534, 110121, and A80333, divided by 4 as an estimate

of the combined reach of the four 4-shooter CCDs. A80334 is omitted from the average because of its anomalous non-linear light response (see Section 4.1.3). The limit curve in Figure 6-6 has been scaled so that it is a limit not on $\sigma_{\chi F}^{SD}$ but $\sigma_{\chi p}^{SD}$, the spin-dependent WIMP-proton interaction cross-section. This scaling is performed as described in [18] and is accomplished by multiplying the limit on $\sigma_{\chi F}^{SD}$ at each value of the WIMP mass M_χ by

$$\sigma_{\chi p}^{SD} = \frac{\mu_p^2}{\mu_F^2} \frac{1}{C_F/C_p} \times \sigma_{\chi F}^{SD}, \quad (6.2)$$

where μ_p (μ_F) is the proton-WIMP (^{19}F -WIMP) reduced mass, $M_\chi M_p / (M_\chi + M_p)$ ($M_\chi M_F / (M_\chi + M_F)$) and $C_F/C_p = 0.778$ as given in [18].

Figure 6-6 compares the predicted reach of the 4-shooter with a year live-time to the world's best experimental direct detection limits on the WIMP-proton spin-dependent interaction cross-section. The relatively high energy threshold of the 4-shooter ($\approx 50 \text{ keV}_r$) makes the 4-shooter a poor competitor for WIMP masses below $100 \text{ GeV}/c^2$. Evidently, even for a $100 \text{ GeV}/c^2$ WIMP, which for a fixed WIMP- ^{19}F interaction cross-section yields the largest detectable rate in the 4-shooter, approximately one hundred 4-shooters operating continuously for a year would be required to compete with the limits that have been set by COUPP [17] and SIMPLE [23] on $\sigma_{\chi p}^{SD}$.

6.4 Sensitivity to the WIMP-wind direction

The estimated nuclear recoil energy-dependent fraction of WIMP-induced recoils reconstructed within 45° of the WIMP-wind axis and within 90° of the WIMP-wind vector direction can be used to estimate how many detected nuclear recoils would be required before a preferred axis or vector direction could be eked out of a 4-shooter WIMP recoil dataset. We define the axial and vector nuclear recoil two-dimensional directional asymmetries as follows

$$A_{\text{axial}}^{2D}(E_R, M_\chi) = \left(\frac{N_{<45^\circ} - N_{>45^\circ}}{N_{<45^\circ} + N_{>45^\circ}} \right), \quad A_{\text{vector}}^{2D}(E_R, M_\chi) = \left(\frac{N_F - N_B}{N_F + N_B} \right) \quad (6.3)$$

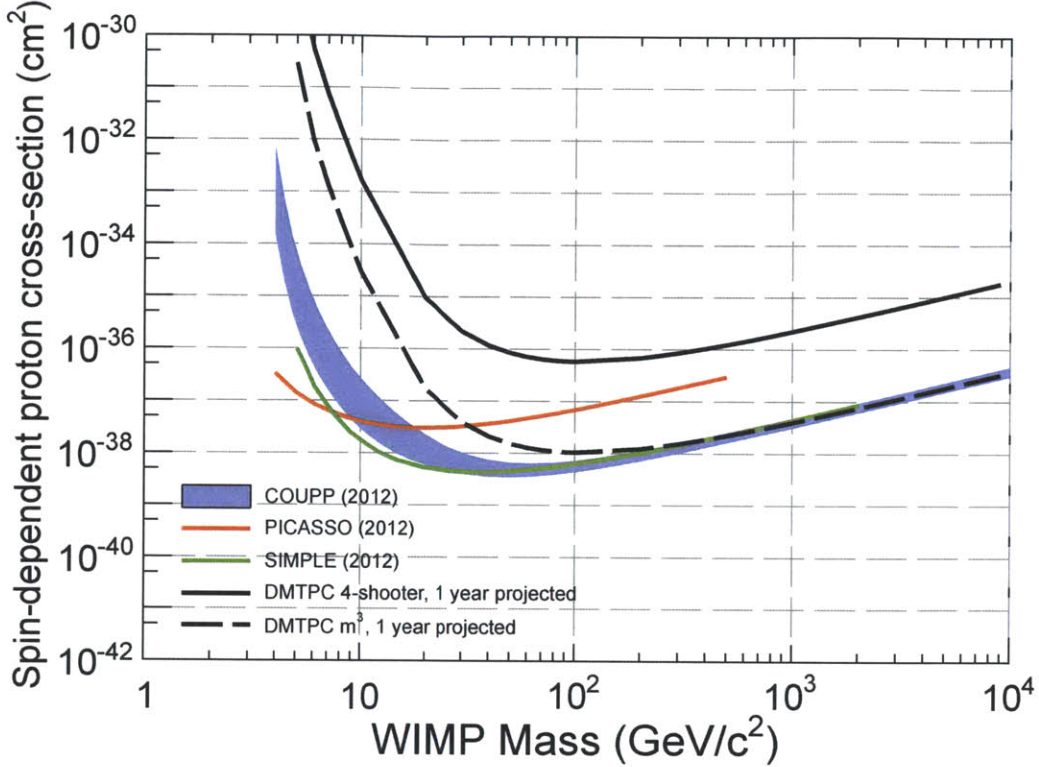


Figure 6-6: The projected background-free sensitivity of the 4-shooter to the WIMP-proton spin-dependent interaction cross-section as a function of WIMP mass assuming a year of continuous operation (solid black line). The dashed black line shows the sensitivity achievable assuming zero backgrounds for a larger m^3 -sized detector if it had the same response to nuclear recoils as the 4-shooter. Also shown are the best limits on $\sigma_{\chi p}^{SD}$ obtained to date by direct detection experiments without directional sensitivity [69], including results from the PICASSO (2012) [24], SIMPLE (2012) [23], and COUPP (2012) [17] experiments.

where $N_{<45^\circ}$ ($N_{>45^\circ}$) is the number of nuclear recoils whose reconstructed angle with the WIMP-wind axis projected into the plane of the 4-shooter is less than (greater than) 45° , and N_F (N_B) is the number of nuclear recoils whose reconstructed angles with the WIMP-wind vector direction projected into the plane of the 4-shooter is less than (greater than) 90° . Note that the dependence of $N_{<45^\circ}$, $N_{>45^\circ}$, N_F and N_B on the nuclear recoil energy E_R and the WIMP mass M_χ has been suppressed in writing Equation 6.3. A_{axial}^{2D} can be computed directly from Figure 6-3 as $A_{\text{axial}}^{2D} = 2\epsilon_{45^\circ} - 1$, while A_{axial}^{2D} can be computed directly from Figure 6-4 as $A_{\text{vector}}^{2D} = 2\epsilon_F - 1$.

The expected total two-dimensional directional asymmetry $\langle A_X^{2D} \rangle$ can be obtained

from A_X^{2D} (with X either axial or vector) by integrating A_X^{2D} against the expected, detected differential WIMP-nuclear recoil rate in nuclear recoil energy E_R for a given WIMP mass M_χ as follows:

$$\langle A_X^{2D} \rangle(M_\chi) = \frac{1}{R_{\text{det}}(M_\chi)} \int_0^\infty \frac{dR_{\text{det}}}{dE_R}(E_R, M_\chi) \times A_X^{2D}(E_R, M_\chi) dE_R \quad (6.4)$$

where R_{det} is the total detected recoil rate and dR_{det}/dE_R is the differential detected recoil rate in recoil energy.

The statistical error $\sigma_{\langle A_X^{2D} \rangle_{\text{det}}}^{\text{stat}}$ on a detected total asymmetry $\langle A_X^{2D} \rangle_{\text{det}}$ is [155, 156]

$$\sigma_{\langle A_X^{2D} \rangle_{\text{det}}}^{\text{stat}} = \sqrt{\frac{(1 - \langle A_X^{2D} \rangle_{\text{det}}^2)}{N_{\text{det}}}} \quad (6.5)$$

where N_{det} is the total number of detected recoils used to compute the total asymmetry. Substituting the expected total asymmetry $\langle A_X^{2D} \rangle$ given by Equation 6.4 into Equation 6.5 for the detected total asymmetry $\langle A_X^{2D} \rangle_{\text{det}}$ enables an estimate to be made of the number of detected nuclear recoils N_{det} required to measure a total asymmetry with a pre-determined statistical error $\sigma_{\langle A_X^{2D} \rangle_{\text{det}}}^{\text{stat}}$. Specifically, the required number of detected events is given by

$$N_{\text{det}} = \frac{(1 - \langle A_X^{2D} \rangle^2)}{\xi^2 \langle A_X^{2D} \rangle^2}, \quad \xi = \left(\frac{\sigma_{\langle A_X^{2D} \rangle_{\text{det}}}^{\text{stat}}}{\langle A_X^{2D} \rangle} \right). \quad (6.6)$$

Figure 6-7 shows N_{det} as a function of assumed WIMP mass for $\xi = 1.00, 0.50,$ and 0.10 . Estimated in this way, the 4-shooter's sensitivity to the axis and vector direction of the WIMP wind is approximately independent of WIMP mass for masses greater than $100 \text{ GeV}/c^2$, and decreases rapidly for lower WIMP masses, as anticipated in Section 6.2. Neglecting systematic errors, and for WIMP masses in excess of $100 \text{ GeV}/c^2$, $\mathcal{O}(100)$ detected recoils would be required to observe the axis of the WIMP-wind axis with the 4-shooter, while $\mathcal{O}(10^4)$ detected recoils would be required to observe the WIMP-wind vector direction with statistical significance.

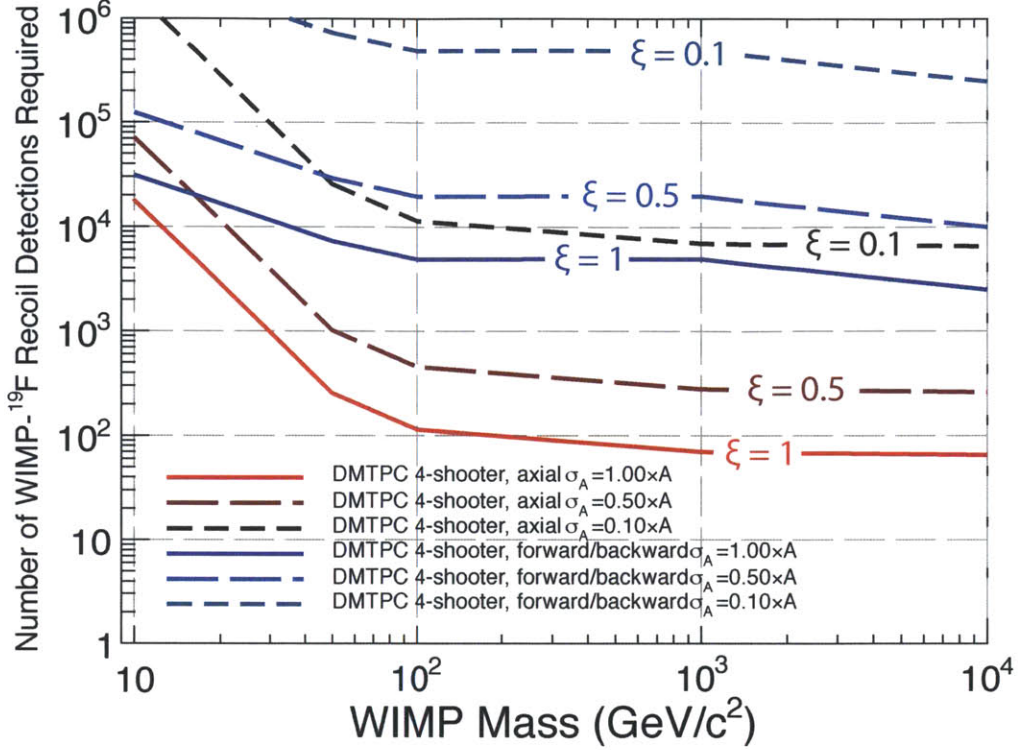


Figure 6-7: Each curve represents the number of detected WIMP-induced nuclear recoils that would be required to observe a statistically significant asymmetry in the two-dimensional recoil direction, at a level of significance ξ where ξ is the ratio of the statistical error on the measured asymmetry to the measured asymmetry value. The cases $\xi = 1, 0.5,$ and 0.1 are considered for both a vector total recoil asymmetry ($\langle A_{\text{vector}}^{2D} \rangle$ in the text) and an axial total recoil asymmetry ($\langle A_{\text{axial}}^{2D} \rangle$ in the text). The energy dependence of the axial and vector recoil asymmetry given by Equation 6.3 was assumed to be the same as that for a $100 \text{ GeV}/c^2$ WIMP for WIMP masses less than $100 \text{ GeV}/c^2$ in making this plot.

6.5 Conclusions

It is clear from the 4-shooter's sensitivity to the predicted rate of WIMP-induced nuclear recoils as estimated in Section 6.3 that the 4-shooter is not a suitable detector with which to discover dark matter, given the limits that have been set by other direct detection groups on σ_{XP}^{SD} . The 4-shooter, however, was never intended to be a discovery instrument, but a platform for prototyping new techniques for a much larger detector. The DMTPC collaboration is presently designing a much larger detector capable of the same sensitivity to WIMP-recoils as the 4-shooter but with

a 1 m^3 *active* volume. If such a detector could be successfully built, it would have the equivalent reach of more than 50 4-shooters combined. An example of the reach of a 1 m^3 detector assuming that the sensitivity scales only with the TPC volume is shown in Figure 6-6. Additional sensitivity could then be obtained by operating an array of 1 m^3 detectors in tandem.

The estimated ability of the 4-shooter to identify the axis or vector direction of the WIMP-wind discussed in Section 6.4 is disappointingly modest. In particular, while the 4-shooter would require in excess of 100 detected recoils to begin to observe the WIMP-wind axis with statistical significance, theoretical estimates of the reach of an ideal directional detector have found that as few 5 events would be required to reject isotropy of the recoil directions at the 90% confidence level with a similar energy threshold as that of the 4-shooter [34].⁵ Luckily, the results presented here are only the first comprehensive assessment of the 4-shooter’s ability to reconstruct the directions of the low energy nuclear recoils of interest to a dark matter search, and there remain many open approaches to improving the detector’s response.

For one, there is no scientific consensus on the best metric to be used in assessing the directional sensitivity of a directional dark matter direct detector like the 4-shooter. One particular approach was pursued in Section 6.4, but many others have been proposed in the literature [157, 158, 32, 159, 33, 160, 161], and one of them may be better suited to the 4-shooter than the method reported here. Another approach is to vary the operating parameters of the 4-shooter to better optimize its directional sensitivity. At present the two most promising lines of attack are thought to be 1) running at lower pressure with higher amplification stage gain and 2) decreasing the diffusion in the drift stage.

The directional sensitivity estimates of this chapter assume the operating parameters of the Am-Be neutron exposure described in Chapter 5. In that study, however, excessive discharging in the amplification stage at low pressures in the 4-shooter limited the operating pressure to no less than 45 Torr CF_4 pressure, as discussed in

⁵This estimate assumes that the ideal detector possesses three-dimensional vector read-out, a 50 keV_r recoil energy threshold, that there are no backgrounds counted, and that the recoils are ^{32}S nuclei.

Section 5.1. Monte Carlo studies, however, have indicated that directional reconstruction is optimized at much lower pressures [147]. Work is presently being undertaken at MIT to construct an amplification stage capable of operating stably at pressures below 45 Torr CF_4 and with a gain high enough to overcome the decreased surface brightness of tracks at lower pressure.

The drift field in the 4-shooter was chosen to minimize the lateral electron diffusion as discussed in Section 4.1.3. Nevertheless, images of tracks interacting in the middle of the TPC or higher are distorted by in excess of 1 mm RMS lateral diffusion. Given that a 40 keV_r ^{19}F ion has a range of approximately 1 mm in 60 Torr CF_4 and that the directional sensitivity of the 4-shooter is predicated on the ability to measure the fine spatial features of tracks, it is likely that the lateral diffusion in the 4-shooter severely limits the 4-shooter's directional sensitivity for low energy recoils. Gains on this front may be achievable by running with a shorter drift stage, although this approach sacrifices precious active volume for only a modest decrease in average lateral diffusion. A more promising approach may involve the use of a different fill gas or fill gas mixture than pure CF_4 , with more suitable electron transport properties. In fact, the DRIFT collaboration has already demonstrated much lower lateral diffusion in a negative ion TPC operated with a CS_2/CF_4 mixture [162].

The 4-shooter has been an invaluable test bed for developing the necessary methods and capabilities for a much larger optical TPC for the direct detection of dark matter currently being built by the DMTPC collaboration at MIT. It is the author's hope that the results presented here will serve as a valuable baseline for the level of directional sensitivity achievable with a detector of this kind, and as a guidepost to promising avenues for improving detector performance.

Chapter 7

Bibliography

- [1] D. Clowe et al. A direct empirical proof of the existence of dark matter. *The Astrophysical Journal Letters*, 648(2):L109, 2006.
- [2] W. Tucker et al. 1E 0657–56: A Contender for the Hottest Known Cluster of Galaxies. *The Astrophysical Journal Letters*, 496(1):L5, 1998.
- [3] Snowmass on the Mississippi a.k.a High Energy Physics Community Summer Study 2013, <http://www.snowmass2013.org>.
- [4] P. A. R. Ade et al. Planck 2013 results. XVI. Cosmological parameters. *ArXiv e-prints*, March 2013.
- [5] G. Bertone, D. Hooper, and J. Silk. Particle dark matter: evidence, candidates and constraints. *Physics Reports*, 405(5-6):279 – 390, 2005.
- [6] J. Beringer et al. Review of particle physics. *Phys. Rev. D*, 86:010001, Jul 2012.
- [7] G. Bertone (editor). Particle dark matter : observations, models and searches. Cambridge University Press, Cambridge, UK, first edition, 2010.
- [8] G. Aad et al. Observation of a new particle in the search for the Standard Model Higgs boson with the ATLAS detector at the LHC. *Physics Letters B*, 716(1):1 – 29, 2012.
- [9] S. Chatrchyan et al. Observation of a new boson at a mass of 125 GeV with the CMS experiment at the LHC. *Physics Letters B*, 716(1):30 – 61, 2012.
- [10] The CMS Collaboration. CMS Physics Technical Design Report, Volume II: Physics Performance. *Journal of Physics G: Nuclear and Particle Physics*, 34(6):995, 2007.
- [11] G. Jungman, M. Kamionkowski, and K. Griest. Supersymmetric dark matter. *Physics Reports*, 267(5-6):195 – 373, 1996.

- [12] J. Ellis, K. A. Olive, and G. Bertone (editor). Particle dark matter : observations, models and searches : Supersymmetric dark matter candidates. chapter 8, pages 142–163. Cambridge University Press, Cambridge, UK, first edition, 2010.
- [13] M. W. Goodman and E. Witten. Detectability of certain dark-matter candidates. *Phys. Rev. D*, 31:3059–3063, Jun 1985.
- [14] J. D. Lewin and P. F. Smith. Review of mathematics, numerical factors, and corrections for dark matter experiments based on elastic nuclear recoil. *Astroparticle Physics*, 6(1):87 – 112, 1996.
- [15] M. Kamionkowski and A. Kinkhabwala. Galactic halo models and particle dark-matter detection. *Phys. Rev. D*, 57:3256–3263, Mar 1998.
- [16] D. G. Cerdeño, A. M. Green, and G. Bertone (editor). Particle dark matter : observations, models and searches : Direct detection of WIMPs. chapter 17, pages 347–390. Cambridge University Press, Cambridge, UK, first edition, 2010.
- [17] E. Behnke et al. First dark matter search results from a 4-kg CF₃I bubble chamber operated in a deep underground site. *Phys. Rev. D*, 86:052001, Sep 2012.
- [18] D. R. Tovey et al. A new model-independent method for extracting spin-dependent cross section limits from dark matter searches. *Physics Letters B*, 488(1):17 – 26, 2000.
- [19] The XENON Dark Matter Project, <http://xenon.astro.columbia.edu/>.
- [20] J. Angle et al. Search for light dark matter in XENON10 data. *Phys. Rev. Lett.*, 107:051301, Jul 2011.
- [21] E. Aprile et al. Dark matter results from 225 live days of XENON100 data. *Phys. Rev. Lett.*, 109:181301, Nov 2012.
- [22] M. Garny et al. On the spin-dependent sensitivity of XENON100. *Phys. Rev. D*, 87:056002, Mar 2013.
- [23] M. Felizardo et al. Final analysis and results of the phase II SIMPLE dark matter search. *Phys. Rev. Lett.*, 108:201302, May 2012.
- [24] S. Archambault et al. Constraints on low-mass WIMP interactions on ¹⁹F from PICASSO. *Physics Letters B*, 711(2):153 – 161, 2012.
- [25] P. C. Divari et al. Shell model calculations for light supersymmetric particle scattering off light nuclei. *Phys. Rev. C*, 61:054612, Apr 2000.
- [26] C. E. Aalseth et al. Results from a search for light-mass dark matter with a *p*-type point contact germanium detector. *Phys. Rev. Lett.*, 106:131301, Mar 2011.

- [27] G. Angloher et al. Results from 730 kg days of the CRESST-II Dark Matter search. *European Physical Journal C*, 72:1971, April 2012.
- [28] A. K. Drukier, K. Freese, and D. N. Spergel. Detecting cold dark-matter candidates. *Phys. Rev. D*, 33:3495–3508, Jun 1986.
- [29] R. Bernabei et al. New results from DAMA/LIBRA. *European Physical Journal C*, 67:39 – 49, May 2010.
- [30] M. Fairbairn and T. Schwetz. Spin-independent elastic WIMP scattering and the DAMA annual modulation signal. *Journal of Cosmology and Astroparticle Physics*, 2009(01):037, 2009.
- [31] D. N. Spergel. Motion of the earth and the detection of weakly interacting massive particles. *Phys. Rev. D*, 37:1353–1355, Mar 1988.
- [32] B. Morgan, A. M. Green, and N. J. C. Spooner. Directional statistics for realistic weakly interacting massive particle direct detection experiments. *Phys. Rev. D*, 71:103507, May 2005.
- [33] J. Billard et al. Directional detection as a strategy to discover galactic dark matter. *Physics Letters B*, 691(3):156 – 162, 2010.
- [34] A. M. Green and B. Morgan. Optimizing WIMP directional detectors. *Astroparticle Physics*, 27(2-3):142 – 149, 2007.
- [35] S. Ahlen et al. The case for a directional dark matter detector and the status of current experimental efforts. *International Journal of Modern Physics A*, 25(01):1 – 51, 2010.
- [36] K. Freese, J. Frieman, and A. Gould. Signal modulation in cold-dark-matter detection. *Phys. Rev. D*, 37:3388–3405, Jun 1988.
- [37] N. J. C. Spooner and G. Bertone (editor). Particle dark matter : observations, models and searches : Directional detectors. chapter 22, pages 437–466. Cambridge University Press, Cambridge, UK, first edition, 2010.
- [38] CYGNUS2013, 4th Workshop on Directional Detection of Dark Matter, 10 June - 12 June 2013, Toyama, Japan, <http://ppwww.phys.sci.kobe-u.ac.jp/~newage/cygnus2013/>.
- [39] A. Drukier et al. New Dark Matter Detectors using DNA for Nanometer Tracking. *ArXiv e-prints*, June 2012.
- [40] D. Nygren. High-pressure Xenon Gas Electroluminescent TPC Concept for Simultaneous Searches for Neutrino-less Double Beta Decay & WIMP Dark Matter. Talk at American Physical Society April Meeting. Denver, Colorado, 2013.

- [41] M. Kimura and T. Naka. Submicron track readout in fine-grained nuclear emulsions using optical microscopy. *Nuclear Instruments and Methods in Physics Research Section A: Accelerators, Spectrometers, Detectors and Associated Equipment*, 680(0):12 – 17, 2012.
- [42] S. R. Bandler et al. Angular distribution of rotons generated by alpha particles in superfluid helium: A possible tool for low energy particle detection. *Phys. Rev. Lett.*, 74:3169–3172, Apr 1995.
- [43] K. N. Buckland et al. Low pressure gaseous detector for particle dark matter. *Phys. Rev. Lett.*, 73:1067–1070, Aug 1994.
- [44] G. Charpak, J.-P. Fabre, F. Sauli, M. Suzuki, and W. Dominik. An optical, proportional, continuously operating avalanche chamber. *Nuclear Instruments and Methods in Physics Research Section A: Accelerators, Spectrometers, Detectors and Associated Equipment*, 258(2):177 – 184, 1987.
- [45] C.J. Martoff et al. Suppressing drift chamber diffusion without magnetic field. *Nuclear Instruments and Methods in Physics Research Section A: Accelerators, Spectrometers, Detectors and Associated Equipment*, 440(2):355 – 359, 2000.
- [46] E. Daw et al. Spin-dependent limits from the DRIFT-II_d directional dark matter detector. *Astroparticle Physics*, 35(7):397 – 401, 2012.
- [47] G. Sciolla et al. DMTPC: a new apparatus for directional detection of Dark Matter. *ArXiv e-prints*, October 2008.
- [48] K. Miuchi et al. First underground results with NEWAGE-0.3a direction-sensitive dark matter detector. *Physics Letters B*, 686(1):11 – 17, 2010.
- [49] J. Billard et al. Directional detection of Dark Matter with MIMAC: WIMP identification and track reconstruction. *Journal of Physics Conference Series*, 309(1):012015, August 2011.
- [50] S. E. Vahsen et al. The Directional Dark Matter Detector (D³). In F. Mayet and D. Santos, editors, *EAS Publications Series*, volume 53 of *EAS Publications Series*, pages 43 – 50, February 2012.
- [51] G. Charpak et al. The use of multiwire proportional counters to select and localize charged particles. *Nuclear Instruments and Methods*, 62(3):262 – 268, 1968.
- [52] A. Takada et al. A very large area micro pixel chamber. *Nuclear Instruments and Methods in Physics Research Section A: Accelerators, Spectrometers, Detectors and Associated Equipment*, 573(1-2):195 – 199, 2007. Proceedings of the 7th International Conference on Position-Sensitive Detectors, PSD-7, 7th International Conference on Position-Sensitive Detectors.

- [53] Y. Giomataris et al. Micromegas: a high-granularity position-sensitive gaseous detector for high particle-flux environments. *Nuclear Instruments and Methods in Physics Research Section A: Accelerators, Spectrometers, Detectors and Associated Equipment*, 376(1):29 – 35, 1996.
- [54] F. Sauli. GEM: A new concept for electron amplification in gas detectors. *Nuclear Instruments and Methods in Physics Research Section A: Accelerators, Spectrometers, Detectors and Associated Equipment*, 386(2-3):531 – 534, 1997.
- [55] G. Aad et al. Atlas pixel detector electronics and sensors. *Journal of Instrumentation*, 3(07):P07007, 2008.
- [56] A. Pansky et al. The scintillation of CF_4 and its relevance to detection science. *Nuclear Instruments and Methods in Physics Research Section A: Accelerators, Spectrometers, Detectors and Associated Equipment*, 354(2-3):262 – 269, 1995.
- [57] A. C. Kaboth et al. A measurement of photon production in electron avalanches in CF_4 . *Nuclear Instruments and Methods in Physics Research Section A: Accelerators, Spectrometers, Detectors and Associated Equipment*, 592(1-2):63 – 72, 2008.
- [58] J. F. Ziegler. SRIM-2003. *Nuclear Instruments and Methods in Physics Research Section B: Beam Interactions with Materials and Atoms*, 219-220(0):1027 – 1036, 2004. Proceedings of the Sixteenth International Conference on Ion Beam Analysis.
- [59] S. Burgos et al. First measurement of the head-tail directional nuclear recoil signature at energies relevant to WIMP dark matter searches. *Astroparticle Physics*, 31(4):261 – 266, 2009.
- [60] D. Dujmic et al. Observation of the “head-tail” effect in nuclear recoils of low-energy neutrons. *Nuclear Instruments and Methods in Physics Research Section A: Accelerators, Spectrometers, Detectors and Associated Equipment*, 584(2-3):327 – 333, 2008.
- [61] K. Nakamura et al. NEWAGE. *Journal of Physics Conference Series*, 375(1):012013, July 2012.
- [62] J. Billard, F. Mayet, and D. Santos. Three-dimensional track reconstruction for directional dark matter detection. *Journal of Cosmology and Astroparticle Physics*, 2012(04):006, 2012.
- [63] A. M. Green and B. Morgan. Consequences of statistical sense determination for WIMP directional detection. *Phys. Rev. D*, 77:027303, Jan 2008.
- [64] K. Miuchi et al. Direction-sensitive dark matter search results in a surface laboratory. *Physics Letters B*, 654(3-4):58 – 64, 2007.

- [65] S. Ahlen et al. First dark matter search results from a surface run of the 10-L DMTPC directional dark matter detector. *Physics Letters B*, 695(1-4):124 – 129, 2011.
- [66] K. Nakamura. NEWAGE. Talk at CYGNUS2013, the 4th International Workshop on the Directional Detection of Dark Matter. Toyama, Japan, 2013.
- [67] N. J. C. Spooner. DRIFT-IIe and DRIFT-III. Talk at CYGNUS2013, the 4th International Workshop on the Directional Detection of Dark Matter. Toyama, Japan, 2013.
- [68] M. Pipe. *Limits on spin-dependent WIMP-proton cross-sections using the DRIFT-IIId directional dark matter detector*. PhD dissertation, University of Sheffield, Department of Physics and Astronomy, December 2011.
- [69] The Dark Matter Community Website : DM Tools Plotter. <http://dmttools.brown.edu:8080/>. Accessed May 29, 2013.
- [70] A. C. Kaboth. *Detecting the invisible universe with neutrinos and dark matter*. PhD dissertation, Massachusetts Institute of Technology, Department of Physics, 2012. <http://dspace.mit.edu/handle/1721.1/76980>.
- [71] J. P. Lopez et al. Background rejection in the DMTPC dark matter search using charge signals. *Nuclear Instruments and Methods in Physics Research Section A: Accelerators, Spectrometers, Detectors and Associated Equipment*, 696(0):121 – 128, 2012.
- [72] T. Caldwell et al. Transport properties of electrons in CF4. *ArXiv e-prints*, May 2009.
- [73] D. Dujmic et al. Charge amplification concepts for direction-sensitive dark matter detectors. *Astroparticle Physics*, 30(2):58 – 64, 2008.
- [74] A. Roccaro et al. A background-free direction-sensitive neutron detector. *Nuclear Instruments and Methods in Physics Research Section A: Accelerators, Spectrometers, Detectors and Associated Equipment*, 608(2):305 – 309, 2009.
- [75] H. Tomita. *Detector development for direction-sensitive dark matter research*. PhD dissertation, Boston University, 2011.
- [76] J. A. Formaggio and C. J. Martoff. Backgrounds to Sensitive Experiments Underground. *Annual Review of Nuclear and Particle Science*, 54:361 – 412, December 2004.
- [77] D.-M. Mei and A. Hime. Muon-induced background study for underground laboratories. *Phys. Rev. D*, 73:053004, Mar 2006.
- [78] C. Zhang et al. Measuring Fast Neutrons with Large Liquid Scintillation Detector for Ultra-low Background Experiments. *ArXiv e-prints*, April 2013.

- [79] R. Hennings-Yeomans and D. S. Akerib. A neutron multiplicity meter for deep underground muon-induced high-energy neutron measurements. *Nuclear Instruments and Methods in Physics Research A*, 574:89–97, April 2007.
- [80] BC-517S, BC-517H, BC-517L, BC-517P Mineral Oil Based Liquid Scintillators. Data Sheet. Saint-Gobain Ceramics & Plastics, Inc..
- [81] J. B. Birks. *The theory and practice of scintillation counting*, volume 27 of *International series of monographs on electronics and instrumentation*. Macmillan, New York, 1964.
- [82] J. Amann et al. A Proposal to Search for Neutrino Oscillations with High Sensitivity in the Appearance Channels $\nu_\mu \rightarrow \nu_e$ and $\bar{\nu}_\mu \rightarrow \bar{\nu}_e$. Technical Report LA-11842-P, Los Alamos National Laboratory, 1990.
- [83] M. B. Chadwick et al. ENDF/B-VII.0: Next Generation Evaluated Nuclear Data Library for Nuclear Science and Technology. *Nuclear Data Sheets*, 107(12):2931 – 3060, 2006.
- [84] J. H. Moore, C. C. Davis and M. A. Coplan. *Building Scientific Apparatus*, section 4.4.1. Cambridge University Press, New York, fourth edition, 2009.
- [85] XP4500B Photomultiplier Tubes Product Specification. Data Sheet. PHOTONIS Sensor Imaging Technologies.
- [86] VD105K Photomultiplier Tube Voltage Divider Product Specification. Data Sheet. PHOTONIS Sensor Imaging Technologies.
- [87] High Voltage Power Supply N1130. Data Sheet. Wenzel Elektronik.
- [88] WaveRunner[®] Xi-A Series. Data Sheet. Teledyne LeCroy.
- [89] P. W. Lisowski et al. The Los Alamos National Laboratory Spallation Neutron Sources. *Nucl. Sci. Eng.*, 106(2):208–218, 1990.
- [90] S. A. Wender et al. A fission ionization detector for neutron flux measurements at a spallation source. *Nuclear Instruments and Methods in Physics Research Section A: Accelerators, Spectrometers, Detectors and Associated Equipment*, 336(2):226 – 231, 1993.
- [91] C. Fuentes. LANSCE Nuclear Science Research Facilities User Guide. Technical Report LA-UR-11-05278, Los Alamos National Laboratory, Los Alamos, NM (USA), 2011.
- [92] P. W. Lisowski, LANL private communication, 1999.
- [93] J. L. Ullmann, LANL private communication, 1999.
- [94] N. Fotiadis, LANL private communication, 2011.

- [95] The Waste Isolation Pilot Plant : Pioneering Nuclear Waste Disposal. Technical Report DOE/CAO-00-3124, U.S. Department of Energy Carlsbad Area Office, 2000.
- [96] The MAJORANA Neutrinoless Double-beta Decay Experiment, <http://www.npl.washington.edu/majorana/>.
- [97] M. Auger et al. Search for neutrinoless double-beta decay in ^{136}Xe with EXO-200.
- [98] E.-I. Esch et al. The cosmic ray muon flux at WIPP. *Nuclear Instruments and Methods in Physics Research Section A: Accelerators, Spectrometers, Detectors and Associated Equipment*, 538(1-3):516 – 525, 2005.
- [99] E.-I. Esch. *Detector Development for Dark Matter Research*. PhD dissertation, Justus-Liebig Universität Giessen, Fachbereich Physik, September 2001. Los Alamos National Laboratory Technical Report LA-UR-01-3974.
- [100] M. J. Balbes et al. Evaluation of the WIPP site for the supernova neutrino burst observatory. *Nuclear Instruments and Methods in Physics Research Section A: Accelerators, Spectrometers, Detectors and Associated Equipment*, 399(2-3):269 – 274, 1997.
- [101] D.-M. Mei et al. Neutron Background Evaluation at the WIPP Site for Dark Matter Experiments. In *APS Division of Nuclear Physics Meeting Abstracts*, page C16, October 2004.
- [102] R. D. Boyer L. S. Pendlebury and O. L. Cordes. Radon monitoring at the Waste Isolation Pilot Plant. Technical Report DOE/WIPP-90-029C, CONF-910270-54, Westinghouse Electric Corp., Carlsbad, NM (USA). Waste Isolation Div., 1991.
- [103] L. W. Brewer and D. M. Minnema. Background radiation measurements at the Waste Isolation Pilot Plant (WIPP) Site, Carlsbad, New Mexico. Technical Report SAND-83-1296, Sandia National Labs., Albuquerque, NM (USA), 1983.
- [104] S. Agostinelli et al. Geant4-a simulation toolkit. *Nuclear Instruments and Methods in Physics Research Section A: Accelerators, Spectrometers, Detectors and Associated Equipment*, 506(3):250 – 303, 2003.
- [105] E. Aguayo et al. Depth Requirements for a Tonne-scale ^{76}Ge Neutrinoless Double-beta Decay Experiment. *ArXiv e-prints*, September 2011.
- [106] D. S. Leonard et al. Systematic study of trace radioactive impurities in candidate construction materials for EXO-200. *Nuclear Instruments and Methods in Physics Research Section A: Accelerators, Spectrometers, Detectors and Associated Equipment*, 591(3):490 – 509, 2008.

- [107] M. Auger et al. The EXO-200 detector, part I: detector design and construction. *Journal of Instrumentation*, 7:5010, May 2012.
- [108] B. E. Berger et al. The KamLAND full-volume calibration system. *Journal of Instrumentation*, 4(04):P04017, 2009.
- [109] J. Benziger et al. The nylon scintillator containment vessels for the Borexino solar neutrino experiment. *Nuclear Instruments and Methods in Physics Research Section A: Accelerators, Spectrometers, Detectors and Associated Equipment*, 582(2):509 – 534, 2007.
- [110] J. F. Amsbaugh et al. An array of low-background ^3He proportional counters for the Sudbury Neutrino Observatory. *Nuclear Instruments and Methods in Physics Research Section A: Accelerators, Spectrometers, Detectors and Associated Equipment*, 579(3):1054 – 1080, 2007.
- [111] P.J. Linstrom and W.G. Mallard, Eds., NIST Chemistry WebBook, NIST Standard Reference Database Number 69, National Institute of Standards and Technology, Gaithersburg MD, 20899, <http://webbook.nist.gov>, (retrieved April 28, 2013).
- [112] Tetrafluoromethane (Halocarbon 14); MSDS No. 001051 [Online]; Airgas Inc.: Radnor, PA, April 26, 2010, <http://www.airgas.com/documents/pdf/001051.pdf> (accessed April 28, 2013).
- [113] A. Morozov et al. Secondary scintillation in CF_4 : emission spectra and photon yields for MSGC and GEM. *Journal of Instrumentation*, 7(02):P02008, 2012.
- [114] D. Dujmic. Charge readout of DMTPC amplification plane. DMTPC Internal Note 29, Massachusetts Institute of Technology, October 2010.
- [115] L. G. Christophorou et al. Electron Interactions with CF_4 . *Journal of Physical and Chemical Reference Data*, 25:1341 – 1388, September 1996.
- [116] E. Basurto and J. De Urquijo. Mobility of CF_3^+ in CF_4 , CHF_2^+ in CHF_3 , and C^+ in Ar. *Journal of Applied Physics*, 91(1):36 – 39, 2002. cited By (since 1996)4.
- [117] R. Brun and F. Rademakers. ROOT - an object oriented data analysis framework. *Nuclear Instruments and Methods in Physics Research Section A: Accelerators, Spectrometers, Detectors and Associated Equipment*, 389(1-2):81 – 86, 1997. New Computing Techniques in Physics Research V. See also <http://root.cern.ch/>.
- [118] Bertan MWPC Module Models 375N/375P/375X, 377N/377P/377X, 380N/380P/380X. Installation and Operating Instruction Manual. Bertan Associates, Inc..
- [119] MKS Type 1479A Mass-Flo[®] Controller. Instruction Manual. MKS Instruments.

- [120] J. R. Janesick. *Scientific charge-coupled devices*, volume 83 of *SPIE Monograph*. The International Society for Optical Engineering Press, Bellingham, Washington, first edition, 2001.
- [121] A. Hitachi. Bragg-like curve for dark matter searches: Binary gases. *Radiation Physics and Chemistry*, 77(10-12):1311 – 1317, 2008. The International Symposium on Charged Particle and Photon Interaction with Matter - ASR 2007.
- [122] F. Sauli. Principles of operation of multiwire proportional and drift chambers. In *Lectures given in the Academic Training Programme of CERN, 1975-1976*, Geneva, 1977. CERN.
- [123] O. Guillaudin et al. Quenching factor measurement in low pressure gas detector for directional dark matter search. In F. Mayet and D. Santos, editors, *EAS Publications Series*, volume 53 of *EAS Publications Series*, pages 119 – 127, February 2012.
- [124] S. Henderson. Surface Commissioning of the DMTPC 4-Shooter Directional Dark Matter Detector Prototype. Talk at the 9th International Identification of Dark Matter Conference, July 2012.
- [125] J. P. Lopez. Updates from the DMTPC Dark Matter Search. In *APS Meeting Abstracts*, page 11008, April 2013.
- [126] S. B. Howell. *Handbook of CCD Astronomy*, volume 5 of *Cambridge observing handbooks for research astronomers*. Cambridge University Press, Cambridge, UK, second edition, 2006.
- [127] Berger, M.J., Hubbell, J.H., Seltzer, S.M., Chang, J., Coursey, J.S., Sukumar, R., Zucker, D.S., and Olsen, K. (2010), XCOM: Photon Cross Section Database (version 1.5). [Online] Available: <http://physics.nist.gov/xcom> [Sunday, 28-Apr-2013 21:40:00 EDT]. National Institute of Standards and Technology, Gaithersburg, MD. Originally published as Berger, M.J. and Hubbell, J.H., "XCOM: Photon Cross Sections on a Personal Computer," NBSIR 87-3597, National Bureau of Standards (former name of NIST), Gaithersburg, MD (1987); and as Berger, M.J. and Hubbell, J.H., "NIST X-ray and Gamma-ray Attenuation Coefficients and Cross Sections Database," NIST Standard Reference Database 8, Version 2.0, National Institute of Standards and Technology, Gaithersburg, MD (1990).
- [128] M. R. Bhat. Nuclear Data Sheets for $A = 57$. *Nuclear Data Sheets*, 85(3):415 – 536, 1998.
- [129] C. Tomasi and R. Manduchi. Bilateral filtering for gray and color images. In *Computer Vision, 1998. Sixth International Conference on*, pages 839 – 846, 1998.

- [130] V. Gregoric, private communication, 2012.
- [131] S. F. Ray. *Applied photographic optics : imaging systems for photography, film, and video*. Focal Press, Boston, 1988.
- [132] M. S. Basunia. Decay data evaluation, gamma-ray energies and multipolarities, decay scheme. *Nuclear Data Sheets*, 107:3323, 2006.
- [133] H. Raether. *Electron avalanches and breakdown in gases*. Butterworths advanced physics series. Monographs on ionization and electrical discharges in gases. Butterworths, Washington, D.C., 1964.
- [134] A. Bressan et al. High rate behavior and discharge limits in micro-pattern detectors. *Nuclear Instruments and Methods in Physics Research Section A: Accelerators, Spectrometers, Detectors and Associated Equipment*, 424(2ÄS3):321 – 342, 1999.
- [135] T. Skwarnicki. A study of the radiative CASCADE transitions between the Upsilon-Prime and Upsilon resonances. 1986.
- [136] G. F. Reinking, L.G. Christophorou, and S. R. Hunter. Studies of total ionization in gases/mixtures of interest to pulsed power applications. *Journal of Applied Physics*, 60(2):499 – 508, 1986.
- [137] A. Sharma. Properties of some gas mixtures used in tracking detectors. 1998.
- [138] I. C. Wolfe. *Measurement of work function in CF₄ gas*. Bachelor of science thesis, Massachusetts Institute of Technology, Department of Physics, 2010. <http://hdl.handle.net/1721.1/61268>.
- [139] CR-112 Charge Sensitive Preamplifier: Application Guide. Rev. 2.1 (Sep. 2012). Cremat, Inc..
- [140] CR-113 Charge Sensitive Preamplifier: Application Guide. Rev. 2.1 (Sep. 2012). Cremat, Inc..
- [141] S. Burgos et al. Measurement of the range component directional signature in a DRIFT-II detector using ²⁵²Cf neutrons. *Nuclear Instruments and Methods in Physics Research Section A: Accelerators, Spectrometers, Detectors and Associated Equipment*, 600(2):417 – 423, 2009.
- [142] H. Sekiya et al. Measurements of anisotropic scintillation efficiency for carbon recoils in a stilbene crystal for dark matter detection. *Physics Letters B*, 571(3-4):132 – 138, 2003.
- [143] H. Sekiya et al. Development of gaseous tracking devices for the search of WIMPs. *Nuclear Instruments and Methods in Physics Research Section A: Accelerators, Spectrometers, Detectors and Associated Equipment*, 573(1-2):204 – 207, 2007. Proceedings of the 7th International Conference on Position-Sensitive Detectors, PSD-7, 7th International Conference on Position-Sensitive Detectors.

- [144] G. F. Knoll. *Radiation detection and measurement*. John Wiley, Hoboken, N.J., fourth edition, 2010.
- [145] J.W. Marxh, D.J. Thomas, and M. Burke. High resolution measurements of neutron energy spectra from Am-Be and Am-B neutron sources. *Nuclear Instruments and Methods in Physics Research Section A: Accelerators, Spectrometers, Detectors and Associated Equipment*, 366(2-3):340 – 348, 1995.
- [146] Reference neutron radiations – Part 1: Characteristics and methods of production. Technical Report ISO 8529-1, 2001.
- [147] I. Jaegle et al. Simulation of the Directional Dark Matter Detector (D³) and Directional Neutron Observer (DiNO). In F. Mayet and D. Santos, editors, *EAS Publications Series*, volume 53 of *EAS Publications Series*, pages 111 – 118, February 2012.
- [148] R. A. Fisher. The use of multiple measurements in taxonomic problems. *Annals of Eugenics*, 7(2):179–188, 1936.
- [149] A. Hoecker et al. TMVA: Toolkit for Multivariate Data Analysis. *PoS, ACAT:040*, 2007.
- [150] ENDF/B-VI: Cross Section Evaluation Working Group, ENDF/B-VI Summary Document, Report BNL-NCS-17541 (ENDF-201) (1991), edited by P.F. Rose, National Nuclear Data Center, Brookhaven National Laboratory, Upton, NY, USA.
- [151] J. Billard. Neutron Monitoring with He-3 NCDs at MIT. Assay and Acquisition of Radiopure Materials Neutron Benchmarking Data Group Bi-weekly Meeting. <http://zzz.physics.umn.edu/lowrad/nmm>, 2013.
- [152] S. T. Thornton and J. B. Marion. *Classical Dynamics of Particles and Systems*. Brooks/Cole—Thomson Learning, Belmont, California, fifth edition, 2004.
- [153] V. A. Bednyakov and F. Šimkovic. Nuclear spin structure in dark matter search: The finite momentum transfer limit. *Physics of Particles and Nuclei*, 37(1):S106 – S128, 2006.
- [154] G. Belanger et al. micrOMEGAs3.1 : a program for calculating dark matter observables. *ArXiv e-prints*, May 2013.
- [155] F. James. *Statistical Methods in Experimental Physics: 2nd Edition*. World Scientific Publishing Co., Singapore, second edition, 2006.
- [156] L. Lyons. *Statistics for Nuclear and Particle Physicists*. Cambridge University Press, Cambridge, UK, first edition, April 1989.
- [157] M. S. Alenazi and P. Gondolo. Directional recoil rates for WIMP direct detection. *Phys. Rev. D*, 77:043532, Feb 2008.

- [158] B. Morgan and A. M. Green. Directional statistics for realistic weakly interacting massive particle direct detection experiments. II. 2D readout. *Phys. Rev. D*, 72:123501, Dec 2005.
- [159] S. Henderson, J. Monroe, and P. Fisher. Maximum patch method for directional dark matter detection. *Phys. Rev. D*, 78:015020, Jul 2008.
- [160] C. J. Copi and L. M. Krauss. Angular signatures for galactic halo weakly interacting massive particle scattering in direct detectors: Prospects and challenges. *Phys. Rev. D*, 63:043507, Jan 2001.
- [161] O. Host and S. H. Hansen. What it takes to measure a fundamental difference between dark matter and baryons: the halo velocity anisotropy. *Journal of Cosmology and Astroparticle Physics*, 2007(06):016, 2007.
- [162] Dinesh Loomba. R&D with Implications for a Directional Low Mass Dark Matter Search. Talk at CYGNUS2013, the 4th International Workshop on the Directional Detection of Dark Matter. Toyama, Japan, 2013.